Timing Observations

of

Southern Pulsars

by

Franco D'Alessandro, B.App.Sc., B.Ed.

Submitted in fulfilment of the
requirements for the degree of
Doctor of Philosophy

Physics Department
University of Tasmania
Hobart

December, 1995

Declaration

This thesis contains no material which has been accepted for the award of any other degree or diploma by the University or any other institution, except by way of background information and duly acknowledged in the thesis, and to the best of my knowledge and belief, no material previously published or written by another person, except where due reference is made in the text of the thesis.

Franco D'Alessandro

Authority of Access

This thesis may be made available for loan. Copying of any part of this thesis is prohibited for two years from the date this statement was signed; after that time, limited copying is permitted in accordance with the *Copyright Act 1968.*

Franco D'Alessandro

Thesis Summary

Pulse arrival-time measurements made at frequencies near 670 and 800 MHz over a 7-year period have been used to study the timing behaviour of 45 southern pulsars. These measurements have resulted in more accurate estimates of the period, period derivative, position and dispersion measure of most of these pulsars. Changes in some of the dispersion measures have been detected and used to estimate the scale-sizes and electron densities of irregularities in the interstellar medium. The timing measurements also revealed distinct jumps in the rotation rate of five pulsars, most of which have not been reported elsewhere.

Polarimetric data at 670 and 800 MHz are presented for eighteen of the more luminous pulsars. The integrated profiles display properties in general agreement with trends extrapolated from other frequencies. Rotation measures have been derived for these pulsars. Nine are more accurate than previous determinations, and two have changed since they were last measured. These changes suggest a dense, magnetised electron cloud has moved into or out of the line of sight.

It has been confirmed that the level of pulsar timing noise is correlated with spin-down rates. Further analyses have revealed that, in most pulsars, the observed timing noise is due to a mixture of different kinds of activity, such as random walk processes, microjumps, and for one pulsar, free precession of the spin axis. The microjumps are characterised by a variety of signatures, involving both positive and negative changes in the rotation frequency and frequency derivative. The amplitudes of these microjumps form the tail-end of a continuous distribution of amplitudes extending down to microglitch level. An investigation of timing noise in the Vela pulsar has shown that the microactivity during the postglitch recovery period is dominated by microjumps in the rotation frequency and frequency derivative which occur every 30–40 days. This microactivity is also punctuated by less frequent events, such as large steps in the frequency derivative, discrete changes in the frequency second derivative, and in one isolated case, a small glitch. The above results have been discussed in terms of current theories of pulsar timing noise and it was found that no theoretical model, in isolation, is able to explain the range of observed timing activity in the pulsars studied.

Power spectra of the pulsar timing residuals have been derived using a novel technique based on the CLEAN algorithm. Most of the spectra are well described by a single- or double-component power-law model. Some of these spectra can be interpreted in the context of one or more of the current timing noise models.

Acknowledgements

I wish to thank my supervisors, Prof. P.M. McCulloch and Prof. P.A. Hamilton, for their expert guidance and good advice during the course of my research project. I acknowledge the valuable contributions made by Dr. D. McConnell, Dr. E.A. King, Mr. A.B. Neilson and Mr. S.T. Hutchinson to the early stages of the pulsar timing survey. I am also grateful to Dr. E.A. King and Dr. T.D. van Ommen, for their assistance with matters related to the computing facilities and software in the Physics Department, and the Mt Pleasant Observatory manager, Mr. G. Gowland, for his assistance with the many technical problems arising during the observing runs. The ionospheric data for Hobart was kindly supplied by Mr. G. Goldstone, to whom I am grateful for providing such an accurate and prompt service.

I acknowledge receipt of nine months of study leave in 1991 from my employment as a full-time Physics Lecturer at the University of Tasmania at Launceston. I wish to thank Dr. R.P. Rodgers for ensuring that my teaching load over the last three years was kept down to a bearable level, and Mr. A.V. Kidd for assistance with proof-reading the thesis.

I am greatly indebted to my good friend Dr. A.A. Deshpande, for countless helpful discussions, critical reading of this thesis and for helping me to understand some of the wonders of digital signal processing. Last, but not least, I extend a very special "thank you" to my family, for their love and support, and particularly my wife, for being so patient during many lonely evenings, and over the last 12 months, my baby boy, who has forced me to keep up my energy levels.

Contents

List of Tables

List of Figures

Chapter 1

Introduction

1.1 Overview

The unexpected discovery of pulsating radio sources (Hewish *et al.* 1968), or pulsars, in 1967 by a team of astronomers at Cambridge opened a new era in radio astronomy. Soon after their discovery, Gold (1968) concluded that they must be highly magnetised, rapidly rotating neutron stars. In the basic model, beams of radio emission sweep past the Earth once every rotation period, like signals from celestial lighthouses.

Long-term observations of pulsars have provided a wealth of information about the structure and emission processes of neutron stars, yet there are still many unanswered questions. Over recent years, considerable progress has been made in gaining a better understanding of neutron star interiors, but comparatively little is known about their mechanism of radiation. The pulsed nature of the emission has provided a unique probe of many properties of the interstellar medium, such as the scale-sizes of irregularities, electron densities, and magnetic fields. Pulsar observations have also provided a new avenue for studying the end-points of stellar evolution.

In recent times, a number of radio pulsars have been observed at optical, X-ray and γ-ray frequencies (e.g., see Mereghetti *et al.* 1994). Measurements across a wide range of the electromagnetic spectrum such as these have necessitated the development of a number of new observing techniques. It is anticipated that these multiwavelength studies will also address a number of fundamental questions, such as those relating to the emission process and the thermal evolution of neutron stars.

More generally, pulsar research provides serious tests of a number of the major physical theories, under conditions not reproducible in a laboratory. The physics involved in this process ranges from classical dynamics and electromagnetism to quantum mechanics and general relativity. For further discussion of the relationship between pulsar research and physics in general, the reader is referred to the

monogram *Pulsars as Physics Laboratories*, 1993 (eds. Blandford, R.D., Hewish, A., Lyne, A.G. & Mestel, L.), Oxford University Press.

The study of pulsars presents many challenges to both observers and theorists. With questions remaining about the structure and emission processes of pulsars, more accurate models can be developed provided there is a comprehensive data set of pulsar observations. This thesis presents the data and results of the analysis of up to 7 years of timing observations on 45 pulsars located at southerly declinations. The aim is twofold, namely to: (i) provide a more complete description of the pulsar sample studied, and (ii) add to the existing knowledge concerning the structure and dynamics of pulsars.

This project has involved work in software development, receiver modification, monthly observing sessions, data processing and analysis of the results. All of these aspects are described in the chapters which follow. A brief synopsis of these chapters is given below.

The remainder of this chapter presents an overview of pulsar topics relevant to the chapters which follow. Chapter 2 presents an overview of current theoretical models of rotational irregularities in pulsars, namely glitches and timing noise. A working knowledge of these theories is needed for the data analyses and conclusions presented in later chapters. Chapter 3 describes the observing hardware and procedures used to collect and calibrate the pulsar data. Chapter 4 describes the method of analysis of the pulsar timing data. It also presents and discusses the basic results obtained from the analysis. Chapter 5 describes the method of analysis of the polarization data. Integrated polarization profiles and Faraday rotation measurements are presented and discussed. Chapter 6 presents an in-depth time-domain analysis of the timing noise of the 45 pulsars under study. Chapter 7 presents an in-depth analysis of the timing noise of the Vela pulsar, using data obtained from daily observations with a dedicated 14-metre telescope. Chapter 8 analyses the timing noise of all 46 pulsars in the frequency domain. Power spectra are computed using a novel technique which can recover steep spectra from unevenly sampled data. The results of the research presented in the thesis are summarised and conclusions are drawn in Chapter 9. Several appendices follow the main body of the thesis. Appendices A and B provide supporting material for the polarization work presented in Chapter 5. Appendices C and D contain plots of phase residuals and templates, respectively, for each pulsar in the study. Appendix E lists the author's publications in scientific journals resulting from particular aspects of the research conducted during the course of this project.

1.2 Basic Pulsar Properties

At the present time, over 600 pulsars are known. They all share some basic characteristics, which will be summarised in this section.

Most pulsars have rotation periods between 0.1 and 2.5 seconds. These pulsars are relatively young and mostly isolated. Henceforth, these will be termed "long-period" pulsars. In contrast, there is a small class of pulsars with very short periods. These "millisecond" pulsars are believed to be neutron stars that have evolved through the normal age span, but have subsequently undergone a spin-up process involving a binary companion. "Recycled" millisecond pulsars with rotation periods as small as 1 ms have been discovered. Over half of the known millisecond pulsars are in binary systems.

The basic unit of emission is the *pulse* – the radiation received during one rotation of the neutron star. The duration of the pulse is typically only a few percent of the rotation period, indicating that the emission is localised to some extent. The rotation period is usually described in terms of longitude, where 360° of longitude is one rotation period. Following from this representation, the arbitrary position of the pulse within a period is referred to as the *pulse phase*, where the phase is simply expressed as a fraction of the rotation period (i.e., 0 to 1.0). The relationship between the accumulated phase, ϕ, after a time $t - t_o$ and the rotation frequency, ν, of the neutron star is

$$\phi(t) - \phi(t_o) = \int_{t_o}^{t} \nu(t')dt'. \tag{1.1}$$

Although much can be learnt about the emission mechanism from a study of individual pulses, a general view of processes occurring can be obtained from the *integrated profile* of a pulsar. This is a mean pulse profile which is obtained by summing hundreds of consecutive pulses synchronously with the pulsar period "on-line", or by folding a continuous data stream "off-line". The integrated profile is sometimes referred to as the "pulse window". Although emission occurs at varying phases with respect to the rotation period, it is confined to this well-defined pulse window. The profile is very stable and is a distinguishing characteristic of the pulsar. The shapes of the pulse windows range from simple profiles with a single peak or *component*, to complex profiles consisting of up to five separate components, which may partially overlap. The separation, width, and relative amplitudes of the components of a profile are generally slowly varying functions of the observing frequency (Manchester & Taylor 1977). Initially, a simple classification scheme was used for the different profile shapes: Type S for "single" profiles, Type C for "complex" profiles, and Type D for pulsars with drifting subpulses (Manchester & Taylor 1977). This simple scheme has been extended by a number of authors over the years (e.g., see Backer 1976, Rankin 1983, *et seq.*, and Lyne & Manchester 1988).

A small number of pulsars exhibit a temporary alteration of the pulse profile to another stable form. This phenomenon is known as *mode changing*. The mode change lasts for 100's to 1000's of periods before returning back to the original mode. This feature is most common in multicomponent pulsars and appears to

be a redistribution of the emitting regions of the neutron star (Rankin 1986).

Some pulsars emit a second pulse separated from the main pulse by about half the rotation period. These *interpulses* have been interpreted as radio emission from the opposite magnetic pole of the neutron star.

One characteristic of pulsar emission is the variation of its intensity. The observed pulse intensities vary over a wide range of time-scales, ranging from microseconds to hundreds of days. Most of the variations with time-scales up to 1000 seconds are attributed to effects intrinsic to the pulsar. Pulsar observations conducted with high time resolution reveal that individual pulses consist of two or more *subpulses* with characteristic widths of one or two percent of the period. These subpulses exhibit large changes in intensity and can occur at fixed longitudes within a pulse or move randomly about a mean location. Some pulsars exhibit a phenomenon known as *drifting subpulses*, where the successive subpulses drift uniformly in longitude across the pulse. At even higher time resolutions, the subpulses from some pulsars contain bursts of micropulses, with characteristic widths of 0.1 percent of the period. On a time-scale of many rotation periods, the pulse intensity may suddenly drop to a low value for a time interval lasting from a few periods to hundreds of periods. There is a correlation of pulsar age with this *pulse nulling* behaviour, suggesting that this phenomenon may represent the last stages of pulsed emission (Ritchings 1976, Rankin 1986).

In general, the individual pulses of radio emission from a pulsar are highly polarized (see Appendix A for a description of polarization), sometimes completely linearly polarized. The polarization properties vary from pulse to pulse, often in a systematic fashion. On the other hand, integrated profiles exhibit relatively stable polarization features. In most pulsars, the linear polarization dominates the circular component. The latter rarely exceeds 20 percent of the total intensity. Unlike most radio sources, the average degree of polarization of pulsar profiles generally decreases with increasing observing frequency (Manchester *et al.* 1973). The position angle of the linearly polarized emission (i.e., the orientation of the electric vector on the sky) usually shows a smooth variation across the pulse window. For a given pulsar, the variation in position angle is the same at all frequencies. For Type C pulsars, the position angle curve often has a characteristic "S" shape, with a rapid variation near the centre of the profile and slow variation near the leading and trailing edges of the profile (Manchester & Taylor 1977). In some pulsars, the polarization profiles show abrupt changes of the position angle by 90°. This effect is thought to be related to the two orthogonal modes of polarized emission observed in individual pulses, where the average profile reflects the dominant mode at different points in the pulse.

Variations in pulse intensities over longer time-scales (e.g., days to months) make it difficult to determine the spectrum of the radio emission from pulsars. Careful investigations have shown that the emission spectrum at radio frequencies

above 100 MHz approximates a power law, $S = S_o f^{\alpha}$, where S is the flux density, f is the observing frequency and α is the *spectral index*, which is typically between -1 and -2 (Manchester & Taylor 1981, Lorimer *et al.* 1995). Further, there appears to be a spectral turnover at lower frequencies, where the spectral index becomes positive. Since the mean flux density of most pulsars is weaker than the galactic background radio emission, it is often only possible to observe them by taking advantage of their pulsed nature. At 400 MHz, the mean flux densities are typically less than 0.1 Jy (Jy:Jansky; 1 Jy = 10^{-26} $\mathrm{Wm^{-2}Hz^{-1}}$).

1.3 Pulsar Timing

One of the outstanding properties of pulsars is the regularity of their rotation period. In many cases, the rotation period is more stable than 1 part in 10^{12}. The period can be determined with great accuracy by measuring the arrival times of the emitted pulses. These measurements must be corrected for a number of effects, such as the motion of the Earth around the Sun. If the period is known with sufficient accuracy, it can be used to predict the arrival time of a pulse at some time in the future. However, over an interval of months, the measured pulse arrival times begin to show signs of departure from the predicted arrival times (if the period is assumed constant). The difference between the measured and predicted arrival times (or *residuals*) defines a parabolic curve, showing that the pulsar period is changing at a uniform rate over the time span of the observations. This measured period derivative is positive, that is, the pulsar is slowing down or losing energy. Most pulsars have period derivatives of the order of 10^{-15} $\mathrm{ss^{-1}}$. Millisecond pulsars have period derivatives $3-4$ orders of magnitude smaller.

The loss of rotational energy implies that some form of braking torque is acting on the pulsar. A number of theoretical models have been proposed for this secular deceleration in the rotation rate. They predict that the torque is proportional to some power of the rotation frequency,

$$\dot{\nu} = -k\nu^n \tag{1.2}$$

where k is a constant and n is known as the "braking index". If the pulsar has a measurable frequency second derivative, $\ddot{\nu}$, then from Equation 1.2, the braking index is given by

$$n = \frac{\nu\ddot{\nu}}{\dot{\nu}^2} \tag{1.3}$$

The simplest of the theoretical models, energy loss by constant magnetic dipole radiation and particle emission (Pacini 1968, Ostriker & Gunn 1969), gives a braking index $n = 3$. Variations of this basic model give braking indices between 1 and 5. For example, a model of energy loss from gravitational radiation or decay of the magnetic field gives $n > 3$, and a model in which there is a secular change

in the orientation of the magnetic field relative to the rotation axis gives $n < 3$ (Manchester & Taylor 1977).

Integration of Equation 1.2 yields a time-scale for the loss of rotational energy from which an upper limit for the age of the pulsar (or the "characteristic age") can be obtained, namely

$$\tau = -\frac{\nu}{(n-1)\dot{\nu}} \tag{1.4}$$

For the Crab pulsar, this gives a characteristic age of about 1240 years (using $n = 3$), compared to a time span of about 940 years since its birth in the supernova event of 1054 AD.

Long-term timing observations have shown that, superimposed on the secular spin-down of pulsars, there are unpredictable variations in the pulse periods. For most pulsars, the residuals show the signs of small, random fluctuations known as "timing noise". In a statistical sense, these fluctuations are nonstationary in nature, producing excursions in the timing residuals of up to one pulse period over several years. On the other hand, a number of pulsars have been observed to undergo one or more large, discontinuous increases in their rotation frequency, known as "glitches". Analyses of both these types of period irregularities provide valuable information about the interior of neutron stars. The nature of these irregularities is described further in Chapter 2.

It would be inappropriate to conclude this section without briefly mentioning two recent astronomical findings of great significance which have resulted directly from pulsar timing observations. Firstly, the detection of Doppler-shifted arrival times from a millisecond pulsar has revealed two or more planet-sized companions (Wolszczan & Frail 1992). This planetary system is the first to be discovered outside our solar system. Second, J.H. Taylor and R. Hulse won the 1993 Nobel Prize in Physics for their work on binary pulsar timing which has conclusively verified Einstein's General Theory of Relativity (Taylor 1992, Taylor *et al.* 1992, and references therein). Both of these achievements demonstrate that pulsar timing is a powerful astronomical tool.

1.4 Pulsar Polarization

Pulsar emissions are unique because of the relatively high degree of polarization they contain. Polarization observations and their interpretation provide an avenue for understanding the magnetospheric structure and emission mechanisms of pulsars. As a detailed review of pulsar magnetospheres and emission mechanisms is beyond the scope of this thesis, only a brief summary follows. The reader is referred to the reviews by Smith (1977), Manchester & Taylor (1977), Michel (1982, 1987) and Lyne & Smith (1990) for more detailed information.

Not long after the discovery of pulsars, Goldreich & Julian (1969) showed that

a neutron star would have an atmosphere of charged particles which depends on a strong electric field generated by the rotating magnetic dipole field. The predicted magnetic and electric field strengths of the order of $10^{10} - 10^{12}$ G and 10^{12} V cm^{-1} respectively. The electric field is large enough to detach electrons and protons from the surface of the neutron star, forming a charged region called the *magnetosphere* (Fig. 1.1). The magnetic field co-rotates with the star at a velocity which increases with radius, out to the *light cylinder*, where the velocity reaches the speed of light (radius, $r_c = c/\omega$). Co-rotation must stop short of the light cylinder, at which point the magnetic field is swept back. Hence, the dipole field contains two distinct zones: an "open" field region along the dipole axis where the field lines do not close inside the light cylinder, and an electrically inactive "closed" field region where the lines loop inside the light cylinder. The model attributes the radio emission to clumps of charges accelerated along the open magnetic field lines. Goldreich & Julian only considered a pulsar with aligned rotation and magnetic axes, although an inclination of the two axes is thought to be more common. The theory has a number of other problems, even though the observed pulse shapes and polarization variations are roughly consistent with the standard model.

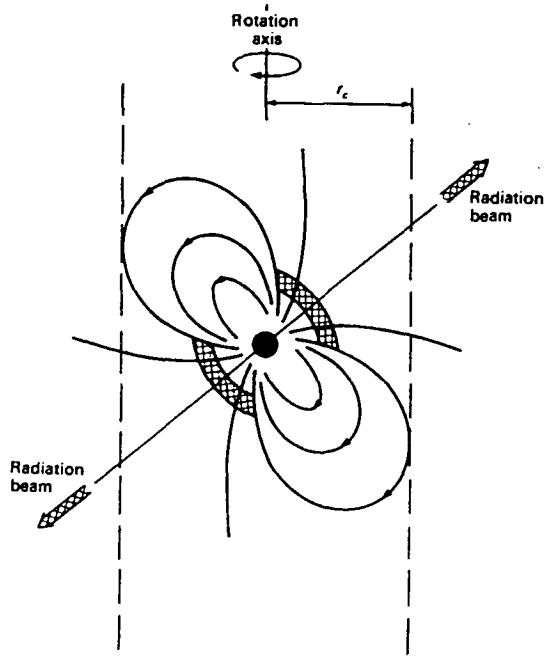

Figure 1.1: The rotating magnetosphere of a neutron star. Radio emitting regions are shown cross-hatched; (from Lyne & Smith 1990).

The *spark gap* model proposed by Ruderman & Sutherland (1975) corrected some of the flaws in the Goldreich & Julian model. In this model, acceleration of charged particles away from the surface of the neutron star creates a vacuum gap with a potential difference of $\sim 10^{12}$ V. Energetic photons (e.g., γ-rays) entering this region produce electron-positron pairs which are accelerated by the electric

field and produce more photons, which trigger further pair production, culminating in a spark discharge. This mechanism explains the phenomena of micropulses and subpulses to some extent, although there are difficulties with the model. For example, it does not easily account for the high radiated powers.

The Ruderman & Sutherland mechanism implies that the emission originates near the magnetic poles of the neutron star. In general, two pulsar emission models have been explored in detail. These are commonly known as the *polar cap* and *light cylinder* models. The names refer to the location of the emission region in the pulsar magnetosphere, i.e., immediately above a magnetic pole and near the light cylinder respectively. The mechanism that produces the emission in these locations is expected to be different. In the polar cap model, charged particles streaming along the open field lines near the magnetic poles may be expected to emit *curvature radiation*, whereas a location near the light cylinder involves pulse formation by a geometrical *relativistic beaming* process (Smith 1977). The main evidence for polar cap models stems from the observed duty cycle of the pulsations and observations of linear polarization. Light cylinder models are supported by the observed widths of subpulses and high energy observations of the young Crab and Vela pulsars. On the other hand, drifting sub-pulses, orthogonal polarization modes and circular polarization have proven difficult to model. Light cylinder models also face the difficulty of producing stable profiles at a large distance from the neutron star, where the particle energies are comparable to or larger than the magnetic field energy (Taylor & Stinebring 1986).

In general, the polar cap models have been more successful in accounting for the phenomenological aspects of pulsar emission than light cylinder models. However, to the present day, there is no single theory of pulsar electrodynamics that provides an explanation of all the observed emission features from pulsars. These features include (Backer 1989; Smith 1977, Chapter 16):

- an extremely high brightness temperature;
- a stable mean pulse profile consisting of one or more components;
- swing in the linear polarization vector with a signature that depends on the component structure of the pulse profile;
- slow decrease of the pulse width with increasing radio frequency and rotation period;
- an interpulse located about halfway between the main pulses;
- 90° (orthogonal) transitions in the position angle of the linear polarization vector, and circularly polarized emission;
- memory in the pulse-to-pulse fluctuations (such as drifting subpulses), pulse nulling and mode changes;
- erratic pulse-to-pulse amplitude fluctuations; and
- micropulses.

A discussion of present inconsistencies and future directions can be found in the review by Radhakrishnan (1990).

The polar cap model has received considerable attention because it is reasonably successful in explaining the linear polarization observations of pulsars. Since the main thrust of this section is pulsar polarization, this aspect will be reviewed in a little more detail. The rotating-vector model of Radhakrishnan & Cooke (1969) is particularly useful for this purpose.

Based on polarization observations of the Vela pulsar, Radhakrishnan & Cooke (1969) suggested that the monotonic swing of the linear polarization angle across the pulse results from a projection of the linear vector (which is aligned along the magnetic field lines) onto the sky as the neutron star rotates. This *rotating-vector* model predicts a range of possible position angle (PA) swings for emission at a fixed altitude in a dipole field, given by

$$\tan PA(t) = \frac{\sin\alpha \sin\phi(t)}{\sin\xi \cos\alpha - \cos\xi \sin\alpha \cos\phi(t)} \tag{1.5}$$

where α and ξ are the stellar colatitudes of the magnetic axis and the line of sight respectively, and ϕ is the longitude of the magnetic axis relative to the plane defined by the rotation axis and the line of sight. The maximum PA sweep is 180° and polarization observations show that most pulsar emission occurs within $\alpha - \xi \simeq 10°$ of the magnetic axis (Backer 1989).

The observation by Radhakrishnan & Cooke (1969) that the linear polarization position angle varies smoothly through the pulse and that some profiles have two main components led to the suggestion that the emission is strongest in a *hollow-cone* beam which is symmetric about the magnetic axis. This morphology also suggested that these beams originate near the magnetic poles of the neutron star (Lyne & Manchester 1988). The S-shaped sweep of the PA in pulsars with two-component integrated profiles (e.g., see Figure 5.15) is precisely what is predicted by the above model. Another typical example comes from pulse profile studies which show that the widths of single-component profiles are narrower than the two-component profiles. This is to be expected if the single component arises when the Earth-pulsar line of sight passes through the outer rim of the hollow cone. The fact that most profiles decrease in width with increasing radio frequency (distinct from interstellar effects, which are described later) suggests that higher frequency emission is produced close to the poles while lower frequencies are produced at higher altitudes where the field lines subtend a greater angle (Cordes 1978).

The emission from some pulsars includes a centrally located third component (e.g., see Figure 5.19), the so-called "core" component. This is consistent with a "cone" which is filled in some inner regions. The empirical study by Rankin (1983, 1986, 1990), based on the polarization data from 100 pulsars, has been significant in gaining a better understanding of pulsar emission characteristics. The results show that the properties of cone components are distinctly different from

the core components, and suggest that there are two distinct emission processes. Lyne & Manchester (1988), using data from more than 200 pulsars, confirmed the existence of the differing properties of core and conal emission but found that the observations are best described by a gradual change in the emission characteristics from the core to the outer edge of the beam, rather than two distinct emission processes.

1.5 The Interstellar Medium

Pulsar observations provide the astronomer with a unique probe of the interstellar medium (ISM). Measurement of absorption at 1420 MHz by clouds of neutral hydrogen atoms gives information about HI cloud structure and sometimes provides an estimate of the pulsar distance (Manchester & Taylor 1977). The pulsed nature of pulsar emission is ideal for measuring signal dispersion resulting from free electrons in the ISM. The ionisation that produces these electrons comes from the ultraviolet radiation of hot stars, cosmic rays, and shocks generated by star-forming events and supernova explosions. These shocks are thought to be the source of turbulence in the ISM (Backer 1989). The resulting irregularities alter the frequency-time structure of pulsar signals because these objects are effectively point sources. Measurements of these effects can be used to infer some of the parameters of the medium along the line of sight. Furthermore, large-scale plasma currents give rise to interstellar magnetic fields, whose strength can be measured from observations of the rotation of the plane of linearly polarized pulsar emission.

1.5.1 Interstellar Dispersion

The theory of radio wave propagation in a plasma is needed in order to describe the effect of the ISM on pulsar signals. A basic result is that signals are *dispersed* as a result of the frequency-dependent index of refraction, i.e., pulses at lower observing frequencies arrive later than those at higher frequencies. The refractive index is given by

$$n = \left[1 - \left(\frac{f_p}{f}\right)^2\right]^{-\frac{1}{2}} \tag{1.6}$$

where f is the observing frequency (Hz) and f_p is the plasma frequency (Hz), given by

$$f_p = \frac{1}{2\pi}\sqrt{\frac{n_e e^2}{\epsilon_o m_e}}. \tag{1.7}$$

Here, n_e is the free electron number density, e is the charge on an electron, m_e is the mass of an electron and ϵ_o is the permittivity of free space. The frequency-dependent group velocity of the radio waves is given by

$$v_g = c\left[1 - \left(\frac{f_p}{f}\right)^2\right]^{\frac{1}{2}}. \tag{1.8}$$

The effects of this dependence are only observed for pulsed radiation. The arrival time of a pulse is the integral of the inverse of the group velocity over the path, L, and so the difference in arrival time between pulses emitted at frequencies f_1 and f_2 will be

$$t_2 - t_1 = \frac{e^2}{2\pi m_e c}\left(\frac{1}{f_2^2} - \frac{1}{f_1^2}\right)\int_0^L n_e dl \tag{1.9}$$

where c is the speed of light.

The column density along the path, $\int_0^L n_e dl$, is known as the *dispersion measure* (DM) and this can be calculated directly from the measured difference in arrival times by using

$$DM = \alpha_d\,(t_2 - t_1)\left(\frac{1}{f_2^2} - \frac{1}{f_1^2}\right)^{-1} \tag{1.10}$$

where $\alpha_d = 2.410 \times 10^{-16}$ cm^{-3}pc s, t_1 and t_2 are in seconds, f_1 and f_2 are in Hz, with the DM in units of cm^{-3}pc. As Taylor *et al.* (1993) point out, the precision of α_d is not critical as Equation 1.10 is only an approximation. It ignores the effects of heavy ions in determining the interstellar refractive index.

The dispersion measures for known pulsars extend from less than 10 cm^{-3}pc to more than 1000 cm^{-3}pc. Changes in the DM over a period of time for a particular pulsar indicate that a region of excess electron density has moved into or out of the line of sight. The magnitude of the change can be used to obtain estimates of the density and scale-sizes of the electron clouds.

If an independent estimate of the average electron density, $<n_e>$, along the line of sight to a pulsar is available, the DM can be used to compute the pulsar distance. Alternatively, if the distance to the pulsar is determined independently, an estimate of $<n_e>$ can be obtained. A value of about 0.03 cm^{-3} is thought to be typical for the ISM.

Pulsar dispersion measures have been used to develop models of the electron distribution in the Galaxy. There is evidence for three components to the dispersion: (i) nearby, intervening ionised hydrogen (HII) regions; (ii) a thin disk associated with ionisation from hot, young stars; and (iii) a large halo whose scale-height exceeds the scale-height of the pulsar population (Manchester & Taylor 1977). As more data have been gathered over the years, more comprehensive models of the galactic distribution of free electrons have been developed (e.g., see Cordes *et al.* 1991, Taylor & Cordes 1993).

Observations of the intrinsically weak and dispersed signals from pulsars always pose limitations on the time resolution of the pulse structure or the sensitivity achieved. For a given time resolution, the maximum bandwidth that can be employed is determined by the frequency drift resulting from dispersion. The time smearing due to dispersion, τ_d (s), within a finite bandwidth, Δf (MHz), at an observing frequency, f (MHz), is given by

$$\tau_d \simeq 8299\, DM \left(\frac{\Delta f}{f^3}\right) \tag{1.11}$$

This equation can be inverted to obtain the maximum bandwidth which can be employed for a given time resolution. For a constant fractional time resolution, τ_d/P (where P is the pulsar period), the observing bandwidth is determined by the ratio P/DM, making short-period, high-dispersion pulsars the most difficult to observe. Chapter 3 describes how dispersion smearing was minimised for the pulsar observations made in this study.

1.5.2 Interstellar Faraday Rotation

The ISM is threaded by weak magnetic fields, and so waves from a radio source travel to the Earth through a "magnetoplasma". The index of refraction for such a medium is given by

$$n^2_{O,X} = 1 - \frac{f_p^2}{f^2\left(1 \pm \frac{f_c}{f}\right)} \tag{1.12}$$

where f_p (Hz) is the plasma frequency, as before, and f_c (Hz) is the cyclotron frequency ($f_c \simeq 2.8 B_{||}$ Hz/μGauss). $B_{||}$ is the longitudinal component of the magnetic field, i.e., the line of sight field. A linearly polarized signal can be considered as the sum of two equal-amplitude, oppositely rotating, circularly polarized signals (as described in Appendix A). In Equation 1.12, the subscripts O and X and the $+$ and $-$ signs correspond to the ordinary (right circular) and extraordinary (left circular) modes of propagation. The difference in group delay for these two modes is about seven orders of magnitude less than the dispersive delay, and so it is ignored in dispersion calculations.

The position angle of a linearly polarized signal is determined by the phase relationship between the two circularly polarized components (see Appendix A). Hence, as the signal propagates through the ISM, the changing phase between the propagation modes will cause the plane of polarization to rotate. This phenomenon is known as *Faraday rotation*. The effect is cumulative, and so weak interstellar magnetic fields can cause substantial rotation over long distances. The angle of rotation (in radians) along a path of length L is given by

$$\theta = 0.812\, \lambda^2 \int_0^L n_e B_{||} dl \tag{1.13}$$

where λ is the observing wavelength (m), and n_e, $B_{||}$, and l are in units of cm^{-3}, μG and parsecs respectively. The *rotation measure* (RM) of the pulsar is defined as

$$RM = 0.812 \int_0^L n_e B_{||} dl \tag{1.14}$$

It represents the mean value of the longitudinal magnetic field weighted by the electron density. The RM is positive for a magnetic field directed toward the observer and negative for a field directed away, following the "modern" convention (see Appendix A).

In practice, the RM is found by measuring the difference in position angle at two wavelengths λ_1 and λ_2, so that

$$RM = \frac{\theta_2 - \theta_1}{\lambda_2^2 - \lambda_1^2} \tag{1.15}$$

To obtain accurate rotation measures, the measurements are made at two widely separated frequencies. The separation required to achieve a given accuracy decreases as the observing centre frequency decreases, since the amount of rotation is relatively large at lower frequencies (Equation 1.13). "Instrumental" Faraday rotation effects which can lead to depolarization of the linearly polarized content must also be considered. The measurements must be made with a receiver whose bandwidth (Δf) is small enough so that differential Faraday rotation across the passband ($\Delta\theta$) is only a small fraction of the rotation itself (at a particular observing centre frequency, f), where

$$\frac{\Delta\theta}{\theta} = -2\frac{\Delta f}{f} \tag{1.16}$$

For a given amount of differential rotation (in radians), the fraction of the linear polarization remaining is given by

$$F_L = \frac{\sin \Delta\theta}{\Delta\theta} \tag{1.17}$$

(Gardner & Whiteoak 1966).

Together with the DM of the pulsar, the RM can be used to estimate the mean longitudinal magnetic field (in μG), given by

$$<B_{||}> \simeq \frac{\int_0^L n_e B_{||} dl}{\int_0^L n_e dl} = 1.232 \frac{RM}{DM}, \tag{1.18}$$

demonstrating that pulsars are very useful tools for studying the Galactic magnetic field. Their importance is enhanced by the fact that the emission often has a high degree of linear polarization and there is apparently no intrinsic Faraday rotation (Manchester & Taylor 1977).

Based on a sample of 61 pulsars, Manchester (1972, 1974) found that the local magnetic field is directed along the local spiral arm of the Galaxy, close to galactic longitude $\ell = 90°$ and latitude $b = 0°$, with a field strength of $2-3\ \mu$G. This local field extends to a distance of at least 1 kpc. These results are similar to those obtained from the rotation measures of extragalactic radio sources (Gardner *et al.* 1969). There appear to be irregularities superimposed on this uniform field, with comparable field strengths and scale-sizes up to a few hundred parsecs (Manchester 1974). Thomson & Nelson (1980) have found that the strength of the irregular component of the magnetic field may be as high as $14\,\mu$G. These irregularities may result from disturbances created by the expansion of supernova remnants, or HII regions, or from the contraction of cold clouds.

More recently, Hamilton & Lyne (1987) extended the number of known pulsar rotation measures by 119, increasing the number available for statistical analyses by a factor of three. Many of the new rotation measures are for distant pulsars, providing a probe of the magnetic field over greater distances than was previously possible. The individual field strengths reach values up to about $\pm 4\,\mu$G, with most regions of the sky containing only one sign of the field component. Lyne & Smith (1989) used the RMs and DMs of 185 pulsars to model the Galactic magnetic field. They found: (i) the local magnetic field has a strength of $2-3\ \mu$G and it is directed towards $\ell = 90°$, (ii) a reversed field of $5-7\ \mu$G between longitudes in the range $0° - 90°$, (iii) evidence for field reversals in other directions. Rand & Lyne (1994), using the data for an additional 27 distant pulsars, obtained similar results but also found further evidence of large-scale magnetic field reversals.

1.5.3 Interstellar Turbulence

In propagating through the ISM, pulsar signals undergo intensity modulations due to interference between rays scattered by small-scale irregularities in the electron density (Scheuer 1968). The modulations are correlated over narrow bandwidths (typically < 1 MHz) and time-scales of minutes (Figure 1.2). The effect has been analysed by using a simple method in which the perturbing medium is collapsed into a thin scattering screen situated between the pulsar and the earth (see Scheuer 1968, Manchester & Taylor 1977). The scattering is associated with scale-sizes of the order of the Fresnel-zone radius $r_f = \sqrt{fD}$, where f is the frequency of the signal and D is the distance of the scattering screen from the observer (Backer 1989). The temporal modulation, known as *diffractive interstellar scintillation* (DISS), is a result of the relative motion of the observer, the medium and the pulsar, and is analogous to the familiar "twinkling" of optical stars due to atmospheric density fluctuations.

The spectral features such as those shown in Figure 1.2 can be described statistically by a characteristic frequency bandwidth and a characteristic time span

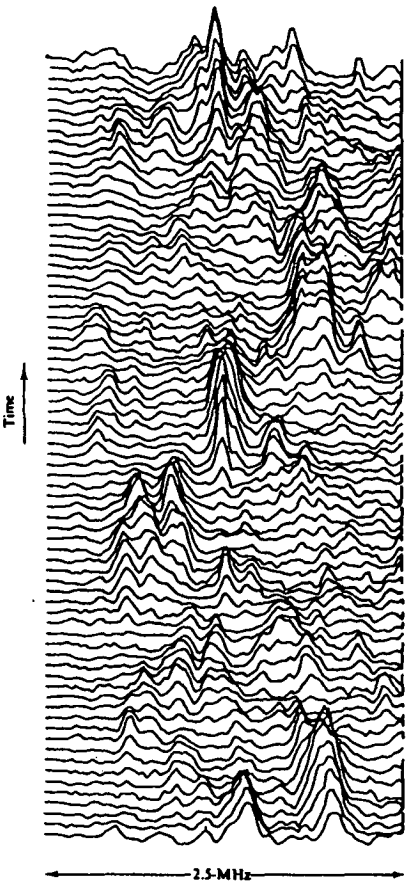

Figure 1.2: Spectral structure of the pulses from PSR B0329+54, produced by interstellar scintillation. Successive mean pulse spectra at 408 MHz are shown at intervals of 50 seconds; (after Rickett 1969).

over which the observed intensities decorrelate. These quantities are known as the *decorrelation bandwidth*, Δf_s, and *decorrelation time*, τ_s, respectively. A simple analysis (e.g., see Manchester & Taylor 1977) shows that

$$\Delta f_s \propto \frac{f^4}{DM^2} \tag{1.19}$$

and

$$\tau_s \propto \frac{f}{\sqrt{DM}} \tag{1.20}$$

where f is the observing frequency and DM is the dispersion measure. That is, the parameters are related to the path length traversed through the turbulent interstellar plasma. The modulation in frequency arises from the frequency dependence of the location of the maxima and minima in the diffraction pattern.

DISS is only observed if the source diameter is less than the scale of the diffraction pattern at the earth. Otherwise, patterns from different parts of the source overlap and cancel out. Hence, pulsars are ideal objects for an investigation of these effects. Scintillation is only observable for other radio sources if their angular diameter is less than the scattering angle, typically 10^{-7} arcsec (Stinebring

& Condon 1990), but pulsars are the only known sources to exhibit strong DISS (Rickett 1990).

In addition to amplitude scintillations, the multipath propagation is also responsible for an increase in the apparent angular size of the source and a broadening of the pulses received at the earth. The latter effect is most noticeable at lower observing frequencies. Propagation along direct and scattered ray paths causes the emitted pulse to be asymmetrically broadened in time. The observed pulse profile is therefore a convolution of the actual pulse shape with a truncated exponential whose characteristic time width τ_B is just Δf_s^{-1} (Lyne & Smith 1990), and so

$$\tau_B \propto \lambda^4 DM^2 \tag{1.21}$$

This λ^4 dependence has been verified for a number of pulsars. In the present study, the profile of the high DM pulsar PSR B1641-45 is a striking example of pulse broadening due to interstellar scattering (see Appendix D).

A more general model of interstellar scattering assumes a medium whose properties are defined by a spatial power spectrum of the electron density irregularities. In the simple thin-screen model used to derive the above results, this power spectrum is assumed to be Gaussian. Evidence has been accumulating that the interstellar turbulence conforms to a spatial power-law spectrum of the form

$$P_{\delta n_e}(k) = C_n^2 k^{-\alpha}, \quad \frac{2\pi}{l_0} \leq k \leq \frac{2\pi}{l_1} \tag{1.22}$$

where k is the wavenumber, C_n^2 is the spectral coefficient (or the level of turbulence), l_0 and l_1 are the outer and inner scale-sizes respectively (Cordes *et al.* 1985). The power-law index has been determined empirically for many lines of sight, and is consistent with the "Kolmogorov" value ($\alpha = \frac{11}{3}$) for fully developed incompressible fluid turbulence (Cordes *et al.* 1991). For small-scale irregularities (10^9 to 10^{11} cm), this power-law spectrum yields scaling rules similar to Equations 1.19 to 1.21.

In addition to DISS, the early pulsar observations showed slow variations (days to years) in the apparent intensity. These were considered to be intrinsic effects, but upon re-examination of the data, Sieber (1982) found that the time-scales of the variations were correlated with the dispersion measure. It was suggested that the flux variations were caused by propagation effects. Sieber's work led Rickett *et al.* (1984) to propose that *refractive interstellar scintillation* (RISS) may produce the slow intensity variations in pulsars and possibly compact extragalactic sources. RISS is thought to be due to focusing or defocusing of rays from the source by inhomogeneities with scale-sizes larger than the Fresnel-zone scale (e.g., 10^{11} to 10^{15} cm). Rickett *et al.* also suggested that the fluctuations in electron density are part of the same power-law spectrum which produces DISS (e.g., an extended Kolmogorov power-law spectrum).

Following these proposals, theoretical investigations by a number of workers (Blandford & Narayan 1985, Romani *et al.* 1986, Cordes *et al.* 1986, Rickett 1986, Coles *et al.* 1987) have predicted many new, observable phenomena. Some examples include fluctuations in the angular sizes, pulse arrival times and pulse widths of pulsars, and the amplitude of the intensity fluctuations. The time-scale of the flux variations is predicted to increase as a positive power of the observing wavelength and the DM.

Following Sieber's work and the theoretical predictions, there have been a number of new RISS studies of pulsar fluxes (Stinebring & Condon 1990, Rickett & Lyne 1990, Kaspi & Stinebring 1992, Gupta *et al.* 1993, LaBrecque *et al.* 1994). The results tend to support an extended Kolmogorov power-law spectrum of interstellar plasma turbulence, with some modifications. The full extent of the spectrum is not known, but recent work suggests inner scales as small as $\sim 10^7$ cm and outer scales as large as 10^{18} cm (Cordes *et al.* 1991). The standard Kolmogorov model prediction of the amplitude of the intensity variations does not agree with all the pulsar flux observations. Early evidence of this discrepancy led some theoreticians to propose a steeper spectrum, with $\alpha \geq 4$ (Blandford & Narayan 1985). The nature of the power spectrum is still being debated and clearly, more observational data are needed.

In summary, observations of the effects of both DISS and RISS are useful probes of the ISM, and are essential to constrain theoretical models of the scattering medium. DISS observations can also be used to determine the space velocities of pulsars, and hence, provide a means of investigating the correlation between pulsar velocity and other parameters (Cordes 1986).

Chapter 2

Rotational Irregularities in Pulsars

2.1 Introduction

Long-term timing observations have shown that the rotation rates of pulsars are subject to two types of irregularities: continuous, erratic fluctuations known as "timing noise", and a more spectacular discontinuous increase in the rotation frequency known as a "glitch". Some degree of timing noise has been observed in most pulsars, whereas glitches have been observed in only a small percentage of the pulsar population. A feature common to both of these types of irregularities is that they are more prominent in younger pulsars. Two relatively young pulsars, Crab and Vela, are well-known for their high level of intrinsic timing noise and regular glitches. Over the last 27 years, Vela has undergone 10 large glitches and Crab has undergone 6 small glitches.

This chapter describes the observational aspects of glitches and timing noise and reviews the theoretical models that have been developed to explain these phenomena. While a detailed study of glitches is beyond the scope of this thesis, a review is included here as a background to the material presented in Chapters 4 (Pulsar Timing Observations) and 7 (Vela Timing Noise). Hence, the main emphasis will be on the Vela pulsar glitches. Furthermore, some glitch models (e.g., the theory of vortex creep) have been extended in an attempt to explain timing noise in pulsars and a review is therefore necessary. Timing noise is reviewed in considerable detail as this aspect of pulsar timing forms the main thrust of the thesis.

2.2 Glitches

Glitches have now been observed in a total of fourteen pulsars (see Alpar & Baykal 1994, Table 1, and references therein). In addition, the Mt Pleasant timing observations described in this thesis have revealed the first observed glitch in PSR B1727-47 (see Chapter 4). Glitches are characterised by fractional increases in the rotation rate ($\Delta\nu/\nu$) of 10^{-6} to 10^{-9} and a simultaneous increase in the magnitude of the frequency derivative, $\dot{\nu}$. The magnitude of the changes in the latter parameter vary greatly, with values ranging from 0.1% to 10%. The glitch is followed by a relatively slow exponential recovery of the rotation frequency and decay of the frequency derivative toward their preglitch values. This "postglitch relaxation" takes place over a period of days to years.

The postglitch behaviour differs considerably from one pulsar to another, as shown in Figure 2.1. After a glitch, the frequency derivative is larger than the preglitch value but the rate at which it decays is variable. In the Vela pulsar, about half of the initial increment in $\dot{\nu}$ decays away in a matter of days, followed by a slow relaxation of the remainder of the increment (McCulloch *et al.* 1987, 1990, Cordes *et al.* 1988, Alpar *et al.* 1993). In PSR B0355+54, almost all of the frequency derivative increment decayed away with a time-scale of 44 days, possibly leaving a permanent step in the rotation frequency (Lyne 1987). The glitches in the Crab pulsar are characterised by a persistent and cumulative increase in the frequency derivative (Lyne *et al.* 1993). This means that this pulsar is now rotating more slowly than it would have without the glitches.

The glitches in some pulsars do not appear to be followed by any relaxation. This can arise if the relaxation time is short and the timing observations are relatively sparse. In this case, the jump parameters obtained from the observations will be the permanent or long-term values. Another possibility is that the relaxation time is so long that the relaxation is not yet obvious.

A number of glitch models have been proposed to explain the observations. Discussion of these models depends on an understanding of the theoretical neutron star structure. Hence, a brief summary of the predictions about the structure of neutron stars is provided here as background material.

2.2.1 Neutron Star Structure

A neutron star is believed to form a number of distinct layers soon after its creation, including an outer crust and a superfluid neutron interior. The specific structure is heavily dependent on the model used, although most theories predict a common general structure.

Neutron stars are predicted to have masses between 0.2 and 2.0 solar masses ($M_\odot$). A typical neutron star with a mass of $1.4M_\odot$ has a radius of 10–15 km and

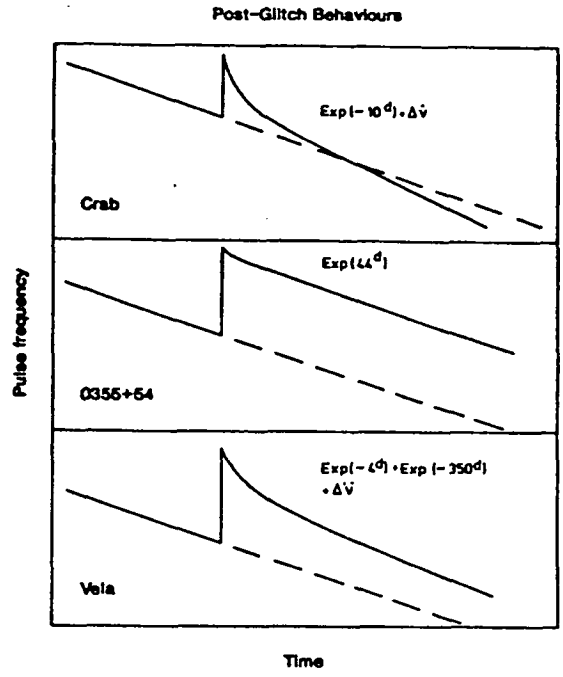

Figure 2.1: Diagram showing the different types of postglitch relaxation observed in pulsars; (after Manchester 1992).

a central density between 10^{14} and 10^{15} g cm^{-3}. The general structure of a $1.4M_{\odot}$ neutron star is shown in Figure 2.2. The main uncertainty in the theoretical models is the *equation of state* (EOS) of neutron matter which, at densities exceeding the density of nuclear matter ($\rho_o \simeq 2.8 \times 10^{14}$ g cm^{-3}), determines the mass-radius relation, the extent of the crust, the central density, etc. (Pandharipande *et al.* 1976). More recent calculations have led to a stiffer EOS than the results of 20 years ago.

The outer crust of a neutron star is a very rigid and strong crystalline lattice, with an approximate density range of $10^6 - 10^{11}$ g cm^{-3}. At these densities, electrons penetrate the nuclei and combine with protons to form neutron-rich nuclei, surrounded by an electron plasma (Ruderman 1969). The electrons only weakly screen the nuclei because they are relativistic and so the nuclei become strongly coupled. Any local stresses in the lattice are rapidly dissipated throughout the crystal.

As the pressure increases further into the star, the nuclei become increasingly neutron rich. When the density reaches approximately 4.3×10^{11} g cm^{-3}, the so-called *neutron drip* point, it becomes energetically favourable for neutrons to occupy continuum states and the nuclei become surrounded by a highly degenerate neutron liquid (Pines & Alpar 1985). This neutron liquid is a superfluid, i.e., it has no viscosity. There exist different states of superfluidity, depending on the quantum state of the pairing between neutrons resulting from the attractive force.

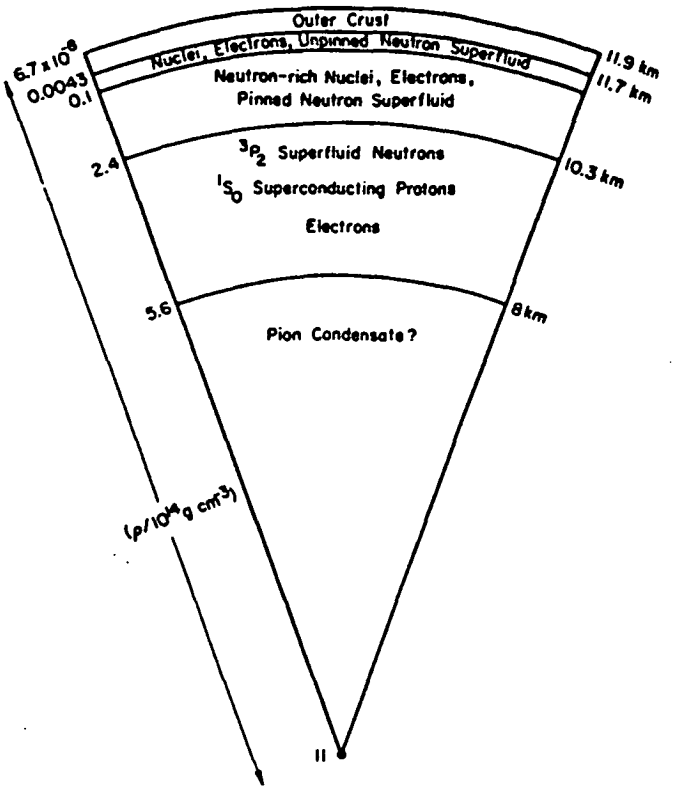

Figure 2.2: Theoretical cross-section of a 1.4 solar mass neutron star; (after Pines & Alpar 1985).

At the densities present in this *inner crust* region of the star, the superfluid is isotropic, with neutrons pairing in a $^1S_0$ quantum state.

At densities above 2×10^{14} g cm^{-3}, a lattice of nuclei can no longer exist. Hence, the core of a neutron star is expected to consist mainly of superfluid neutrons, with an admixture of a few percent of superconducting protons and normal electrons (Pines & Alpar 1985). The higher pressure in the core means that the neutrons will pair in the $^3P_2$ state, giving an anisotropic superfluid. The protons pair in the $^1S_0$ superconducting state. There remains a possibility that the neutron star has a solid core for densities greater than 3×10^{14} g cm^{-3} (Lyne & Smith 1990).

2.2.2 Glitch Models

There are two aspects of glitches which, to some extent, can be considered separately: the cause of the sudden increase in rotation frequency and the postglitch relaxation. Many models have been proposed to explain one or both of these aspects of glitches, such as the heat pulse, starquake, two-component and vortex creep models. The latter three models will be briefly reviewed here. The reader is referred to Greenstein (1981), and references therein, for details relating to the

heat pulse model. Of all the models proposed so far, the theory of vortex creep has been the most successful in explaining the glitch observations.

Starquakes

Shortly after the first Vela glitch, Ruderman (1969) proposed the *crustquake* glitch model. This model was based on investigations of the surface structure of neutron stars (Ruderman 1968). It assumes that a neutron star solidifies with an oblate and highly rigid crust. As the spin rate of the neutron star slows (and hence the requirement for a change toward a more spherical shape), stresses steadily build up in the crust until they reach a point where the crust cracks and readjusts to a less oblate form. This decreases the moment of inertia and, by conservation of angular momentum, results in a sudden increase in the rotation rate

$$\frac{\Delta\Omega}{\Omega} = -\frac{\Delta I}{I} \tag{2.1}$$

where Ω is the angular frequency and I is the moment of inertia of the neutron star. The radial displacement required to produce a glitch is typically ≤ 1 cm.

It is likely that crustquakes are responsible for some glitches. For example, Alpar *et al.* (1994) have proposed that the Crab pulsar glitches are caused by starquakes induced by pulsar spin-down. However, starquakes only explain the glitch itself. The postglitch relaxation requires an additional explanation. Models which allow for both of these aspects have typically involved superfluid vortex pinning and unpinning (Ruderman 1976), which is discussed below.

The crustquake model does not explain the Vela pulsar glitches. These glitches are about 100 times larger ($\Delta\nu/\nu \simeq 10^{-6}$) than those observed in the Crab pulsar and require a change in the crust oblateness of more than 3% each time. Furthermore, based on the estimated energy release in a typical Vela glitch, the crustquake model predicts an interval of hundreds of years between glitches rather than the observed $2-3$ years (Lyne & Smith 1990).

Pines *et al.* (1972) proposed an alternative theory for the Vela glitches in terms of their *corequake* model. This model relies on the possibility of a solid core in the neutron star. The shear modulus of an oblate solid core is expected to be much larger than that of the crust. Consequently, the core would possess a substantial reservoir of gravitational and elastic energy. Hence, the corequake model is capable of accommodating the magnitude and frequency of the Vela glitches.

The main problems with the corequake model are: (i) doubt about the existence of solid cores in neutron stars (Alpar & Ho 1983), and (ii) the amount of energy released and the frequency with which this energy is released would heat the neutron star to the point where it would be a much stronger source of X-rays than is actually observed for the Vela pulsar (Manchester & Taylor 1977).

Two-component Model

The starquake model makes no predictions about the postglitch relaxation. Baym *et al.* (1969) developed the *two-component* neutron star model in order to explain the relaxation after the first Vela glitch. This model is too simple to explain the range of postglitch behaviours observed since that time, but the theory behind it is valuable in understanding more complex models.

In this model, the neutron star consists of a charged, non-superfluid crust and a neutron superfluid interior which is loosely coupled to the crust. The superfluid interior is rotating more rapidly than the crust, since the external torques responsible for the secular spin-down of the star act on the crust rather than the interior. The pulse frequency obtained from pulsar timing observations is simply the rotation rate of the crust (since the magnetic field is locked to the crust) and so information about the interior of the star can be deduced from the effect it has on the crust.

Under the influence of the external braking torque, N, the crust and superfluid components slow down according to the relations

$$I_c\dot{\Omega}_c = -N + (I_c/\tau_r)(\Omega_n - \Omega_c) \tag{2.2}$$

and

$$I_n\dot{\Omega}_n = -(I_c/\tau_r)(\Omega_n - \dot{\Omega}_c) \tag{2.3}$$

where Ω_c and Ω_n represent the angular velocity of the crust and neutron superfluid, I_c and I_n are the moments of inertia of the two components, and τ_r is the relaxation time describing the frictional coupling between the two components. The total moment of inertia is given by $I = I_c + I_n$. In the equilibrium situation, $\dot{\Omega}_c = \dot{\Omega}_n = -N/I$ and so

$$\Omega_n - \Omega_c = \frac{I_n}{I_c}\frac{\tau_r}{T}\Omega_c \tag{2.4}$$

where $T = -\Omega_c/\dot{\Omega}_c$. Hence, the frictional coupling between the two components is proportional to the difference in angular velocities.

A sudden increase in the angular velocity of the crust (e.g., as a result of a starquake) forces $\Omega_n - \Omega_c$ below its equilibrium value. As a result, the braking torque on the crust increases, producing an increase in $\dot{\Omega}_c$ until equilibrium is restored. From Equations 2.2 and 2.3, the time dependence of Ω_c after the glitch is described by the "glitch function"

$$\Omega_c(t) = \Omega_o(t) + \Delta\Omega_c[1 - Q(1 - e^{-t/\tau})] \tag{2.5}$$

where $\Omega_o(t)$ is the extrapolated pre-glitch value of Ω_c and $\tau = \tau_r I_n/I$ is the time constant of exponential decay of the frequency step. The parameter Q ($0 \leq Q \leq 1$) measures the fraction of the frequency step that decays away. It is related to

the relative moments of inertia of the two components, given approximately by $Q \approx I_n/I$, and therefore,

$$\tau \approx Q\tau_r \approx TQ\frac{\Delta\Omega_c/\Omega_c}{\Delta\dot{\Omega}_c/\dot{\Omega}_c} \tag{2.6}$$

(Manchester & Taylor 1977).

Although the first few Vela glitches could be adequately modelled using the two-component theory, the parameters it suggested for the internal structure of the star were incompatible with the starquake hypotheses of glitches. Furthermore, using timing data recorded within one day of the 5th Vela glitch, McCulloch *et al.* (1983) found that a second exponential term was required to adequately model the data. These authors proposed that the new term was due to a superfluid region that is closely coupled with the crust of the neutron star. Hence, this new behaviour demanded a closer investigation of the physics involved in the glitch process. The two-component model was also found to be inconsistent with the persistent shift in the frequency derivative following the 1975 glitch in the Crab pulsar and the glitch in PSR B0525+21 (Downs 1982). These inconsistencies led to increased scrutiny of the superfluid dynamics in neutron stars and the subsequent development of the *vortex creep* theory of glitches.

Coupling and Vorticity in Neutron Stars

As discussed in the previous sections, the combined starquake and two-component models do not adequately describe the amplitude, rate and relaxation processes of the Vela pulsar glitches, as well as some other glitches. Models proposed after the two-component model attempted to explain the first few Vela glitches, and involved an explanation in terms of interactions between the neutron star crust and the superfluid neutrons.

A quantitative explanation was presented in terms of the pinning and unpinning of microscopic *vortices* within the neutron star (Anderson & Itoh 1975, Ruderman 1976). This work used the results of laboratory experiments with hard superconductors. The two important results are: (i) the rotational state of a superfluid is determined by an array of quantised, angular momentum vortex lines, each carrying vorticity $\kappa = h/2m_n$, where h is Planck's Constant and m_n is the mass of a neutron; and (ii) the motion of these vortex lines is governed by interactions with normal matter, including the possible *pinning* of the lines to crustal nuclei.

The area density of the vortices is a measure of the rotation rate of the superfluid. Hence, spin-down of the superfluid requires that the vortices move radially outward from the spin axis. This is believed to take place in the superfluid core of neutron stars, which comprises the bulk of the moment of inertia of the star. This component is predicted to be tightly coupled to the crust, via interactions of

the population of the core protons and electrons with the crust (Ruderman 1976, Alpar *et al.* 1981). The coupling time is expected to be of the order of a few seconds (Alpar *et al.* 1984).

It is the small component ($\sim 1\%$ of the total mass) of the superfluid coexisting with the inner crust nuclei that is believed to be responsible for glitches. Anderson & Itoh (1975) pointed out that vortices may become pinned to the crustal nuclei as a result of attractive or repulsive interactions in this region of the neutron star. Pinned vortices cannot move outwards and so the angular velocity of the crustal superfluid, Ω_s, remains constant. Thus, a differential rotation is maintained between the two components as the angular velocity of the crust, Ω_c, decreases. The different rotation rates give rise to a radial Magnus force which acts outwards because $\Omega_s > \Omega_c$. The magnitude of this force is proportional to the difference in angular velocity, $\omega = \Omega_s - \Omega_c$. If the pinning force is greater than the Magnus force, then the vortices will remain pinned. However, during the course of pulsar spin-down, there is a critical value ω_{cr} of the crust-superfluid lag that may be reached which corresponds to the point where the Magnus force exceeds the pinning force. A glitch results from the catastrophic unpinning of the vortices, which move rapidly outward and impart their angular momentum to the crust.

Ruderman (1976) extended the vortex pinning theory of glitches, with specific reference to the Vela pulsar. He proposed that, in certain density regimes, the pinning force is strong enough that the vortex lines will never unpin. Instead, the build up of stresses will ultimately fracture the crust of the neutron star. These stresses are directed away from the spin axis. The resulting outward motion of the crustal lattice also carries outwards the pinned crustal superfluid vortices. This results in a sudden transfer of angular momentum to the crust, causing a glitch in the observed rotation rate of the star. Ruderman (1991,1992) recently refined this model and has applied it to the glitches observed in a number of pulsars.

Hence, the pinned crustal neutron superfluid can be responsible for glitches by: (i) catastrophic unpinning of vortex lines, or (ii) stressing the crustal lattice to the point where the crust cracks. In either case, the estimated time interval between glitches in the Vela pulsar is close to the observed times (Pines & Alpar 1992).

In both of these models, a different mechanism is needed to explain the postglitch relaxation. Ruderman (1976) has suggested that *crustal lattice creep* occurs in response to the large pinning stresses that develop as ω increases. This process effectively reduces the magnitude of $\dot{\Omega}_c$. An increase in the magnitude of $\dot{\Omega}_c$ is observed at the time of the glitch as these stresses are relieved by the crustquake. However, a much more detailed model of the postglitch relaxation has been presented by Alpar *et al.* (1984a). This model is described in the next section.

Vortex Creep Model

Alpar *et al.* (1984a,b) have greatly extended these basic ideas into their theory of *vortex creep*. This theory attempts to explain both the process that causes glitches and the postglitch relaxation on the basis that there exist a number of distinct superfluid regions in the inner crust with differing pinning energies. The model has been successful in providing a quantitative explanation of the postglitch behaviour of a number of pulsars, most notably the Vela and Crab pulsars.

In this theory, the pinned crustal neutron superfluid follows the spin-down of the crust (which includes all components of the star that couple to the crust on shorter than observable time-scales) by means of thermally induced outward creep of vortex lines against the pinning energy barriers. Physically, vortex creep is a process of quantum tunnelling in a radial direction between adjacent pinning sites (Alpar *et al.* 1984a). Alpar *et al.* (1984a) suggest that there are regions where the crustal superfluid transfers angular momentum to the crust by continuous vortex creep. In these regions, there exists a steady state lag, ω_∞, where the crust and superfluid spin down at the same rate ($\dot{\Omega}_s = \dot{\Omega}_c = \dot{\Omega}_\infty$). Regions where the lag is greater than ω_∞ do not undergo steady state vortex creep. If local fluctuations raise ω above ω_{cr} (the critical lag where the Magnus force exceeds the pinning energy), there will be a sudden catastrophic unpinning and outward motion of a large number of vortices. This number is thought to be $\geq 10^{13}$ in the Vela pulsar. By conservation of angular momentum, there will be an increase in the angular velocity of the crust given by

$$I_c \Delta\Omega_c = \sum_i I_i \delta\Omega_i \tag{2.7}$$

where I_i and $\delta\Omega_i$ represent the moment of inertia and the decrease in the angular velocity, respectively, of the various regions of superfluid through which the free vortices move at the time of the glitch.

Using the notation of Alpar *et al.* (1984a), during the course of a glitch a large number of vortices unpin in some region G (the glitch site), move radially outward through a region B, and eventually repin in another region G′. If δN vortices unpin at a radius r_G and move to a radius $r_{G'} = r_G + \delta r_G$ (where $\delta r_G \ll r_G$), then the average change in the superfluid velocity between regions G and G′ is

$$\delta\Omega_B = \kappa \delta N / 2\pi r_B^2 \tag{2.8}$$

where $r_B = r_G + \delta r_G/2$. From Equation 2.7, the angular momentum transferred from the superfluid to the crust due to this vortex motion is

$$I_c \Delta\Omega_c = (\frac{1}{2} I_A + I_B)\delta\Omega_B \tag{2.9}$$

where $I_A \equiv I_G + I_{G'}$ is the total moment of inertia of the pinned superfluid in regions G and G′ and I_B is the moment of inertia of the pinned superfluid in

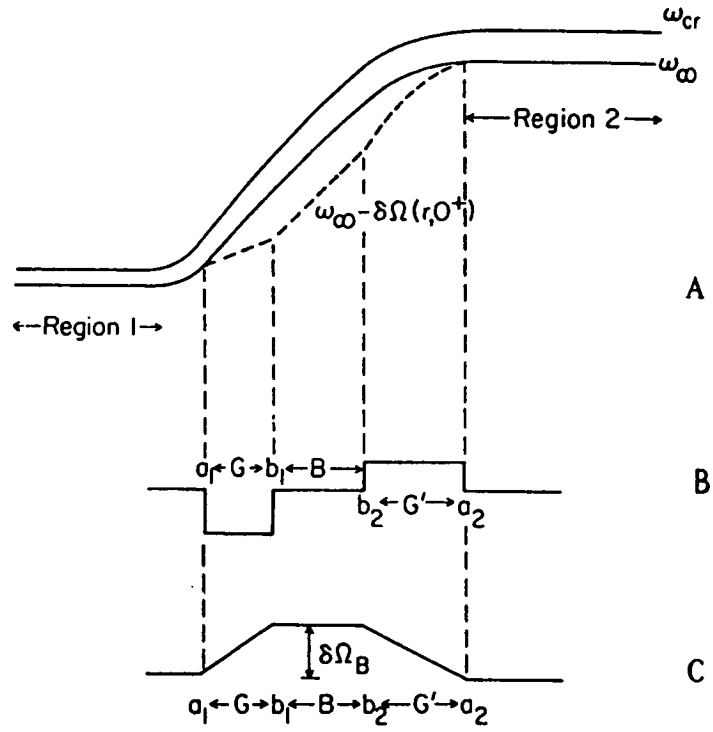

Figure 2.3: Model of a glitch, in which vortices unpin in region G, move through region B, and repin in region G′. The distance from the rotation axis increases to the right, and density to the left. A. Variation of ω_{cr} and ω_∞; B. The change in vortex density at a glitch; C. The change in the superfluid angular velocity; (after Alpar *et al.* 1984a).

region B. The factor of $\frac{1}{2}$ arises from taking a mean value based on the assumption that there is a linear decrease in the superfluid angular velocity across regions G and G′.

For the Vela pulsar, the distribution of pinning centres and ω_{cr} in region B is such that a vortex density and vortex creep current cannot be sustained (Cheng *et al.* 1988). Therefore, the superfluid torque from region B is zero both before and after the glitch. Although this region cannot contribute to any change in the internal torque exerted by the superfluid on the crust, the passage of vortices through it gives rise to a change in the crustal superfluid angular momentum $I_B\delta\Omega_B$ (Pines & Alpar 1992, Alpar *et al.* 1993). Figure 2.3 illustrates the behaviour at the boundary between regions G and G′.

Because the glitch decreases the superfluid angular velocity, the lag between the superfluid and the crust decreases by an amount $\delta\omega$. In regions A, this decrease temporarily stops the continuous vortex creep process and, hence, uncouples these regions from the crust. Therefore, the external torque acts on less moment of inertia and the spin-down rate suddenly increases by

$$\frac{\Delta\dot{\Omega}_c}{\dot{\Omega}_c} = \frac{I_A}{I} \tag{2.10}$$

This assumes that vortex creep cannot occur in region B. The observed behaviour and time interval between glitches support this assumption (Alpar *et al.* 1993). If vortex creep occurred in region B, the inter-glitch times would be much longer. After the glitch, region A will slowly recouple to the crust as vortex creep recommences.

According to Alpar *et al.* (1989,1993), in a given region of the star, there can be two different regimes of dynamical response to the glitch. A *linear* regime occurs when the temperature, T, is sufficiently large so that (thermally induced) vortex creep is fast enough to bring about a steady state situation with a small lag. Each part of the superfluid that responds in the linear creep regime will have a simple exponential relaxation as a function of time. The amplitude of the exponential is linear in the perturbation of the lag, $\delta\omega$, affected by the glitch in that particular region (Alpar *et al.* 1993). This regime will produce a predictable response in the spin-down rate of the crust, since the crust obeys the equation

$$I_c\dot{\Omega}_c = N_{\rm ext} + N_{\rm int} \tag{2.11}$$

where $N_{\rm ext}$ is the external spin-down torque and $N_{\rm int}$ is the total internal torque coupling various parts of the superfluid to the crust, given by $N_{\rm int} = \sum_i I_i\dot{\Omega}_i$. The exponential decay of the perturbation $\Delta\dot{\Omega}_{c,i}(t)$ in the spin-down rate due to a region i will occur with a time-scale $\tau_{l,i}$ characteristic of that region (Alpar *et al.* 1989) such that

$$\Delta\dot{\Omega}_{c,i}(t) = -\frac{I_i}{I}\frac{\delta\omega_i(0)e^{-t/\tau_{l,i}}}{\tau_{l,i}} \tag{2.12}$$

where $\delta\omega_i(0) = \Delta\Omega_c + \delta\Omega_i(0)$ is the decrease in the superfluid lag induced by the glitch. The characteristic relaxation time τ_l is given by

$$\tau_l = \frac{kT}{E_p}\frac{\omega_{cr}r}{4\Omega_c v_o}e^{E_p/kT} \tag{2.13}$$

where $v_o \sim 10^7$ cm s^{-1} is the typical velocity of microscopic vortex motion and E_p is the pinning energy of the region of superfluid. Hence, the relaxation time constants can be used to estimate the internal temperature of neutron stars.

A *nonlinear* regime occurs when the temperature is sufficiently low compared to the pinning energy and a large steady state lag, close to ω_{cr}, is needed for the superfluid to spin down under the external torque (Alpar *et al.* 1993). The response has a nonlinear dependence on the offset in the lag and a Fermi-function dependence on time (Alpar *et al.* 1984a,b) although under certain circumstances, the time dependence may be simplified, as described below. The contribution of nonlinear creep region k to the relaxation of the perturbation in $\dot{\Omega}_c$ is

$$\frac{\Delta\dot{\Omega}_{c,k}(t)}{\dot{\Omega}_c} = -\frac{I_k}{I}\left\{1 - \frac{1}{1 + [e^{(t_{0,k}/\tau_{n,k})} - 1]e^{(-t/\tau_{n,k})}}\right\} \tag{2.14}$$

where

$$t_{0,k} = \delta\omega_k/|\dot{\Omega}| \tag{2.15}$$

and the relaxation time τ_n is given by

$$\tau_n = \frac{kT}{E_p}\frac{\omega_{cr}}{|\dot{\Omega}|} \tag{2.16}$$

The term $|\dot{\Omega}|$ in Equation 2.15 is sometimes quoted as the steady state spin-down rate, $|\dot{\Omega}|_\infty$. Since the magnitude of $\Delta\dot{\Omega}_c/\dot{\Omega}_c \sim 10^{-2}$ for glitches, any observed value of $|\dot{\Omega}_c|$ can be used to represent $|\dot{\Omega}|_\infty$ (Alpar *et al.* 1989). The observed relaxation of the crust in response to a perturbation from steady state in the linear regime is always a simple exponential decay in time. By contrast, the response of the crust in the nonlinear creep regime can be either linear or nonlinear in time, depending on the size of the glitch (Alpar *et al.* 1989). For large glitches, where $t_0 \geq \tau_n$, the recovery in $\dot{\Omega}_c$ is essentially linear in time, but may also be characterised by a sudden increase in $\dot{\Omega}_c$ some time after the glitch. For weaker perturbations, where $t_0 \ll \tau_n$, the response becomes a simple exponential in time.

In general, contributions from linear and nonlinear creep regimes can be determined by combining and integrating Equations 2.12 and 2.14 (see Alpar *et al.* 1993, Eq. 11). Alpar *et al.* (1993) conclude that creep will be linear if $\tau_l < \tau_n$ and nonlinear if $\tau_n < \tau_l$. The transition from linear to nonlinear response takes place when $\tau_n = \tau_l$ at a particular value of the pinning energy. Regions with weaker pinning energies will respond linearly and those with stronger pinning energies will respond nonlinearly. Theoretical calculations suggest that the superfluid pinning can be weak, superweak or strong. Observational data indicate that strong pinning is not present in any substantial parts of the crustal superfluid (Alpar *et al.* 1993). Weak pinning prevails at lower densities than superweak pinning (Pines & Alpar 1992). Furthermore, a weak or superweak pinning region can respond in either the linear or nonlinear regime.

Alpar *et al.* (1984b) successfully modelled the first few Vela glitches using their theory of vortex creep, although their analysis was hampered by the lack of data immediately following each glitch. Alpar *et al.* (1993) and Chau *et al.* (1993) refined the earlier model and have obtained a consistent fit to all of the Vela glitch data. The data reveal three distinct components of short and intermediate timescale exponential relaxation, with time constants of 10 hr, 3.2 days and 32 days, followed by a long-term recovery of the glitch-induced change in the spin-down rate that is linear in time.

Alpar *et al.* obtained this result using a "minimalist" phenomenological model for the first nine Vela glitches, given by

$$\frac{\Delta\dot{\Omega}_c(t)}{|\dot{\Omega}|_\infty} = -\sum_{i=1}^{2}\frac{I_i}{I}\frac{\Delta\Omega_c(0)}{|\dot{\Omega}|_\infty\tau_i}e^{-t/\tau_i} - \frac{I_3}{I}\frac{\delta\omega(0)}{|\dot{\Omega}|_\infty\tau_3}e^{-t/\tau_3} - \frac{I_A}{I} + \frac{I_A}{It_g}t \tag{2.17}$$

Using this model, Alpar *et al.* have shown that the 10 hr and 3.2 d exponential relaxations are due to the linear response of vortex creep in regions of the crust through which there is no sudden vortex motion at the time of the glitch. These regions, with moments of inertia I_1 and I_2, are part of the passive region 1 shown in Figure 2.3, within which the pinning is expected to be superweak. Because there is no movement of vortices through these regions, there can be no change in the superfluid velocity, so $\delta\Omega_i(0) = 0$ and $\delta\omega_i(0) = \Delta\Omega_c$. The response in these linear regions of vortex creep is described by the first term in Equation 2.17.

The origin of the 32 d exponential relaxation is not as straightforward as the short time-scale response. Alpar *et al.* (1993) have found that it can reflect either nonlinear or linear response. However, they conclude that the 32 d response is most likely to be from a superweak pinning region in the nonlinear regime. This region is thought to lie near the boundary of the passive region, close to where vortex unpinning takes place at a glitch (i.e., region G in Figure 2.3). Hence, $t_0 = \Delta\Omega_c/|\dot{\Omega}|_\infty \simeq 10$ days (the so-called "postglitch delay time"), so that $t_0 < \tau_n$ and the relaxation can be exponential in time. On the other hand, if vortex motion took place in this region, $\delta\omega_i \simeq \delta\Omega_i$ (since $\delta\Omega_i$ is typically large compared to $\Delta\Omega_c$), and so $t_0 = \delta\Omega_i/|\dot{\Omega}|_\infty$. This time offset is typically several years in the Vela pulsar, implying a very slow relaxation process (Alpar *et al.* 1993). The second term in Equation 2.17 describes the intermediate time-scale response.

The last two terms in Equation 2.17 describe the long-term response which is linear in time (i.e., $\Delta\dot{\Omega}_c \sim t$), representing the nonlinear response of regions through which there is a sudden motion of vortices at the time of the glitch. These regions correspond to regions A and B in Figure 2.3. The long-term response has been interpreted by Alpar *et al.* (1993) as a gradual recoupling of nonlinear creep region A with the crust. This process is complete after a time

$$t_g = \frac{\delta\Omega}{|\dot{\Omega}|_\infty} \tag{2.18}$$

where $\delta\Omega$ is the average change in superfluid angular velocity. Therefore, t_g is an estimate of the time between glitches, and it can be calculated with the use of Equation 2.9. The slope of the long-term recovery, $\Delta\ddot{\Omega}_c$, is given by

$$\frac{\Delta\ddot{\Omega}_c}{|\dot{\Omega}|_\infty} = \frac{I_A}{I t_g}. \tag{2.19}$$

The vortex creep model has been applied with success to other glitching pulsars. The Crab pulsar undergoes smaller and less frequent glitches than the Vela pulsar, with a somewhat different postglitch relaxation. The recovery is characterised by time-scales between 1 and 200 days, but it is incomplete in the sense that there is a persistent and cumulative increase in the spin-down rate (Lyne *et al.* 1993). Alpar *et al.* (1985) successfully applied the vortex creep model to the earlier Crab glitches and PSR B0525+21. They explained the persistent shift in

$\dot{\Omega}_c$ for both these pulsars as due to the pile-up of vortices in a trapping zone within a weak pinning region. The trapped vortices add to the internal torque following a glitch. A more recent analysis of the Crab pulsar glitches by Alpar *et al.* (1994) has revealed that the differences between the Crab and Vela glitches can be understood on evolutionary grounds. They suggest that the Crab pulsar glitches are caused by starquakes induced by pulsar spin-down (Ruderman 1976) and that the observed postglitch relaxation is due to: (i) vortices transported inward during a quake, (ii) both linear and nonlinear vortex creep, and (iii) the creation of a new vortex depletion region.

The vortex creep model has also been applied by Alpar *et al.* (1988) to the large glitch in PSR B0355+54 (Lyne 1987). The postglitch relaxation of this pulsar could not be explained solely in terms of nonlinear creep. This led Alpar *et al.* (1988) to suggest that the short (44-day) exponential relaxation was due to linear creep in a part of the superfluid where the pinning is superweak. On the other hand, the persistent shift in $\dot{\Omega}_c$ is attributed to nonlinear creep in another region of the superfluid with a minimum recovery time $t_o = 4.9$ years, assuming the region did not experience any sudden vortex motion at the time of the glitch.

The vortex creep model, applied to observations of glitches in pulsars, has enabled theoreticians to make a number of important generalisations and predictions about neutron stars. Some examples include: (i) linear creep is important in the early stages ($\leq 10^6$ yr) of the life of a pulsar, while nonlinear creep becomes the dominant response as a pulsar ages and cools (Alpar *et al.* 1989); (ii) internal temperatures derived from the observed relaxation times, e.g., $\sim 10^7$ K in the Vela pulsar (Alpar *et al.* 1984b); (iii) the internal structure of neutron stars, e.g., for Vela, the moment of inertia in the crustal superfluid is at least 2.4% of the total moment of inertia (Alpar *et al.* 1993), and the mass of the star is most likely to be less than 1.4 $M_\odot$ (Chau *et al.* 1993); and (iv) constraints on calculations of pinning energies and the equation of state, e.g., observations suggest a moderately stiff EOS (Pines & Alpar 1992).

2.2.3 Other Theories

While most theoreticians agree that vortex unpinning is responsible for the actual glitches, there is some debate as to the mechanism responsible for the postglitch relaxation. Jones (1990a,b,c, 1991, 1992, 1993) has proposed a different theory of vortex-lattice interaction, called the *corotating vortex* model, which is also able to explain postglitch relaxation in pulsars. Jones states that there are only two possible steady states of vortex motion. The vortices can be pinned to the crustal lattice, with radial movement occurring as a result of thermally activated creep (Alpar *et al.* 1984a, 1989). Alternatively, there exists an unpinned component in which the vortices are in almost exact corotation with the superfluid.

In the latter state, proposed by Jones, the postglitch relaxation time is determined by the resistive force per unit length of vortex which produces a finite, but extremely small, deviation from exact corotation with the superfluid. The resistive force is believed to be comprised of a temperature-dependent and a temperature-independent component (Jones 1990a,b), and is approximately independent of pulsar age (Jones 1990c). Jones (1990d) has also shown that the presence of a corotating component can explain the timing noise observed in pulsars. This aspect is discussed in Section 2.3.

Importantly, the corotating vortex model makes completely different predictions about the relationship between internal temperature and postglitch relaxation than the vortex creep model. Jones (1993) has found that the relaxation in some pulsars is temperature-independent. The corotating vortex model also differs on a more fundamental level, requiring a relatively soft equation of state (Jones 1993).

Most of the work done by Jones has been based on the glitch observations of the Vela pulsar and PSR B0355+54. Future glitches, both "caught in the act" and observed with reasonably high time resolution, will undoubtedly assist in reducing some of the uncertainties in the calculations. Furthermore, new glitch data should seriously test both major theories of postglitch relaxation.

2.2.4 Conclusions

Glitch models have undergone extensive development since the phenomenon was first identified. This development has been largely a result of the good quality timing data obtained from observations of the Vela and Crab pulsars. The vortex creep model has been successful in explaining the postglitch behaviour of some pulsars, particularly the Vela pulsar.

With the substantial improvement in the statistics of glitches in recent times, a clear trend is emerging in relation to the "glitch activity" of pulsars (defined as the fractional decrease in rotation period due to glitches per year). The younger and, particularly, older pulsars show relatively little glitch activity. Young pulsars, such as the Crab, have occasional small glitches, whereas old pulsars, such as PSR B0355+53, tend to have large but very infrequent glitches. On the other hand, the "adolescent" pulsars, with ages of the order of $10,000 - 20,000$ years, seem to be the most prone to glitching (Lyne 1993).

This trend in glitch activity has a natural explanation in terms of the vortex creep theory. Young pulsars have higher internal temperatures, allowing a fast vortex creep rate, hence preventing the build-up of large stresses that are thought to cause the large glitches. In fact, Alpar *et al.* (1994) have proposed that the small glitches in young pulsars are caused by starquakes. As a pulsar ages and cools down, the thermal creep rate is not sufficient to relieve the stresses, resulting in

large glitches such as those observed in the Vela pulsar. In old pulsars, the rotation rate is slow enough so that the stresses take much longer to build up to a critical point, resulting in very infrequent glitches.

Observations of glitches provide an important avenue for studying the structure and dynamics of neutron stars. It remains a great challenge for both observers and theoreticians to account for the diversity of postglitch behaviour observed in pulsars and, as a result, to provide further insights into neutron star interiors.

2.3 Timing Noise

After extensive modelling of pulse arrival times including glitches, the phase residuals from the analysis display erratic fluctuations in the rotation of the pulsar (see Appendix C). Short data spans can usually be well-fitted by a second or third order polynomial function, but over a period of years, significant deviations from the simple model are seen in many pulsars. Further, the braking index calculated from a third order fit to the data is generally much larger than that expected for magnetic dipole radiation.

The characterisation of timing noise is an important step towards gaining a better understanding of neutron star dynamics. Furthermore, timing noise ultimately limits the usefulness of most pulsars as a precision time standard and as tools for the detection of low frequency gravitational radiation. Millisecond pulsars exhibit very little timing noise and consequently have received considerable attention in this regard (e.g., Blandford *et al.* 1984, Rawley *et al.* 1988, Stinebring *et al.* 1990, Ryba & Taylor 1991, Kaspi *et al.* 1994, and references therein).

It is highly likely that timing noise in isolated pulsars is due to genuine changes in the rotation rate of the neutron star crust, rather than processes that may influence the emission and propagation of the pulses (Cordes & Greenstein 1981). Given the complexity of the internal structure and magnetosphere of neutron stars, more than one physical process may be responsible for the timing activity of some pulsars. However, each of these processes must involve a time-varying component of the torque on the neutron star crust. In general, there are two possible sources of such a torque: (i) an *internal* torque that may stem from the coupling between the crust and the superfluid interior of neutron stars, as in the case of glitches, and (ii) an *external* torque related to the pulsar magnetosphere (the "radiation torque").

Several detailed investigations of pulsar timing noise have been undertaken in the past. Such investigations make it possible to restrict models of the underlying mechanisms. The results of these investigations are summarised in the next section, while Section 2.3.2 reviews the physical processes that have been proposed to explain timing noise.

2.3.1 The Characterisation of Timing Noise

Timing noise was first recognised by Boynton *et al.* (1972), who examined the first two years of timing data from the Crab pulsar. After modelling the pulsar slow-down and a glitch, they found that a quasi-sinusoidal structure remained in the residuals over time spans of a month or more. This led them to propose that a noise process was responsible for the observed behaviour. Boynton *et al.* considered three simple noise models in which the pulse phase ϕ, frequency ν or frequency derivative $\dot{\nu}$ undergoes a *random walk*, i.e., small jumps with random amplitudes occurring at random times. These processes were termed "phase noise" (PN), "frequency noise" (FN) and "slowing-down noise" (SN) respectively. In a time interval T, the number of such events follows a Poisson distribution with a mean RT, where R is the average number of jumps per unit time. For the three types of noise, the *strength* is defined as $S \equiv RX$, where X is the mean-square value of the jumps in the relevant variable, viz. $<\Delta\phi^2>$, $<\Delta\nu^2>$, or $<\Delta\dot{\nu}^2>$. Using such a description, Boynton *et al.* found that the statistical properties of the Crab data were consistent with a random walk in the rotation frequency.

A number of problems in the analysis encountered by Boynton *et al.* (1972) led Groth (1975a) and Cordes (1980) to improve the methodology of random walk analysis. These methods are described in Chapter 8. However, Groth (1975b) and Cordes (1980) both obtained the same result as Boynton *et al.* for the Crab pulsar, namely that it exhibits a random walk in frequency. Cordes & Helfand (1980) applied the technique of Cordes (1980) to the timing data of 11 pulsars from a sample of 50 pulsars. The results indicated that 2, 7 and 2 pulsars show a random walk in rotational phase, frequency and frequency derivative respectively.

Cordes & Downs (1985) later investigated the timing noise in a sample of 24 pulsars. Their analysis shows that the timing activity in a number of pulsars cannot be modelled in terms of idealised, large rate random walks. Instead, the activity is due to discrete events in one or more of the timing parameters, possibly superimposed on an idealised random walk process, or a mixture of such processes, or another type of process. Unlike glitches, these discrete events have been found to exhibit both positive and negative changes in ν and $\dot{\nu}$. However, some objects did show timing activity consistent with an idealised random walk process, supporting the results obtained by Cordes & Helfand (1980).

Cordes *et al.* (1988) have analysed 14.5 years of Vela timing data in order to characterise the timing noise in this pulsar. Their results show that much of the timing activity is due to discrete events (or *microjumps*) in ν and $\dot{\nu}$, i.e., the jumps are too large to be due to fluctuations of a random walk process comprised of many, much smaller events. The latter events have been called *microglitches* (Lamb 1978a,b). The microjumps in the Vela pulsar have fractional magnitudes of $|\Delta\nu/\nu| \leq 10^{-9}$ and $|\Delta\dot{\nu}/\dot{\nu}| \leq 10^{-4}$. Cordes *et al.* found that these events can have positive or negative magnitudes and that they occur roughly once every 100

days.

In the next section, consideration is given to the theoretical models of mechanisms thought to produce the torque fluctuations responsible for timing noise. In most cases, an explanation has been sought in terms of statistical fluctuations in the mechanism, which in turn gives rise to torque fluctuations (and pulsar timing noise) that can be described in terms of a noise process. There is a degree of support for models involving a random (or *stochastic*) origin of the observed fluctuations, e.g., the behaviour of some pulsars is consistent with a random walk process or possibly a mixture of such processes. Furthermore, the rate and amplitude of resolved events can be readily understood in terms of a random process, both from the point of view of a series of random jumps comprising such a process, or as the large-amplitude end of a broad distribution of microglitches in one or more of the rotation variables that comprise the noise process. The random walks in ϕ, ν and $\dot{\nu}$ considered by Boynton *et al.* (1972) and other workers can be explained by random changes in the emission region or beam direction, moment of inertia of the star, and the process of rotational energy loss respectively.

In recent times, attention has turned to causes of timing noise that do not involve random torque fluctuations. These alternative investigations were prompted by the observation of periodicities or, at least, quasi-periodicities in the timing residuals of some pulsars. One example is the quasi-sinusoidal oscillation observed in the Crab pulsar residuals with a period of approximately 20 months (Lyne *et al.* 1988). In this and other cases, the period and possibly the amplitude of the observed oscillation is the same regardless of the time span of the data that is analysed. A noise process, or one or more discrete events, can also produce a pseudo-periodicity in the timing residuals but, in contrast, the period and amplitude depends on the data span. Some examples of non-random causes of true periodicities in pulsar timing residuals include: (i) oscillations of the vortex lattice in the rotating superfluid; (ii) free precession of the neutron star; (iii) the presence of an orbiting companion, and (iv) an unusually high value of $\ddot{\nu}$, that may be due to the long-term linear recovery in $\dot{\nu}$ from a past glitch. The timing activity of only a few pulsars has been associated with such non-random causes. Hence, this aspect of timing noise is deferred to Chapter 6 of the thesis, where the various alternatives are explored further.

Regardless of the type of mechanism responsible for timing noise, another unresolved issue is that of location – does timing noise originate from within the neutron star, or does it originate in the magnetosphere ? These questions can only be answered by thorough testing of the theoretical models with the observational data.

2.3.2 Theories of Pulsar Timing Noise

The results described above were obtained predominantly from analyses in the time domain, which overcame the problems associated with conventional power spectrum analysis. These problems, such as unevenly sampled data sets and the nonstationarity of the timing noise have been discussed by Groth (1975a), Boynton (1981), Deeter & Boynton (1982). However, Deeter & Boynton (1982) and Deeter (1984) developed a spectral technique that was applied successfully to pulsar data by Boynton & Deeter (1986) and Deeter *et al.* (1989). A description of timing noise in terms of the power spectrum of fluctuations in the rotation phase and its derivatives is particularly useful for making comparisons with the theoretical models described below. Hence, Chapter 8 of the thesis is devoted to the analysis of timing noise in the frequency domain, using a new technique for power spectral estimation.

A brief mention of the nature of such power spectra is necessary for the purposes of the review of theoretical models which follows. A more detailed summary is presented in Chapter 8. The three simple noise processes mentioned earlier (PN, FN, SN) have *red* power spectra, i.e., excess power at low frequencies. The power spectrum of rotational phase fluctuations, $P_\phi(f)$, for PN, FN and SN has a logarithmic slope of -2, -4 and -6 respectively. Since the rotation variables ϕ, ν and $\dot{\nu}$ are simply related by differentiation, the slope of the spectrum will increase by 2 (become more positive) for each noise process if one computes $P_\nu(f)$, and by 4 if one computes $P_{\dot{\nu}}(f)$. The last of these is the most common representation used in theoretical models as it relates directly to the fluctuations in the torque acting on the crust of the neutron star.

A number of theories have been proposed to explain the underlying cause of timing noise. The theories can be classified as those relating to internal torque fluctuations and those that are external to the neutron star.

Internal Torque Fluctuations

Soon after the starquake hypothesis of glitches was proposed, Pines & Shaham (1972) suggested that the "restless behaviour" observed in pulsars was due to *microquakes* in the neutron star crust. In their theory, Pines & Shaham consider an axially symmetric neutron star in which the rotation axis and an elastic reference axis are misaligned by an angle θ_o. They found that the action of a component of the radiation torque perpendicular to the rotation axis may increase the misalignment and also the crustal stress. These stresses tend to be localised and give rise to microquakes, whereas the more global macroquakes are induced by a decrease in the stellar oblateness, ϵ. Importantly, their theory predicts that microquakes can give rise to small frequency jumps having either sign. The sign of the resulting jump depends on the relative magnitude of the change in ϵ and θ_o during a given

time interval. Furthermore, the microquake model makes no predictions about the rate and magnitude of the frequency jumps. That is, timing noise can be due to a small number of "large" microquakes, such as the discrete events observed in some pulsars, or a larger number of "small" microquakes, such as the stochastic models involving idealised random walk processes. The only prediction made in this respect is that the time to the next microquake is proportional to the size of the quake which preceded it.

Anderson & Itoh (1975) suggested that, in addition to crustquakes, the restless behaviour of pulsars could be due to the random pinning and unpinning of vortex lines as they creep outward through the crustal lattice. Hence, the slowing down of the superfluid and the crust proceeds in an irregular fashion and is observed as timing noise in the rotation rate of the pulsar.

Lamb *et al.* (1978a,b) demonstrated how valuable information can be obtained about accretion flows and neutron star structure from timing observations of period irregularities in pulsating X-ray sources[1]. They investigated two sources of torque variations that could be responsible for the period irregularities: (i) external torque variations, associated with large- or small-scale variations in the accretion flow, and (ii) internal torque variations, associated with oscillations of the fluid core or the unpinning of vortices in the inner crust. Using observations of Her X-1, Cen X-3 and other pulsating X-ray sources, Lamb *et al.* developed a statistical description of the possible torque variations in terms of noise processes. The model predictions relating to the internal torque variations are briefly reviewed here, as these are relevant to a discussion of timing noise in isolated pulsars.

Lamb *et al.* extended the work of Anderson & Itoh (1975) by proposing that random internal pinning and unpinning of vortices produces a substantial torque on the crust which can be described in terms of a random noise process. Two basic types of events were considered, namely microglitches occurring as small *pulses* or, alternatively, as small *steps* in the angular velocity, Ω_c, of the crust. These basic events can be represented mathematically as

$$\Delta\Omega_c(t) = \sum_i \Delta\phi_i \delta(t - t_i) \tag{2.20}$$

and

$$\Delta\Omega_c(t) = \sum_i \Delta\Omega_i \theta(t - t_i), \tag{2.21}$$

where $\delta(t)$ and $\theta(t)$ are the delta and unit step functions, and $\Delta\phi_i = \Delta\Omega_i \delta t_i$ in terms of the size $\dot{\Omega}_i$ and duration δt_i of the ith event (Lamb 1981). Provided that there are a large number of events in the observing interval T (such that $RT \gg 1$, where R is the event rate) and no events are resolved ($\delta t \ll \delta T$, where δT is the

[1]These sources are thought to be rotating neutron stars which are accreting matter from a binary companion. The accretion process causes the rotation frequency of the neutron star to slowly increase.

sampling interval of the observations), the only observable quantity besides the type of noise is its strength. The noise processes involving the two basic events correspond to "phase noise" and "frequency noise", respectively, considered by Boynton *et al.* (1972). The noise strengths for these two processes are given by $R<\Delta\phi^2>$ and $R<\Delta\Omega^2>$ respectively. The unpinning and repinning of a fraction of the vortices causes jumps in the angular momentum (steps in Ω_c) that are equivalent to white noise in the torque and hence $\dot{\Omega}_c$. Lamb *et al.* (1978a) showed that such a process would produce a noise strength

$$S_{FN} = R_p(\epsilon\gamma_p I_p \Omega_c)^2 \tag{2.22}$$

where R_p is the rate of unpinning events, I_p is the moment of inertia of the pinned superfluid, γ_p is the fraction of vortices that become unpinned and ϵ is a fraction describing the difference between the crust and superfluid rotation rates.

A neutron star is expected to display a complex dynamical response to torque fluctuations. The response is due to a combination of factors, such as the multi-component structure of neutron stars, excitation of "normal modes" in these components (e.g., superfluid oscillations), and a range of possible relaxation times. Using the terminology of Lamb *et al.* (1978a), the "applied signal" represented by the source of torque variations is "filtered" by the coupled crust-superfluid system to produce the "output" represented by pulse phase fluctuations. This relationship can be expressed as

$$P_o(\omega) = F(\omega)P_n(\omega) \tag{2.23}$$

where P_n is the power density of the exciting noise process, F is the power transfer function and P_o is the observed power density. F depends on the internal dynamical properties of the neutron star. The form of the power transfer function is obtained by working with the variable in which the exciting noise is white, since then $P_n(\omega)$ is a constant and hence $P_o(\omega) \propto F(\omega)$ (Lamb 1981).

Lamb *et al.* considered three simple models, namely: (i) a completely rigid star, (ii) the two-component model of Baym *et al.* (1969), and (iii) a modified two-component neutron star model that takes into account the existence of a low-frequency internal mode of the star. An internal mode will appear as a narrow-band signature in the power spectrum of the fluctuations (if there is sufficient resolution in the spectrum), whereas the pure two-component model predicts a shoulder in the spectrum at $\omega \simeq 1/\tau$, where τ is the crust-core coupling time. Upon application of the response models to the Her X-1 and Cen X-3 data, Lamb *et al.* (1978a) found that the results could be interpreted within the context of the simple two-component model, with the addition of large-amplitude internal oscillations for the Her X-1 observations. However, they could not distinguish between the various possible noise models with the data available at the time.

The work of Lamb *et al.* (1978a,b) showed that the rate and size of microglitches provide information about the processes that cause them, while the

response of the star reveals its internal structure, such as the inertial moments of the stellar components and the crust-core coupling time. Boynton (1981) used the work of Lamb *et al.* to place limits on the two-component model of neutron star structure. The power spectrum of the timing noise in the Crab pulsar was found to be consistent with white torque noise, failing to reveal the power density step of a viscously-coupled crust-core model driven by such a noise process. This suggested that small amplitude perturbations, in contrast to the large amplitude glitches, yield a simple rigid body response.

Greenstein (1979a,b, 1981) has suggested that timing noise arises from the dynamical response of a neutron star to a *heat pulse*. The model is based on two assumptions: (i) the superfluid interior of a neutron star rotates more rapidly than the crust, and (ii) the frictional coupling between the superfluid and crust increases with temperature. The validity of both of these assumptions has been established by the observational data. In the Greenstein model, a sudden pulse of heat causes a sudden increase in the frictional coupling which is then observed either as a glitch or slower variations associated with timing noise[2]. Clearly, this type of coupling is only applicable in density regimes where vortex pinning is very weak or absent. Also, the model is complicated by the theoretical uncertainties regarding the junction between the pinning and frictional regimes. A boundary layer of tangled vorticity is expected to form. In this regard, Greenstein assumed that the tangled vorticity does not significantly affect the frictional regime.

Greenstein made a number of theoretical predictions using the heat pulse model. For example, the internal temperature of neutron stars was constrained to lie between 2 and 4 million Kelvin, with individual events occurring no more than once every year. The internal temperature estimates translate into surface temperatures lying between 3×10^4 K and 4×10^5 K, depending on the mass of the star.

Using the results obtained by Cordes & Helfand (1980) from a random walk analysis of 11 pulsars, Cordes & Greenstein (1981) evaluated eight mechanisms that had been proposed to account for the timing noise observed in isolated pulsars. These were: (i) continuous and erratic quaking of the crust or core of the neutron star; (ii) random pinning and unpinning of superfluid vortices; (iii) accretion from the interstellar medium; (iv) vortex annihilation at the outer boundary of the superfluid; (v) pulse shape changes; (vi) superfluid response to random heat pulses; (vii) crust breaking by vortex pinning; and (viii) external torque fluctuations related to the luminosity of the star. Each physical model was evaluated by comparing the noise strength expected from such a mechanism with the estimates obtained from the observations.

Cordes & Greenstein found the first five of these mechanisms to be so severely

[2]The identification of resolved events at a later date (Cordes & Downs 1985) clearly casts some doubt over the adequacy of this model.

constrained that they could not be considered viable. In each case, the predicted noise strengths were found to be too small or too large, often by several orders of magnitude, and in some cases the mechanism is not able to produce all three types of simple random walk processes. On the other hand, the last three mechanisms were found to be severely constrained, but not ruled out, by the observations. Mechanisms (vi) and (vii) are capable of yielding the observed PN and FN strengths but cannot readily explain SN. However, Cordes & Greenstein suggest that, in the latter mechanism, crustal lattice creep induced by temperature variations may cause the requisite variations in $\dot{\nu}$ which give rise to SN. Finally, external torque fluctuations can arise from perturbations in the plasma flow or current braking, assuming a polar cap emission model. According to Cordes & Greenstein, corresponding variations in radio luminosity can produce FN of the observed strength, and if the torque variations are of the form of step functions, also SN. However, this model cannot readily explain PN. As of 1981, models of external torque fluctuations had not been explored as fully as models involving internal processes. Since that time, Cheng (1987a,b) has developed a magnetospheric model of pulsar timing noise. This model is described in some detail in the next section.

Using the vortex creep theory, Alpar *et al.* (1986) constructed model noise power spectra for three different types of events that might give rise to timing noise. These are: (i) "pure" vortex unpinning events (i.e., scaled-down versions of the large glitches), (ii) a process which is accompanied by vortex unpinning (e.g., breaking of the crustal lattice by pinned vortices), and (iii) "external" events that do not involve vortex unpinning.

An event that is characterised by a sudden jump in the crustal angular frequency, $\Delta\Omega_c$, will be accompanied by a change in the spin-down rate of the form

$$\Delta\dot{\Omega}_c(t) = \Delta\Omega_c\delta(t) + \Delta\dot{\Omega}_{c,r}(t), \tag{2.24}$$

where $\Delta\dot{\Omega}_{c,r}(t)$ represents the response of the internal torques to the jump (Alpar *et al.* 1986). Alpar *et al.* based their calculations on the nonlinear response of vortex creep (described by Equations 2.14–2.16) to small, unresolved jumps in the rotation frequency, thus enabling a simple noise description. Although Alpar *et al.* present a general mathematical analysis of the response to the three types of events, they restrict the comparison of theory and observation to the situation where $t_0 \ll \tau_n$. As described in Section 2.2.2, t_0 is the post-jump delay time and τ_n is the relaxation time. This condition is to be expected when the frequency jumps are very small. In this case, the response becomes a simple exponential in time. Assuming that $t_0 \ll \tau_n$, Alpar *et al.* predict the power spectrum of the timing noise in $\dot{\Omega}$ to be

$$P_{\dot{\Omega}}(f) = R\Delta\Omega_c^2\frac{(1-Q)^2+\omega^2\tau^2}{(1+\omega^2\tau^2)} \tag{2.25}$$

where $f = \omega/2\pi$ is the fluctuation frequency, R is the jump rate, $\Delta\Omega_c$ is the magnitude of the jump in the crustal angular velocity, and Q is the fraction of the jump that decays away.

For the pure unpinning events, Alpar *et al.* assumed each jump to be a scaled-down version of a glitch by direct application of the nonlinear theory of vortex creep (Section 2.2.2). For pure unpinning, $Q = 1$, and so the spectrum given by Equation 2.25 will have characteristic shoulder at $\omega = 1/\tau$ if the range of autocorrelation times spanned by the data includes either the relaxation time or the delay time. This is shown in Figure 2.4(a). At the point where $\omega = 1/\tau$, the logarithmic slope of the spectrum changes from +2 ("blue") to zero ("white"). The jump signature for unpinning events is identical to that of a glitch, namely $(\Delta\Omega_c, \Delta\dot{\Omega}_c) = (+, -)$.

For mixed events, the initial jump receives a contribution from the cause of the event and an unpinning event. One possible cause is crust-breaking resulting from vortex pinning stresses (Ruderman 1976). In this case, the crustal moment of inertia can change by a small amount ΔI, giving rise to a positive or negative change in Ω_c. In contrast, vortex unpinning will only lead to an increase in Ω_c. For mixed events, all possible values of Q are of interest. For example, events where $Q \gg 1$ might be initiated by a small crustquake in which $\Delta\Omega_c$ is negative, triggering vortex unpinning. The outward movement of vortices produces an increase in Ω_c until such time that the net change is zero. Such a sequence of events would be characterised by a sudden change in $\dot{\Omega}_c$, without an accompanying step in Ω_c (Alpar *et al.* 1986). Figures 2.4(b),(c) show the power spectrum of the noise resulting from mixed events when $(1-Q)^2 > 1$ (comprised of logarithmic slopes of 0,−2,0) and $(1-Q)^2 < 1$ (slopes 0,+2,0). The transition from one spectrum to the other occurs at $Q = 2$. For this value of Q, the power spectrum is white. In general, mixed events may involve a net frequency jump, $\Delta\Omega_c$, with a positive, negative or zero amplitude, but the change in $\dot{\Omega}$ will always be negative because the unpinning process reduces the moment of inertia acted on by the external braking torque (Cordes *et al.* 1988).

In the third type of event considered by Alpar *et al.* (1986), i.e., events that do not involve vortex unpinning, the only contribution of the pinned superfluid is the response of vortex creep to the perturbation in Ω_c. In this case, $t_0 = \Delta\Omega_c/|\Omega_\infty|$ and $Q = I_p/I_c$, where I_p and I_c are the moments of inertia of the pinned superfluid and crust respectively. Alpar *et al.* show that the response, $\Delta\dot{\Omega}_c$, is proportional to I_p/I_c. Since $I_p/I_c \simeq 0.01$ (see Section 2.2.2), the magnitude of the response is negligible compared to the initial event, and Equation 2.25 reduces to give a constant power spectral density, $P_{\dot{\Omega}}(f) = R(\Delta\Omega_c)^2$, i.e., a white noise spectrum in $\dot{\Omega}$. Hence, the jump signature for such events is $(\Delta\Omega_c, \Delta\dot{\Omega}_c) = (+, 0)$ and $(-, 0)$.

In order to test the three models, Alpar *et al.* (1986) examined the observational power spectra in $\dot{\Omega}$ for 25 pulsars resulting from the work of Boynton &

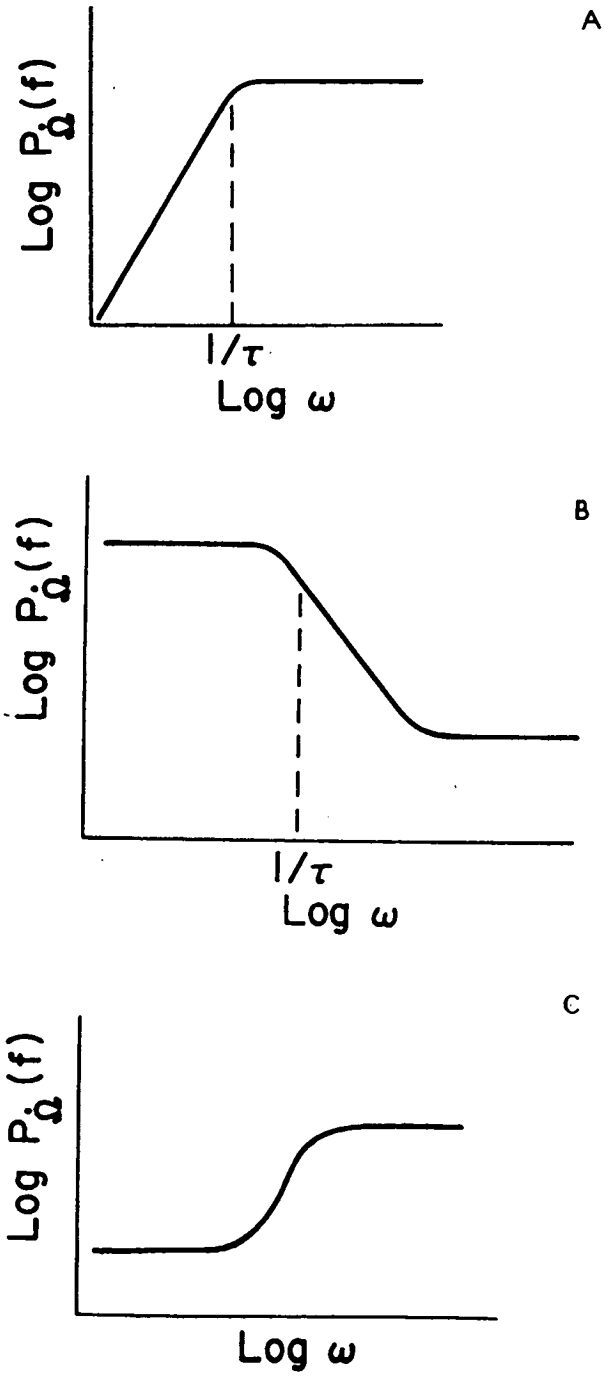

Figure 2.4: Theoretical timing noise power spectra resulting from a vortex creep response to perturbations in the rotation rate. The logarithm of the power density in $\dot{\Omega}$ is plotted as a function of the fluctuation frequency for: (a) pure unpinning noise, (b) mixed events when $(1-Q)^2 > 1$, and (c) mixed events when $(1-Q)^2 < 1$, in the limiting case where $t_0 \ll \tau$; (after Alpar *et al.* 1986).

Deeter (1986). Alpar *et al.* searched for structure in the observed power spectra that might provide information on relaxation time-scales, particularly spectra with logarithmic slopes of +2, 0 or −2 which are accommodated by the three models. Under the assumption that $t_0 \ll \tau$, they used a hypothesis test to quantify the range of possible τ and Q values, with the noise strength $R(\Delta\Omega_c)^2$ as a free parameter. For the Vela pulsar, all values of Q and τ in the range $1 - 10^4$ days were rejected with more than 98% confidence. For the Crab pulsar, $Q = 0, 2$ and $\tau < 1$ day were not rejected by the data with more than 30% confidence. These results suggest that pure unpinning events are not responsible for the timing noise of the Vela and Crab pulsars, nor is there a continuous range of magnitudes of unpinning events extending from glitches down to the unresolved events (microglitches) that lead to some of the timing noise. That is, there is some threshold for glitches produced by vortex unpinning. The results for the other, older pulsars were inconclusive for a variety of reasons. These include: (i) level of timing noise that is too low to observe structure, (ii) insufficient number of points in the spectrum to obtain reliable results, (iii) complicated (multi-component) power spectra, and (iv) no obvious structure in the red power spectra.

In summary, "pure unpinning" and "mixed" events are not entirely rejected by the data for the range of examinable t_0 and τ. However, Alpar *et al.* (1986) conclude that timing noise is probably due to physical processes in regions external to the weak and superweak pinning regions of the crustal superfluid that are thought to be responsible for glitches.

The most recent theory of pulsar timing noise has been proposed by Jones (1990d). The theory is based on the existence of separate regions of pinned and corotating superfluid vortices within the neutron star, which have also been used to explain the postglitch relaxation in some pulsars (Section 2.2.3). In this model, the cylindrical surfaces dividing the regions have time-averaged radii which may show secular change as the pulsar rotation rate decreases. Microjumps in the rotation frequency and frequency derivative with both positive and negative magnitudes, as found by Cordes & Downs (1985), are caused by transitions between pinned and corotating vortex states which produce small movements of the surfaces. The model can also explain the two-component (red and white) power spectra of rotation fluctuations observed for some pulsars. Following is a summary of the mechanism proposed by Jones to explain both of these observational aspects.

A region of superfluid with corotating vortices has a steady state angular velocity

$$\Omega_n = \Omega - \tau\dot{\Omega} \tag{2.26}$$

where τ is the radius-dependent relaxation time (Jones 1990a). In an adjacent region of pinned vortices, there exists a critical superfluid angular velocity

$$\Omega_n^s = \Omega - k_s\tau\dot{\Omega} \tag{2.27}$$

such that the Magnus force unpins the vortices if $\Omega_n > \Omega_n^s$ (Jones 1990d). Transitions from the pinned to the corotating vortex states are caused by an increase in the angular velocity difference $\Omega_n - \Omega$ with time. The opposite transitions must also occur if the dividing surface is to retain its time-averaged radius (Jones 1990d).

Jones (1990d) has obtained an approximate expression for the change in $\dot{\Omega}$, $\delta\dot{\Omega}(t)$, produced by a sequence of such transitions of either kind. The important features of the expression are: (i) pinned regions with moments of inertia I_{ni}; vortices unpin at times t_i, producing discontinuous changes $\delta\Omega_i$ in the crustal angular velocity I_c; the superfluid has an angular velocity $\Omega_{ni}(t_i)$ when corotation begins; (ii) corotating regions with moments of inertia I_{nj}; vortices pin at times t_j, producing discontinuous changes $\delta\Omega_j$ in the crustal angular velocity; the superfluid has an angular velocity $\Omega_{nj}(t_j)$ at the instant before pinning occurs. Jones adds that the transitions between the two states are probably cooperative phenomena, so that the dimensionless parameter k_s cannot be defined precisely, nor can it be assumed that successive I_{ni} and I_{nj} are identical. The existence of a long-term average radius for the surface dividing the different regions is the sole constraint on the sequences involving $I_{ni,j}$.

Jones (1990d) provides a qualitative explanation of the occurrence of $\delta\Omega_{i,j} < 0$ in terms of a non-axisymmetric vortex density distribution. If a vortex distribution is to retain an axisymmetric form, the pinning or unpinning of vortices must occur in a time δt such that

$$\delta t \gg \frac{2\pi}{\Omega_n - \Omega}. \tag{2.28}$$

For most pulsars, the right hand side of this inequality is several orders of magnitude greater than the upper limit on the rise time obtained from observations of the Vela pulsar, i.e., $\delta t \leq 120$ s (McCulloch *et al.* 1990). Hence, transitions between the pinned and corotating vortex states can produce non-axisymmetric vortex density distributions. Under these circumstances, the superfluid has a very small non-azimuthal velocity component which can result in a transfer of a small amount of angular momentum from the crust to the superfluid. This prediction is in agreement with the nature of the microjumps observed by Cordes & Downs (1985), where the $\delta\Omega < 0$ are smaller in magnitude than the positive events.

Assuming a series of microjumps that occur over a long time interval T with random $t_{i,j}$ and identical $\tau_{i,j}$, Jones obtained a general expression for the power spectrum in $\dot{\Omega}$, where

$$P_{\dot{\Omega}} = f(\omega, \tau, R_u, R_p, a_{i,j}, b_i, \delta\Omega_{i,j}). \tag{2.29}$$

R_p, R_u are the pinning and unpinning event rates, and a, b are constants for an individual pulsar, given by

$$a_i = \frac{I_{ni}}{I_c}[\Omega_{ni}(t_i) - \Omega(t_i)] \tag{2.30}$$

and

$$b_i = \frac{I_{ni}}{I_c}\dot{\Omega}_{ni}\tau. \tag{2.31}$$

In the limits $\omega\tau \rightarrow 0$ and $\omega\tau \rightarrow \infty$, the power spectrum is a superposition of red and white components. Using the power spectrum obtained for the Vela pulsar by Boynton & Deeter (1986), Jones has found that the red component requires

$$R_u\bar{b_i^2} + R_p\bar{a_j^2} = 1.8 \times 10^{-22} \text{ rad}^2\text{s}^{-3}. \tag{2.32}$$

For $R_{u,p} > 10^{-7}$ s^{-1} (found by Cordes *et al.* 1988), the moments of inertia involved are $I_{ni,j} \leq 10^{-4} I_c$. The white spectrum of the Crab pulsar can be explained if the a_i and $\delta\Omega_{i,j}$ terms dominate the power spectrum equation.

Jones also points out that transitions to or from the corotating vortex state involving relatively small moments of inertia can produce large period derivative changes

$$\left|\frac{\Delta\dot{P}}{\dot{P}}\right| \leq k_s\frac{I_{ni}}{I_c} \tag{2.33}$$

provided $k_s \gg 1$. This explanation is necessary to account for the large fractional jumps in $\dot{P}$ observed in some pulsars (Cordes & Downs 1985).

In summary, the corotating vortex model proposed by Jones (1990d) has made considerable progress toward explaining the nature and variety of microjumps observed in pulsars. The only weakness of this model is that it does not explain the blue component of the power spectrum in $\dot{\Omega}$ observed in some pulsars, and it appears as if it has only been tested on the power spectra for the Crab and Vela pulsars.

External Torque Fluctuations

The quantitative analysis of timing noise mechanisms conducted by Cordes & Greenstein (1981) did not rule out magnetospheric torque fluctuations as a possible cause. Since that time, Cheng (1987a,b, 1989) has developed a detailed model of pulsar timing noise in terms of magnetospheric fluctuations. There are a number of facets to the model, involving: (i) rapid fluctuations in the outer magnetospheric gap of some pulsars; (ii) magnetospheric fluctuations that are induced by microglitches; (iii) microglitches produced by pure unpinning with a vortex creep response; and (iv) a spontaneous unpinning scenario for the microglitches. This hybrid model is capable of explaining most of the timing noise observations.

Cheng (1987a) first investigated pulsar timing noise in the context of the outer magnetospheric gap model of emission from fast-spinning pulsars (Cheng *et al.* 1986a,b), with particular reference to the Crab pulsar. According to Cheng (1987a), pair production processes in the outer gap can give rise to fluctuations which result in rapid variation of the current braking torque, and hence the stellar

rotation frequency. The steady value of this torque, $N_{\mathbf{JxB}}$, is also partly responsible for the slow-down of the stellar rotation, which occurs as a result of current flows across the field lines on the stellar surface. Cheng used a statistical description of torque variations in terms of the noise processes developed by Lamb *et al.* (1978a,b). The time-scale of the fluctuations is expected to be short (~ 10 ms), resulting in a series of δ-function-like fluctuations in the current braking torque. Furthermore, because the fluctuation time-scale is much shorter than the crust-core coupling time, the neutron star can be idealised as a rigid body (i.e., the relaxation effects due to coupling processes can be ignored). Hence, these fluctuations in the torque will produce a random walk in the rotation frequency (FN) with a strength parameter given approximately by

$$S_{FN} \approx \frac{\Omega}{8\pi^2}\left(\frac{I_{\rm tot}}{I_c}\right)^2\left(\frac{\delta N_{\mathbf{JxB}}}{N_{\rm tot}}\right)^2\frac{1}{t_{\rm age}^2} \tag{2.34}$$

where $t_{\rm age} = \Omega/2\dot{\Omega}$ (the characteristic age of the pulsar), I_c and $I_{\rm tot}$ correspond to the crustal and total moments of inertia, and $\delta N_{\mathbf{JxB}}$ is the fluctuation in the current braking torque, based on the assumption that $N_{\mathbf{JxB}}$ is the dominant stellar slow-down torque so that $N_{\mathbf{JxB}} \approx N_{\rm tot} = I_{\rm tot}\dot{\Omega}$. The squared fractional variation in the current braking torque is estimated to be approximately 0.1 for rapidly spinning pulsars and about ten times larger for slowly spinning pulsars (Cheng 1987a).

The quantity $I_{\rm tot}/I_c$ depends on the equation of state. Hence, Cheng (1987a) compared the theoretical values of S_{FN}, assuming soft and stiff equations of state, with the observed values for a selection of pulsars showing consistency with a random walk in frequency. The results for several pulsars, including the Crab pulsar, were consistent with a stiff EOS. This result is in agreement with the requirements of the vortex creep model when applied to postglitch data. The results also provided some evidence for the existence of a superfluid core in neutron stars.

Upon inspection of the power spectra in $\dot{\Omega}$ obtained by Boynton & Deeter (1986), Cheng (1987a) found that a number of the FN candidates had a composite spectrum containing blue or white noise at the high frequency end and red noise at low fluctuation frequencies. This finding led Cheng (1987b) to propose another magnetospheric noise model. This model is applicable to pulsars with a steady current flow in the outer magnetosphere, e.g., the Vela pulsar. In such cases, the current braking torque is perturbed by microglitches in the rotation rate of the neutron star. The perturbed torque remains unchanged until the next microglitch and hence, the rate of the torque variations is the same as the rate of microglitches.

Using the statistical description of torque variations developed by Lamb *et al.* (1978a,b), these step-like changes in the torque give rise to a random walk in $\dot{\Omega}$,

described by

$$S_{SN} = R(\Delta\dot{\Omega}_c)^2 = \frac{R}{4\pi^2}\frac{\Omega_c^2}{4t_{\rm age}^2}\left(\frac{\delta N_{\rm JxB}}{N_{\rm JxB}}\right)^2\left(\frac{N_{\rm JxB}}{N_{\rm tot}}\right)^2 \tag{2.35}$$

where R is the rate of magnetospheric noise and

$$\frac{|\delta N_{\rm JxB}|}{|N_{\rm JxB}|} \equiv f(\Delta\Omega_c/\Omega_c, \Delta\dot{\Omega}_c/\dot{\Omega}_c) \approx f(\Delta\dot{\Omega}_c/\dot{\Omega}_c) = f(I_p/I_c) \tag{2.36}$$

is an unknown function which depends upon the detailed responding mechanism of the magnetosphere to the microglitches (Cheng 1987b). However, this term is taken to be a constant, as described earlier. The value of $(N_{\rm JxB}/N_{\rm tot})^2$ is of the order of unity for most pulsars, but can be ten times larger, as in the case of the Vela pulsar (Cheng *et al.* 1986b). The power spectrum in $\dot{\Omega}$ for this magnetospheric noise model is

$$P_{\dot{\Omega}}(f)_{\rm ex} = S_{SN} f^{-2} \tag{2.37}$$

where the "ex" indicates that the timing noise is produced in an external region of the neutron star.

Cheng (1987b) assumed that microglitches are due to the small-scale superfluid unpinning events considered by Alpar *et al.* (1986). These microglitches are thought to occur spontaneously (Cheng *et al.* 1988, Cheng 1989), producing δ-function-like perturbations in the rotation frequency (equivalent to a random walk in ϕ). In this spontaneous unpinning scenario, one free vortex line initiates the whole mechanism. Such free vortex lines could be created as the pinned vortex lines creep outward and encounter a spatially irregular region with missing pinning sites (Cheng 1988). This situation can happen anytime, but the mean time for such events must be the relaxation time-scale τ for excursions from the steady state of vortex creep, given by

$$R_{\rm vu}^{-1} \propto \tau = \frac{\omega_{cr} k T_{in}}{E_p |\dot{\Omega}_\infty|} \tag{2.38}$$

where $R_{\rm vu}$ is the unpinning rate of vortex lines, T_{in} is the internal temperature of the neutron star and ω_{cr}, E_p depend on the internal structure of the neutron star, as described earlier. In order to simplify the testing of the model, Cheng (1987b) assumed that every neutron star has the same structure, taking E_p/ω_{cr} to be constant.

In addition to the pure unpinning model of microglitches, Cheng (1987b) considered the typical time-scale for the "mixed events" model of Alpar *et al.* (1986), e.g., crustbreaking of the inner crustal lattice by pinned vortex lines (Ruderman 1976). Ruderman estimated that the time-scale between such fractures is

$$\Delta t_{\rm cf} \sim \frac{\theta_m \mu G M}{\bar{P} R^3 \dot{\Omega}_c} \tag{2.39}$$

where θ_m is the maximum strain angle before fracture, μ is the shear modulus, M is the mass of the pulsar, R is the stellar radius and $\bar{P}$ is the pressure of the superfluid. Hence, the time-scales τ and $\Delta t_{\rm cf}$ can be distinguished by the difference in their temperature dependence (Cheng 1987b). If the glitches are induced by crust fractures, then the rate of such events is $R_{\rm cf} = 1/\Delta t_{\rm cf}$. Furthermore, Cheng considered the case where $Q \approx 1$ as being of most physical relevance for the mixed events.

In both the pure unpinning and mixed event models, the predicted power spectrum contains a blue or white noise component [as in Figures 2.4(a),(c)], given by

$$P_{\dot{\Omega}}(f)_{\rm in} = S_{PN} f^2 \tag{2.40}$$

for $\omega\tau \ll 1$ and

$$P_{\dot{\Omega}}(f)_{\rm in} = S_{FN} \tag{2.41}$$

for $\omega\tau \gg 1$, where "in" indicates that the timing noise is produced in the neutron star interior, $S_{PN} = R(2\pi\Delta\Omega_c\tau)^2$ and $S_{FN} = R(\Delta\Omega_c)^2$. Hence, the microglitch-induced magnetospheric noise model predicts that the power spectrum in $\dot{\Omega}$ will exhibit blue or white noise at high fluctuation frequencies (microglitch noise dominant regime) and red noise at low fluctuation frequencies (magnetospheric noise dominant regime). The observed noise power spectrum should then be of the form

$$P_{\dot{\Omega}}(f) = P_{\dot{\Omega}}(f)_{\rm in} + P_{\dot{\Omega}}(f)_{\rm ex}. \tag{2.42}$$

Cheng (1987b) compared the theoretical strength parameters with the observational values derived from the power spectra for a selection of pulsars (Boynton & Deeter 1986). The theoretical noise strengths in the pure unpinning case ($R^{-1} \approx \tau$) are given by

$$S_{PN}^{th} = R(2\pi\Delta\Omega_c\tau)^2 \propto \frac{(\Delta\Omega_c)^2}{|\dot{\Omega}_c|} T_{in}, \tag{2.43}$$

$$S_{FN}^{th} = R(\Delta\Omega_c)^2 \propto \frac{(\Delta\Omega_c)^2}{T_{in}} |\dot{\Omega}_c|, \tag{2.44}$$

$$S_{SN}^{th} = \frac{R\Omega_c^2}{16\pi^2 t_{\rm age}^2} \left(\frac{N_{\rm JxB}}{N_{\rm tot}}\right)^2 f^2 \left(\frac{I_p}{I_c}\right) \propto \frac{\Omega_c^2}{t_{\rm age}^2} \left(\frac{N_{\rm JxB}}{N_{\rm tot}}\right)^2 \frac{|\dot{\Omega}_c|}{T_{in}}. \tag{2.45}$$

For mixed events ($R^{-1} = \Delta t_{\rm cf}$), the relations are

$$S_{PN}^{th} \propto \frac{(\Delta\Omega_c)^2 T_{in}^2}{|\dot{\Omega}_c|}, \tag{2.46}$$

$$S_{FN}^{th} \propto (\Delta\Omega_c)^2 |\dot{\Omega}_c|, \tag{2.47}$$

$$S_{SN}^{th} \propto \frac{\Omega_c^2}{t_{\rm age}^2} \left(\frac{N_{\rm JxB}}{N_{\rm tot}}\right)^2 |\dot{\Omega}_c|. \tag{2.48}$$

Hence, a comparison of the theoretical results with the observational data requires an estimate of the internal temperature of pulsars. Alpar *et al.* (1984a) state that

old pulsars have already radiated away almost all of the original heat content, so that vortex creep is the ultimate heating mechanism of the star. In such a case (*nonisothermal* star), the internal temperature

$$T_{in} \propto |\dot{\Omega}|^{0.455} \tag{2.49}$$

If the pulsar has lost all of its original heat content (*isothermal* star), then

$$T_{in} \propto |\dot{\Omega}|^{0.25} \tag{2.50}$$

(Cheng 1987b). Cheng found that the observational data were consistent with the theory within a factor of three. In general, the pure unpinning model gave better results than the crustquake model, especially for the younger pulsars. Importantly, Cheng concludes that vortex creep is indeed the dominant heating mechanism inside pulsars, controlling the internal temperature and hence the thermal relaxation time.

2.3.3 Other Theories

The theories of timing noise described in the previous sections involve a statistical description in terms of random walk processes. In a completely different approach, astrophysical data from a variety of sources have been investigated for evidence of *chaotic* behaviour. A nonlinear dynamical process intrinsic to the spin-down of the pulsar will produce structure or non-randomness in the data which can be measured.

Harding *et al.* (1990) have analysed 14 years of timing residual data from the Vela pulsar in order to determine if a chaotic dynamical process is the origin of the timing noise. They applied the popular "correlation sum" technique which allows the "fractal dimension" of the system to be estimated. A low dimension is suggestive of a chaotic process. Harding *et al.* obtained a dimension of 1.5, suggesting that nonlinear dynamics may be the cause of timing noise in the Vela pulsar. However, when a similar analysis was performed on simulated random walk data, they also obtained low fractal dimensions. They concluded that the correlation sum estimator for dimension is unable to distinguish between chaotic and random processes.

The possibility remains, however, that the timing noise in some pulsars is due to a chaotic dynamical process. Harding *et al.* suggest that non-linear effects in the spin-down are capable of producing chaotic torque variations. For example, the Euler equations for a rotating object with a magnetic dipole moment that is misaligned with the rotation axis exhibit chaotic spin-down behaviour under certain conditions. Apart from the inconclusive results obtained with the correlation sum technique, future chaos analyses will be difficult to interpret because of the sparsely sampled data sets available from most pulsar timing observations.

2.3.4 Conclusions

The study of pulsar timing noise is an important probe of the structure and dynamics of neutron stars. While a number of theories have been proposed, e.g., involving crustquakes, heat pulses, superfluid vortex unpinning, superfluid rotation and external torque fluctuations, or a combination of two such mechanisms, the origin of timing noise is still uncertain. None of the models explain *all* of the timing activity observed in the limited sample of pulsars investigated. Long-term timing observations of a much larger sample of pulsars are needed in order to gain a better understanding of this phenomenon. In subsequent chapters, this thesis presents the observational results from a long-term study of 45 pulsars with a view toward this goal.

Chapter 3

The Observing System

3.1 Introduction

Pulsar timing observations commenced in September 1987 using a 26-metre parabolic antenna located at the Mt Pleasant Radio Astronomy Observatory in southern Tasmania. Unlike the majority of antennas used in astronomy, it has an XY mount, with the X-axis aligned East-West and the Y-axis aligned North-South. The XY mount is a result of its design by NASA as a satellite tracking antenna. The antenna was originally based at Orroral Valley near Canberra for this purpose before being relocated to Mt Pleasant in 1985. Since that time, the antenna has been owned and operated by the Physics Department of the University of Tasmania. Both axes are fully steerable and operate under computer control. The receivers are located at the prime focus of the dish. Observing sessions have been conducted approximately monthly up to the present day. In this chapter, the observing hardware and data acquisition procedures are described.

The timing observations were established as a result of extensive work on the relevant hardware and software aspects of the 26-m telescope system by Profs P.M. McCulloch and P.A. Hamilton. Dr E.A. King was involved with the development of the initial pulsar timing receiver and conducted the observations up to the end of 1988. In 1989, the observations were conducted by Mr A.B.Neilson, who was also involved in the construction of the second stage of the dual frequency receiver. During 1990, the observations were carried out by Mr S.T. Hutchinson in conjunction with the author.

Since 1990, all aspects of the pulsar timing survey have been the sole responsibility of the author. This work has involved the modification and calibration of the existing receiver for polarization measurements, modifications and improvements to the existing timing analysis software, the development of new timing and polarization analysis software, and the collection, processing, analysis and interpretation of the timing and polarization data. As part of this work, the data collected prior to 1990 were re-processed.

3.2 The Receiving Hardware

The observations were made simultaneously in two frequency bands centred near 670 and 800 MHz, hereafter called bands A and B respectively, using a dual channel polarimeter receiver. The feed consisted of broad-band, cavity-backed, crossed dipoles, with an isolation better than 30 dB, thus minimising the coupling effects which can produce spurious polarization at the output. The use of a common pair of dipoles, hereafter called the X and Y dipoles, restricts the frequency separation achievable, but avoids potential problems associated with coupling effects between two pairs of dipoles. For polarization observations, it is necessary to measure the X and Y orthogonal polarization states and the phase difference between these signals. The former is also necessary for accurate timing measurements. Summation of the X and Y signals to produce the total intensity signal eliminates arrival-time errors arising from distortion of the pulse shape, due to the high degree of linear polarization present in most pulsar emission.

Pre-amplification was achieved with low-noise GaAs FET amplifiers operated at the ambient temperature, and whose noise performance was optimised within the two bands. The output from each amplifier was split into the two bands, amplified and mixed with separate local oscillators (650 and 760 MHz) to produce intermediate frequencies (IFs) centred near 20 and 40 MHz respectively. The local oscillator signals used to achieve the mixing were phase-locked to the observatory frequency standard.

A schematic diagram of the receiver "front end" (RF section) is presented in Figure 3.1. The diagram includes a change made in September 1991. At that time, a high frequency quadrature hybrid (Anzac JH-140) was incorporated into the receiver to enable phase calibration of the observing system for polarization measurements. An RF switch was used to shunt a 90° phase delay into and out of the X channel, under computer control. Although the hybrid presented a 90° phase difference between its two outputs, the RF switch introduced an extra $-15°$ phase (the phase difference between the two input ports of the switch). This made the effective phase difference between the two outputs of the hybrid equal to 105°. This is acceptable, provided the phase difference is constant across the observing passband. Further tests revealed that this was the case. In principle, any known phase difference between the two outputs, except $n\pi$ radians (where n is an integer), is satisfactory for calibration purposes, as shown in Chapter 5.

Prior to the installation of the hybrid/switch circuit, the lengths of the IF cables going from the front end to the back end of the receiver system were adjusted. This was done to ensure that the relative phase difference between the X and Y channels was constant across the observing band. However, the introduction of this circuit resulted in a phase gradient and a constant (positive) phase offset in the X channel of the receiver. An extra length of ~ 21 cm of cable was inserted

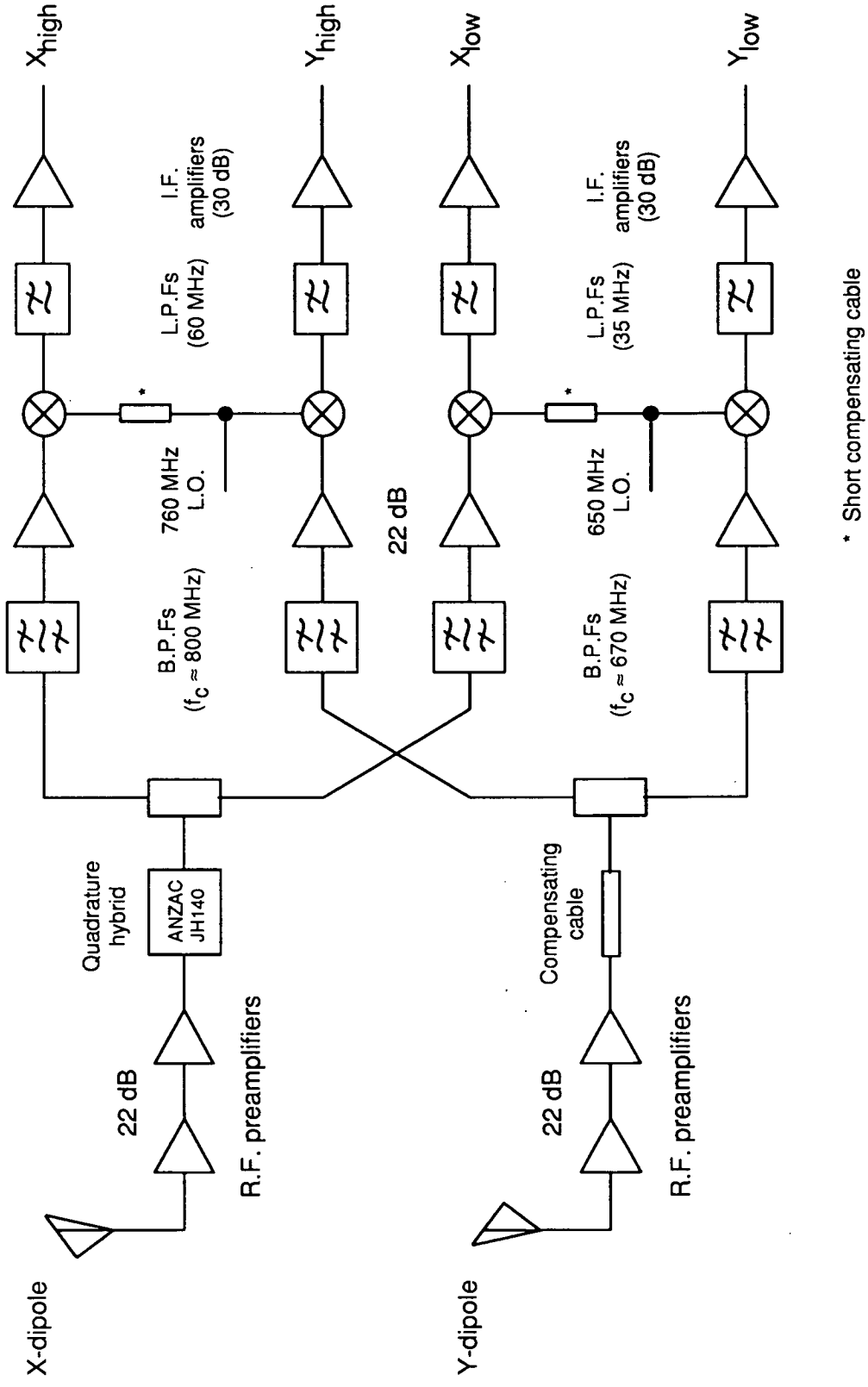

Figure 3.1: Schematic diagram of the receiver "front end" (RF section).

into the Y channel and a short length, corresponding to a constant phase of $\sim 68°$, was inserted into the X channel local oscillator lines to compensate for these respective effects (see Figure 3.1). Any small remaining phase difference between the X and Y channels is calibrated out of the data during the post-processing in the manner described in Chapter 5.

The minimum detectable temperature, or sensitivity, of the receiving system is given by

$$\Delta T_{\min} = \frac{\alpha K T_{\rm sys}}{\sqrt{\Delta f t}} \tag{3.1}$$

where α is the signal-to-noise ratio desired, K is a constant ($K \approx 1$ for a total power receiver), $T_{\rm sys}$ is the system noise temperature (K), Δf is the pre-detection bandwidth (Hz), and t is the total integration time (s). The system temperature includes noise contributions from the antenna, transmission line losses, and the receiver (mainly from the RF amplifiers). Calibration of the system using a continuum source yielded an equivalent system temperature at each frequency of about 100 K. The two other factors which determine the sensitivity (Δf and t) are referred to in the description which follows.

Each of the two outputs at an IF of ~ 20 MHz (band A) were further amplified and split into sets of four separate spectral channels, centred at 15, 20, 25, 30 MHz, while each of the IF outputs at ~ 40 MHz (band B) were split into channels centred at 20, 30, 40, 50 MHz. The use of four separate channels of narrow bandwidth effectively doubles the sensitivity that can be attained with a single narrow channel without increasing the dispersion smearing of the pulse or depolarization due to differential Faraday rotation, provided the outputs are summed after appropriate time delays or rotation of the position angles respectively. This is illustrated in Figure 3.2 for dispersion removal. The signal in each of the four frequency channels was passed through filters having the same bandwidths. Two-pole Butterworth bandpass filters (BPFs) were used as they preserve the phase relationship of the signals. Three alternate bandwidths were available — 0.5, 1.5 and 5.0 MHz for band A and 1.0, 3.0 and 10.0 MHz for band B. These were selected by relays, under computer control. The bandwidth to be used for a given pulsar was chosen such that dispersion smearing of the pulse was less than 2% of the pulsar period.

Averaged signals proportional to the polarization parameters, I_X and I_Y, were produced by passing the filtered X and Y signals, E_x and E_y, to square law detectors (multipliers) with low pass filters (LPFs) on the outputs. Likewise, outputs proportional to the Stokes parameters U and V were produced by forming the in-phase and quadrature product of the signals respectively (see Appendix A). Due to the general-purpose nature of the hardware, the post-detection time constants were fixed at 0.6 ms for band A and 0.2 ms for band B. For all the pulsars observed in this study, these values were less than the sampling interval. A schematic diagram of the receiver "back end" is presented in Figure 3.3.

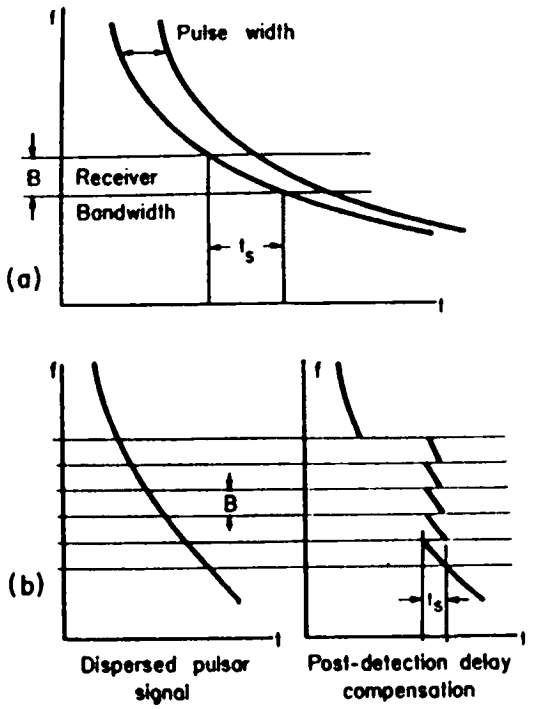

Figure 3.2: (a) A diagrammatic representation of a dispersed pulsar signal, whose frequency decreases with time. (b) By dividing the receiver passband into narrower frequency channels, the time resolution can be improved by shifting the pulses in each channel and summing the detected outputs; (after Hankins & Rickett 1975).

3.3 Data Acquisition

The detected outputs were digitised using voltage-to-frequency converters (VFCs) and followed by 16-bit digital counters. These counters were read and reset by the observatory PDP 11/60 minicomputer a fixed number of times during the apparent pulsar period. The apparent period was obtained by computer prediction of the current period by allowing for the pulsar spin-down and its Doppler offset at the observatory. Timing for the sampling interval was provided by a Rockland Programmable Frequency Synthesiser, which was phase-locked to the observatory frequency standard — a Rubidium source prior to 1990, and a Hydrogen maser since 1990. The synthesiser was linked to a Pulsar Timing Unit (PTU) which produced equally spaced pulses throughout the period and a "frame" pulse once every period, providing the data sampling synchronisation for the PDP 11/60. This arrangement is illustrated in Figure 3.4.

Stable pulse profiles, or integrated profiles, were obtained on-line by averaging the digitised signals synchronously with the pulsar period. This procedure improves the signal-to-noise ratio by a factor of $\sqrt{N}$, where N is the number of pulses averaged. A series of these superposed-epoch integrations, most with 256 samples (or *bins*) per apparent period, were recorded for each pulsar. The start

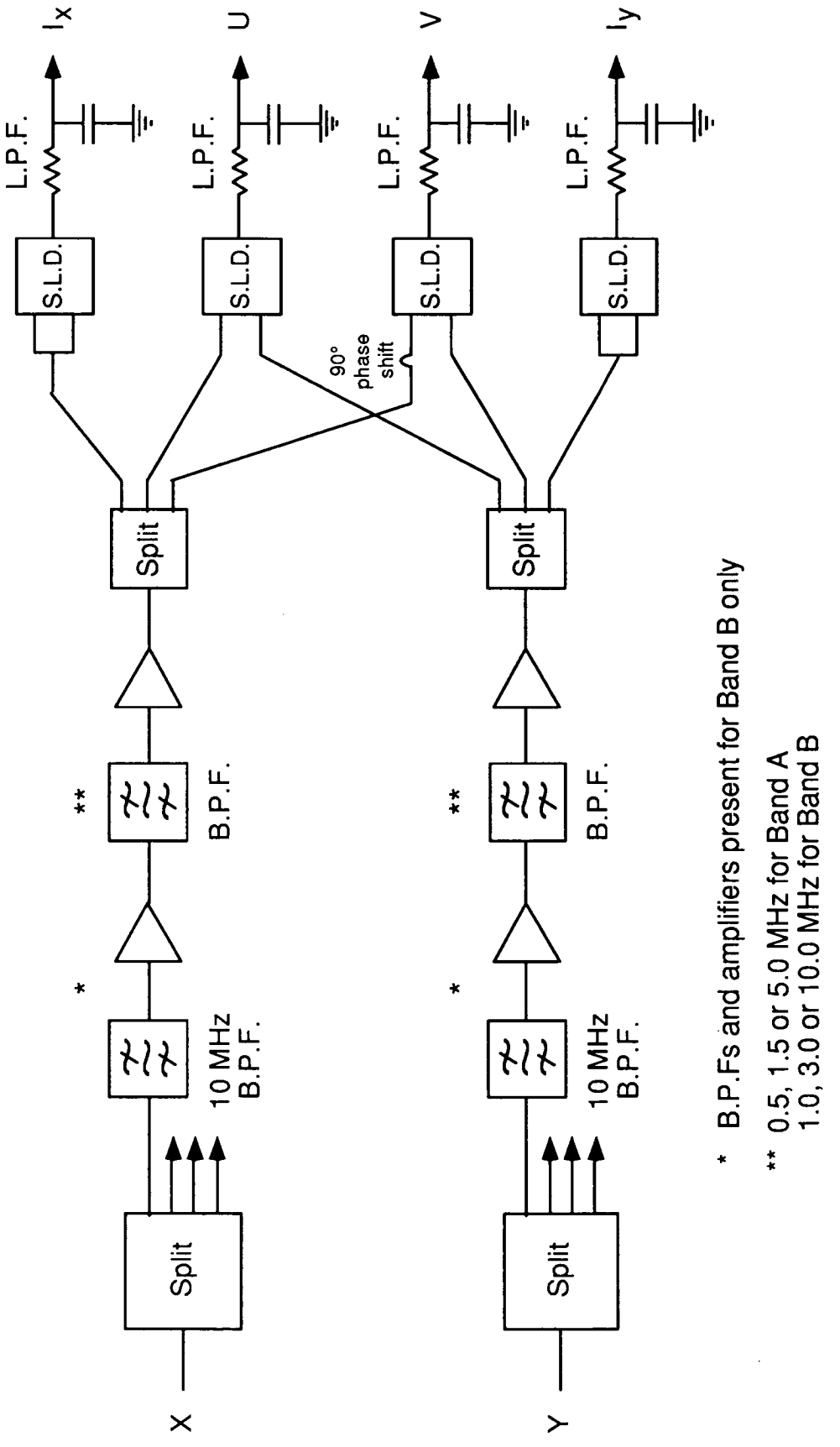

Figure 3.3: Schematic diagram showing one channel of the receiver back end (IF stage).

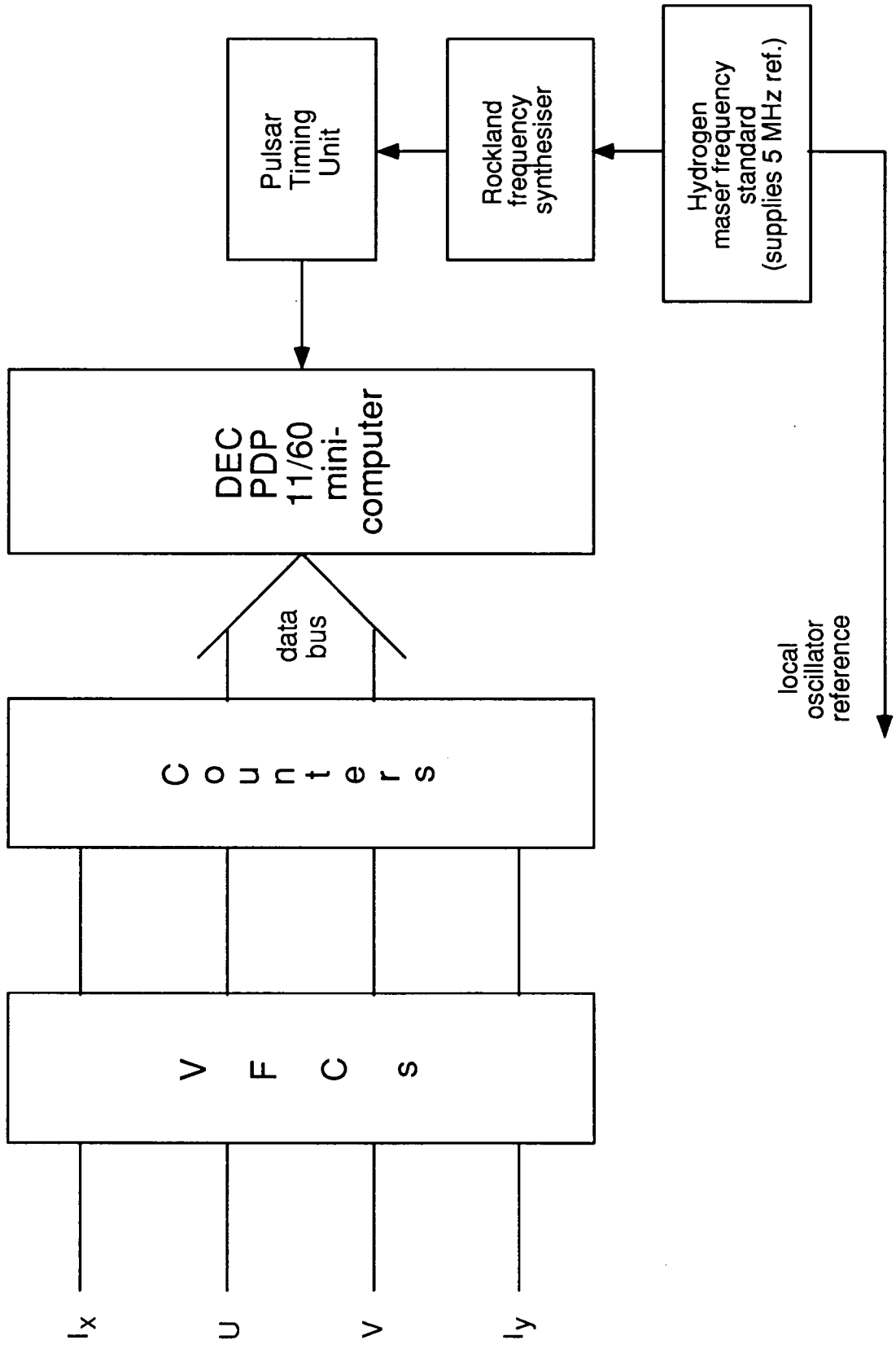

Figure 3.4: Schematic diagram illustrating the data acquisition system.

time of each integration was recorded with a resolution of one microsecond. Integration times ranged from 5 minutes for the stronger sources to 20 minutes for the weakest sources in the Mt Pleasant pulsar sample. At least three integrations were obtained for each pulsar in each observing session. For each integration, 32 channels of data were recorded onto a data disk — I_X, I_Y, U and V for the four adjacent frequencies in both bands A and B. A summary of the typical observing parameters for the timing measurements is provided in Table 3.1.

Calibration of the channel gain was accomplished by radiating a weak ($\sim$20% of the system temperature) broadband, linearly polarized noise signal into the feed via a small probe mounted at 45° to the X and Y dipoles (hereafter called the "CAL" signal). This CAL signal has the effect of introducing a DC offset to the mean baseline of an integrated profile. The CAL signal was injected into the system during every second integration. A relative calibration scheme was used for the timing measurements in order to make receiver gain corrections. Both this and the more elaborate polarization calibration scheme are described in Chapters 4 and 5 respectively.

During 1991, a series of polarization measurements were made in conjunction with the timing measurements. The data acquisition procedure employed on these occasions differed from that described above. For polarization work, measurement of the outputs corresponding to the Q, U and V Stokes parameters and extraction of the position angle of the linear polarization vector depends critically on precise calibration of the data. The measurements consisted of several "sets" of integrations, each set consisting of four distinct integrations, viz.

Integration 1: CAL *off*, X signal through 0° port of the hybrid,
Integration 2: CAL *on*, X signal through 0° port of the hybrid,
Integration 3: CAL *off*, X signal through −90° port of the hybrid,
Integration 4: CAL *on*, X signal through −90° port of the hybrid,

making it possible to estimate and remove the instrumental phase in the system and to rescale each data channel to obtain equal gains during the post-processing (see Appendix B for details). This enabled correct calibration of all four polarization parameters. Short integration times were used (typically 60 seconds) in order to complete a set of four measurements in a time shorter or comparable to the time over which there could be noticeable gain drifts in the I_X, I_Y, U or V multipliers. This practice ensures correct calibration of the parameters. It also avoids smearing of the linearly polarized radiation because of relative rotation of the (fixed) dipoles with respect to the source position angle while tracking the source. Between 10 and 30 sets of these integrations were recorded for a subset of the Mt Pleasant pulsar sample. This subset was chosen mainly on the basis of higher flux density, as these pulsars would be more suited for polarization measurements given the sensitivity-limit of the 26m telescope.

Table 3.1: Typical observing parameters for the pulsar timing measurements. The columns contain respectively the pulsar name, bandwidth code (1 = 0.5/1.0 MHz, 2 = 1.5/3.0 MHz, 3 = 5.0/10.0 MHz at 670/800 MHz), dispersion smearing (in milliperiods) at 670 and 800 MHz, and typical integration time for one measurement (in minutes). A total of 256 bins were used across the pulsar period in all cases except for PSRs B0740-28 and B1449-64, for which 200 bins were used.

Pulsar PSR B	B/W code	Smearing (mP) 670 MHz	800 MHz	Integration time (min.)
0403-76	3	5.7	6.7	20
0538-75	3	2.0	2.4	10
0628-28	3	3.8	4.5	10
0736-40	2	17.7	20.8	10
0740-28	2	18.3	21.5	10
0808-47	2	17.2	20.2	20
0835-41	2	8.1	9.5	5–10
0839-53	2	8.9	10.5	20
0905-51	2	17.0	19.9	20
0923-58	3	11.2	13.1	20
0932-52	3	9.5	11.1	20
0940-55	2	11.2	13.2	10
0959-54	3	12.5	14.7	10
1054-62	1	10.5	12.4	15
1056-57	3	12.5	14.7	20
1154-62	1	11.2	13.2	10
1221-63	2	18.5	21.7	15
1240-64	1	10.5	12.4	5–10
1323-58	1	8.2	9.6	20
1323-62	1	8.3	9.7	10
1358-63	3	16.0	18.8	10
1426-66	3	11.5	13.5	5–10
1449-64	2	16.4	19.2	5–10
1451-68	3	4.5	5.3	10
1530-53	3	2.5	2.9	10
1556-44	2	9.5	11.1	5–10
1558-50	2	8.1	9.5	10
1600-49	2	17.8	20.9	10
1641-45	1	14.4	16.9	5–10
1648-42	1	8.6	10.1	20
1700-32	3	12.0	14.1	20
1706-16	3	5.2	6.2	10
1718-32	2	10.9	12.8	15
1727-47	2	6.1	7.1	5–10
1737-30	2	10.2	12.0	20
1737-39	2	12.8	15.0	15
1742-30	2	10.0	11.8	10–15
1747-46	3	4.0	4.7	10
1749-28	3	12.5	14.7	5
1857-26	3	8.5	10.0	10
1937-26	3	17.1	20.1	20
2045-16	3	0.8	1.0	10
2048-72	3	7.3	8.6	20
2321-61	3	0.9	1.1	20
2327-20	3	0.7	0.8	20

Chapter 4

Pulsar Timing Observations

4.1 Introduction

Much information can be derived from precise measurements of pulse arrival times and pulsar coordinates. The extreme regularity of some pulsars has provided unique tests of general relativity and may mean they are used for precision time-keeping over long periods in the future (Weisberg & Taylor 1984, Davis *et al.* 1985). On the other hand, deviations from a simple model have provided a wealth of information about the internal structure of neutron stars. Comparison of positions obtained from pulsar timing and radio interferometry provides an important check on the fundamental reference frames used in astronomy (Backer 1989). Measurements of proper motion and trigonometric parallaxes provide a greater understanding of the origin of pulsars. Pulse dispersion in the interstellar medium provides a means of estimating the column density of electrons along the line of sight (dispersion measure) which aids in understanding the composition of our Galaxy (Cordes *et al.* 1991, Taylor & Cordes 1993), and from which distances can be estimated.

This chapter presents the method and results of the analysis of pulse arrival-time data from pulsar observations made at the Mt Pleasant Radio Astronomy Observatory. Data have been collected at approximately monthly intervals for a total of 45 pulsars. For most of the pulsars, observations commenced in September 1987, while a few were added to the survey in September 1990. The results presented in this chapter (and the rest of the thesis) have been derived from observational data recorded up to the end of 1994. All the pulsars observed are south of declination $-16°$. Many of these are relatively unstudied objects because much of the pulsar work has been conducted in the northern hemisphere.

Some of the results that appear in this chapter have already been published (D'Alessandro *et al.* 1993). However, many of the parameters have been improved or revised because the time span of the data set has increased by an additional 3 years since that paper was written.

4.2 Timing Analysis

The pulsar timing analysis involves comparison of the arrival time of pulses at the observatory with the expected arrival time based on timing models of the pulsar's rotation. The timing analysis was performed off-line and in a series of stages, as described below.

4.2.1 Calibration and Data Reduction

As described in Chapter 3, integrated profiles were recorded for the four channels in each of bands A and B, centred at ~ 670 MHz and ~ 800 MHz respectively. Hence, for each integration on a pulsar, there were a total of 16 integrated profiles to process — eight I_X and eight I_Y profiles. In the first step of the data reduction, the differential delays due to dispersion in the interstellar medium were compensated by shifting these pulse profiles in time to a channel frequency near the passband centre frequency, viz. 675 and 790 MHz. The time delays were computed according to Equation 1.10, using the best available estimate of the pulsar's DM. In most cases, these values were obtained from the pulsar catalogue compiled by Manchester & Taylor (1981). Henceforth, this (first) step in the procedure shall be termed "dedispersion". The I_X and I_Y data recorded for each channel were then plotted to enable an assessment of the quality of the data and removal of data from channels affected by interference.

The next step involved calibration of the data, to allow for differences in gain between the X and Y channels of the receiver. Absolute calibration of the data was not attempted. Rather, a relative calibration scheme was employed, based on the assumption that the linearly polarized CAL signal radiates equally into the X and Y dipoles. Comparison of the CAL strength in the X and Y channels with observations of the continuum source Virgo A, whose flux density is well known, showed this to be a valid assumption. The CAL height, i.e. the difference in the mean baseline height between successive CAL-off and CAL-on integrations, was used to determine the relative gain of the I_X and I_Y channels. Using this information, the I_X data recorded for each channel were rescaled with respect to the I_Y data.

After calibration, a final integrated profile for each band was obtained by summing the profiles from individual integrations and from adjacent channels (after scaling the latter so that they all had the same off-pulse rms noise in order to maximise the signal-to-noise ratio) to obtain the total intensity profile, $I = I_X + I_Y$.

4.2.2 Local Arrival Times

The local arrival time of an individual pulse refers to the arrival time of a unique point in the pulse (such as the centroid of the pulse) at the observatory. The pulse phase, expressed as a fraction of the apparent period, was estimated by cross-correlation of each profile at a given radio frequency with a standard "template". This template is simply a high signal-to-noise profile obtained by averaging a large number of integrated profiles. Templates for both observing frequencies for all the Mt Pleasant pulsars are shown in Appendix D. This cross-correlation procedure involves interpolation of the cross-correlation function using a second order polynomial. The polynomial is fitted to a set of sampled cross-correlation values over five lags around the lag of the sampled maximum correlation, in order to more accurately locate the lag at which the correlation function reaches a maximum.

At this point the band A and B profiles were dedispersed to nearby "reference frequencies" of 650 and 800 MHz, respectively, and the arrival phases were adjusted accordingly. The choice of these reference frequencies is partly historical, arising from uncertainty in the selection of the original receiver centre frequencies because of interference from terrestrial transmitters. Such a change took place in May 1990, a few months after the band B observations commenced. The local oscillator frequency for this band was changed from 795 to 760 MHz to avoid radio interference. Another such change took place on July 1, 1994, after it was discovered that new UHF television transmissions were affecting band A. In this case, a shift in the local oscillator frequency from 650 to 647.5 MHz alleviated the problem. However, the interference is still present and the solutions for future observations are either to move further down the radio band or to redesign the receiver front-end to filter out the interference.

Arrival phases determined in the manner described above can yield an accuracy of about one milliperiod, depending on the sharpness of the pulse and the signal-to-noise ratio. The rms "measurement" uncertainty in the arrival phases, σ_M, was estimated using the formula given by Downs & Reichley (1983),

$$\sigma_M = \frac{(P\tau_b)^{\frac{1}{2}}}{\frac{S}{N}\left[\int_0^1 (\frac{dU}{d\phi})^2 d\phi\right]^{\frac{1}{2}}} \tag{4.1}$$

where P is the pulse period, τ_b is the sampling interval, $\frac{S}{N}$ is the signal-to-noise ratio of the pulse peak, and U is the template whose peak and extent are normalised. For the Mt Pleasant pulsar sample, the measurement uncertainties lie between 0.1 and 2 milliperiods.

The local arrival time is taken to be the start time of the observation, plus an integral number of periods close to the middle of the observation, plus the arrival phase (expressed in seconds). These times are corrected for any drift in

the observatory hydrogen maser frequency standard. The drift was measured by a daily comparison with Universal Coordinated Time (UTC) through ABC TV signals transmitted via AUSSAT. At appropriate times, corrections were made for the leap seconds inserted into the UTC scale to maintain rough consistency with solar time.

4.2.3 Barycentric Arrival Times

The arrival time of pulses at the observatory is greatly affected by the Earth's complex motion through space. By referring the arrival times to an inertial reference frame, the Solar System Barycentre (SSB), these times are made independent of the Earth's motion. The following section describes the relevant corrections applied to the local arrival times.

Corrections to the SSB

The barycentric arrival time is given by

$$T_b = t_o + \Delta t_{ob} - \Delta t_d + \Delta t_r - \Delta t_g \tag{4.2}$$

where t_o is the local arrival time, Δt_{ob} is the classical observatory to barycentre delay, Δt_d is the dispersion delay at the Doppler-shifted observing frequency, Δt_r is the relativistic correction of the Earth-bound clock for the effects of a changing gravitational potential, and Δt_g is the Shapiro relativistic delay.

The first correction term, the time difference between the observatory and SSB with respect to the pulsar, is given by

$$\Delta t_{ob} = \frac{\mathbf{r_s} \cdot \mathbf{n}}{c} \tag{4.3}$$

(Manchester & Taylor 1977) where $\mathbf{r_s}$ is the vector from the SSB to the observatory, $\mathbf{n}$ is a unit vector in the assumed direction to the pulsar, and c is the speed of light. The vector $\mathbf{r_s}$ was calculated in three steps: the observatory to Earth-centre vector, allowing for nutation ($\leq$ 22 ms); the Earth-centre to Earth-Moon Barycentre (EMB) vector ($\leq$ 20 ms); and the EMB to SSB vector ($\leq$ 500 s). Calculations involving barycentres require the use of a precise ephemeris of the location of the Moon and planets. The Jet Propulsion Laboratories DE200 ephemeris (Standish 1982) was used to evaluate the vector $\mathbf{r_s}$, with the FK5 stellar reference system at the epoch J2000.0. The accuracy expected from the ephemeris is about 1μs over a period of several years, the major uncertainty arising from the assumed masses of the outer planets. For all pulsars, the vector $\mathbf{n}$ was initially evaluated using the positions given by Manchester & Taylor (1981) or more recent values if they were available.

The signal delay, Δt_d, due to interstellar and interplanetary dispersion, was calculated using the true observing frequency f (in MHz) at the barycentre, Doppler

shifted to allow for the Earth's motion around the Sun. From Equation 1.10, the time delay (in seconds) relative to a pseudo-infinite frequency is given by

$$\Delta t_d = \frac{DM}{2.410 \times 10^{-4} f^2} \tag{4.4}$$

where DM is the best available estimate of the pulsar's dispersion measure, in units of $\mathrm{cm}^{-3}\mathrm{pc}$.

The third correction term in Equation 4.2, Δt_r, accounts for the annual variation in the terrestrial clock rate relative to a clock at an infinite distance in a reference frame which is inertial with respect to the SSB. This variation results from the changing gravitational potential experienced by the terrestrial clock as the Earth moves around its elliptical orbit. The relativistic clock correction to Barycentric Dynamical Time (TDB) was made using the accurate approximation given by Blandford & Teukolsky (1976),

$$\Delta t_r = 1.66145 \times 10^{-3} \left[\left(1 - \frac{1}{8} e^2 \right) \sin M_e + \frac{1}{2} e \sin 2M_e + \frac{3}{8} e^2 \sin 3M_e \right] \tag{4.5}$$

where e and M_e are the eccentricity and mean anomaly of the Earth's orbit respectively. The first term introduces an annual peak to peak sinusoidal amplitude of 3.4 ms, which is significant for timing observations. The higher order terms neglected in Equation 4.5 contribute an error of approximately 20 μs, mainly due to the effects of the Moon and planets. The software used for the barycentric arrival-time analysis in the Physics Department at the University of Tasmania did not allow for these effects until the program was upgraded early in 1995 (McCulloch 1995, private communication). However, an error of 20 μs is not significant in observations of long-period pulsars, nor with respect to the uncertainties associated with such measurements (see Section 4.3.6). If account is taken of the effects of the Moon and planets, the error is less than 100 ns over a span of ~ 30 years (Backer & Hellings 1986).

The final correction, Δt_g, is the relativistic delay due to the curvature of the path of the pulsar signal as it traverses the gravitational field of the Sun. The delay is variable because it depends on the orientation of the Sun, pulsar and Earth. It reaches a maximum of 250 μs when the line of sight is close to the Sun's limb (Backer & Hellings 1986).

Contributions to the Barycentric Phase

It is worthwhile considering the various contributions to the barycentric phase or arrival time as these will have a bearing on the analyses to be performed on the data and the interpretation of the results. Using a similar notation to Cordes & Downs (1985), the barycentric phase (in units of periods or cycles) may be written as

$$\phi = \phi_S + \phi_{TN} + \phi_G + \phi_M + \phi_J + \phi_{\text{other}}. \tag{4.6}$$

The terms represent, respectively, the phase due to pulsar spin-down, timing noise, glitches, measurement noise, pulse jitter, and a range of other sources which, in general, contribute a relatively small or negligible component to the barycentric phase. The procedure for modelling pulsar spin-down and glitches is discussed in the next section. The terms ϕ_{TN}, ϕ_M and ϕ_J are considered in Section 4.3.6. Some sources of ϕ_{other} include: (i) pulse shape changes [due to "mode changes" (e.g., see Rankin 1986), or as a result of free pulsar precession (Suleymanova & Shitov 1994)]; (ii) instrumental effects such as a variable polarization response of the receiving system which causes distortion of the pulse shape (this is avoided by taking the sum of two orthogonal polarizations); (iii) diffractive interstellar scintillation and dispersion, where arrival-time variations are due to alteration of the effective observing centre frequency (Rickett 1977); (iv) dispersion measure fluctuations not accounted for by Equation 4.4; (v) interstellar refractive effects, including time delays (which scale steeply with observing wavelength) and wandering of the pulsar "image" (Cordes *et al.* 1986, Cordes *et al.* 1990, Foster & Cordes 1990, Phillips & Wolszczan 1991, 1992, Rickett 1990); (vi) errors in the atomic time standard used for the observations; and (vii) uncertainties in the planetary ephemeris. In general, these terms are important considerations only in observations of millisecond pulsars with high timing accuracy.

4.2.4 Timing Models

In order to obtain the pulsar spin-down parameters, a truncated Taylor series was used in the usual manner (Manchester & Taylor 1977). That is, a three-parameter model of the barycentric pulse phase $\phi(t)$ as a function of time t was fitted to the barycentric arrival-time data, where

$$\phi(t) = \phi_o + \nu(t - t_o) + \tfrac{1}{2}\dot{\nu}(t - t_o)^2 \tag{4.7}$$

and ϕ_o is the phase at time t_o. The terms ν and $\dot{\nu}$ represent estimates of the pulse frequency and frequency derivative respectively. The barycentric arrival-time analysis allows for estimates of the pulsar position and proper motion terms, $\phi_A(\alpha, \delta, \mu_\alpha, \mu_\delta)$. In most cases, initial estimates of these rotation and astrometric parameters were taken from the catalogue compiled by Manchester & Taylor (1981).

More accurate parameters were obtained as follows. The phase model given by Equation 4.7 was used to calculate the predicted phase at each barycentric arrival time, using the initial estimates of the frequency terms. Provided the estimates were sufficiently precise so that pulse numbering remained valid, i.e., free of integral phase cycle ambiguities, the phase at any observed time was close to an integral number of actual phase cycles. The difference between each phase estimate and the nearest whole cycle yielded a set of "prefit" phase residuals.

Errors in the assumed parameters then appeared as trends in these residuals. The observed trend is linear for errors in ν, quadratic for errors in $\dot{\nu}$ and, for data spanning one year or more, an annual sinusoid for errors in the position terms. Over a number of years, a change in the sinusoidal amplitude may indicate an error in the proper motion terms. The residuals may also include contributions from other sources (Equation 4.6). If a position fit was required, the astrometric term, ϕ_A, was added to the model at this point, where

$$\phi_A = A \times [\Delta\alpha + \mu_\alpha(t - t_o)] \quad + \quad B \times [\Delta\delta + \mu_\delta(t - t_o)]. \tag{4.8}$$

The terms $\Delta\alpha$, $\Delta\delta$ are corrections to the assumed right ascension and declination at $t = t_o$ and the terms μ_α, μ_δ are the proper motion components in these coordinates. The coefficients A and B include the pulsar and earth coordinates with respect to the solar system barycentre at a standard epoch (Manchester & Taylor 1977).

An iterative, unweighted least squares procedure was then used to fit the model to the prefit residuals to obtain more accurate values and hence, a new phase model. Final or "postfit" phase residuals were obtained by subtracting the phases predicted by this model from the observed phases.

A "bootstrapping" process was necessary for a number of pulsars for which the initial timing parameters were not known with sufficient accuracy. This was achieved by obtaining a series of closely spaced arrival times (minutes to hours), fitting for a more accurate period, extending the data span, and recalculating the period with greater accuracy. The usual analysis was then performed on the arrival-time data for these pulsars.

Some of the analyses described later in this chapter require an extension to the basic timing model given by Equation 4.7. For example, pulsar timing residuals that display a cubic term may require a third order polynomial phase fit, in which case the phase model

$$\phi(t) = \phi_o + \nu(t - t_o) + \tfrac{1}{2}\dot{\nu}(t - t_o)^2 + \tfrac{1}{6}\ddot{\nu}(t - t_o)^3 \tag{4.9}$$

is used, where $\ddot{\nu}$ is the frequency second derivative.

For timing data that required fits for period discontinuities or jumps, the arrival-time model given by Equation 4.7 was extended to include the jump parameters, such as the change in frequency and frequency derivative, and the short- and long-term time constants associated with the post-jump relaxation (McCulloch *et al.* 1987, McCulloch *et al.* 1990). The software used for the timing model fits, TEMPO2, was recently modified by Physics Department researchers to accommodate the latest jump models (as described in Chapter 2) in order to analyse the Vela glitch data. This software expresses all the parameters in terms of the rotation frequency, so that $\nu(t) = \nu_p(t) + \Delta\nu(t)$, where $\nu_p(t)$ is the extrapolated pre-jump frequency, $\Delta\nu(t)$ is the change in frequency caused by the jump at time

T_g, given by

$$\Delta\nu(t) = \Delta\nu_c + \Delta\dot{\nu}_c(t - T_g) + \tfrac{1}{2}\Delta\ddot{\nu}_c(t - T_g)^2 + \sum_{i=1}^{3} \Delta\nu_i e^{-(t-T_g)/\tau_i} \qquad (4.10)$$

The parameters $\Delta\nu_c$, $\Delta\dot{\nu}_c$, and $\Delta\ddot{\nu}_c$ are the permanent changes in frequency, frequency derivative and frequency second derivative due to the jump and the $\Delta\nu_i$ terms are the amplitudes of the three exponential relaxations with decay time constants τ_i. For the Mt Pleasant data, the fitting procedure only required the parameters $\Delta\nu_c$, $\Delta\dot{\nu}_c$ and possibly one exponential term.

The models presented here are defined in terms of the pulsation frequency and its derivatives. These quantities are more useful for describing pulsar dynamics than do parameters based on the pulse period and its derivatives. Neither of these quantities have become standard in pulsar work, often being used interchangeably. In this thesis, period parameters will be used when tabulating the spin-down terms, as is commonly the case. Otherwise, only frequency parameters will be used. The two quantities are related by the transformations $P = \nu^{-1}$, $\dot{P} = -\dot{\nu}\nu^{-2}$ and $\ddot{P} = 2\dot{\nu}^2\nu^{-3} - \ddot{\nu}\nu^{-2}$. For abrupt changes,

$$\Delta P = -\nu^{-2}\Delta\nu, \qquad (4.11)$$

$$\Delta\dot{P} = -\nu^{-2}\Delta\dot{\nu} + 2\nu^{-3}\dot{\nu}\Delta\nu, \qquad (4.12)$$

$$\Delta\ddot{P} = -\nu^{-2}\Delta\ddot{\nu} + 4\nu^{-3}\dot{\nu}\Delta\dot{\nu} + \Delta\nu(2\nu^{-3}\ddot{\nu} - 6\nu^{-4}\dot{\nu}^2). \qquad (4.13)$$

4.2.5 Dispersion Measure Calculations

The dual frequency timing measurements were used to correct or improve the dispersion measure estimate for a given pulsar if the arrival times showed a significant and systematic offset between timing residuals derived from the band A and band B data. This required careful alignment of the two templates. Profiles affected by interstellar scattering were aligned using the leading edge of the pulse.

The mean time offset, Δt, between the dual frequency data points of coincident epoch was calculated and then used to estimate the DM correction which, from Equation 1.10, is given by

$$\Delta DM_c = \frac{\Delta t}{k} \qquad (4.14)$$

where

$$k = 4149.378\left(\frac{1}{f_{r_2}^2} - \frac{1}{f_{r_1}^2}\right) \qquad (4.15)$$

and f_{r_2}, f_{r_1} are the band B and band A reference frequencies (800 and 650 MHz) respectively. The uncertainty in ΔDM_c, $\delta(\Delta DM_c)$, was calculated using

$$\delta(\Delta DM_c) = \frac{\sigma_{\Delta t}}{|k|\sqrt{N}} \qquad (4.16)$$

where N was the number of coincident epochs used to compute the mean time offset. However, this uncertainty was generally less than the DM uncertainty associated with the centre frequencies of the filters in each IF channel. The centre frequencies were measured by injecting a swept frequency into the back-end of the receiving system, recording the data, and then using a program to calculate the *centroid* of the bandpass, which was taken to be the centre frequency of the filter. The worst case centre frequency offset for each band was used to calculate the maximum possible error in the DM, given by

$$\delta(\Delta DM_c)' = 2\,DM \left(\frac{\Delta f_{r_1}}{f_{r_1}^3} - \frac{\Delta f_{r_2}}{f_{r_2}^3} \right) \left(\frac{1}{f_{r_1}^2} - \frac{1}{f_{r_2}^2} \right)^{-1}. \tag{4.17}$$

The overall uncertainty, δDM, was taken to be the root-square-sum of the uncertainties from Equations 4.16 and 4.17.

The DM correction had to be adjusted to compensate for the effect of dedispersing the profiles to the reference frequencies (see Section 4.2.2) using the *old* DM ($DM_{\rm old}$). This caused the DM correction derived from the residuals to be underestimated. The true DM correction is given by

$$\Delta DM = \left(\frac{1}{f_{r_1}^2} - \frac{1}{f_{r_2}^2} \right) \left(\frac{1}{f_{c_1}^2} - \frac{1}{f_{c_2}^2} \right)^{-1} \Delta DM_c \tag{4.18}$$

where f_{c_1} and f_{c_2} are the centre frequencies of bands A and B respectively. The new DM was then computed using $DM_{\rm new} = (DM_{\rm old} + \Delta DM) \pm \delta DM$.

4.3 Results and Discussion

Table 4.1 lists the best-fitting timing and astrometric parameters obtained from the arrival-time analysis for each pulsar. The periods (P) and period derivatives ($\dot{P}$) are quoted for an epoch near the middle of the data span. The coordinates are based on the J2000 reference frame, as described earlier. This is in line with the general trend toward the J2000 coordinate system (Taylor *et al.* 1993). However, when naming individual pulsars, the B1950-based name is used since most of the 45 pulsars in the present study were discovered when that coordinate system was in widespread use. For clarity, in most instances a "B" has been added before the numbers in a pulsar name throughout the thesis.

4.3.1 Periods and Period Derivatives

For 34 of the pulsars in Table 4.1, one or both of the period terms resulting from the second order polynomial fits are significantly more accurate than previously published values (Manchester & Taylor 1981, Taylor *et al.* 1993). In many cases,

Table 4.1: Timing parameters from second order polynomial and position fits. The columns contain respectively the pulsar name, the period (P) and its uncertainty, the period derivative ($\dot{P}$) and its uncertainty, the epoch to which the period is referred (expressed as a truncated Julian Day, JD - 2440000), the pulsar position (for the standard epoch J2000) and uncertainty, and the dispersion measure and uncertainty determined from the dual frequency data. All quoted uncertainties are twice the formal standard errors from the analysis and refer to the last digit quoted.

Pulsar	P (s)	Err	$\dot{P}$ ($10^{-15} ss^{-1}$)	Err	Epoch (TJD)	RA	Err	DEC	Err	DM ($cm^{-3}pc$)	Err	Notes
0403-76	0.545252954568	4	1.5391	1	8396.3325	04 01 51.72	6	-76 08 13.5	2	21.6	4	1,2
0538-75	1.245855675502	9	0.5753	3	8395.5467	05 36 30.83	6	-75 43 56.7	2	18.0	5	1,2
0628-28	1.24441969715	1	7.1190	4	8393.7436	06 30 49.45	1	-28 34 43.5	2	34.6	6	1
0736-40	0.37491952199	1	1.6101	4	8393.7699	07 38 32.31	1	-40 42 40.5	2	161.4	9	
0740-28	0.1667609371645	5	16.82239	2	8393.7949	07 42 49.11	1	-28 22 43.7	2	73.8	4	1,4
0808-47	0.547199659921	3	3.0806	1	8394.6055	08 09 43.87	4	-47 53 55.4	4	229	1	
0835-41	0.751622605855	4	3.5434	1	8393.8274	08 37 21.19	1	-41 35 14.1	2	147.2	9	
0839-53	0.720612455794	8	1.6445	2	8395.5840	08 40 33.90	6	-53 32 35.5	6	158	1	1,2
0905-51	0.253556262843	1	1.83040	3	8367.8332	09 07 15.92	2	-51 57 59.0	2	103.7	7	1,2
0923-58	0.73950160632	4	4.855	1	8394.7667	09 24 31.0	1	-58 14 06.3	8	58	1	1,2
0932-52	1.44477342960	1	4.6522	4	8367.9209	09 34 28.32	6	-52 49 27.0	4	100	2	1,2
0940-55	0.6643706188	1	22.739	4	8393.8460	09 42 15.72	8	-55 52 55.2	6	180	1	3
0959-54	1.4365897078	4	51.47	1	8393.8687	10 01 38.0	2	-55 07 06	2	130	2	
1054-62	0.422447681037	3	3.57110	8	8395.7089	10 56 25.63	6	-62 58 47.2	4	320.5	6	1
1056-57	1.18499918534	1	4.3000	3	8366.7500	10 59 00.91	6	-57 42 14.0	4	108	2	1
1154-62	0.400522590098	2	3.93055	5	8395.7415	11 57 15.27	4	-62 24 50.5	2	324.7	6	1
1221-63	0.2164768855477	7	4.95392	2	8394.9221	12 24 22.19	2	-64 07 53.7	1	97.7	6	1
1240-64	0.3884815405836	3	4.499568	9	8393.9645	12 43 17.14	2	-64 23 23.7	1	297.4	4	1,2,4
1323-58	0.47799103865	3	3.2372	8	8395.7797	13 26 58.27	4	-58 59 29.0	4	287.2	4	1
1323-62	0.52991419160	3	18.8831	8	8395.0096	13 27 17.4	1	-62 22 44.4	6	317.7	6	1,2
1358-63	0.84279267645	9	16.801	6	8897.6872	14 01 52.52	4	-63 57 46.2	4	98	1	
1426-66	0.785441138934	7	2.7697	2	8395.0320	14 30 40.84	4	-66 23 05.4	4	65.3	8	
1449-64	0.1794851323269	7	2.74611	2	8395.0492	14 53 32.703	6	-64 13 15.49	4	71.2	4	1,2
1451-68	0.2633768284973	4	0.09880	1	8395.0659	14 56 00.077	6	-68 43 39.18	4	8.6	2	1,2
1530-53	1.368881105911	5	1.4292	2	8394.0159	15 34 08.33	4	-53 34 18.9	6	24.7	4	1

Table 4.1: continued.

Pulsar	P (s)	Err	$\dot{P}$ ($10^{-15}ss^{-1}$)	Err	Epoch (TJD)	RA	Err	DEC	Err	DM ($cm^{-3}pc$)	Err	Notes
1556-44	0.2570562380038	5	1.01950	1	8394.0388	15 59 41.530	4	-44 38 45.9	1	56.1	4	1,2
1558-50	0.8642310437	3	69.500	9	8395.0893	16 02 18.8	2	-51 00 02	4	172	1	1
1600-49	0.327417712875	3	1.01482	8	8395.1109	16 04 22.97	2	-49 09 57.6	6	140.7	8	1
1641-45	0.45506254212	2	20.0965	5	8394.0601	16 44 49.28	3	-45 59 09.9	7	478.9	8	4
1648-42	0.84408138332	6	4.792	2	8533.7633	16 51 48.7	2	-42 46 10	4	487	3	1
1700-32	1.211785001279	7	0.6601	2	8368.2122	17 03 22.6	1	-32 41 48	2	110	1	1,2
1706-16	0.65305481058	6	6.296	2	8535.7368	17 09 26.47	2	-16 40 59	3	24.6	4	
1718-32	0.477157442497	3	0.64690	9	8535.6546	17 22 02.96	1	-32 07 46	1	126.3	8	1
1727-47	0.829792928034	7	163.5929	2	8395.1557	17 31 42.08	1	-47 44 34.7	2	124	2	1,2,4
1737-30	0.6066537816	2	465.62	1	8934.7841	17 40 33.7	2	-30 15 42	3	152.5	9	3,4
1737-39	0.512210847068	8	1.9554	3	8395.1829	17 41 18.06	1	-39 27 38.3	6	158.0	9	1,2
1742-30	0.367427503581	5	10.6657	1	8533.9196	17 45 56.30	2	-30 40 23.1	9	87.8	6	
1747-46	0.742352573567	2	1.29260	7	8395.2790	17 51 42.21	2	-46 57 25.1	4	20.5	4	1
1749-28	0.56255895890	1	8.1236	4	8367.3909	17 52 58.70	2	-28 06 37	4	50.4	6	1
1857-26	0.612209195661	2	0.20437	6	8394.3097	19 00 47.57	2	-26 00 43	2	38.2	6	1
1937-26	0.402857767789	1	0.95604	4	8368.4845	19 41 00.40	4	-26 02 05	2	50.3	6	1
2045-16	1.96157416964	1	10.9595	3	8394.3721	20 48 35.6	1	-16 16 44	6	11.6	2	
2048-72	0.341336242881	2	0.19579	5	8368.5298	20 53 47.14	6	-72 00 42.2	2	17.4	4	1,2
2321-61	2.34748626902	4	2.5800	9	8368.5713	23 24 26.99	8	-60 54 06.4	6	14.2	6	1,2
2327-20	1.64362158080	1	4.6310	4	8367.5196	23 30 26.89	6	-20 05 31	1	8.2	4	1

Notes: (1) One or both of the period terms have more precision than those listed in the catalogue compiled by Taylor *et al.* (1993).
(2) These positions are more accurate than the positions listed in the catalogue compiled by Taylor *et al.* (1993).
(3) A position fit was not possible for these pulsars (see text for explanation).
(4) The period terms represent a fit over the whole data span after removal of period discontinuities (see later section).

the period derivatives have been improved by 2–4 significant figures. The period derivative obtained for PSR B1648-42 by D'Alessandro *et al.* (1993) had not been previously measured, although a similar estimate was obtained soon after by Siegman *et al.* (1993).

4.3.2 Astrometric Terms

For many pulsars, the residuals over long time spans are dominated by timing noise, making position fits unreliable. Hence, in many cases position fits were made over time spans of only 2–3 years. In some cases, the timing noise over the whole data span was almost completely absorbed by a third order polynomial fit. For these pulsars, the position fit was performed after the third order fit. A number of pulsars in the Mt Pleasant pulsar sample have known proper motions, namely PSRs B0628-28, B0736-40, B0740-28, B1426-66, B1449-64, B1451-68, B1556-44, B1600-49, B1706-16, B1749-28, B1857-26 and B2045-16 (Bailes *et al.* 1990, Fomalont *et al.* 1992). The proper motion terms for these pulsars were taken into account when the barycentric arrival times were computed. The position fits were then performed as usual.

The positions of 34 and 16 of the pulsars listed in Table 4.1 are more accurate than those listed in the catalogues compiled by Manchester & Taylor (1981) and Taylor *et al.* (1993) respectively. Large position corrections were needed for a number of pulsars whose declinations were not well known, in particular, PSR B1648-42 (previous uncertainty ±30 arc min) and PSRs B1700-32, B1718-32, B1742-30, B1937-26 (previous uncertainty ±30 arc sec or more). One such example is shown in Figure 4.1. Position fits were not possible for PSRs B0940-55 and B1737-30 because of the large uncertainties arising from the presence of timing noise, even over reasonably short data spans. The positions of these pulsars were taken from Manchester & Taylor (1981) and McKenna & Lyne (1990) respectively.

The effects of proper motion were not detected in the timing residuals for any of the pulsars in the Mt Pleasant sample. Limiting factors such as measurement uncertainties, timing noise and limited data span length for such a measurement made it possible only to obtain upper limits for some of the sources. These upper limits were typically an order of magnitude greater than previously determined proper motions (Bailes *et al.* 1990, Fomalont *et al.* 1992).

4.3.3 Dispersion Measures

Dual frequency timing observations have been carried out for the past five years in order to detect any changes in the dispersion measure along the line of sight to the pulsars, and to improve some of the existing estimates. The DMs and their uncertainties were calculated as described in Section 4.2.5. More accurate DM estimates

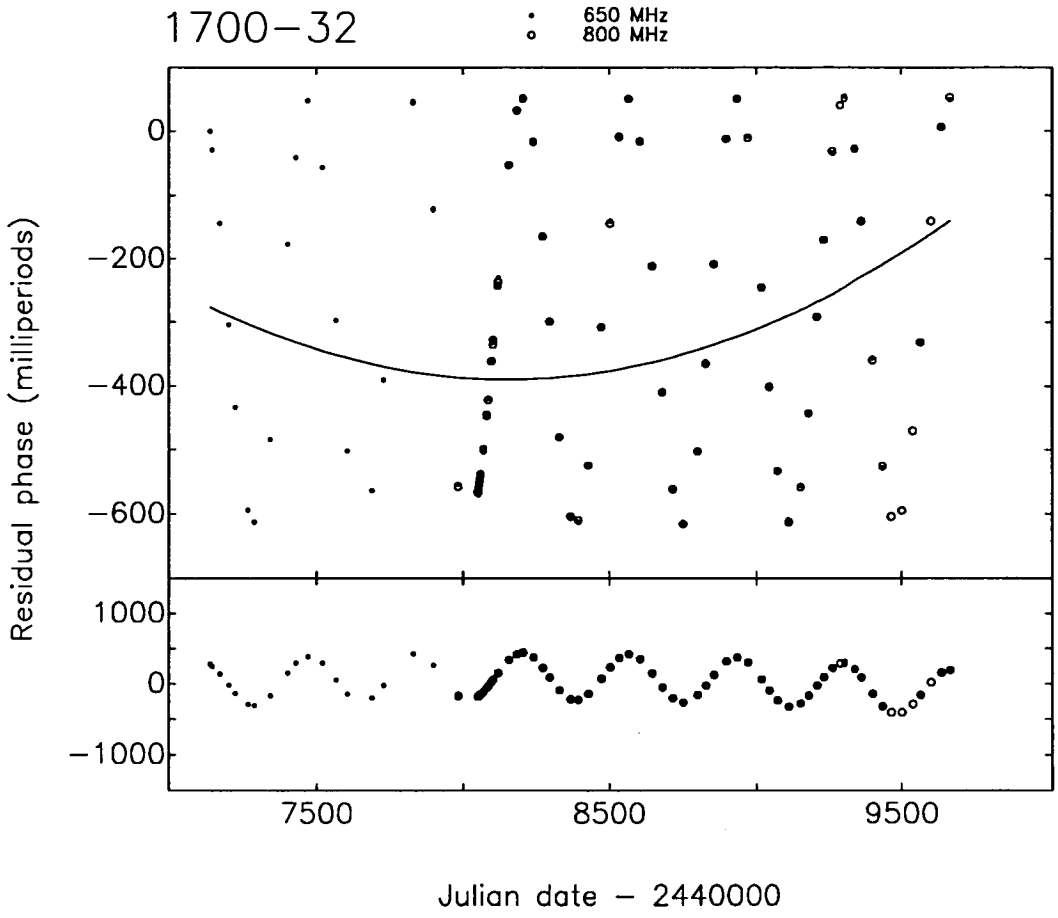

Figure 4.1: Example of the effect of a large position error on the measured arrival times. The position of PSR B1700-32, taken from Taylor *et al.* (1993), has been improved significantly by fitting for right ascension and declination.

were obtained for 18 pulsars, while some appear to have changed since they were last measured, typically 15–25 years ago. In general, but particularly for the latter cases, a third frequency is needed to confirm that the changes are related to truly dispersive effects. However, non-dispersive delays such as interstellar refractive delays and ray-bending in the pulsar magnetosphere are unlikely causes, being time-variable and relatively small by comparison (Phillips & Wolszczan 1991).

Many of the previously published DM estimates for southern pulsars were obtained by Newton *et al.* (1981), who quoted 2σ errors. Some of the other references, however, do not state the level of the quoted uncertainties — in these cases, 1σ errors have been assumed. The uncertainties are important in determining if significant long-term DM changes have taken place. The significance test

$$\frac{\Delta DM}{\sigma_{\Delta DM}} \quad \text{where} \quad \Delta DM = |DM_1 - DM_2| \quad \text{and} \quad \sigma_{\Delta DM} = \sqrt{\sigma_1^2 + \sigma_2^2}, \qquad (4.19)$$

was applied to the old and new DMs (with uncertainties of σ_1 and σ_2 respectively) for all the pulsars in Table 4.1, and the results of this test for significance levels $\geq 2\sigma$ are given in Table 4.2.

Table 4.2: Significant dispersion measure changes.

Pulsar PSR B	Old DM ($cm^{-3}pc$)	Ref.	New DM ($cm^{-3}pc$)	σ level
1054−62	323.4 ± 5	3	320.5 ± 3	5σ
1221−63	96.9 ± 3	3	97.7 ± 3	2σ
1556−44	58.8 ± 5	2	56.1 ± 2	$\geq 5\sigma$
1558−50	169.5 ± 8	1	171.7 ± 6	2σ
1648−42	525 ± 4	3	487 ± 2	$\geq 5\sigma$
1700−32	105 ± 1	1	110.1 ± 7	3σ
1727−47	121.9 ± 1	2	123.5 ± 8	2σ
1747−46	21.7 ± 2	3	20.6 ± 2	4σ

Notes: Uncertainties are 1σ and refer to the last digit quoted.

Ref. (1) Hamilton, P.A., McCulloch, P.M. & Manchester, R.N., 1979, private communication.
(2) McCulloch *et al.* (1973).
(3) Newton *et al.* (1981).

Apparent changes because of instrumental effects can be ruled out on several grounds. Firstly, the centre frequency error would have to be of the order of megahertz and therefore would be easily discovered. Secondly, the measured DM changes are of both signs and some pulsars with similar DM/period ratios (and using the same filter set) show no significant change. Thirdly, the DMs of four pulsars which overlap with the sample of newly determined DMs by Hamilton & Lyne (1987) agree within the quoted 1σ uncertainties. Alteration of the effective centre frequencies within the filter band by interstellar scintillation was considered to be negligible because of the relatively long integration times ($\sim 0.5 - 1$ hr) and large bandwidths used.

It is possible that the previously quoted uncertainties were underestimated in some cases. One example is PSR B1648-42, for which the DM has apparently changed from 525 $cm^{-3}pc$ (Newton *et al.* 1981) to 487 $cm^{-3}pc$. However, Newton *et al.* do state that a timing solution for this pulsar was not obtainable because of poor sensitivity. At their observing frequency of 410 MHz the profile is severely affected by interstellar scattering.

Assuming (i) the DM changes are caused by the movement of a single region of excess electron density (δn_e) into or out of the line of sight, (ii) this region is roughly spherical and $\sim 10^{15}$ cm in diameter, and (iii) the pulsar transverse velocity is ~ 100 km/s, then the DM changes of all the pulsars in Table 4.2 imply densities of $\sim 10^2 - 10^3$ cm^{-3} except for PSR B1648-42, where the implied density is $\sim 10^4$ cm^{-3}. If the clouds are not the assumed spherical shape but elongated along the line of sight, the implied densities can be reduced by a factor equal to

the "axial ratio" of the clouds. These densities are at least an order of magnitude higher than expected for large HII regions (Prentice & ter Haar 1969), fractionally ionised HI clouds and supernova remnant shock fronts (McKee & Ostriker 1977). However, recent radio recombination line and synthesis observations of compact HII regions (see Gordon 1988) suggest that electron densities up to $\sim 10^5$ cm^{-3} are not unrealistic. These estimates are also supported by the work of Megeath *et al.* (1990), who made infrared and radio measurements on a number of compact HII regions.

Alternatively, if the observed DM changes are the result of AU-scale turbulence in the interstellar medium (ISM), a simple model can be used to estimate the upper and lower limits of the ratio $\frac{f}{s}$, the volume filling factor to the scale-size (pc) of the irregularities. For N clouds along the line of sight to the pulsar, assuming zero electron density between the clouds and a statistical fluctuation of $\sqrt{N}$, the fractional change in DM is given by

$$\frac{\Delta DM}{DM} = \frac{1}{\sqrt{\frac{f}{s}}\sqrt{D}} \tag{4.20}$$

where D is the pulsar distance (pc). For the largest (PSR B1648-42, $\sim 7\%$) and smallest (PSR B1054-62, $\sim 1\%$) fractional DM changes from Table 4.2 with significance $\geq 3\sigma$, the ratio $\frac{f}{s}$ obtained is ~ 0.03 and ~ 0.7 respectively, using the distance estimates given by Taylor *et al.* (1993). Cordes *et al.* (1985) have estimated the filling factor to be 10^{-4} – 10^{-2} and ≥ 0.5 for a scale-heights ≤ 100 pc and ≥ 500 pc respectively. Most of the pulsars in Table 4.2 fall into the first scale-height range. Using a volume filling factor of $\sim 10^{-4}$, the cloud density is $n_c = \frac{\bar{n}_e}{f} \simeq 3 - 300$ cm^{-3}, i.e., the cloud density requirement is relaxed by a factor of $\sqrt{N}$ compared to the analysis based on a single cloud. Further, using a volume filling factor of 10^{-2} gives an upper limit on the irregularity scale-size of ~ 0.5 pc ($\sim 10^{18}$ cm). Recent observations (see Cordes *et al.* 1991) suggest that "outer scales" of this magnitude are not unreasonable, implying an extended electron density turbulence spectrum with scales ranging from $\sim 10^9$ cm to $\sim 10^{18}$ cm. Two of the pulsars in Table 4.2 fall into the second scale-height range, namely PSRs B1054-62 and B1727-47. Using a volume filling factor of 0.5, the cloud density is $n_c \simeq 0.05$ cm^{-3}, and the implied irregularity scale-size is of the order of 0.7 pc.

Using a recent comprehensive model for the interstellar electron density distribution (Taylor & Cordes 1993), all of the pulsars listed in Table 4.2 have DM-derived distances greater than 1 kpc. The DM changes for the two nearest pulsars (PSRs B1556-44 and B1747-46) may be due to the movement of a dense, compact HII region out of each line of sight. For the more distant pulsars, a statistical explanation is more appropriate. The DM variations may be due to the movement of (i) a number of compact HII regions or (ii) density irregularities within larger HII

regions, all beyond 1 kpc, or (iii) a combination of both (i) and (ii). The compact HII regions have sizes of about 10^{16} cm (Gordon 1988), while the large regions have typical sizes of $\sim 10 - 100$ pc (Prentice & ter Haar 1969). Prentice & ter Haar note that the line of sight to PSR B1727-47 passes close to the region of I Scorpius situated at a distance of ~ 1.3 kpc. The DM change for this pulsar may be due to density gradients within this region. An independent distance measurement (e.g., derived from HI line observations) would be useful in determining the DM contribution from this cloud. Independent distance estimates are available for PSRs B1054-62 (14.9 kpc), B1558-50 (6.3 kpc) (Taylor *et al.* 1993), B1556-44 (~ 2 kpc) (Koribalski *et al.* 1995) and B1648-42 (> 4.8 kpc) (Weisberg *et al.* 1995). These estimates are comparable to the DM-derived distances of 13.7, 3.8, 1.6 and 7.2 kpc respectively, using the Taylor & Cordes (1993) model. The line of sight to PSR B1054-62 is in a direction that is tangential to the Sagittarius-Carina spiral arm (Georgelin & Georgelin 1976). Density irregularities within HII regions along the arm could explain the observed DM change for this pulsar. However, Koribalski *et al.* (1995) have recently presented evidence to suggest that the distance to PSR B1054-62 is only ~ 3 kpc. If this is the case, an alternative explanation for the DM change is required. Koribalski *et al.* suggest that PSR B1054-62 is located behind, or in, the reflection nebula BBW 328 (Brand *et al.* 1986), which lies along the line of sight to this pulsar. Such a nebula, with a typical electron density of ~ 100 cm^{-3}, would contribute significantly to the DM, and could also account for the observed change in the DM.

A standard model of galactic rotation (e.g., see Kraus 1986) was used to investigate whether differential galactic rotation might give rise to the DM change for some of the pulsars in Table 4.2, that is, from a high relative transverse velocity of the interstellar medium between the Earth and the pulsar. A relative velocity higher than the assumed 100 km/s for pulsar "proper motion" implies that even larger HII regions or irregularities may be responsible for the DM change. Using the pulsar distances listed in the catalogue compiled by Taylor *et al.* (1993), the departure of the transverse velocity curve from that of "rigid body" rotation was found to be negligible for half of the pulsars in Table 4.2, ~ 20 km/s for PSRs B1558-50 and B1727-47, ~ 50 km/s for PSR B1054-62 and ~ 80 km/s for PSR B1648-42. PSR B1648-42 is one of the more distant sources listed in Table 4.2. The relative velocity of the interstellar medium in the direction of this pulsar suggests that regions with reasonably large scale-sizes may be responsible for the observed DM changes. For a given volume filling factor, this implies that there are less clouds along the line of sight, and so the movement of one such region would result in a larger percentage DM change.

DM variations over shorter intervals (e.g., 1 - 2 years) are much more difficult to detect in the data as measurement uncertainties are generally large enough to mask the slight offsets expected in the dual-frequency phase residuals. Hence,

these variations are more easily observed in the direction of millisecond pulsars, or at decametre wavelengths for longer-period pulsars. Significant variations of this nature have not been detected in the data for the Mt Pleasant pulsar sample.

Phillips & Wolszczan (1991) have detected DM variations over a two-year interval in the direction of six longer-period pulsars. Their results show a roughly linear correlation between the amplitude of the variations and the DM, and a power-law density fluctuation spectrum with spatial scales ranging from 10^9 to 10^{15} cm. Backer *et al.* (1993) also made observations of DM variability, toward a selection of millisecond pulsars. Their results indicate that the assumed relationship between plasma fluctuations (which cause the DM variations) and those causing scattering effects is questionable. The relationship between DM variability and the DM is not as strong as expected from an extrapolation of results from DISS studies. Also, they use a simple model of wedgelike perturbations, randomly distributed out to a few kpc, to explain the dominance of temporal linear gradients in the DMs and their dependence on the DM.

Wu & Chian (1995) recently proposed a new theory of dispersion measure variations in pulsars. In their theory, the pulsar radio waves in the vicinity of the source region within the magnetosphere obey a nonlinear dispersion relation that depends on the pulse amplitude. Hence, the DM variations are caused by changes in the radio luminosity. The magnitude of the variation is proportional to the rotation rate of the pulsar and the magnetic field strength. These theoretical predictions are yet to be verified, e.g., they require simultaneous measurement of the DM and the pulsar flux density. Wu & Chian (1995) do not propose that all DM variability is due to this nonlinear dispersion effect. In fact, they conclude that the observed variations may arise from the combined effects of the pulsar magnetosphere, individual ionised regions and electron density irregularities in the ISM.

4.3.4 Intrinsic Cubic Terms

Plots of the phase residuals resulting from fits for the period, period derivative and position (where possible) for each pulsar are shown in Appendix C. The plots represent approximately seven years of timing observations, from 1987 to 1994.

For thirteen of the pulsars listed in Table 4.1, namely PSRs B0628-28, B0736-40, B0835-41, B0923-58, B0959-54, B1221-63, B1449-64, B1556-44, B1648-42, B1706-16, B1727-47, B1737-30 and B1742-30, the phase residuals show a dominant cubic term. For some other pulsars, other nonstationary, random timing behaviour is evident, in some cases appearing to be dominated by a higher order term. Some of the remaining cases show apparently disjointed wandering in the residuals (e.g., PSR B0740-28) while others show only small random variations.

A third order polynomial was fitted to the arrival-time data on the 13 pulsars

showing an intrinsic cubic term in the residuals. The results are presented in Table 4.3. Only about half of these pulsars have a negative sign for the apparent $\ddot{P}$, as would be expected from the "braking" of a simple torque process. Furthermore, the observed cubic behaviour is unlikely to be the result of such a process since the calculated braking indices, given by $n = \nu\ddot{\nu}/\dot{\nu}$, are inconsistent with the values predicted from theoretical considerations. The theoretical values range from 1 to 5 (Manchester & Taylor 1977). To date, reliable period second derivatives have been measured for only six pulsars, and only three of these pulsars have been found to possess braking indices in the range 1 to 5 — the Crab pulsar (PSR B0531+21) (Groth 1975b, Lyne *et al.* 1988), PSR B1509-58 (Manchester *et al.* 1985) and PSR B0540-69 (Manchester & Peterson 1989). One interpretation is that the large cubic terms for the pulsars listed in Table 4.3 (and higher order terms for other pulsars) result from low frequency terms in the timing noise power spectrum.

The only exception in Table 4.3 is PSR B1727-47. The apparent braking index for this pulsar is $n = 2.6 \pm 2$, if the timing parameters derived from the whole data set are used. If this is a *true* braking index, then the value of n should be independent of the data span used to estimate the timing parameters. Low-level timing activity and course sampling make it difficult to obtain reliable estimates from short data spans. However, the braking indices obtained from the first and second halves of the data set were $n = 8 \pm 2$ and $n = 1.7 \pm 0.9$ respectively (1σ errors). These results cast some doubt over the reality of a measured braking index for this pulsar, although they agree at the 3σ level.

Cordes & Helfand (1980) have proposed that random walk processes are responsible for the apparent third (and higher) order terms, pointing out that the period second derivative can have either sign. They presented a diagnostic quantity to see if the third order term is the result of pulsar braking. This test uses the ratio, r_{32}, of the rms phase residuals after fitting third order and second order polynomials. If pulsar braking is responsible for the third order term, then

$$0 \leq r_{32} \leq \frac{120\sqrt{7}\sigma_M}{\ddot{\nu}T^3\sqrt{N-4}} \tag{4.21}$$

where σ_M is the measurement uncertainty, N is the number of data points (and $N \gg 4$), and T is the time span of the fit. For the observations made in this study, pulsar braking may be responsible if $r_{32} \leq 0.043$. If the third order term is due to a random walk, they find $0.04 \leq r_{32} \leq 1.0$. The measured values of r_{32} are shown in Table 4.3. They all fall into the latter category except the value for PSR B1737-30 which has $r_{32} \simeq 0.04$. However, the upper limit from Equation 4.21 for this pulsar is 0.0007, and so this value of r_{32} also falls into the latter category. These results support the idea that the observed behaviour is not due to a secular change in the period derivative. In particular, the test indicates that the measured braking index for PSR B1727-47 ($n \simeq 3$) is not real.

Table 4.3: Results of a third order polynomial fit, giving the period second derivative. The columns contain respectively the pulsar name, the period (P), period derivative ($\dot{P}$), period second derivative ($\ddot{P}$) and their 2σ uncertainties, the epoch to which the period is referred, the rms residual remaining after the third order fit (corrected for measurement uncertainty in the manner described in the section on timing noise), the absolute value of the braking index and r_{32}, the ratio of the rms from third and second order fits respectively).

Pulsar	P	Err	$\dot{P}$	Err	$\ddot{P}$	Err	Epoch	rms3	Braking	r_{32}
	(s)		($10^{-15} ss^{-1}$)		($10^{-25} s^{-1}$)		(TJD)	(mP)	index	
0628-28	1.24441969703	2	7.1182	2	1.1	1	8393.7436	1.00	2700	0.42
0736-40	0.374919521824	4	1.60958	5	1.26	3	8393.7699	3.88	18000	0.12
0835-41	0.751622605893	3	3.54364	5	-0.32	3	8393.8274	0.76	1900	0.39
0923-58	0.73950160681	2	4.8564	3	-4.0	2	8394.7667	3.62	12000	0.15
0959-54	1.4365897039	3	51.446	4	31	2	8393.8687	22.14	1600	0.39
1221-63	0.2164768855532	7	4.95396	1	-0.052	6	8394.9221	1.67	48	0.42
1449-64	0.1794851323358	5	2.746148	6	-0.066	3	8395.0492	1.81	150	0.25
1556-44	0.2570562379995	7	1.01949	1	0.035	5	8394.0388	1.23	860	0.57
1648-42	0.84408138293	5	4.789	1	5.0	5	8533.7633	3.89	18000	0.28
1706-16	0.65305481093	4	6.3010	8	-4.3	4	8535.7368	9.32	7000	0.40
1727-47	0.82979074663	1	163.5941	2	-0.19	2	8240.8172	1.39	3	0.47
1737-30	0.60665378499	2	465.6822	6	-84.8	8	8934.7841	4.64	26	0.04
1742-30	0.367427503545	2	10.66539	3	0.43	2	8533.9196	1.18	140	0.17

4.3.5 Period Discontinuities

Before presenting the results in this section, it is helpful to define the terms that will be used. The abrupt, discontinuous increases observed in the rotation frequency of a few pulsars, for example, the Vela pulsar (McCulloch *et al.* 1987, McCulloch *et al.* 1990), PSR B1641-45 (Manchester *et al.* 1983) and PSR B0355+54 (Lyne 1987), are generally termed "glitches". Glitches are characterised by a simultaneous increase in the magnitude of the frequency derivative. Cordes *et al.* (1988) have extended this terminology, using the term "macrojump" to describe these large fractional changes in the rotation frequency of the Vela pulsar, and "microjumps" to describe much smaller but discrete or resolvable events in ν and $\dot{\nu}$. The latter are distinct from the small, individually indetectable "microglitches" thought to produce some of the irregularities that we observe as timing noise. Alpar & Baykal (1994) have classified the large glitches (macrojumps) using the criterion that $\Delta\nu/\nu > 10^{-7}$. With this classification in mind, the terms "period jump" or simply "jump" will be used to describe the frequency or period discontinuities evident from the arrival-time analysis.

Jumps have been observed in the rotation rates of five pulsars — five times for PSRs B0740-28 and B1240-64, once for PSRs B1641-45 and B1727-47 since 1987, and five times for PSR B1737-30 since December 1990. The jump parameters for each pulsar were obtained by fitting the arrival times with the model given by Equation 4.10 and are summarised in Table 4.4. The parameters are the change in frequency ($\Delta\nu$), the fractional change in frequency ($\Delta\nu/\nu$), the change in frequency derivative ($\Delta\dot{\nu}$, ignoring any short-term features in the post-jump relaxation), the fractional change in frequency derivative, and the epoch of the jump. The uncertainties quoted are 1σ and refer to the last digit quoted.

Two general comments can be made about the results shown in Table 4.4. Firstly, most of the jumps are 2 - 3 orders of magnitude smaller than the large period jumps of the Vela pulsar, where $\Delta\nu/\nu \simeq 10^{-6}$ (McCulloch *et al.* 1987, 1990, Cordes *et al.* 1988), but are comparable to those observed from the Crab pulsar (Boynton *et al.* 1972, Helfand 1977, Lyne & Pritchard 1987). Secondly, while macrojumps have a well-defined signature, $(\Delta\nu, \Delta\dot{\nu}) = (+,-)$, the jumps shown in Table 4.4 display a range of signatures, one being (+,+). Similar results have been obtained for other pulsars (Gullahorn & Rankin 1982, Cordes & Downs 1985, Cordes *et al.* 1988). This aspect will be discussed further in Chapter 6. At this point, some comments about the jumps in the rotation rate of specific pulsars are appropriate.

PSR B0740-28

This pulsar appears to undergo a jump in ν and $\dot{\nu}$ every few hundred days. Figure 4.2 shows two of the observed jumps. The only other long-term timing observa-

Table 4.4: Jump parameters for five pulsars.

Jump	$\Delta\nu$ (10^{-9} Hz)	$\Delta\nu/\nu$ (10^{-9})	$\Delta\dot{\nu}$ (10^{-16} Hz/s)	$\Delta\dot{\nu}/\dot{\nu}$ (10^{-4})	Epoch (TJD)
1	16.8 ± 4	2.80 ± 7	2.0 ± 1	-3.3 ± 2	7655 ± 4
2	2.6 ± 3	0.43 ± 5	2.4 ± 3	-4.0 ± 5	8350 ± 28
3	1.5 ± 8	0.3 ± 1	3 ± 1	-5 ± 2	8670 ± 30
4	-15.4 ± 5	-2.57 ± 8	-0.7 ± 2	1.2 ± 3	8884 ± 3
5	-2.3 ± 6	-0.4 ± 1	-6.5 ± 4	1.07 ± 7	9320 ± 20

(a) PSR B0740-28.

1	0.40 ± 2	0.155 ± 8			7450 ± 40
2	-0.71 ± 4	-0.28 ± 2			7953 ± 10
3	0.45 ± 3	0.17 ± 1	-0.03 ± 1	1.0 ± 3	8468 ± 9
4	-0.55 ± 3	-0.21 ± 1	-0.08 ± 1	2.7 ± 3	9025 ± 7
5	0.61 ± 6	0.24 ± 2			9620 ± 30

(b) PSR B1240-64.

1	3.5 ± 9	1.6 ± 4	-1.3 ± 6	13 ± 6	7590 ± 40

(c) PSR B1641-45.

1	165.58 ± 7	137.40 ± 6	-3.05 ± 5	12.8 ± 2	9387.68 ± 3

(d) PSR B1727-47.

1	25.9 ± 4	15.7 ± 3	3.7 ± 3	-2.9 ± 2	8423.0 ± 8
2	15.2 ± 5	9.2 ± 3	-3.7 ± 6	2.9 ± 5	9046 ± 1
3	278 ± 1	168.6 ± 6	-12.1 ± 7	9.6 ± 6	9239.4 ± 1
4	15 ± 3	9 ± 2	3 ± 7	-2 ± 5	9456 ± 3
5	12.8 ± 8	7.8 ± 5	-5 ± 1	4.0 ± 9	9551 ± 2

(e) PSR B1737-30.

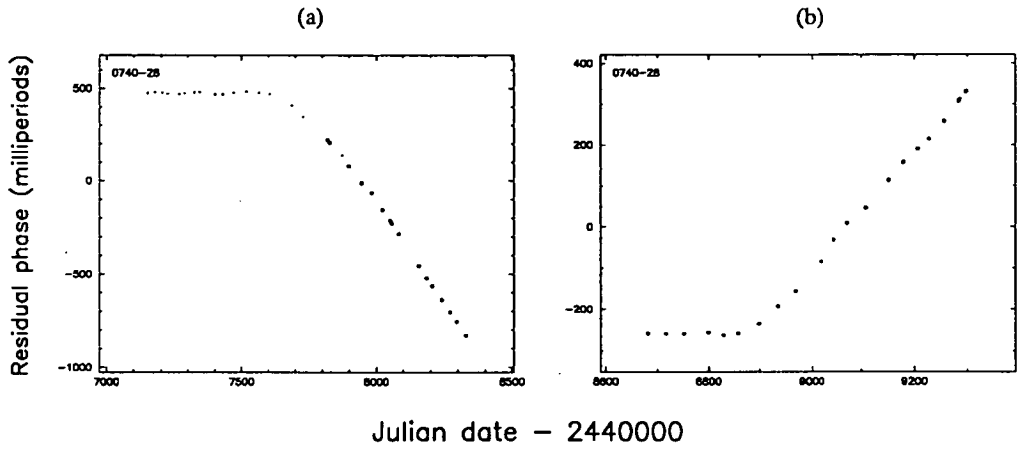

Figure 4.2: Two of the jumps in the rotation rate of PSR B0740-28. (a) Jump 1. (b) Jump 4. The residuals are defined in the sense of observed minus predicted arrival time.

tions published on this pulsar are those of Manchester *et al.* (1983). They found the phase residuals were dominated by a large intrinsic cubic term. However, they noted that the residual curve appeared to consist of a series of straight-line segments of length tens to hundreds of days, corresponding to fractional frequency jumps of order 10^{-9}. The jumps listed in Table 4.4 for this pulsar are similar in magnitude to this estimate, and if allowance is not made for them in the timing fits, a similar cubic term appears in the residuals. The epoch sampling of the Mt Pleasant timing data is not sufficient to identify jumps over intervals of only tens of days, although inspection of the postfit residuals (see Appendix C) reveals many apparently disjointed straight-line segments over short time intervals. These could arise from even smaller jumps in the rotation rate of this pulsar.

PSR B1240-64

The behaviour of this pulsar is most unusual because the sign of the period jump alternates with each successive jump. The jumps have taken place every 500–600 days. At the time of writing, a fifth such jump of opposite sign had only recently taken place. Figure 4.3 shows the timing residuals for this pulsar if the jumps are not taken into account in the arrival-time analysis. The alternating nature of the jumps is immediately obvious. For three of the jumps, the change in $\dot{\nu}$ was insignificant in the sense that the estimated values were less than the formal errors.

The observed behaviour of this pulsar is difficult to explain using conventional superfluid vortex models (Alpar *et al.* 1984a,b). These models do not account for a sudden decrease in the rotation frequency, as evidenced by jumps 2 and 4, listed in Table 4.4. Such behaviour involves a sudden increase in the moment of

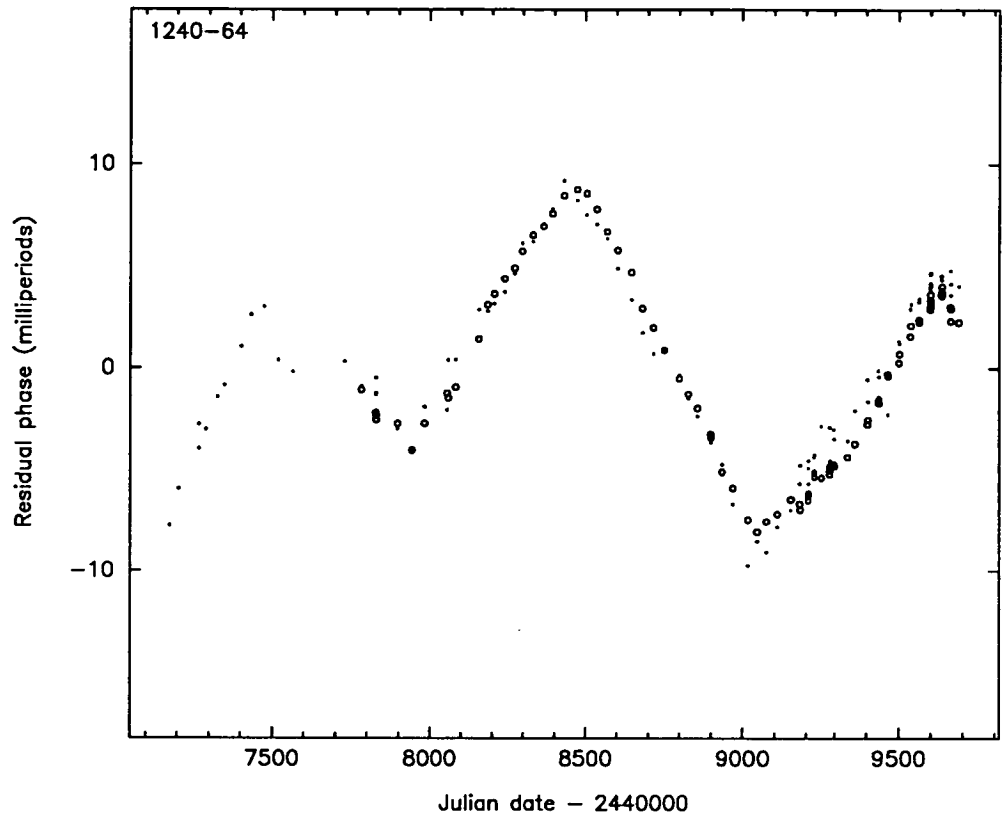

Figure 4.3: The timing residuals from PSR B1240-64, if the jumps are not taken into account in the timing analysis. The residuals are defined in the sense of observed minus predicted arrival time. Key: • = 650 MHz data, ∘ = 800 MHz data.

inertia. One possible scenario is a sudden repinning of vortices or inward movement of vortices, but this possibility has not been discussed in the literature. The model of Jones (1990d), described in Chapter 2, is another possible explanation. Apparently, transitions between pinned and corotating vortex states can produce non-axisymmetric pinned vortex density distributions and give rise to jumps in ν of either sign. As discussed in Chapter 2, starquakes can also produce frequency jumps with both positive and negative magnitudes (Ruderman 1969, Pines & Shaham 1972).

Even if there is a feasible explanation for the sudden decreases in rotation frequency, the alternating nature of the jumps is unexpected. This behaviour has not been observed in any other pulsars monitored over similar, or longer, time intervals. Assuming that jumps occur randomly with positive and negative amplitudes that are equally likely, the probability that five jumps of alternating sign have occurred by chance is $\sim 3\%$. Statistical tests on microjumps observed by Cordes & Downs (1985) and in the present work (see Chapter 6) show that the probability of observing a sudden decrease in ν is closer to 0.3 rather than equally

probable with sudden increases in ν. This observation is based on a sample of 26 pulsars and more than 50 real jumps in ν. Using this information, the probability of the observed behaviour arising by chance is also $\sim 3\%$.

Hence, the observed behaviour requires an explanation in terms of some mechanism, either internal or external to the neutron star. One possibility is that these small jumps are triggered by oscillations in the neutron superfluid interior which couple to the crust, e.g., the oscillations may cause the state transitions proposed by Jones (1990d). The sign of the jump would depend on the direction of flow of angular momentum. Ruderman (1970a) and Lamb *et al.* (1978a) have suggested that angular momentum can flow periodically from the crust to the interior and back again as a result of oscillations of the vortex lattice in the superfluid. It is believed that a glitch could excite such *Tkachenko oscillations*, with the fundamental mode resulting in an oscillation period given by

$$T_o = 140R/\sqrt{\Omega} \tag{4.22}$$

where R is the neutron star radius, in cm, and Ω is its angular frequency, in rad s^{-1} (Ruderman 1970a). Assuming that these oscillations can trigger small jumps of alternate sign, the period would have to be more than 30 months, since the time interval between the jumps is $16-17$ months. Assuming a stellar radius of 10 km, the Tkachenko oscillation period for PSR B1240-64 would be ~ 13 months. Hence, the fundamental oscillation mode may not be responsible for the observed timescale of the jumps. However, the theoretical work leading to Equation 4.22 does not allow for the effects of vortex pinning and coupling between the superfluid and the magnetic field, and so the discrepancy may not be significant.

Tkachenko oscillations of sufficient magnitude would appear as a periodic "wobble" in the timing residuals, such as the quasi-periodic deviations seen in the pulse arrival times from the Crab pulsar (Lyne *et al.* 1988). There is no such wobble in the residuals of PSR B1240-64 (after removal of the frequency jumps). However, the suggestion provided here is that an internal oscillation is triggering some other mechanism to produce sudden changes in the crust rotation rate which alternate in sign, according to the direction of the flow of angular momentum, with inter-jump time intervals of ~ 500 days.

Precession of the neutron star is another possibility, provided there is a mechanism to link the jumps to the precession. Further, Ruderman (1970b) has predicted that starquakes will change the precession frequency. This effect is difficult to ascertain from the present span of data. However, if precession was taking place, one would expect to find accompanying pulse shape changes. A pulse shape analysis was performed on the profiles of this pulsar (as well as a number of other pulsars – see Chapter 6) and no correlation between pulse shape changes and the timing residuals was found.

In the next section, the reality of the jumps is tested with respect to a random walk process. However, even if the jumps are "real" according to such a test,

another mechanism may mimic the regular change seen in the slope of the residuals. One possibility is that PSR B1240-64 has a companion which is in a highly eccentric orbit. In order to test this possibility, an attempt was made to model the arrival times with an additional five parameters which relate to binary orbits. These are the Keplerian orbital parameters, namely the projected semimajor axis, orbital period, longitude of periastron, epoch of periastron and the eccentricity (Taylor *et al.* 1976, Taylor & Weisberg 1989, Taylor 1989). While reasonable values were obtained for the first four of these parameters, the fits were unsuccessful for eccentricities greater than 0.1. Furthermore, the best-fit parameters resulted in postfit residuals that still showed considerable timing activity (rms of 601 μs, against the original rms of 1700 μs and measurement noise with a rms of about 200 μs). In general, the excess rms noise in long-period pulsars could be attributed to low-level timing activity, but in this pulsar, little timing noise remains after the fits for jumps in the rotation rate. Hence, the binary timing model does not appear to account for the observations. Furthermore, two difficulties were encountered during the course of fitting a binary timing model to the data that are inconsistent with the effects expected from a binary system. Firstly, the oscillations seen in the residuals are not strictly periodic (the period can be anything between 1000 and 1150 days). Second, the amplitude of the oscillations changes substantially from one cycle to the next.

The major limitation in this investigation, for which time is the only solution, is that there are not enough cycles in the 7-year data span to be able to confirm or eliminate any of the possibilities. Hence, further monitoring of this pulsar is needed in order to help clarify the nature of the underlying cause of this unusual behaviour.

PSR B1641-45

Flanagan (1993) recently reported two period jumps from this pulsar – a large jump in 1986 (of the same order of magnitude as the 1977 jump, $\Delta\nu/\nu \simeq 10^{-7}$, reported by Manchester *et al.* 1978), and a much smaller jump in 1989. The latter jump has been identified in the Mt Pleasant data. The jump parameters for this pulsar, shown in Table 4.4, agree with the estimates given by Flanagan within the quoted uncertainties.

After allowing for this jump, which occurred at TJD 7590 $\pm$ 40, the residuals indicate that another jump has taken place at $\sim$ TJD 7850 (see Appendix C). The $\dot{\nu}$ data presented by Flanagan (1993) clearly show a change in slope at this approximate epoch, suggesting the possibility of a jump in $\ddot{\nu}$. A fit for the jump parameters using the Mt Pleasant data gives: $\Delta\nu = +(2.68 \pm 3) \times 10^{-9}$ Hz, $\Delta\dot{\nu} = -(1.47 \pm 1) \times 10^{-16}$ Hz s^{-1}, $\Delta\ddot{\nu} = +(1.84 \pm 1) \times 10^{-24}$ Hz s^{-2}, at TJD 7854$\pm$5. A similar analysis of the data obtained by Flanagan is needed to check this interpretation. It is possible that the $\Delta\ddot{\nu}$ is due to unresolved timing activity,

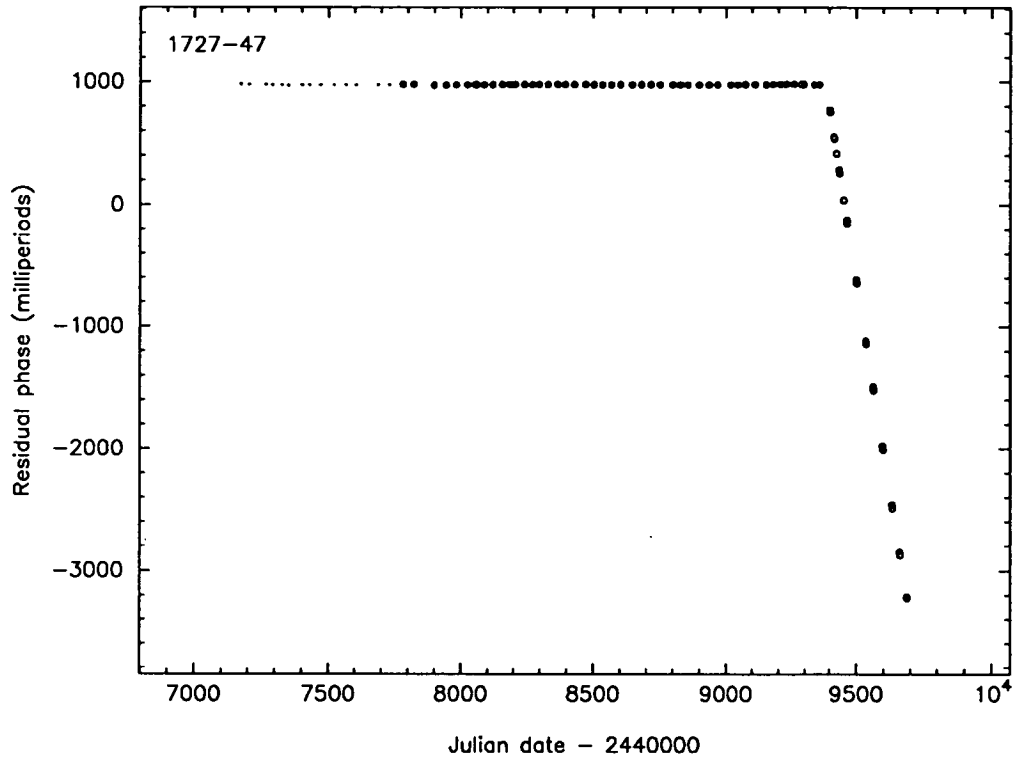

Figure 4.4: The timing residuals from PSR B1727-47, showing the glitch at TJD 9388. The residuals are defined in the sense of observed minus predicted arrival time. Key: • = 650 MHz data, o = 800 MHz data.

as Flanagan (1993) has already noted. Another possibility is that the $\ddot{\nu}$ term is due to some form of post-jump recovery.

PSR B1727-47

The Mt Pleasant timing observations have revealed the first large jump in the rotation rate of this pulsar since its discovery in 1968. The jump occurred at $\sim$ TJD 9388 (4 February, 1994) and is displayed in Figure 4.4. The magnitude of the fractional jump in frequency qualifies it as a large glitch, according to the classification scheme employed by Alpar & Baykal (1994), and adds to the existing database of 28 glitches.

Accompanying the frequency jump, there was also a small increase in the magnitude of $\dot{\nu}$ ($\Delta\dot{\nu}/\dot{\nu} \simeq 1.3 \times 10^{-3}$). However, the 10 months of observations after the glitch have failed to reveal a recovery in $\dot{\nu}$ which is characteristic of the postglitch relaxation observed in a number of other glitching pulsars. This implies that the time-scale of any relaxation must have been of the order of days (smaller than the time interval between observing sessions) or alternatively, of the order of years and hence is not yet measurable, i.e., below the level of the timing

uncertainties, such as measurement errors and low-level timing noise.

According to the vortex creep theory, the relaxation times are expected to get longer as a pulsar ages, along with a shift toward a non-linear coupling mechanism (Alpar *et al.* 1989). The characteristic age of this pulsar is $\sim$80,000 years, making it the second youngest pulsar after PSR B1737-30 in the Mt Pleasant pulsar sample. While PSR B1727-47 is not an "old" pulsar, it cannot be classified as one of the "adolescent" pulsars such as PSR B1737-30 (Lyne 1992) which undergo frequent glitches. These pulsars fall into an age group of $(1-2)\times 10^4$ years. The relaxation time after a glitch is predicted to be $\tau \propto T/|\dot{\Omega}|$, where T is the internal temperature of the neutron star (Alpar *et al.* 1984a). Assuming a non-linear coupling mechanism, a lower limit on the recoupling time after a glitch can be obtained by using

$$t_r = \frac{\Delta\Omega}{|\dot{\Omega}|} = \frac{\Delta\nu}{|\dot{\nu}|} \tag{4.23}$$

(Alpar *et al.* 1984a, Flanagan 1993). For PSR B1727-47, $t_r \simeq 8$ days. Therefore, it is possible that the relaxation had already taken place by the time of the first postglitch observations.

The vortex creep theory also predicts that glitches occur in all pulsars with a time between glitches $t_g \propto |\dot{\Omega}|^{-1}$ (Alpar *et al.* 1984a). Specifically,

$$t_g = \frac{\delta\Omega}{|\dot{\Omega}|} \tag{4.24}$$

where $\delta\Omega$ is the mean decrease in the crustal superfluid rotation rate and is a critical parameter for glitches arising from vortex unpinning. Alpar & Baykal (1994) have found an average value of $\delta\Omega/\Omega = 1.74\times 10^{-4}$ for the available glitch sample. In the case of PSR B1727-47, this means that we may not see another glitch for $\sim$28 years.

As a final point, it is worth noting that the dual frequency phase residuals after the glitch in this pulsar show an offset of 1–2 milliperiods which is marginally significant. At present, the data are insufficient to allow further investigation into the origin of this offset. If it is dispersion-related, it presently corresponds to a DM change of $+0.31 \pm 0.04$ cm^{-3}pc. Figure 4.5 shows the offset in the residuals for a subset of the arrival-time data recorded from this pulsar.

Monitoring of this pulsar is continuing in an attempt to further investigate the timing offset and also to see if there is any long-term relaxation from the glitch.

PSR B1737-30

This pulsar undergoes period jumps at a greater rate than any other known pulsar (McKenna & Lyne 1990). The Mt Pleasant timing observations have revealed five jumps over a four-year interval. Four of the jumps are shown in Figure 4.6. The timing data up to the first jump was well-modelled by a third order polynomial,

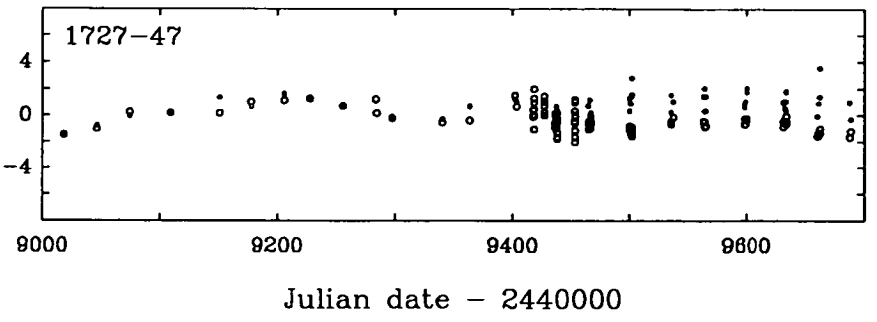

Figure 4.5: The phase residuals (in units of milliperiods) for a subset of the data obtained from PSR B1727-47. The residuals show an arrival-time difference or offset between the 650 and 800 MHz arrival times after the glitch at TJD 9388. The residuals are defined in the sense of observed minus predicted arrival time. Key: • = 650 MHz data, o = 800 MHz data.

using Equation 4.9. The value of $\ddot{\nu}$ and the implied braking index is shown in Table 4.3. Clearly, this term is not due to the star's spin-down but it could be due to relaxation from the previous jump, which took place in October 1990 (Lyne 1992).

Jump 3, which occurred at TJD 9239, can be classified as a large glitch, since $\Delta\nu/\nu \simeq 1.7 \times 10^{-7}$. This glitch was accompanied by an increase in the magnitude of $\dot{\nu}$. A second order polynomial fit to the postglitch data revealed a large cubic term, which could be interpreted as the third-order term in the power series expansion of an exponential function arising from the relaxation of the jump. However, at least part of the large cubic term was due to jumps 4 & 5 (see Table 4.4). Further, an attempt to fit the glitch function given by Equation 4.10 for a single exponential failed because the apparent change in $\dot{\nu}$ was not in the sense of an exponential *decrease* in its magnitude. A simple fit for $\Delta\nu$ and $\Delta\dot{\nu}$ for jumps 3, 4 and 5 adequately modelled the arrival times over this time interval. No long-term relaxation was observed for any of the other four jumps. The $\sim$30-day interval between observing sessions and the large jump rate of this pulsar make it difficult to measure and interpret any postglitch relaxation.

Michel *et al.* (1990) have shown that, for earlier jumps in the rotation rate of this pulsar, the post-jump response is well-fitted by a simple linear model. The implied time constant for the recovery after a jump was found to be $\sim$13 years. The nature of the jumps revealed by the Mt Pleasant data is in agreement with these findings.

Significance test for the jumps

The significance of the jumps listed in Table 4.4 can be tested to determine whether they are merely fluctuations resulting from a random walk process. More detailed tests of this nature are presented in Chapter 6, but a preliminary analysis is useful.

According to Cordes & Helfand (1980), a random walk in frequency can readily

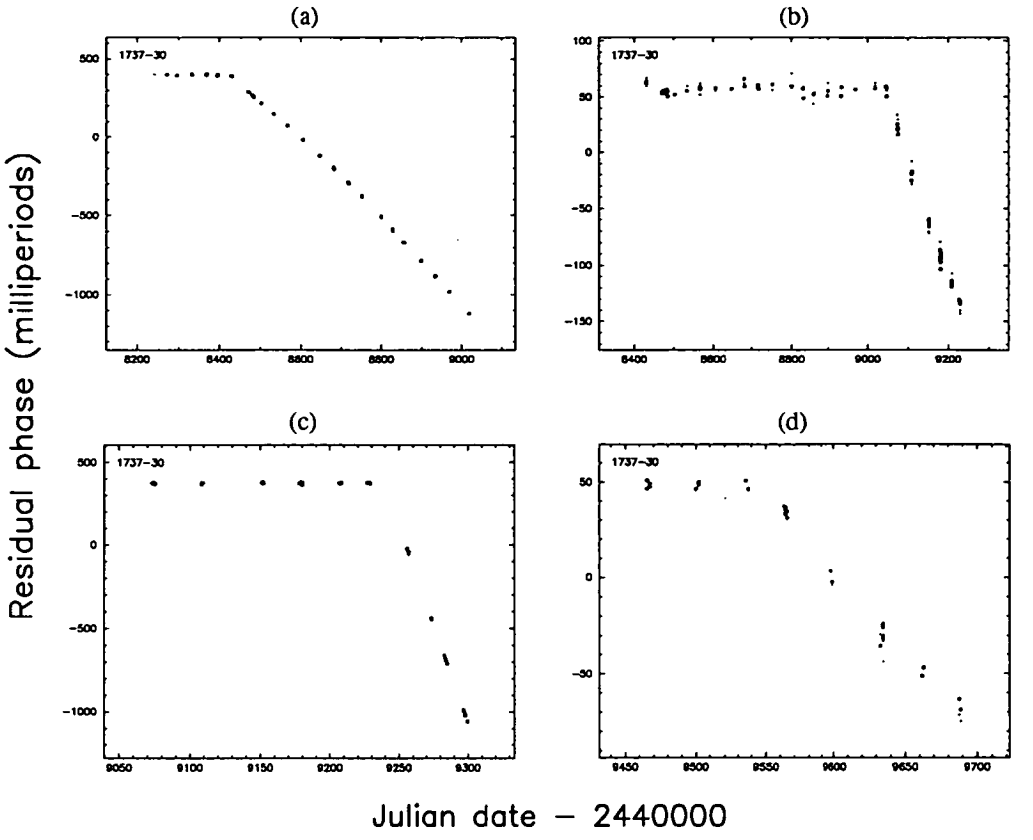

Figure 4.6: Four of the jumps in the rotation rate of PSR B1737-30. (a) Jump 1. (b) Jump 2. (c) Jump 3. The whole data span up to jump 4 is not shown because the phase residuals suffer "period wrapping" as a result of the large magnitude of jump 3. (d) Jump 5. The residuals are defined in the sense of observed minus predicted arrival time.

produce changes in the slope of the phase residuals over a period of time. They propose using a "strength" estimate,

$$S_{FN,\Delta\nu} = \frac{(\Delta\nu/3)^2}{\Delta t} \tag{4.25}$$

and comparing it with that obtained from the residuals to an m^{th} order fit ($m = 2$ in this case),

$$S_{FN,R} = \frac{24 C_m^2 \sigma_R^2(T)}{T^3 P^2} \tag{4.26}$$

where $\Delta\nu$ is the size of frequency step, Δt is the rise time of the discontinuity, taken to be the interval between observations made immediately before and after the event, C_m is the correction factor for the fit ($C_m = 15.5$, Cordes 1980), $\sigma_R(T)$ is the rms residual phase, in seconds, after allowing for the measurement uncertainty (described in Section 4.3.6), T is the length of the data span up to the time of the event, and P is the period of the pulsar (in seconds). The slope change can be considered too large to have been caused by random fluctuations if the ratio

$$r = \frac{S_{FN,\Delta\nu}}{S_{FN,R}} \tag{4.27}$$

is > 1, that is, at a significance level of 3σ or more. Table 4.5 shows the results of this significance test for each of the frequency jumps listed in Table 4.4.

In general, most of the frequency jumps appear to be significant with respect to the 3σ test. The few exceptions can be attributed to the limitations of the test. For example, all the frequency jumps in PSR B1240-64 are of the order of 5×10^{-10} Hz. According to the test proposed by Cordes & Helfand, all the jumps are significant except for jump 1. This is simply due to the fact that T is small and the timing activity in all inter-jump regions is very small (hence, $\sigma_R(T)$ is similar for the data spans leading up to all the jumps).

However, the main factor that limits the sensitivity of this test is the size of Δt. In the present study, the ~ 30-day interval between observing sessions may well be several orders of magnitude larger than the rise time of the jump. Hence, the "epoch sampling" of the timing data is of crucial importance in being able to determine whether the frequency jumps seen in the data are indeed fluctuations resulting from a random walk process, e.g., arising from an ensemble of unresolvable microglitches, or whether they are significant events which produce the bulk of the observed timing activity. For example, if no allowance is made for the small jump in the period and period derivative of PSR B1641-45 when fitting the timing data, the phase residuals show a large fourth-order term (Figure 4.7). If the sampling is such that these discrete events are unresolvable, the effect may be mistaken as "timing noise". A further limitation is that the test does not consider jumps in $\dot{\nu}$. These aspects are considered in Chapter 6.

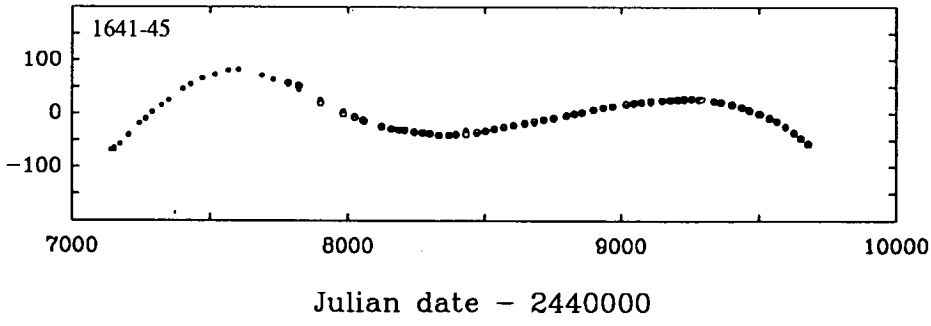

Figure 4.7: The phase residuals (in units of milliperiods) from PSR B1641-45, if no allowance is made for the small jump in period and period derivative when fitting the timing data. Key: • = 650 MHz data, o = 800 MHz data.

4.3.6 Timing Noise

After removal of the period evolution parameters and any period jumps, the timing residuals of many pulsars display the "restless" behaviour known as timing noise. Plots of phase residuals from second order polynomial fits to the Mt Pleasant pulse arrival-time data are shown in Appendix C. For the five pulsars discussed

Table 4.5: Significance tests on frequency jumps from five pulsars.

Jump	Δt (days)	T (days)	$\sigma_R(T)$ (ms)	r
1	83	520	1.22	1.2
2	28	1215	1.12	1.4
3	36	1535	1.10	0.8
4	41	1750	1.06	110
5	42	2185	1.01	5.2

(a) PSR B0740-28.

1	41	300	0.25	0.04
2	40	803	0.22	3.1
3	42	1318	0.20	6.3
4	28	1875	0.23	30.3
5	32	2470	0.22	76.7

(b) PSR B1240-64.

1	37	483	0.85	1.5

(c) PSR B1641-45.

1	39	2235	1.27	480,000

(d) PSR B1727-47.

1	33	182	2.38	1.2
2	29	805	2.56	33.6
3	27	998	2.61	22,000
4	27	1215	2.55	122
5	24	1310	2.53	127

(e) PSR B1737-30.

in Section 4.3.5, the phase residual plots do not show the effects of the period jumps because allowance was made for them in the timing analysis. Timing noise is evident in the rotation of the majority of these pulsars. A preliminary analysis of this timing activity is presented in this section.

Two parameters have been used to quantify the level of timing activity in a pulsar. The "activity parameter" has been used for a number of years and was defined by Cordes & Helfand (1980) as

$$A = \log\left[\frac{\sigma_{TN}(2,T)}{\sigma_{TN}(2,T)_{\rm Crab}}\right] \tag{4.28}$$

where $\sigma_{TN}(2,T)$ is the rms residual phase (in ms) due to timing noise after a second order fit over a data span T, and $\sigma_{TN}(2,T)_{\rm Crab} = 12(T/1628\ {\rm days})^{3/2}$ ms. Hence, the timing activity of a pulsar is specified relative to the activity in the Crab pulsar (using a scaling with time based on "frequency noise"). Arzoumanian *et al.* (1994) have presented a "stability parameter", defined as

$$\Delta(t) = \log\left(\frac{1}{6\nu}|\ddot{\nu}|t^3\right) \tag{4.29}$$

where t is an arbitrary time interval and ν, $\ddot{\nu}$ are the frequency terms obtained from a third order polynomial fit (Equation 4.9) over the time interval t. Hence, this parameter has the advantage that it is defined in an absolute sense, as well as being a measure of the *pulsar clock* error over the reference time interval. Both the activity and stability parameters provide a "broad-brush" assessment of the timing activity for a given sample of pulsars. More detailed analyses of timing noise will be presented in Chapter 6.

Table 4.6 is a summary of some of the relevant timing noise parameters. The columns contain, respectively: the pulsar name, frequency of observation, number of data points (N), time span of the observations (T), estimates of the measurement noise (σ_M), pulse jitter (σ_J) and white noise (σ_W) in units of milliperiods, rms residual phase after a second order fit over the data span T (σ_{TN}), activity parameter (A), stability parameter (Δ_8) and the logarithm of the characteristic age of the pulsar (τ, where $\tau = P/2\dot{P}$, in units of years).

The rms uncertainty in the arrival-time measurements was estimated using Equation 4.1. Fluctuations in the pulsar magnetosphere produce pulse-to-pulse variations, or pulse jitter (Cordes & Downs 1985). Upper limits for the phase error due to pulse jitter were estimated using

$$\sigma_J \simeq \sqrt{\frac{w_s w_p P}{t_{\rm int}}} \tag{4.30}$$

(Hankins & Rickett 1975), where w_p and w_s are the profile and subpulse widths respectively, P is the pulse period and $t_{\rm int}$ is the integration time. A conservative estimate of the profile width was used (for each observing frequency, as the widths

Table 4.6: Timing noise parameters.

Pulsar PSR B	Freq (MHz)	N	T (days)	σ_M (mP)	σ_J (mP)	σ_W (mP)	σ_{TN} (mP)	A	Δ_8	$\log\tau$
0403-76	650	166	2396	1.10	0.36	3.81	1.80	-1.34	-1.74	6.75
	800	171	1880	0.92	0.36	2.33	1.75	-1.35		
0538-75	650	81	2508	0.86	0.98	2.46	2.22	-0.92	<-1.60	7.54
	800	75	1791	0.62	0.98	1.02	1.05	-1.24		
0628-28	650	75	2511	0.71	0.98	1.41	2.57	-0.86	-1.36	6.44
	800	68	1907	0.50	0.98	1.01	1.99	-0.97		
0736-40	650	89	2548	0.91	0.79	1.17	33.81	-0.27	-1.12	6.57
	800	71	1907	0.42	0.73	0.53	30.16	-0.32		
0740-28	650	110	2538	0.37	0.45	1.04	6.74	-1.32	-1.63	5.20
	800	91	1868	0.26	0.42	0.72	6.83	-1.31		
0740-28*	650	110	2538	0.37	0.45	1.04	25.25	-0.74		
	800	91	1868	0.26	0.42	0.72	24.73	-0.75		
0808-47	650	66	2512	1.55	0.47	3.49	1.54	-1.44	<-1.70	6.45
	800	60	1639	1.35	0.44	2.54	0.87	-1.69		
0835-41	650	83	2485	0.20	0.76	0.40	2.01	-1.18	<-2.30	6.53
	800	68	1907	0.15	0.76	0.32	1.94	-1.19		
0839-53	650	66	2457	1.33	0.41	4.75	2.32	-1.12	<-1.62	6.84
	800	74	1839	1.29	0.41	3.14	3.03	-1.01		
0905-51	650	76	2511	1.51	0.34	4.30	4.85	-1.27	<-1.99	6.34
	800	71	1878	1.27	0.34	3.13	1.52	-1.77		
0923-58	650	64	2287	1.93	0.63	3.64	26.03	-0.02	-1.35	6.38
	800	74	1635	1.69	0.51	2.98	22.26	-0.08		
0932-52	650	70	2286	1.05	0.53	2.39	1.87	-0.87	<-1.62	6.69
	800	61	1763	0.86	0.53	1.11	0.38	-1.56		
0940-55	650	83	2537	0.92	0.60	1.50	94.71	0.43	-0.66	5.67
	800	66	1867	0.70	0.60	1.95	95.34	0.43		
0959-54	650	86	2536	0.37	0.67	0.75	56.04	0.54	-0.11	5.65
	800	68	1868	0.25	0.67	0.43	56.54	0.54		
1054-62	650	73	2537	1.49	0.65	1.92	4.45	-1.09	<-1.17	6.27
	800	60	1906	0.94	0.60	1.12	5.08	-1.04		
1056-57	650	66	2292	1.09	0.57	1.90	1.14	-1.17	<-1.70	6.64
	800	55	1580	0.84	0.48	1.25	0.61	-1.44		
1154-62	650	76	2537	1.61	0.58	1.78	2.90	-1.30	<-1.97	6.21
	800	65	1906	1.20	0.50	1.51	2.18	-1.43		
1221-63	650	69	2549	1.13	0.28	2.09	4.07	-1.43	<-2.30	5.84
	800	68	1906	0.87	0.26	1.63	3.65	-1.47		
1240-64	650	95	2513	0.34	0.49	0.54	0.58	-2.01	<-2.59	6.14
	800	84	1906	0.16	0.45	0.21	0.43	-2.14		
1240-64*	650	95	2513	0.34	0.49	0.54	4.32	-1.14		
	800	84	1906	0.16	0.45	0.21	4.52	-1.12		
1323-58	650	85	2515	1.43	0.45	3.51	38.49	-0.10	-0.86	6.37
	800	91	1906	1.03	0.43	2.00	34.90	-0.14		
1323-62	650	73	2537	1.38	0.81	2.15	30.48	-0.16	-0.47	5.65
	800	59	1906	0.61	0.70	1.55	32.23	-0.14		
1358-63	650	68	1503	0.70	0.57	1.37	30.38	0.38	0.08	5.90
	800	80	1531	0.49	0.57	0.77	31.88	0.40		
1426-66	650	78	2516	0.34	0.75	0.61	3.34	-0.94	-1.10	6.65
	800	61	1791	0.20	0.70	0.54	3.88	-0.88		
1449-64	650	83	2537	0.53	0.50	1.08	7.30	-1.25	-1.78	6.02
	800	67	1705	0.31	0.47	0.66	7.08	-1.26		

Timing noise parameters, continued ...

Table 4.6: Timing noise parameters (continued).

Pulsar PSR B	Freq (MHz)	N	T (days)	σ_M (mP)	σ_J (mP)	σ_W (mP)	σ_{TN} (mP)	A	Δ_8	$\log\tau$
1451-68	650	84	2549	0.50	0.53	1.14	1.95	-1.66	<-1.98	7.63
	800	66	1906	0.25	0.49	1.35	1.83	-1.69		
1530-53	650	76	2537	0.51	0.86	0.77	0.45	-1.58	<-1.56	7.18
	800	64	1860	0.32	0.86	0.74	0.32	-1.72		
1556-44	650	76	2536	0.41	0.49	0.54	2.17	-1.62	-2.19	6.60
	800	56	1859	0.25	0.46	0.38	2.38	-1.58		
1558-50	650	82	2549	1.02	0.58	1.41	133.19	0.69	0.37	5.29
	800	68	1906	0.57	0.58	0.82	133.93	0.69		
1600-49	650	70	2516	1.17	0.42	2.32	7.82	-0.95	-1.30	6.71
	800	57	1789	0.96	0.39	1.81	5.82	-1.08		
1641-45	650	89	2549	0.61	1.33	1.28	27.20	-0.28	-0.79	5.55
	800	66	1906	0.32	1.19	0.47	31.03	-0.22		
1641-45*	650	89	2549	0.61	1.33	1.28	35.55	-0.16		
	800	66	1906	0.32	1.19	0.47	27.91	-0.27		
1648-42	650	87	2217	2.57	1.24	8.87	15.54	-0.16	-0.69	6.45
	800	88	1601	1.71	0.87	4.15	13.42	-0.23		
1700-32	650	94	2523	1.00	0.53	1.60	0.52	-1.57	-1.65	7.46
	800	78	1679	0.73	0.53	1.12	0.65	-1.47		
1706-16	650	58	2169	0.45	0.45	0.86	24.19	-0.07	-0.51	6.22
	800	57	1531	0.27	0.45	0.59	21.93	-0.11		
1718-32	650	79	2218	1.23	0.43	3.04	2.87	-1.14	-1.95	7.07
	800	80	1531	0.92	0.40	1.18	1.73	-1.36		
1727-47	650	122	2515	0.48	1.01	0.52	3.95	-0.85	-1.58	4.91
	800	138	1907	0.19	0.88	0.36	3.14	-0.95		
1737-30	650	84	1447	1.42	0.51	3.87	150.71	0.96	0.41	4.31
	800	153	1416	1.38	0.43	2.84	131.94	0.90		
1737-30*	650	84	1447	1.42	0.51	3.87	39.79	0.38		
	800	153	1416	1.38	0.43	2.84	36.61	0.34		
1737-39	650	75	2548	1.16	0.40	1.40	11.39	-0.60	-1.11	6.62
	800	58	1907	0.86	0.36	1.09	7.84	-0.77		
1742-30	650	67	2217	0.71	0.31	0.74	7.69	-0.83	-2.13	5.74
	800	64	1744	0.44	0.31	0.74	6.12	-0.93		
1747-46	650	73	2509	0.50	0.54	1.15	0.92	-1.53	<-2.00	6.96
	800	58	1907	0.34	0.48	0.78	0.76	-1.61		
1749-28	650	80	2548	0.15	0.72	0.53	14.40	-0.46	-1.43	6.04
	800	68	1907	0.12	0.66	0.54	10.43	-0.60		
1857-26	650	75	2540	1.04	0.81	1.36	1.42	-1.43	<-2.00	7.68
	800	55	1866	0.80	0.75	0.84	0.62	-1.79		
1937-26	650	71	2331	1.06	0.28	2.38	2.07	-1.39	<-2.03	6.82
	800	80	1602	0.89	0.28	2.35	2.06	-1.39		
2045-16	650	71	2540	0.26	0.95	0.52	1.00	-1.08	<-1.88	6.45
	800	61	1905	0.21	0.95	0.41	0.43	-1.44		
2048-72	650	96	2452	1.13	0.43	4.68	1.72	-1.58	-1.80	7.44
	800	108	1760	0.65	0.43	3.66	1.46	-1.65		
2321-61	650	71	2234	0.74	0.60	1.19	0.54	-1.18	<-1.50	7.16
	800	118	1678	0.57	0.60	1.14	0.22	-1.58		
2327-20	650	69	2521	0.53	0.50	1.01	1.20	-1.07	<-1.66	6.75
	800	61	1602	0.41	0.50	0.84	0.65	-1.34		

* Results obtained when small period jumps are not removed from the arrival-time data.

may differ), along with a nominal value of 5° of longitude for the sub-pulse width since single-pulse observations are not available to estimate this value. Typical estimates of the sub-pulse width lie in the range 3–10 degrees of longitude (Manchester & Taylor 1977).

Pulse jitter and measurement noise contribute toward a "white noise" component in the rms residual phase, i.e., we should find that $\phi_W = \phi_M + \phi_J$, and $\sigma_W = \sqrt{\sigma_M^2 + \sigma_J^2}$. Measurement noise tends to dominate the white noise for weak pulsars, whereas pulse jitter tends to dominate for stronger pulsars. The rms white noise component was estimated from the data using the "structure function" approach of Cordes & Downs (1985). Their estimator is of the form

$$\sigma_W^2 = \frac{1}{2N} \sum_j (\delta\phi_{j+1} - \delta\phi_j)^2 \tag{4.31}$$

where $\delta\phi_j$ is the phase residual of the jth sample at time t_j and N is the number of phase residual pairs used in the estimate. Such pairs were only included if $t_{j+1} - t_j < 4$ days (the length of a typical observing session). The true timing noise contribution (σ_{TN}) to the phase residuals was then obtained by quadratic subtraction of the white noise estimate from the measured rms phase residual, namely,

$$\sigma_{TN}^2 = \sigma_R^2 - \sigma_W^2. \tag{4.32}$$

The reference time interval for the stability parameter estimate was taken to be $t = 10^8$ s ($\sim$1160 d), hence the notation Δ_8. The longest common time span for all 45 pulsars in the Mt Pleasant sample is $\sim$1400 days, so that $\log(t) \simeq 8.08$ (t in seconds). Hence, little is gained by using the latter reference time, and the use of the former value enables direct comparison with the results of Arzoumanian *et al.* (1994). Upper limits are quoted for the stability parameters if $|\ddot{\nu}| < 2\sigma_{\ddot{\nu}}$, where the upper limit is given by $\Delta(t) = 2\sigma_{\ddot{\nu}} t^3/6\nu$.

The data recorded at the two observing frequencies (650 and 800 MHz) have been treated separately for this preliminary timing noise analysis. In doing so, the relevant parameters for each frequency have been quantified. This is necessary, initially, since the parameters are different. For example, σ_M is smaller for the 800 MHz observations as they were made using larger filter bandwidths (see Chapter 3). While the gross rotational behaviour of pulsars is expected to be independent of observing frequency, there are several small frequency-dependent effects which can contribute to the measured arrival times, e.g., mode changes, DM fluctuations, refractive delays, etc. In most cases, DM fluctuations are negligible when compared with the measurement noise and pulse jitter, as discussed earlier. Also, refractive delays are negligible at these observing frequencies (Phillips & Wolszczan 1991, 1992). For a few objects, mode changes may make a significant contribution to the phase error. In any case, all of these low-level effects will most likely be absorbed into the white noise estimate.

Figure 4.8 is a scatter plot showing estimates of the white noise versus the measurement uncertainty for each pulsar. For most of the sources, the white noise estimates exceed the measurement uncertainties. This result is similar to that obtained by Cordes & Downs (1985). Pulse jitter or pulse shape variations, or both, may be responsible for this excess. The upper limits for pulse jitter given in Table 4.6 show that pulse jitter can account for the excess noise in some pulsars. Downs & Krause-Polstorff (1986) found excess short-term (tens of minutes) phase fluctuations in the JPL pulsar sample. Their analysis showed that pulse shape changes and intensity variations could not account for the excess noise which appeared to be correlated on time-scales of hours. Regardless of its origin, this excess short-term noise will be absorbed into the white noise estimate. The main aim of the timing noise analyses throughout this thesis is to investigate the timing activity of pulsars over longer time-scales.

The lone point in the top right hand corner of Figure 4.8 corresponds to the estimates for PSR B1648-42. The integrated profiles of this pulsar show some evidence of mode changing. A mean profile of each "mode" is shown in Figure 4.9. The profile appears to consist of two components. A change in the intensity of the leading component may be responsible for the two modes shown in Figure 4.9. This observation is supported by Lyne & Manchester (1988), who classified the profile of this pulsar as a "partial cone", i.e., two components not of equal intensity. Wu *et al.* (1993) recently obtained a mean polarization profile of this pulsar at 1560 MHz. At this frequency, the two components are more easily resolved. If mode changing is taking place in the profiles of PSR B1648-42, then this behaviour can cause pulse shape changes which may account for the large white noise estimate for this pulsar. Costa (1989) has reported mode changing in the profiles of PSR B1056-57 at 600 MHz. This is consistent with the fact that the estimated white noise is almost twice the measurement uncertainty for this pulsar. However, most of the profiles are too weak to investigate this aspect any further.

Another possibility relates to the estimate of the measurement uncertainty. The integrated profiles of PSR B1648-42 are highly scattered, with typical signal-to-noise (S/N) ratios of 5–8 for the Mt Pleasant pulsar observing system. Downs & Reichley (1983) point out that their equation for estimating the measurement uncertainty may not be valid for S/N ratios less than 10[1]. Hence, the white noise estimate for this pulsar could appear to be excessive because the measurement uncertainty may be underestimated.

Plots of the activity and stability parameters against the logarithm of the period (in seconds), period derivative (in units of 10^{-15} ss^{-1}) and characteristic

[1]However, recent tests of the performance of some standard pulse phase estimation procedures suggest that the Downs & Reichley equation is valid for S/N ratios as low as ~ 3 (Deshpande & McCulloch 1992). If this is the case, then this possibility is eliminated.

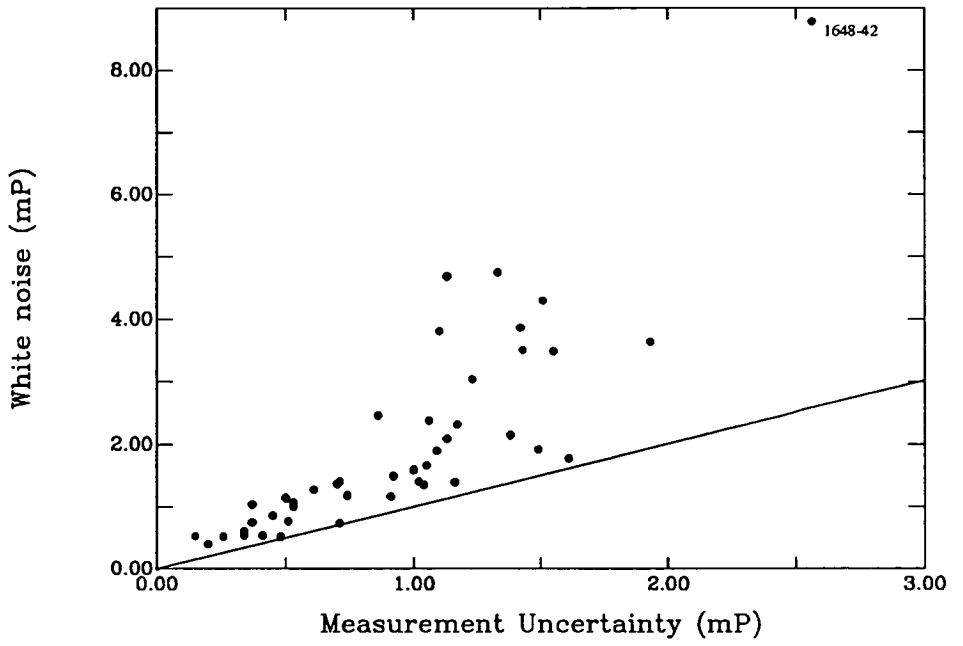

Figure 4.8: A plot of the white noise estimates against the measurement uncertainty estimates for 45 pulsars. White noise in excess of the measurement uncertainty is indicative of pulse jitter and pulse shape variations.

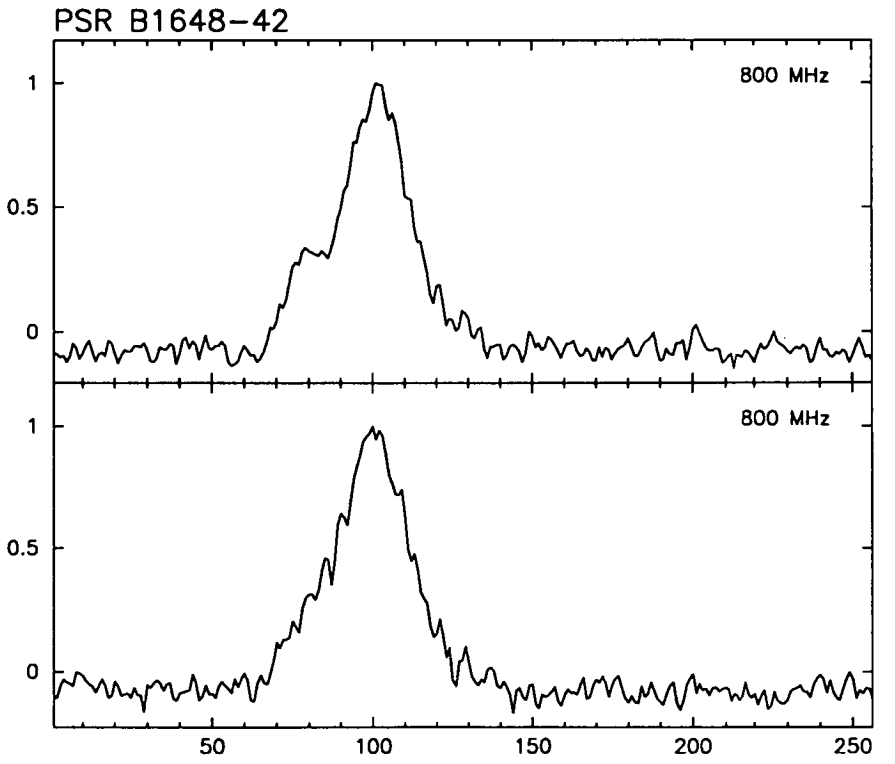

Figure 4.9: Evidence of mode changing in the integrated profiles of PSR B1648-42.

age (in years) of each pulsar are shown in Figure 4.10. Correlation analyses give similar results for the two parameters. The linear correlation coefficients computed for the activity parameter plots were 0.22, 0.69 and −0.61 respectively, using the data recorded at 650 MHz, and 0.12, 0.67 and −0.62 respectively for the data recorded at 800 MHz. The linear correlation coefficients computed for the stability parameter plots were 0.25, 0.60 and −0.51 respectively. Using a Student's t-distribution for 43 degrees of freedom, at a level of 1% there is a significant correlation of both the activity and stability parameter with period derivative and characteristic age, but there is no significant correlation with period. These results agree with those of Cordes & Helfand (1980) and Cordes & Downs (1985), whose analyses were based on samples of 50 and 24 pulsars respectively. The correlation with $\dot{P}$ is not unexpected, since $\dot{P}$ is proportional to the net torque acting on the stellar crust. Torque fluctuations, whatever their origin, produce timing noisewith a strength that ultimately depends on the slowing-down rate of the neutron star. The correlation with pulsar age is also expected, since the age is computed using $\dot{P}$. The relation of A with $\dot{P}$ and τ is given approximately by

$$A = -(1.3 \pm 0.1) + (0.7 \pm 0.1) \log \dot{P} \quad (4.33)$$

$$A = +(3.0 \pm 0.8) - (0.6 \pm 0.1) \log \tau \quad (4.34)$$

and the relation of Δ_8 with $\dot{P}$ and τ is given approximately by

$$\Delta_8 = -(1.8 \pm 0.1) + (0.6 \pm 0.1) \log \dot{P} \quad (4.35)$$

$$\Delta_8 = +(1.8 \pm 0.8) - (0.5 \pm 0.1) \log \tau \quad (4.36)$$

where $\dot{P}$ is in units of 10^{-15} ss^{-1} and τ is in units of years. The relations of A with $\dot{P}$ and Δ_8 with $\dot{P}$ are very similar to those found by Cordes & Downs (1985) and Arzoumanian *et al.* (1994) for other pulsars.

Dewey & Cordes (1989) have conducted a more detailed analysis of the relation of timing noise to pulsar period and period derivative using an extended data set. They have found that

$$A = (-0.4 \pm 0.8) \log P + (0.8 \pm 0.4) \log \dot{P} + (-1.8 \pm 0.4), \quad (4.37)$$

i.e., timing activity depends strongly on period derivative but not period. They also found that the scatter around the best fit to P and $\dot{P}$ is considerably larger than the measurement error, suggesting that other "hidden" variables (e.g., mass or temperature) must play a significant role in timing activity.

4.4 Summary

This chapter has presented the method of analysis of pulse arrival times and the basic results of the analysis for timing measurements made on 45 southern pulsars

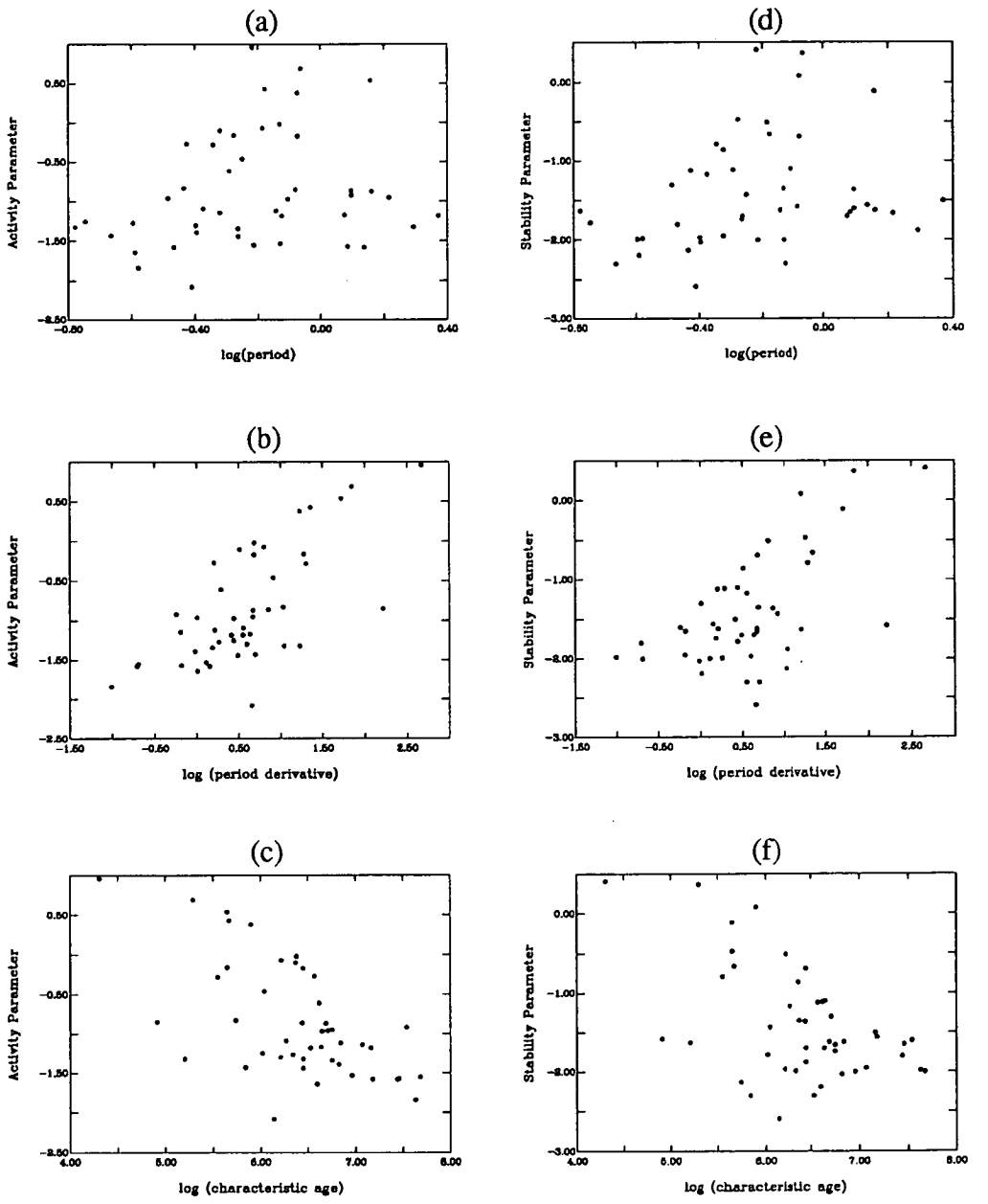

Figure 4.10: Plots showing the relationship between the activity (a–c) and stability (d–f) parameter and period, period derivative, and characteristic age, respectively, for 45 pulsars.

over a seven-year period. Timing model fits to the data collected over this time interval have resulted in more accurate estimates of one or more of the basic parameters for each pulsar, namely, the period, period derivative, position, and dispersion measure. Estimates were obtained for the period second derivative of 13 pulsars. All of the estimates were found to be too large to be due to the secular spin-down of the pulsar. In fact, a diagnostic test has shown that the third order term appearing in the phase residuals of these pulsars could result from a random walk process.

The dispersion measure along the line-of-sight to eight pulsars was found to be significantly different from previous estimates. These changes have been interpreted in terms of the movement of density irregularities across the line-of-sight to the pulsar. Several approaches were used to analyse these changes. For example, if one assumes that the DM changes are due to the motion of a single, ionised cloud with a scale-size of $\sim 10^{15}$ cm and a relative velocity of ~ 100 km/s, then the density must be in the range $10^2 - 10^4$ cm^{-3}. An alternative explanation in terms of turbulence in many clouds, using volume filling factors estimated by Cordes *et al.* (1985), suggests scale-sizes of about 10^{18} cm.

The timing model fits have also revealed jumps in the rotation rate of five pulsars. Most of the jumps were found to be significant with respect to the hypothesis that they are simply the result of fluctuations arising from a random walk process. Two of the jumps are large enough to be classified as "glitches". Relaxation of the rotation rate back toward its pre-jump value was not measured for any of the jumps. The implications were discussed in the light of recent jump models. PSR B1737-30 continues to undergo jumps at a rate of 1–2 per year. In contrast, the glitch in PSR B1727-47 was the first observed since the discovery of this pulsar, reinforcing the theory that, as a pulsar ages, it glitches less frequently. There appear to have been five small jumps in the rotation rate of PSR B1240-64. An extraordinary feature of these jumps is their alternating nature, i.e., the sign of each successive jump changes. The results of analyses suggest that other possible causes of such regular changes in the slope of the residuals (e.g., free pulsar precession or a binary system) are unlikely. An explanation in terms of oscillations of the neutron superfluid interior was discussed.

A preliminary analysis of timing noise has shown that there is a significant positive correlation between timing activity and the period derivative, and a significant negative correlation between timing activity and pulsar age. There was no significant correlation between timing activity and pulse period. It was also found that the short time-scale white noise in the *pulsar clock* could not be accounted for solely by instrumental errors.

Chapter 5

Pulsar Polarization Observations

5.1 Introduction

Polarization measurements are fundamental to gaining a better understanding of pulsar emission mechanisms. The original hollow-cone beam model of Radhakrishnan & Cooke (1969) has been refined by a number of workers, including Lyne & Manchester (1988), Rankin (1983, *et seq.*) and Radhakrishnan & Rankin (1990). Even so, an adequate emission model has so far eluded researchers. The polarized nature of the radiation from pulsars has also been used to probe the properties of the intervening medium. Observations at two or more frequencies provide information about the interstellar magnetic field along the line of sight and within the source of the polarized radio emission. The derived field strengths in a large number of directions have been used to construct a model of the large-scale magnetic field structure of the Galaxy (e.g., see Manchester 1972, 1974, Hamilton & Lyne 1987, Lyne & Smith 1989, Rand & Lyne 1994).

A number of polarimetric surveys have been conducted in the southern hemisphere, namely, those by Hamilton *et al.* (1977), McCulloch *et al.* (1978), Manchester *et al.* (1980), Costa *et al.* (1991) and Wu *et al.* (1993) at observing frequencies of 400, 640, 1612, 600 and 1560 MHz respectively. Further, there exist unpublished observations at 950 MHz (van Ommen 1992). Apart from these surveys, observations of southern pulsars are scarce. A few southern sources have been observed as part of the high frequency studies done by Xilouris *et al.* (1991, 1995).

Dual-frequency polarization data have been routinely recorded as part of the monthly pulsar timing observations at the Mt Pleasant Observatory at observing frequencies near 670 and 800 MHz. Accurate phase calibration is not carried out during a standard timing session. However, on several occasions during 1991, the relevant calibration information was recorded for a total of 18 pulsars from the Mt Pleasant sample which were deemed to be suitable for observations with the 26-m telescope, i.e., pulse fluxes large enough to record profiles with a signal-to-noise

ratio which allow meaningful analyses. These calibrated polarization measurements were the first to be made with the XY-mounted 26-m antenna. The only exception was the single-pulse observations of Vela made by Costa (1989) using a completely different observing system.

This chapter presents the method of analysis of the polarization data collected during 1991, the calibrated polarization profiles resulting from the analysis, the basic polarization parameters derived from these profiles and how they compare with measurements at other observing frequencies. Also, rotation measures have been derived from the dual frequency measurements of position angle (PA) of the linearly polarized component of the pulse.

5.2 Polarization Data Reduction and Calibration

The polarization data files were initially condensed by averaging data in blocks of about five successive sets of integrations, as described in Chapter 3. The selection of the reduction factor was a compromise between processing time and data manipulation and storage, and the maximum practical interval for "corrections" to the data, such as ionospheric Faraday rotation and the change in PA of the telescope feed. Comparison of several test profiles with previously published profiles demonstrated that smearing of the polarization characteristics over the time interval for each block ($\leq$ 20 minutes) was negligible.

Next, the data from the channels within each band were dedispersed to the approximate receiver centre frequencies of 670 and 800 MHz. Each polarization channel (I_X, I_Y, U and V for the four frequency channels in bands A and B) was then plotted to enable data quality assessment and removal of channels affected by interference.

Information about the gain and phase characteristics of each frequency channel was obtained from four independent measurements. The sequence of the four measurements was as follows:

Integration 1: CAL *off*, $\phi = 0°$,
Integration 2: CAL *on*, $\phi = 0°$,
Integration 3: CAL *off*, $\phi = -90°$,
Integration 4: CAL *on*, $\phi = -90°$,

where CAL is the linearly polarized noise signal and ϕ is the phase inserted in the X channel by the quadrature hybrid (as described in Chapter 3). The addition of the quadrature hybrid to the receiver enabled the U and V data to be calibrated. For each channel, the difference between the off-pulse baseline height of the pulse profiles from integrations 1 & 2 and integrations 3 & 4 gave the CAL heights for what will be termed the CAL_0 and CAL_{90} integrations respectively. The I_X, U

and V channel CAL heights and data obtained from the CAL_{90} integrations were adjusted to compensate for the change in gain of the X channel when switched through the $-90°$ port of the quadrature hybrid.

The I_X data were then calibrated with respect to the I_Y data, in the same manner as for the timing data (see Chapter 4). However, it was not assumed that the CAL radiates equally into the X and Y dipoles. Instead, the I_X data were multiplied by the ratio of the CAL contribution in the X and Y dipoles. This ratio was obtained by comparing the CAL strength with observations of an unpolarized, continuum astronomical source (described later). The ratio was found to be very close to the expected value of unity. In this manner, the gain in each X channel was made equal to the corresponding Y channel, allowing the I_X and I_Y data to be combined to obtain the Stokes parameters $I = I_X + I_Y$ and $Q = I_X - I_Y$.

The derivation of the technique used to calibrate the U and V data is outlined in Appendix B. The aim of such a method is to remove any phase difference between the X and Y signals that is introduced by the receiver, for example, because of a difference in the path lengths through the receiver system or between the X and Y filters. This "instrumental phase", ϕ_i, can be removed by "derotating" the data. From Appendix B, the derotation equations are

$$G_U U = U' \cos\phi_i + K_{UV} V' \sin\phi_i, \tag{5.1}$$

$$G_U V = -U' \sin\phi_i + K_{UV} V' \cos\phi_i, \tag{5.2}$$

for the CAL_0 measurements, and

$$G_U U_p = -U'_p \sin[(\phi_i + \gamma)] + K_{UV} V'_p \cos[(\phi_i + \gamma)], \tag{5.3}$$

$$G_U V_p = -U'_p \cos[(\phi_i + \gamma)] - K_{UV} V'_p \sin[(\phi_i + \gamma)], \tag{5.4}$$

for the CAL_{90} measurements. Primes denote measured values (either CAL heights or the data), no prime denotes "true" values, the "p" subscript denotes a measurement with a phase delay inserted (e.g. $-105°$, where $\gamma = 15°$, the excess phase beyond $-90°$, as described in Chapter 3), and G_U is the gain of the U channel. Note that V has been scaled so that it has the same gain as U. The gain difference between them is removed in the derotation process by using the ratio of the U and V channel gains, K_{UV}. Solution of the derotation equations gives,

$$K_{UV} = -\frac{U'_p \cos\gamma}{V' + V'_p \sin\gamma} \tag{5.5}$$

and the instrumental phase,

$$\phi_i = \arctan\left(\frac{-U'_p V' \cos\gamma}{U'V' + U'V'_p \sin\gamma}\right). \tag{5.6}$$

The U and V CAL heights were used to calculate K_{UV} and ϕ_i for each channel of the receiver. The CAL heights and the data were then derotated using Equations

5.1–5.4 to remove the instrumental phase. The derotation process removed the CAL contribution in the V channels, as expected for a linearly polarized CAL signal (with no phase inserted in the X channel). The derotated CAL heights from the U channels were used to calibrate the true, equal-gain U and V data with respect to the I_Y data, in a similar manner to the corrections applied to the I_X data.

After having calibrated the data for the complex receiver gain, the next step was to apply corrections for the effects of (i) a non-rotating telescope feed, (ii) ionospheric Faraday rotation, and (iii) interstellar Faraday rotation differences between the channels in each band. This was achieved by derotating the Q and U data using the equations

$$Q = Q' \cos 2\theta + U' \sin 2\theta, \tag{5.7}$$

$$U = -Q' \sin 2\theta + U' \cos 2\theta, \tag{5.8}$$

where primes denote the measured values, and θ represents the feed PA, ionospheric and interstellar Faraday rotation angles for (i), (ii) and (iii) respectively. The Faraday rotation angles (in radians) were computed according to,

$$\theta = RM\lambda^2 \tag{5.9}$$

where RM is the ionospheric or interstellar rotation measure (rad m^{-2}), and λ is the observing wavelength (in metres) of a given channel.

For polarization measurements, it is important to keep the orientation of the telescope feed constant with respect to the source polarization position angle. Appropriate derotation of the linear polarization parameters Q and U at regular intervals is sufficient to correct for a non-rotating feed. The Mt Pleasant 26-metre telescope has an X-Y mount, and the PA of the feed, ψ_f, relative to the fixed feed angle at the "transit" orientation is given by

$$\psi_f = \arctan\left[\frac{\sin(-h)\sin\delta}{\cos(-h)}\right] \tag{5.10}$$

[de Deuge (1985)], where h and δ are the hour angle and declination of the source respectively. Figure 5.1 shows how the position angle of the feed varies as a source of a given southern declination is tracked across the sky using a telescope with an X-Y mount. Most of the polarization observations, especially of sources at lower declinations where there are regions of rapidly changing feed PA, were made in the hour angle region of $\pm 60°$ to minimise the requirements for more frequent corrections for the relative rotation of the telescope feed. In this hour angle region, the PA of the feed relative to the source PA varies by ≤ 1 degree per degree of hour angle. The feed position angles were computed and used to correct each integration in the manner described by Equations 5.7 and 5.8.

The ionospheric rotation measures were estimated using the critical reflection frequency f_0F2 of the F2 layer and a standard model of the ionosphere (Hamilton *et*

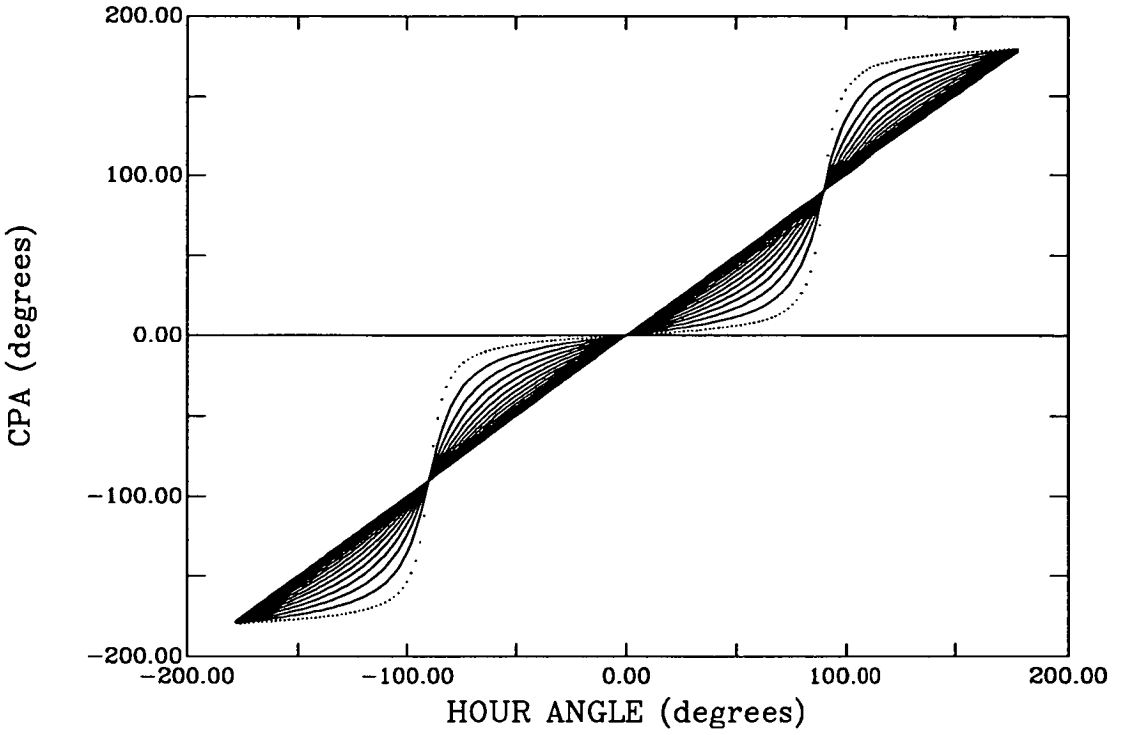

Figure 5.1: Graph showing how the position angle of the feed varies as a source is tracked across the sky using a telescope with an X-Y mount. The dotted line represents a declination of $-5°$, and the curves are plotted in steps of $-5°$.

al. 1977, Costa 1989). The f_0F2 values were supplied for Hobart by the Ionospheric Prediction Service, tabulated at hourly intervals, and ranged from 2 to 10 MHz. The earth's magnetic field strength, longitude, latitude, hour angle and declination were taken to be 0.53 Gauss, 72°, 13.8°, −1.37 hr and −24.3° respectively. The ionospheric rotation measures calculated were typically in the range -1 rad m^{-2} to -3 rad m^{-2}.

The correction of the Q and U data for interstellar Faraday rotation differences between adjacent channels within each band was needed to avoid depolarization due to "smearing" of the PA vector, particularly for high-RM pulsars. Although one aim of the polarimetry was to obtain RMs, previously tabulated values (Manchester & Taylor 1981) were used in this step with the aim of obtaining more precise values or to note whether any RMs had changed since they were last measured. As of 1991, two pulsars did not have previously published RMs, namely, PSRs B0538-75 and B1358-63. In these cases, the unpublished values of 24 ± 2 and 58 ± 13 rad m^{-2} were used [Costa 1989, van Ommen 1991 (private communication), respectively]. Alternatively, an iterative algorithm can be used where one derotates the data, searching for the maximum linear polarization (therefore minimum depolarization), but its applicability depends on a number of factors, one being the signal-to-noise ratio attained. Hence, this technique is difficult to apply to data obtained from a sensitivity-limited instrument such as

the Mt Pleasant 26-metre telescope.

At this point of the analysis, the derotated and normalised I, Q, U and V profiles, as seen from above the ionosphere, were calibrated by dividing the data arrays through by the I_Y CAL heights and multiplying by the absolute flux of the CAL signal in the Y dipole. The flux density scale was established from observations of the continuum source Virgo A, which was assumed to have a flux of 365 Jy at 670 MHz and 325 Jy at 800 MHz. These observations were made at least once during each observing session. The resulting flux density scale is believed to be accurate to within 30%.

Final profiles of I, Q, U and V were obtained by computing weighted means of the calibrated data from each channel for each integration. The linearly polarized intensity, L, and its uncertainty, δL, the position angle of the linearly polarized component, ψ, and its uncertainty, $\delta\psi$, were calculated using the equations,

$$L = \sqrt{Q^2 + U^2}, \tag{5.11}$$

$$\delta L = \frac{Q\delta Q + U\delta U}{\sqrt{Q^2 + U^2}}, \tag{5.12}$$

$$\psi = \frac{1}{2}\arctan\left(\frac{U}{Q}\right), \tag{5.13}$$

$$\delta\psi = \frac{Q\delta U + U\delta Q}{2(Q^2 + U^2)}, \tag{5.14}$$

respectively. The mean off-pulse value from Equation 5.11 was subtracted from the linearly polarized intensity, as this noise makes a net positive contribution to the percentage polarization.

The basic polarization characteristics, namely profiles of the average Stokes parameters, the linearly polarized content, L, and PA, ψ, for the two frequency bands were stored in a data file for each pulsar. The rotation measure for each pulsar was calculated by taking a weighted mean of the PA difference across the pulse at the two frequencies. The $n\pi$ ambiguity in PA between 670 and 800 MHz is 52.48 rad m^{-2}, so the RM value was corrected by adding $52.48n$, where n is the whole number giving a RM nearest the value used earlier to correct for interstellar rotation between the frequency channels.

5.2.1 Polarization tests

The polarization analysis software was tested by using simulated polarization data. Factors such as the instrumental phase, the phase inserted by the quadrature hybrid, channel gains, X and Y CAL strength ratio, sign convention of Stokes parameter V (see Appendices A and B), degree of linear and circular polarization, and the phase of the LC circuit used to produce the quadrature product (if not 90°) were varied in a series of program runs. The input polarization features were

accurately produced at the reduction program output. The amount of spurious circular polarization produced as a result of inserting the incorrect hybrid phase ($\pm 15°$) was found to be $\leq 5\%$. The tests also showed that substantially more spurious polarization could be introduced if the LC circuit phase was not 90°. However, a series of receiver tests using the CAL signal revealed that problems of this nature had not affected the measurements in any appreciable way.

5.3 Polarization Characteristics

Table 5.1 summarises the observing parameters for each pulsar and the pulse and polarization characteristics obtained for both observing frequencies. The columns contain respectively the pulsar name and period, observing frequency and bandwidth, number of samples per apparent period, post-detection RC time constant, number of pulses integrated, mean flux density, mean percentage polarizations and their 2σ uncertainties, pulse widths at 50 and 10 per cent of the peak intensity, and the equivalent width of the pulse (given in units of milliseconds and degrees of pulse longitude).

The mean flux density was computed from the ratio of the area under the total intensity profile (the mean pulse energy) to the pulse period; the equivalent width as the pulse energy divided by the peak intensity; the percentage linear polarization as the ratio of the mean linearly polarized energy (area under the profile of $L = \sqrt{Q^2 + U^2}$) to the mean pulse energy; and the percentage circular polarization as the ratio of the mean circularly polarized energy to the mean pulse energy, calculated in two ways, (i) by disregarding the sign ($|V|$) and (ii) by taking the sign into account (V). The latter calculation is necessary because for some pulsars there is a change in the hand of circular polarization across the pulse.

The results of the 670 MHz polarimetry are generally consistent with the 640 MHz observations presented by McCulloch *et al.* (1978), within the stated uncertainties, for the 16 pulsars overlapping with their sample. Of the two remaining sources, the results for PSR B0538-75 are in close agreement with those given by Costa *et al.* (1991) for an observing frequency of 600 MHz. Polarization observations of PSR B1358-63 at 660 MHz appeared in the literature only very recently (Qiao *et al.* 1995). Their results are in close agreement with those obtained from the Mt Pleasant observations at 670 MHz.

Integrated pulse profiles at observing frequencies of 670 and 800 MHz are presented in Figures 5.2–5.19. Each figure displays the polarization characteristics in the same manner, showing the total intensity (I), the linearly polarized intensity (L, corrected for the contribution of noise as described in Section 5.2), the circularly polarized intensity (V, defined in the sense of left circular minus right circular), and the PA of the linearly polarized component (plotted in the upper

Table 5.1: Observing parameters and dual frequency polarization characteristics.

Pulsar	Period	Freq.	B/W	Bins	T.C.	No. of pulses	Mean flux density	Mean linear poln.	Uncert-ainty	Circular poln. Mean |V|	Circular poln. Mean V	Uncert-ainty	Pulse width w50	Pulse width w10	Equivalent width	
	(ms)	(MHz)	(MHz)		(ms)		(mJy)	(%)	(%)	(%)	(%)	(%)	(deg)		(ms)	(deg)
0538-75	1246	670	5.0	256	0.6	5760	135	50	8	9	-8	5	20	29	61.6	17.8
		800	10.0	256	0.2	5760	69	48	8	6	-4	4	20	29	64.0	18.5
0628-28	1244	670	5.0	256	0.6	5760	552	56	4	6	-5	3	18	37	72.5	21.0
		800	10.0	256	0.2	5760	254	57	4	3	-2	2	18	36	71.9	20.8
0736-40	375	670	1.5	256	0.6	9600	317	13	9	8	-5	8	21	40	23.3	22.4
		800	3.0	256	0.2	9600	306	19	5	6	-3	3	20	40	22.9	22.0
0740-28	167	670	0.5	200	0.6	32760	210	81	10	6	-2	6	11	19	5.2	11.2
		800	1.0	200	0.2	32760	170	82	6	6	-4	2	11	18	5.0	10.8
0835-41	752	670	0.5	256	0.6	4740	210	6	5	25	25	6	4	8	9.5	4.5
		800	1.0	256	0.2	4740	133	9	6	30	30	5	5	9	10.8	5.2
1240-64	388	670	0.5	256	0.6	12320	230	17	7	19	18	6	8	15	9.1	8.4
		800	1.0	256	0.2	12320	192	12	4	9	8	3	7	13	8.2	7.6
1358-63	843	670	5.0	256	0.6	2556	74	15	19	9	3	16	7	16	19.4	8.3
		800	10.0	256	0.2	2556	63	14	8	4	2	5	7	15	18.9	8.1
1426-66	785	670	5.0	256	0.6	6080	154	8	5	5	4	4	9	16	20.2	9.2
		800	10.0	256	0.2	6080	136	4	2	4	4	2	9	15	20.3	9.3
1449-64	179	670	0.5	200	0.6	32760	95	21	12	9	4	10	8	13	3.8	7.7
		800	1.0	200	0.2	32760	89	18	10	8	-2	7	7	16	4.1	8.3
1451-68	263	670	5.0	256	0.6	18160	147	8	12	14	6	11	15	38	13.5	18.4
		800	10.0	256	0.2	18160	208	8	4	6	4	3	18	37	14.4	19.7
1556-44	257	670	1.5	256	0.6	18640	202	47	11	11	-10	8	10	19	8.0	11.2
		800	3.0	256	0.2	18640	157	38	7	8	-7	4	10	20	8.0	11.1
1641-45	455	670	0.5	256	0.6	5240	905	1	9	8	2	9	35	85	56.9	45.0
		800	1.0	256	0.2	5240	846	3	4	3	2	4	26	59	39.5	31.2
1706-16	653	670	5.0	256	0.6	7280	104	17	5	4	-1	5	7	14	13.5	7.5
		800	10.0	256	0.2	7280	99	10	3	4	3	2	7	14	13.4	7.4
1727-47	830	670	1.5	256	0.6	4320	221	13	4	10	9	5	9	14	18.4	8.0
		800	3.0	256	0.2	4320	196	17	3	7	6	2	8	14	18.5	8.0
1747-46	742	670	5.0	256	0.6	6400	88	11	12	15	10	11	7	12	14.6	7.1
		800	10.0	256	0.2	6400	33	6	8	12	9	6	7	11	14.6	7.1
1749-28	563	670	5.0	256	0.6	4240	669	13	6	8	2	5	6	12	10.2	6.5
		800	10.0	256	0.2	4240	512	10	2	4	4	1	7	12	11.6	7.4
1857-26	612	670	5.0	256	0.6	10864	102	31	12	17	-5	8	29	42	44.2	26.0
		800	10.0	256	0.2	10864	80	34	8	15	3	5	33	39	48.4	28.5
2045-16	1962	670	5.0	256	0.6	2400	187	36	5	5	4	3	8	19	64.8	11.9
		800	10.0	256	0.2	2400	85	36	6	5	5	3	8	18	53.8	9.9

part of the figure with 2σ error bars). The latter values are corrected for ionospheric effects (as described in Section 5.2) and so they represent the PA measured above the ionosphere. The uncertainty in the PA is due to random noise, errors in the position of the feed (although this does not contribute to the uncertainty in the rotation measures, which are derived from the PA across the pulse at each frequency made simultaneously with the same feed), the uncertainty in the observing centre frequencies, and errors in estimating the ionospheric Faraday rotation (θ_i). The 1σ uncertainty in θ_i was taken to be 10%. The error box in the bottom left hand corner of the figure has a height of $\pm 2\sigma$, where σ is the rms off-pulse noise in the total intensity profile, and a width equal to the sampling interval or the dispersion smearing, whichever is larger.

The percentage error in the flux scale is believed to be $\leq$ 30%, although the intensity of a number of profiles may be affected by interstellar scintillation. For example, Kaspi & Stinebring (1992) have found that PSRs B0835-41, B1556-44 and B1749-28 undergo slow but significant intensity changes due to interstellar refraction at an observing frequency of 610 MHz.

Profiles of individual pulsars are discussed below, with particular reference to the 800 MHz observations. Where applicable, comparisons are made with the 400, 600, 640, 950, 1560 and 1612 MHz polarization observations of Hamilton *et al.* (1977), Costa *et al.* (1991), McCulloch *et al.* (1978), van Ommen (1992), Wu *et al.* (1993) and Manchester *et al.* (1980).

5.3.1 Integrated Profiles

PSR B0538-75 (Figure 5.2): This pulsar has the classic S-shaped PA variation across the pulse predicted by the rotating vector model of Radhakrishnan & Cooke (1969). The profile is complex, with multiple unresolved components. There is $\sim$50% linear polarization and $\sim$6% right circular polarization at both observing frequencies. The results for both frequencies are very similar to those obtained by Costa *et al.* (1991) and van Ommen (1992) at 600 and 950 MHz respectively.

PSR B0628-28 (Figure 5.3): The results for this pulsar confirm earlier observations at a similar frequency (McCulloch *et al.* 1978), namely that the profile has a relatively high degree of linear polarization ($\sim$50%) with a linear sweep of PA across the pulse and weak right circular polarization. Similar characteristics are found across a wide range of frequencies. The data are consistent with a classification as a conal single profile (Rankin 1990).

PSR B0736-40 (Figure 5.4): The linear polarization profile and PA variation of this pulsar indicate at least two, and possibly three distinct components, as has been suggested by earlier observations (McCulloch *et al.* 1978, Manchester *et al.* 1980). The 670 MHz profile has significant leading and central (main) linear polarization features. In the 800 MHz profile, the main component has a higher

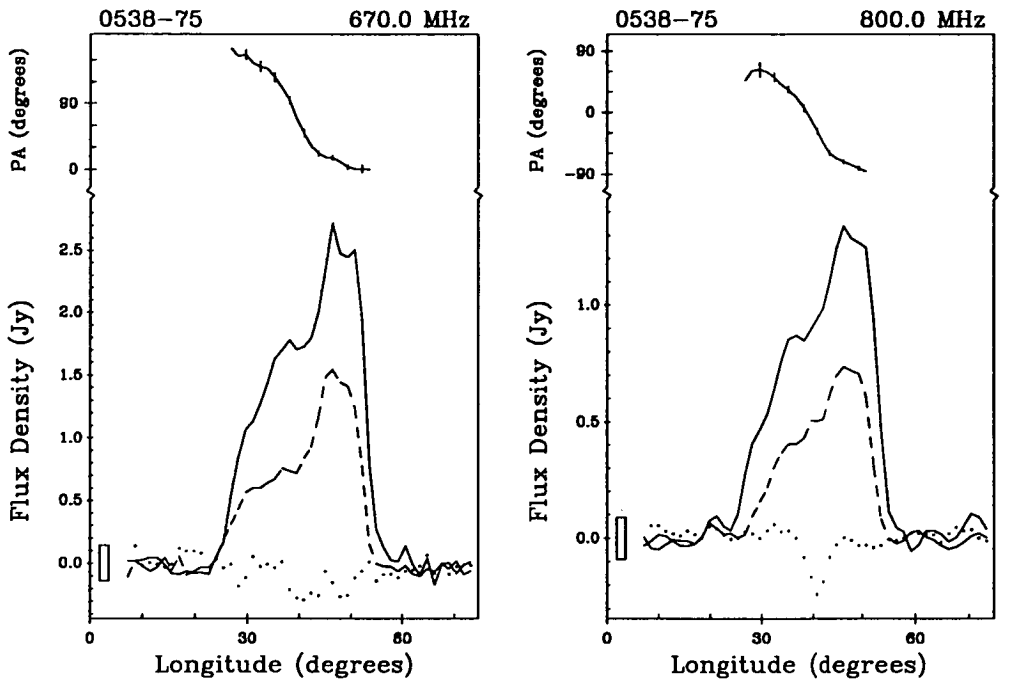

Figure 5.2: Integrated profiles for PSR B0538-75; the lower part of the figure shows the total intensity (solid line), linearly polarized intensity (dashed line) and circularly polarized intensity (dotted line), and the upper part of the figure shows the PA of the linearly polarized component. For the latter, the points are not plotted if the error bar spans more than 60 degrees.

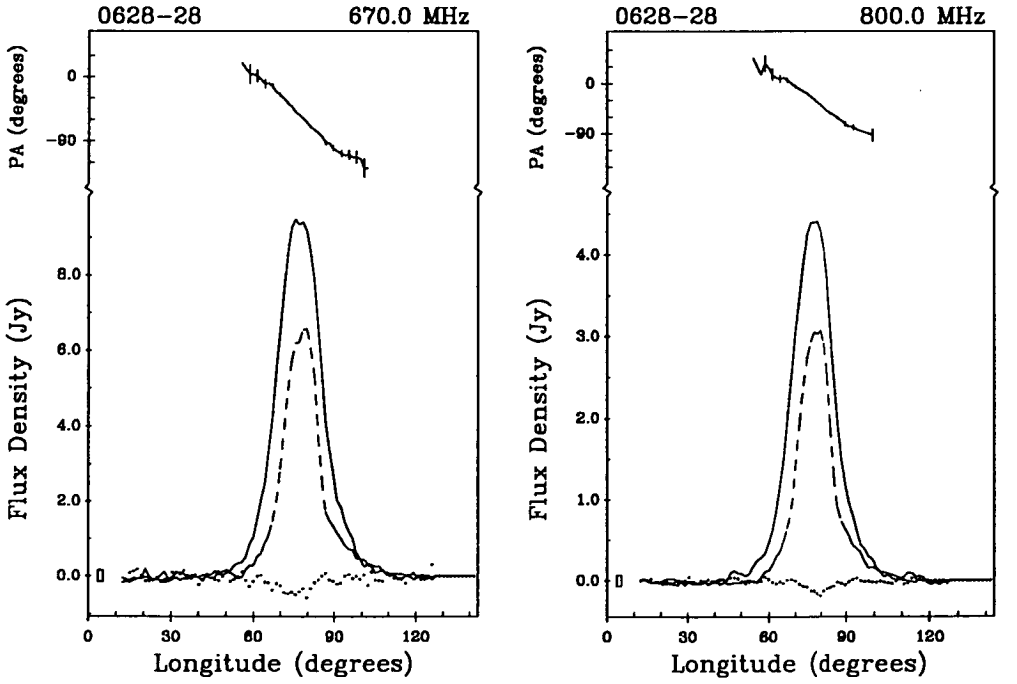

Figure 5.3: Integrated profiles for PSR B0628-28; see Figure 5.2 for the key.

degree of linear polarization with a linearly increasing PA ($\sim 0.5°$ per degree of pulse longitude). This observation is consistent with the trend toward higher observing frequencies for this pulsar (van Ommen 1992, Manchester *et al.* 1980), namely that the percentage linear polarization of the central component increases with frequency. There is a small amount of right circular polarization in the main component.

PSR B0740-28 (Figure 5.5): The polarization features of this pulsar are not unlike those observed from the Vela pulsar. The profile has a high degree of linear polarization ($\sim$80%) and a small amount of right circular polarization. There is a hint of a second component in the trailing edge of the profile. At 1612 MHz, the two components are easily resolved (Manchester *et al.* 1980).

PSR B0835-41 (Figure 5.6): This pulsar has a very narrow pulse (hence the coarse sampling across the pulse) with some linear polarization and relatively strong left circular polarization, in agreement with earlier results.

PSR B1240-64 (Figure 5.7): This pulsar has approximately equal percentages of linear and (left) circular polarization and a linear increase in PA with a gradient of $\sim 5°$ per degree of longitude. The 670 MHz results are in close agreement with those given by Costa (1989) for an observing frequency of 614 MHz. There is less circular polarization at 800 MHz. This is consistent with an interesting trend observed at higher frequencies. Observations at 950 MHz (van Ommen 1992) show a smaller degree of circular polarization and there is evidence of a change in the hand of circular polarization at the pulse centre. The circular polarization becomes entirely right-handed at 1612 MHz and is accompanied by an orthogonal mode flip of the PA at the centre of the pulse (Manchester *et al.* 1980).

PSR B1358-63 (Figure 5.8): This pulsar is the weakest source in the present sample of objects selected for polarization observations. Despite the relatively low signal-to-noise ratios and dispersion smearing due to the large bandwidths used, both profiles (particularly the 800 MHz profile) show that there is some linear polarization ($\sim$ 15%) and little or no circular polarization. The Parkes polarization observations of this pulsar at 660 MHz appeared in the literature only very recently (Qiao *et al.* 1995) and are very similar to the 670 MHz observations presented here. Also, Wu *et al.* (1993) have recorded a profile at 1560 MHz. The only other recorded observation is an unpublished profile at 955 MHz (van Ommen 1992). The profiles obtained by these workers are similar to those shown in Figure 5.8, with approximately 20% linear and negligible circular polarization. van Ommen (1992) has noted a weak precursor component in the profile. Analysis of individual integrations revealed that the profiles undergo mode changing on a time-scale of $\sim$100 periods (van Ommen 1992, Figures 4.47 & 4.48).

PSR B1426-66 (Figure 5.9): Limited time resolution makes it impossible to resolve the two components in the profile of this pulsar noted by other workers over a large range of observing frequencies. There is a small amount of linear polarization near

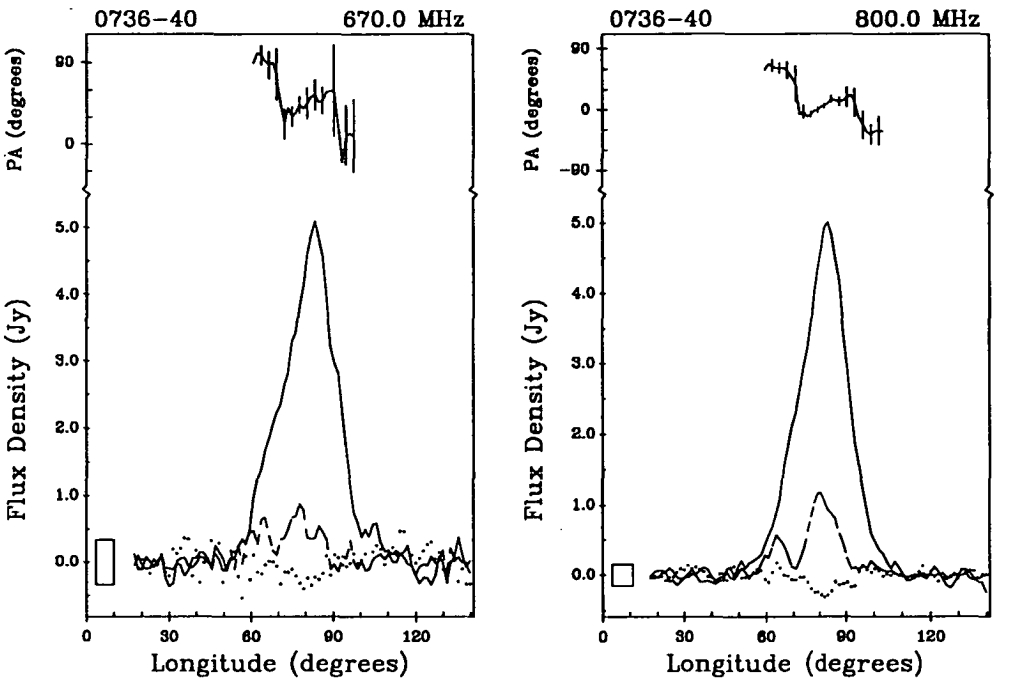

Figure 5.4: Integrated profiles for PSR B0736-40; see Figure 5.2 for the key.

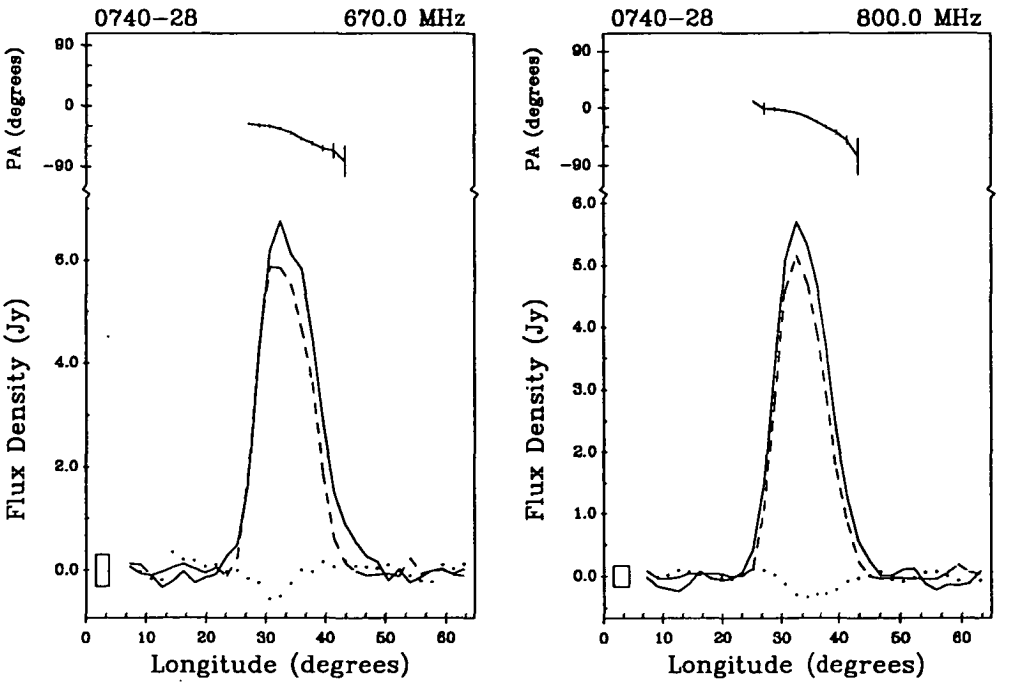

Figure 5.5: Integrated profiles for PSR B0740-28; see Figure 5.2 for the key.

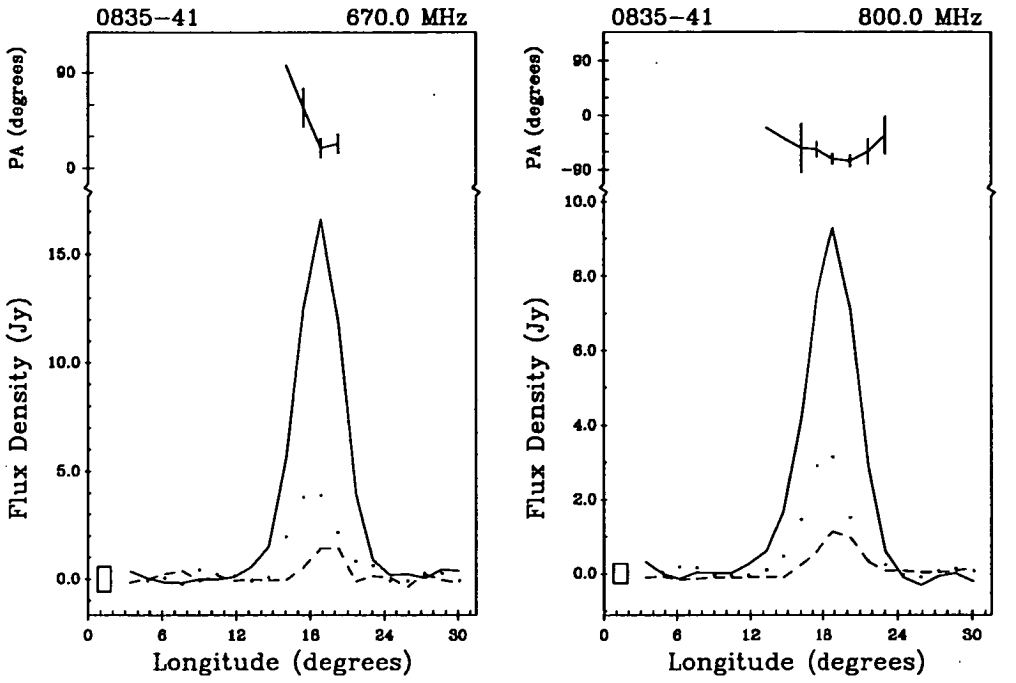

Figure 5.6: Integrated profiles for PSR B0835-41; see Figure 5.2 for the key.

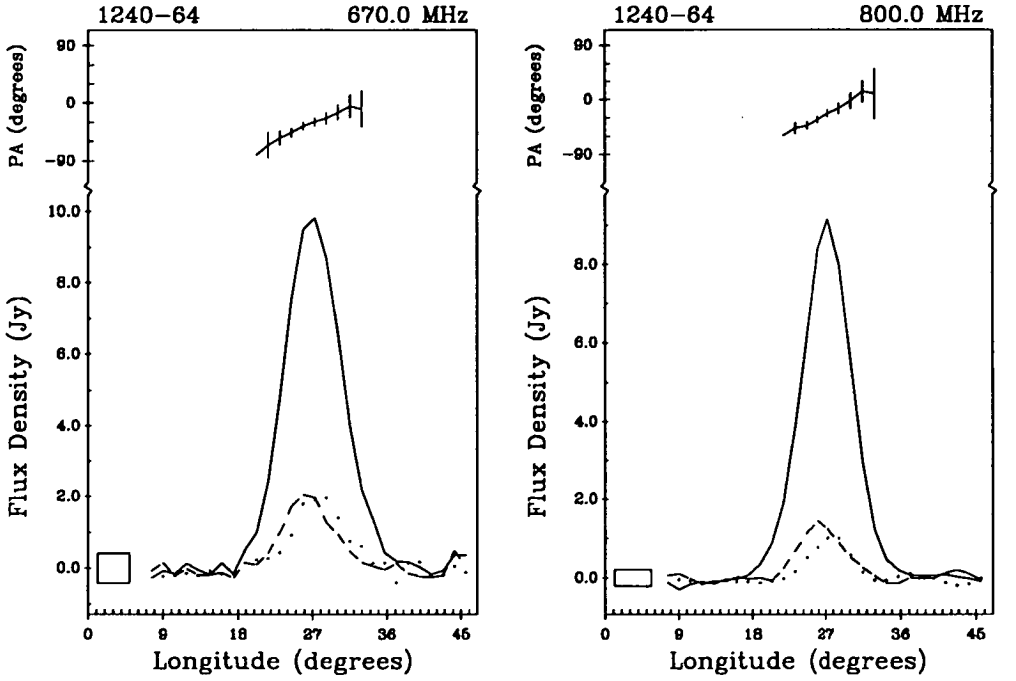

Figure 5.7: Integrated profiles for PSR B1240-64; see Figure 5.2 for the key.

the centre of the profile and little or no circular polarization. Both PA plots suggest there may be a 90° transition between the two components identified by the other workers.

PSR B1449-64 (Figure 5.10): This source has a single profile containing substantial linear polarization which peaks ahead of the peak of the total intensity profile with a corresponding uniform increase in PA. There is no significant difference between the polarization characteristics at 670 and 800 MHz. The results are consistent with previous observations near these frequencies (McCulloch *et al.* 1978, van Ommen 1992).

PSR B1451-68 (Figure 5.11): This pulsar has a complex profile with a strong central component and weaker outer components. At least three linear polarization features are evident as well as a reversal in the hand of circular polarization near the centre of the 800 MHz profile. A slowly varying PA within each feature and abrupt jumps between the features are also noticeable in the 800 MHz profile. It is not possible to identify these features in the 670 MHz PA plot because of the inferior signal-to-noise of the profile. The polarization characteristics of this pulsar have been studied in detail by van Ommen (1992). A single-pulse analysis revealed the presence of orthogonal emission modes across much of the profile. This is evident in the disorderly PA curve and the low polarization.

PSR B1556-44 (Figure 5.12): These profiles have a relatively high degree of linear polarization and some right circular polarization. Within the uncertainties, the 670 MHz results agree with those obtained by McCulloch *et al.* (1978). At 800 MHz, the degree of linear polarization is less, in accordance with the general trend toward higher frequencies for this pulsar (van Ommen 1992, Manchester *et al.* 1980). A weak component preceding the main component can be seen in the 800 MHz profile. This weak component becomes more prominent at higher observing frequencies (Manchester *et al.* 1980, Wu *et al.* 1993). In addition, the PA sweep in the 800 MHz plot indicates that orthogonal transitions occur on both sides of the main component. As Wu *et al.* (1993) have commented, when account is taken of these transitions, there is a classic S-shaped sweep in the PA.

PSR B1641-45 (Figure 5.13): The profile for this pulsar is affected by interstellar scattering, which may cause some smearing of the pulse polarization. This is supported by the fact that there is essentially no linear or circular polarization at 670 MHz. In the 800 MHz profile, there is a small amount of linear polarization in the first part of the pulse but this quickly falls away in the tail of the profile.

PSR B1706-16 (Figure 5.14): This pulsar has a narrow profile which contains some linear polarization ($10-15\%$) and little or no circular polarization. Similar results have been obtained at 950 MHz (van Ommen 1992). In contrast, McCulloch *et al.* (1978) found approximately 10% right circular polarization near the centre of the profile at 636 MHz. There is a decrease in the PA across the profile in both figures. However, in the 800 MHz profile the variation is not continuous. This is

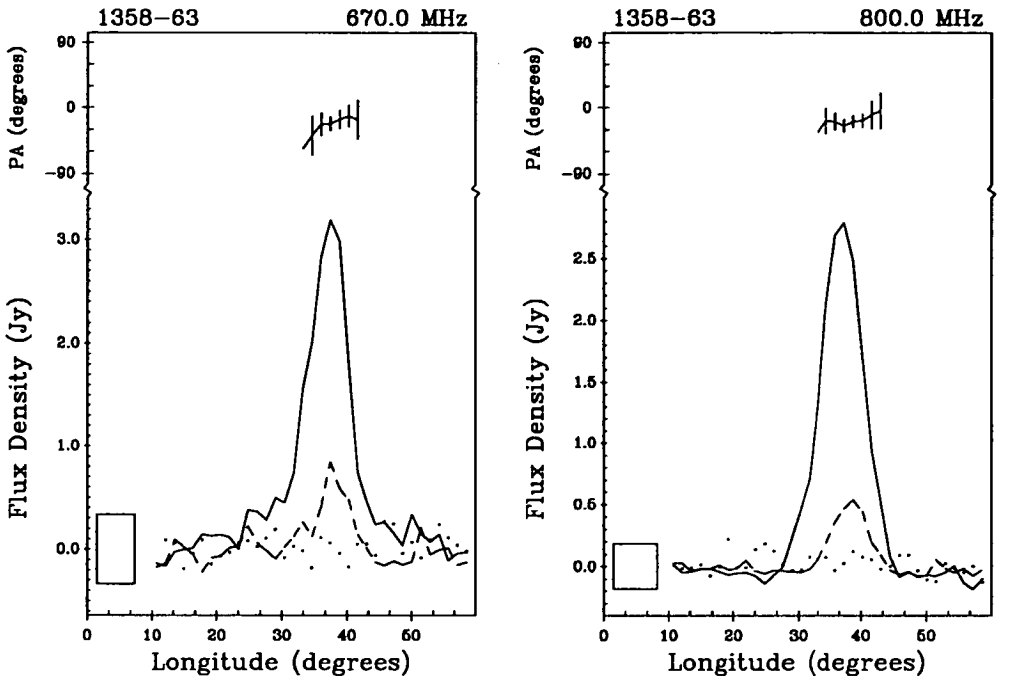

Figure 5.8: Integrated profiles for PSR B1358-63; see Figure 5.2 for the key.

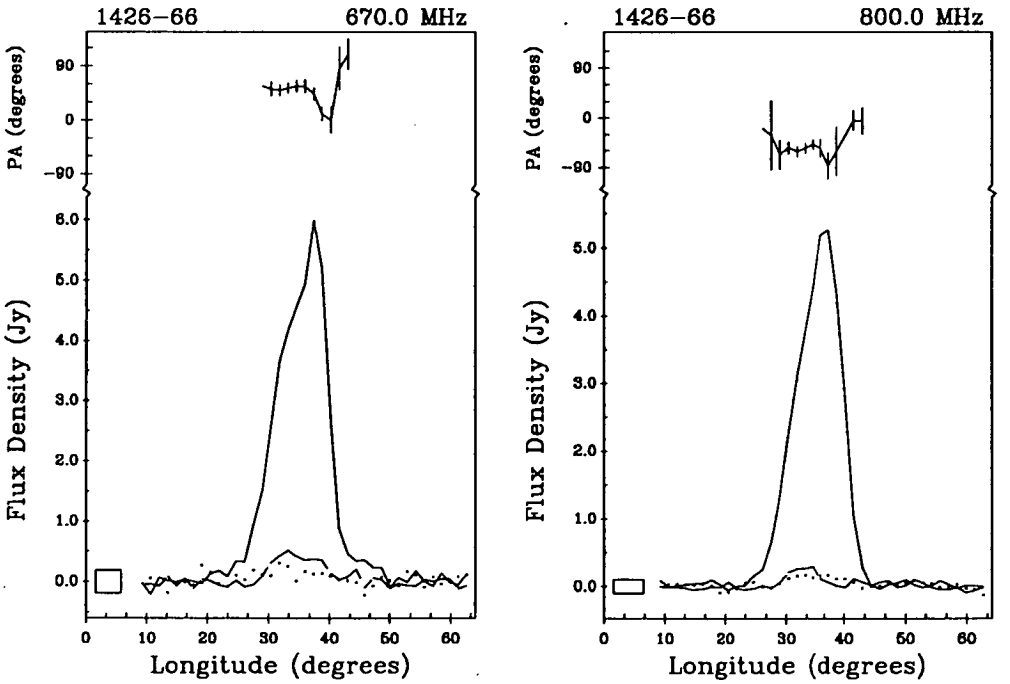

Figure 5.9: Integrated profiles for PSR B1426-66; see Figure 5.2 for the key.

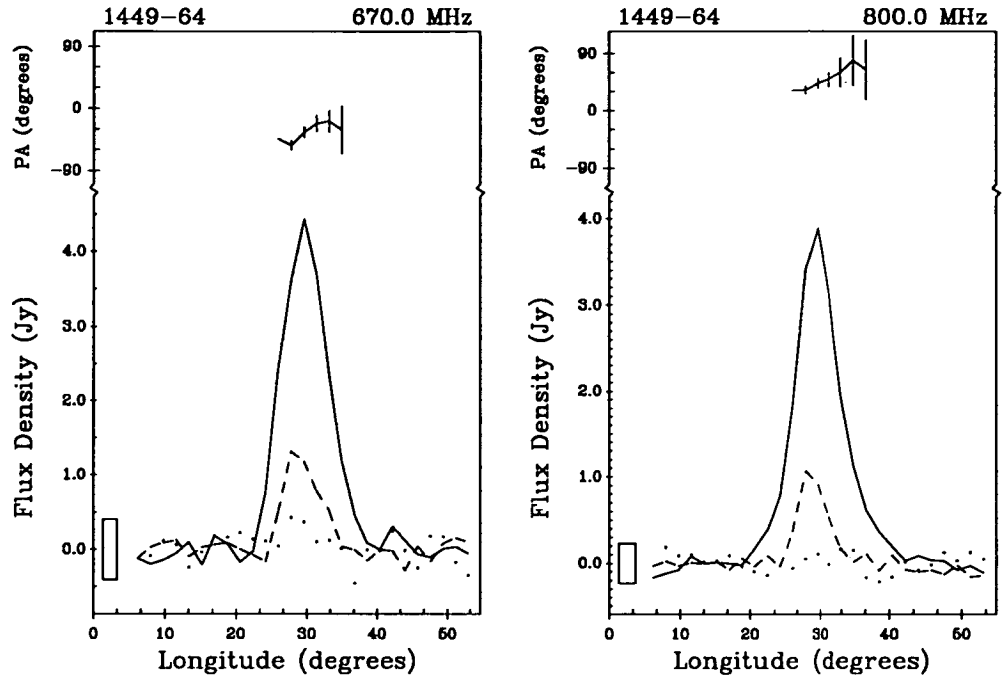

Figure 5.10: Integrated profiles for PSR B1449-64; see Figure 5.2 for the key.

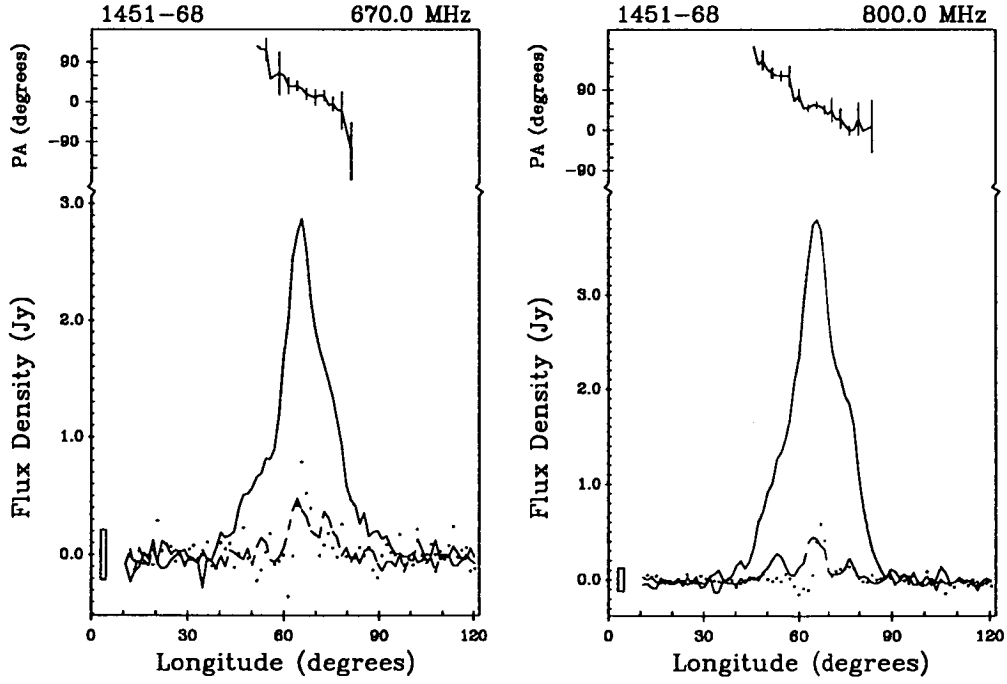

Figure 5.11: Integrated profiles for PSR B1451-68; see Figure 5.2 for the key.

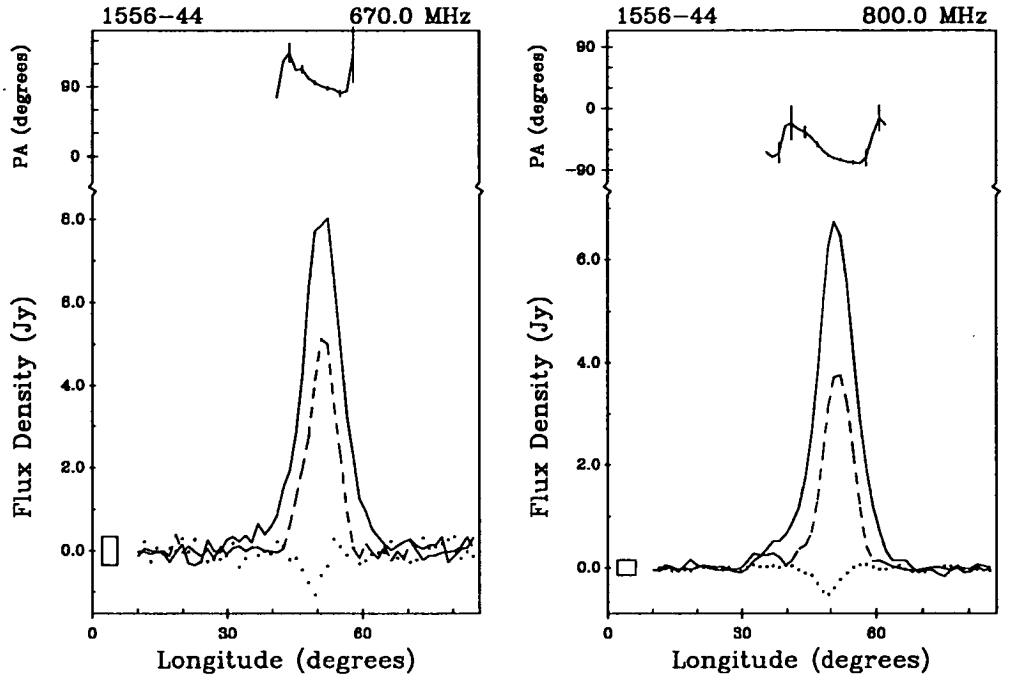

Figure 5.12: Integrated profiles for PSR B1556-44; see Figure 5.2 for the key.

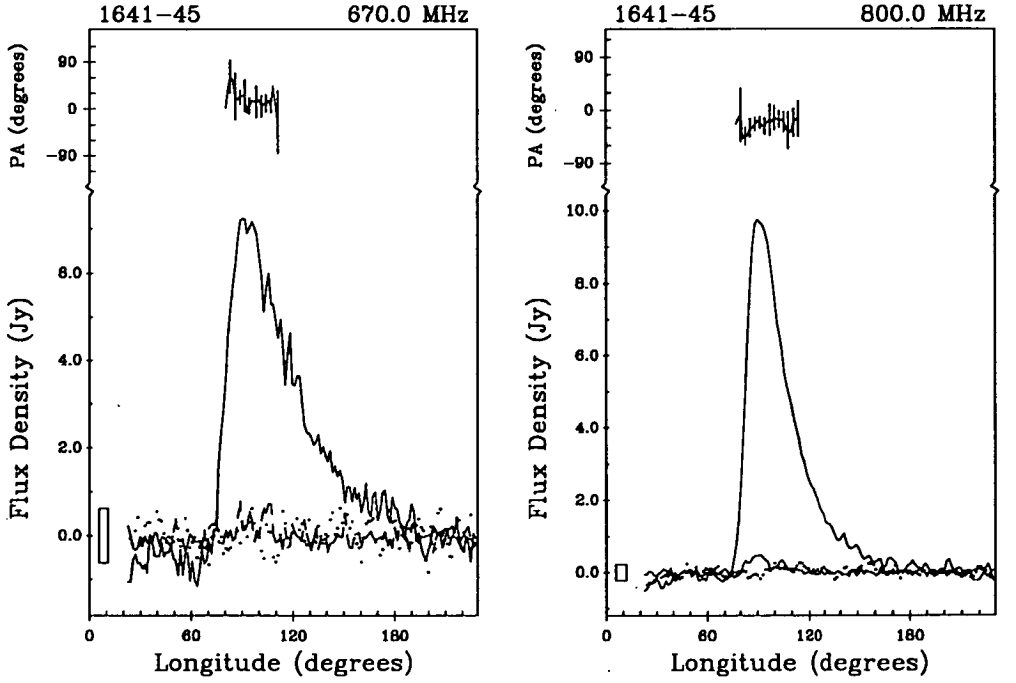

Figure 5.13: Integrated profiles for PSR B1641-45; see Figure 5.2 for the key.

possibly the result of a transition between orthogonal modes.

PSR B1727-47 (Figure 5.15): The profile of this pulsar consists of two overlapping components. The degree of linear polarization is similar for both observing frequencies ($\sim 15\%$). There is also a small but significant amount of left circular polarization (9% at 670 MHz and 6% at 800 MHz). The results are in general agreement with observations at other frequencies although the amount of circular polarization was not always found to be significant (e.g., McCulloch *et al.* 1978, Manchester *et al.* 1980).

PSR B1747-46 (Figure 5.16): The profiles for this pulsar are relatively noisy, but they show small and approximately equal amounts of linear and left circular polarization. The present results are in close agreement with previously published values (McCulloch *et al.* 1978).

PSR B1749-28 (Figure 5.17): The linear polarization characteristics, viz. $\sim 10\%$ linear polarization and a constant PA across the pulse, are similar to those previously published. However, the 631 MHz profile is reported to have about 7% right circular polarization (McCulloch *et al.* 1978) whereas the 670 MHz profile shows little circular polarization and the 800 MHz profile shows $\sim 4\%$ *left* circular polarization or possibly a change in the hand of the polarization near the centre of the pulse. These discrepancies are unexplained, although the latter could be due to spurious circular polarization.

PSR B1857-26 (Figure 5.18): This pulsar has a complex integrated profile with strong linear and circular polarization. An orthogonal transition in the PA coincides with an abrupt dip in the linear and circular polarization plots. The results are in excellent agreement with earlier work (McCulloch *et al.* 1978, Costa 1989, van Ommen 1992).

PSR B2045-16 (Figure 5.19): This pulsar has a well-known triple profile with a classic S-shaped PA swing. The present work confirms earlier results and reinforces the observation that the polarization characteristics of this pulsar are consistent over a wide range of frequencies.

5.4 Rotation Measures

The dual-frequency PA information was used to derive the rotation measure along the line of sight to each pulsar, as described in Section 5.2. The results are presented in Table 5.2. Following the modern convention, a positive RM corresponds to a (positive) longitudinal magnetic field which is directed *toward* the observer. The previously published or "catalogue" RMs (Taylor *et al.* 1993) are included for comparison. The quoted uncertainties are twice the standard errors from the analysis and refer to the last digit quoted. The catalogue uncertainties were taken to be 1σ errors unless otherwise stated in the original reference.

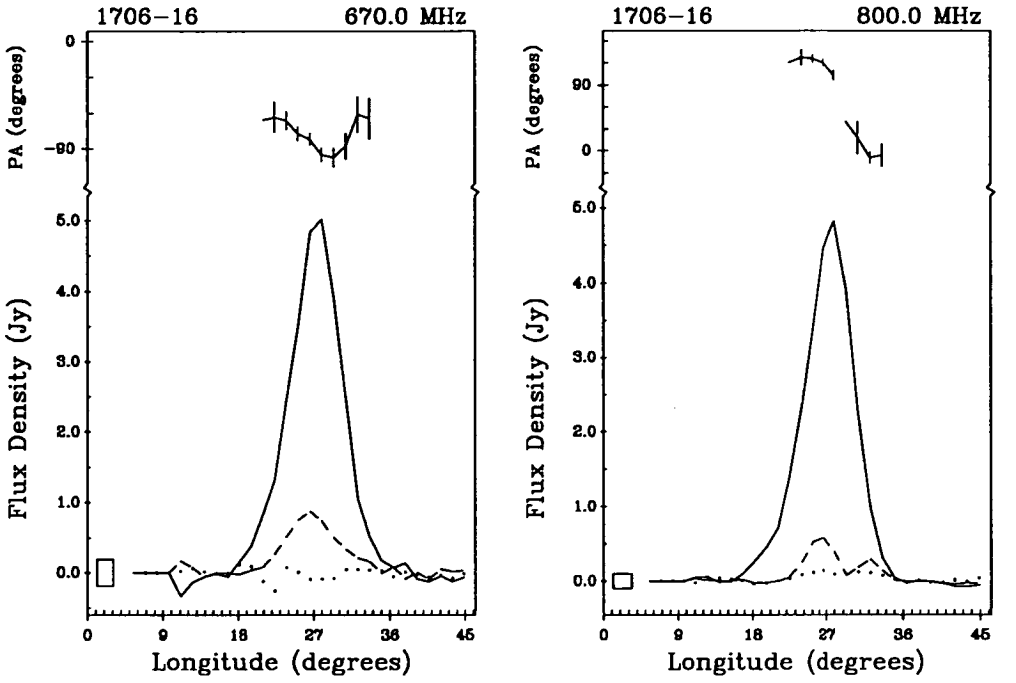

Figure 5.14: Integrated profiles for PSR B1706-16; see Figure 5.2 for the key.

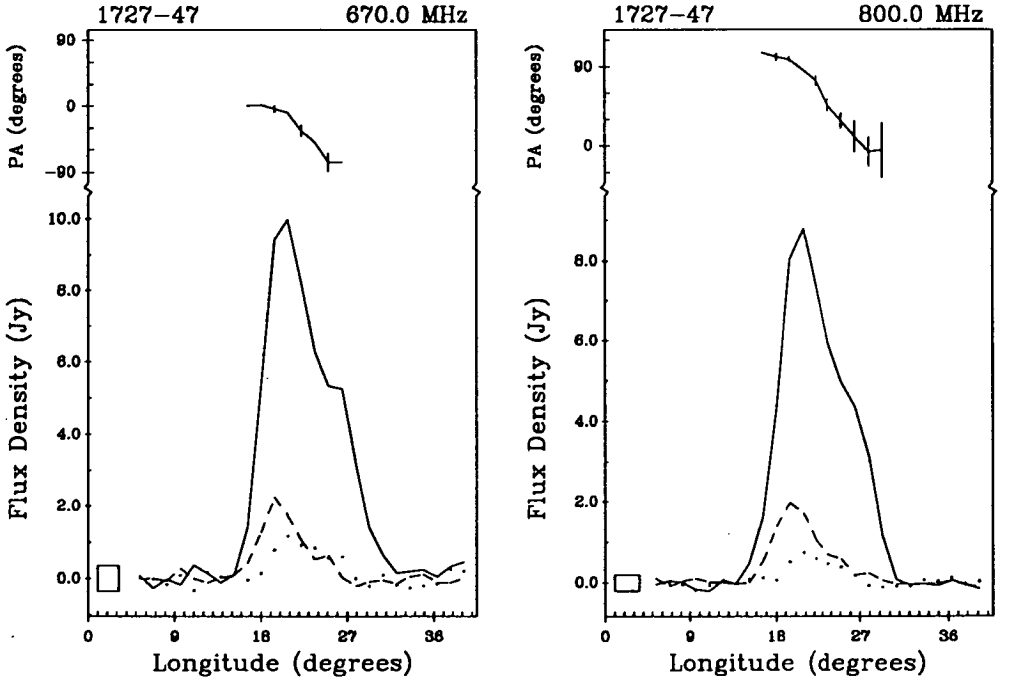

Figure 5.15: Integrated profiles for PSR B1727-47; see Figure 5.2 for the key.

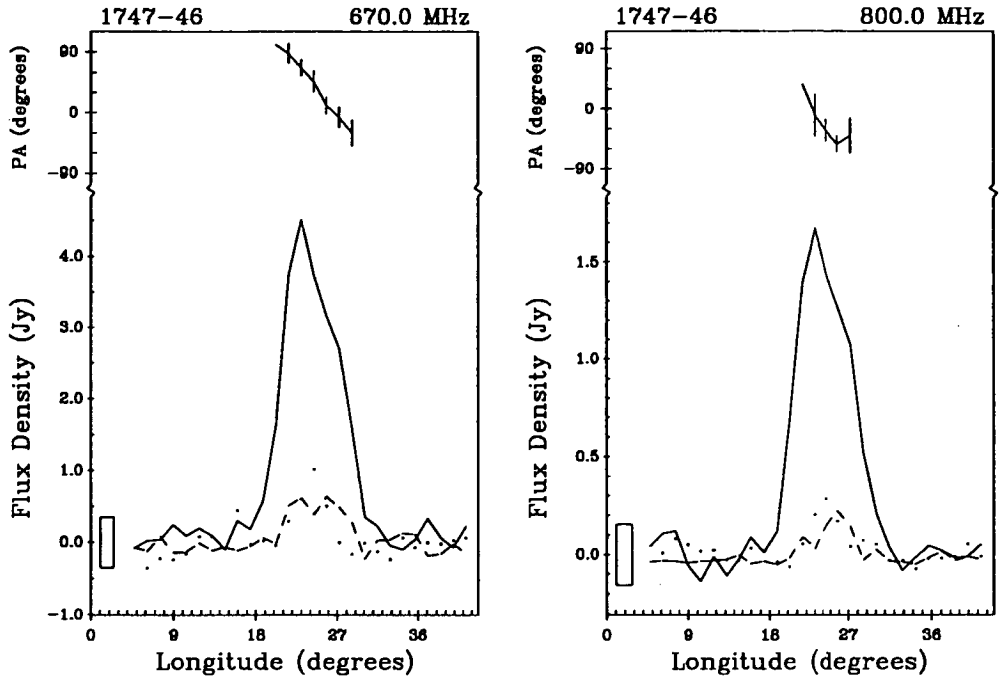

Figure 5.16: Integrated profiles for PSR B1747-46; see Figure 5.2 for the key.

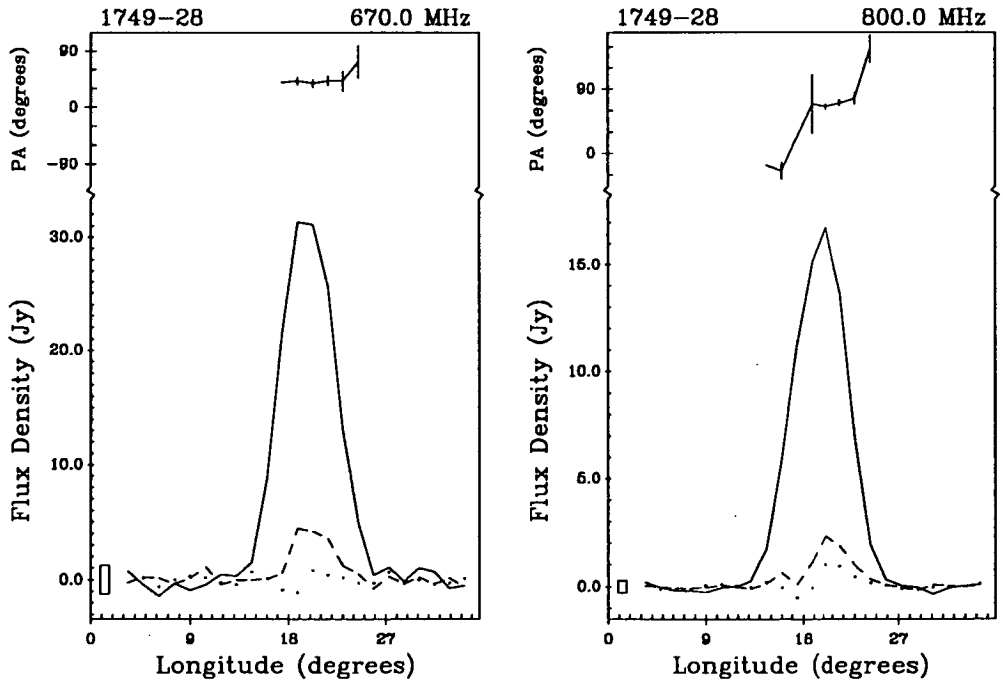

Figure 5.17: Integrated profiles for PSR B1749-28; see Figure 5.2 for the key.

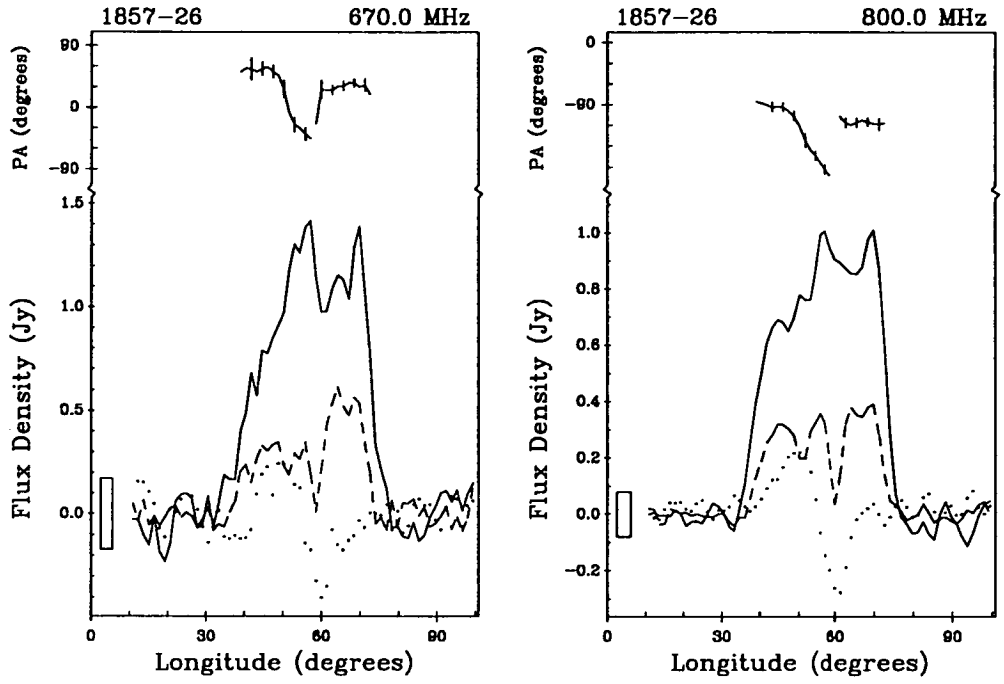

Figure 5.18: Integrated profiles for PSR B1857-26; see Figure 5.2 for the key.

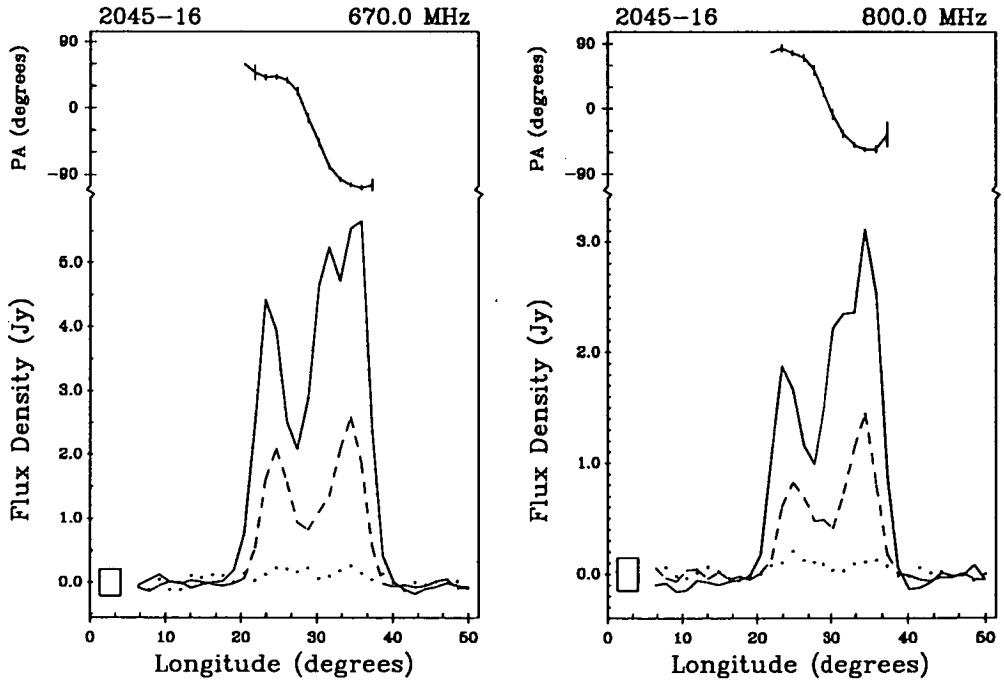

Figure 5.19: Integrated profiles for PSR B2045-16; see Figure 5.2 for the key.

Table 5.2: Rotation measures along the line of sight to 18 southern pulsars.

Pulsar PSR B	RM (rad m^{-2})	Err	Cat. RM (rad m^{-2})	Err	Ref.
0538−75	25	1	24	2	1
0628−28	46	1	46.2	2	2
0736−40	14	1	13.5	8	2
0740−28	150	1	150.4	1	2
0835−41	134	4	135.8	6	2
1240−64	157	2	157.8	8	2
1358−63	54	2	58	13	3
1426−66	−20	2	−12	6	2
1449−64	−23	2	−22	3	2
1451−68	−3	2	−2.0	6	2
1556−44	−5	1	−2.6	6	2
1641−45	−612	4	−611	8	2
1706−16	−3	2	−1.3	6	4
1727−47	−443	4	−429	1	2
1747−46	16	4	18	5	2
1749−28	97	2	96.0	4	2
1857−26	−9	1	−7	2	2
2045−16	−11	1	−10.0	1	2

Ref. 1. Costa (1991).
2. Hamilton *et al.* (1981), unpublished.
3. Van Ommen (1991), private communication.
4. Manchester (1974).

Most of the RMs in Table 5.2 agree with the catalogue values within the quoted uncertainties. However, the RMs for PSRs B1556-44 and B1727-47 appear to have changed since they were last measured. Furthermore, it was noted in Chapter 4 that the DM along the line of sight to both these pulsars has also changed (Table 4.2). The RM changes for these pulsars are significant at levels of 4σ and 6σ respectively (applying the same significance test as for the DM changes). There is possibly a RM change for PSR B1426-66 but it is only marginally significant and the estimate is based on a weakly linearly polarized profile.

Secular RM and DM changes have been noted for the Vela pulsar (Hamilton *et al.* 1977, Hamilton, Hall & Costa 1985) and the Crab pulsar (Rankin *et al.* 1988). For the Vela pulsar, the changes have been interpreted as the motion of a magnetised filament of the Vela supernova remnant out of the line of sight, or

alternatively, the motion of the pulsar behind the filament. From the observed RM changes, the electron density and longitudinal component of the magnetic field in the filament were estimated to be ~ 78 cm^{-3} and $\sim 22\mu$G (directed toward the pulsar) respectively. Using a similar analysis and assuming the RM and DM changes are related, i.e., due to the relative movement of a single region into or out of the line of sight, the implication is that a magnetised region of excess electron density has moved out of the path to PSR B1556-44, in which the electron density is ~ 290 cm^{-3} and the longitudinal magnetic field strength is ~ 2 μG directed away from the pulsar. For PSR B1727-47, the implication is that a similar region has moved into the line of sight, in which the electron density is ~ 170 cm^{-3} and the longitudinal magnetic field strength is ~ 16 μG directed toward the pulsar. Magnetic field irregularities in the ISM of the order of 5–15 μG are not unrealistic (Thomson & Nelson 1980, Rand & Lyne 1994).

The absence of associated supernova remnants for most pulsars[1] necessitates an explanation in terms of a dense, magnetised HII region or irregularities within a larger region with similar features. Studies of the Galactic magnetic field have shown that small-scale irregularities are common in most directions, with strengths of ~ 5 μG. Hence, these could account for the observed RM changes. For PSR B1727-47, the RM change may be due to an irregularity within the HII region of I Scorpius located at a distance of 1.3 kpc. Arguments based on statistical fluctuations, similar to those discussed in Chapter 4, can also be used to explain the RM changes for both pulsars, because their DM-derived distances are > 1 kpc. However, the latter method of analysis is complicated by the fact that the net longitudinal component of the magnetic field arising from the statistical fluctuation of irregularities along the path must favour a particular direction.

RM changes for other pulsars have not, in general, been discussed in the literature. In one exception, Manchester (1974) noted a 1 rad m^{-2} (or 1.5%) change in the RM of PSR B0329+54 over a two-year period, with no corresponding measurable change in the DM. This was attributed to the rotation or translation of one or more dense HI clouds along the line of sight which contain frozen-in magnetic fields.

Costa (1989) has obtained RMs for a sample of 26 pulsars, eight of which were "test" pulsars with previously determined RMs. The RMs for two of the test pulsars (PSRs B1055-52 and B1929+10) do not agree within the quoted uncertainties, even when the quoted uncertainties in both Costa's and the previously published results are taken to be the most conservative value of 1σ. Hamilton & Lyne (1987) have measured Faraday rotation toward 163 pulsars. They found only three pulsars that have RMs which differ from the previously published values by 2σ or more. Hence, all of the results produced to date show that RM changes are not common but may be detectable if the RMs are monitored over a sufficiently

[1]Only a dozen or so are known – see Taylor *et al.* (1993).

long time interval. These measurements can provide additional information about the interstellar medium along the line of sight to the pulsars under observation.

5.5 Discussion and Summary

This chapter has presented integrated profiles with full polarization characteristics for 18 southern pulsars at observing frequencies near 670 MHz and 800 MHz. Polarimetry of two sources, PSRs B0538-75 and B1358-63, has only recently been conducted at several frequencies. In general, the measured polarization properties of the sample of 18 pulsars are similar to those found in previous surveys, with some minor differences. However, small differences in the fractional polarization are often observed in integrated profiles recorded at different times, presumably because of short-term variations in the pulse shape, energy and polarization. The mean linear, absolute circular and net circular polarization for the 18 pulsars at 670 MHz was found to be $\sim$25%, $\sim$10% and $\sim$3% respectively. At 800 MHz the mean values are $\sim$24%, $\sim$8% and $\sim$3% respectively.

Also, the results are generally consistent with the rotating vector model for pulsar polarization (Radhakrishnan & Cooke 1969) in the sense that the variation in position angle across the profile of most of the pulsars was found to be either linear or the classic S-shape characteristic of Type C pulsars.

Rotation measures have been derived from the polarization measurements for the 18 pulsars studied. More accurate RMs were obtained for half of these pulsars. Until very recently, there was no published RM for PSR B1358-63. The RM obtained from the present work is 54 ± 2 rad m^{-2}, in agreement with the unpublished value, 58 ± 13 rad m^{-2}, obtained by van Ommen (1991). Qiao *et al.* (1995) recently obtained a value of 62 ± 4 rad m^{-2}. These authors do not state whether the quoted error is a 1σ or 2σ value. Assuming the former, the RM estimates from both studies are in agreement within the uncertainties.

Occasional monitoring of RMs can provide valuable information about magnetic fields in the interstellar medium along the line of sight to pulsars. For 16 out of the 18 pulsars, the RMs obtained in the present work are the first such measurements for well over 10 years. For PSRs B1556-44 and B1727-47, the RM has changed significantly over the last 20 years. Together with corresponding changes in their DMs, one interpretation of the results for these pulsars is that a dense, magnetised electron cloud has moved into or out of the line of sight to the pulsar. The electron density was estimated to be $\sim$200 cm^{-3} and the longitudinal magnetic field was found to be as large as 16 μG. These values are consistent with estimates of irregularities in these parameters for the interstellar medium.

Together with previously published data, the pulsar fluxes obtained as part of the polarization measurements presented in this chapter can be used to derive

a mean figure for the radio spectrum of flux in this pulsar sample. Typically, the radio spectra of pulsar fluxes are steep but flatten or even turn over at lower frequencies (Lyne & Smith 1990). It is common practice to quote a spectral index, α, where $S \propto f^{\alpha}$ and S is the mean pulsar flux in mJy, and f is the radio frequency in MHz. The mean flux for the sample of 18 pulsars presented in this chapter was computed for frequencies of 410 MHz (taken from Hamilton *et al.* 1977, or Taylor *et al.* 1993 if the former did not observe a given pulsar), 640 MHz (taken from McCulloch *et al.* 1978 and Costa *et al.* 1991), 670 and 800 MHz from the present work, 950 MHz (from the unpublished observations of van Ommen 1992), 1400 MHz (taken from Taylor *et al.* 1993) and 1612 MHz (taken from Manchester *et al.* 1981).

A plot of $\log(S)$ against $\log(f)$ reveals a spectrum that is relatively flat from 400 to 640 MHz, and steep from 640 to 1612 MHz. A linear least squares fit over the latter frequency range resulted in a mean spectral index of $\alpha = -2.2 \pm 2$ (2σ error). This value is not significantly higher than the mean spectral index found for much larger samples of pulsars (Manchester & Taylor 1981, Lorimer *et al.* 1995), typically -1.6. The subset of 6 pulsars from the present work that overlaps with the sample of 280 pulsars observed by Lorimer *et al.* (1995) has a mean spectral index of -2.0. One could argue that the fluxes used to obtain the result from the present work are not reliable because they are not long-term averages, i.e., they may vary due to slow refractive scintillations. However, the time-scale for refractive scintillation is inversely proportional to observing frequency (Rickett *et al.* 1984) and so flux measurements made at observing frequencies < 600 MHz are the most likely to be affected in this way. The fluxes measured at these frequencies have not been used in the calculation, as described above. Furthermore, most of the observations in polarization surveys tend to be biased toward times of stronger emission and so intensity scintillations may not have significantly affected the final result. Alternatively, taking a mean value across the whole sample tends to cancel the effect of any variations if they are uncorrelated.

As a final point, the results presented in this chapter have demonstrated that, despite the limitations of the observing system, e.g., modest time resolution and sensitivity), useful information can still be obtained from such a polarization survey. In particular, the 800 MHz polarimetry has provided an extra "data point" in the frequency range 400 - 1600 MHz, adding to the existing data base of polarization information for a selection of southern pulsars.

Chapter 6

The Timing Noise of 45 Southern Pulsars

6.1 Introduction

After allowing for the deterministic pulsar spin-down ("pulsar braking") and any glitches, pulse arrival-time measurements display irregularities in the rotation rate of pulsars, commonly known as "timing noise". As shown in Chapter 4, these irregularities exceed the uncertainties attributable to the measurement process, namely additive noise and pulse jitter.

As outlined in the review in Chapter 2, most timing activity may be a manifestation of the response of the neutron star to a "noisy" component of the torque acting on the crust. This noisy torque could arise from variations involving the moment of inertia or the magnetosphere of the neutron star. While the timing residuals of some pulsars may be consistent with such a simple random process, others appear to be manifestations of some other cause, e.g., a small number of resolved jumps in ν and $\dot{\nu}$, or quasi-periodic oscillations. The mechanism for the microjumps may be similar to the one that is responsible for a random walk process, e.g., these resolved events may be part of a broad distribution of jump amplitudes. On the other hand, oscillations can arise for totally different reasons. For example, free precession of the neutron star, internal superfluid oscillations, the recovery from a glitch, or planetary systems could be responsible for the quasi-periodic variations that may be apparent in the residuals of some pulsars.

This chapter presents a detailed description of the observed timing activity in each object. The timing residuals are analysed to examine possible evidence of random walk processes and discrete events, as well as quasi-periodic oscillations. The results are used to categorise the timing behaviour of the pulsars in the Mt Pleasant sample. These results, together with the results of the power spectral analyses described in Chapter 8, should provide valuable information regarding

the scope and nature of the underlying mechanism(s) responsible for timing noise in pulsars.

Some of the results that appear in this chapter have already been published (D'Alessandro *et al.* 1995). However, many of the results have been improved or revised because the time span of the data set has increased by an additional 1.5 years since that paper was written.

6.2 Random walk processes

Boynton *et al.* (1972) were the first to suggest that rotational irregularities might arise from a simple random walk process comprising small step functions in one of three observables – the pulse phase, ϕ ("phase noise", PN), frequency, ν ("frequency noise", FN) or frequency derivative, $\dot{\nu}$ ("slowing down noise", SN). The Crab pulsar timing noise was found to be consistent with a random walk in the pulse frequency (Boynton *et al.* 1972, Groth 1975b). A similar analysis by Cordes & Helfand (1980) showed that the timing noise of a number of other pulsars could also be described by a simple random walk process.

This section presents the results of two different methods of analysis, involving the use of strength parameters and structure functions. These methods are ideal for studying random walk processes, as shown below.

6.2.1 Definitions and Terminology

Random Walk Processes

A random walk in the kth derivative of the phase (ϕ) is defined as (Groth 1975a)

$$\frac{d^k\phi(t)}{dt^k} = \sum_j a_j H(t - t_j) \tag{6.1}$$

where a_j is the amplitude of the j-th step occurring at a time t_j and H is a unit step function. The amplitudes are assumed to be random with zero mean. The random walks for $k = 0, 1, 2$ correspond to PN, FN, SN respectively. A simulation of each of these random walk processes is shown in Figure 6.1.

By definition, a random walk in the k-th derivative of the phase is equivalent to a process where the $(k+1)$-th derivative of the phase has stationary statistics with a white noise power spectrum (Groth 1975a). Hence, the phases arising from a random walk in the time derivatives of the pulse phase have nonstationary properties.

A number of authors (e.g., see Groth 1975b, Cordes 1980, Cordes & Greenstein 1981 and Cordes & Downs 1985) have discussed the effect of the choice of the time origin used to describe the random walk. This is important if one is attempting

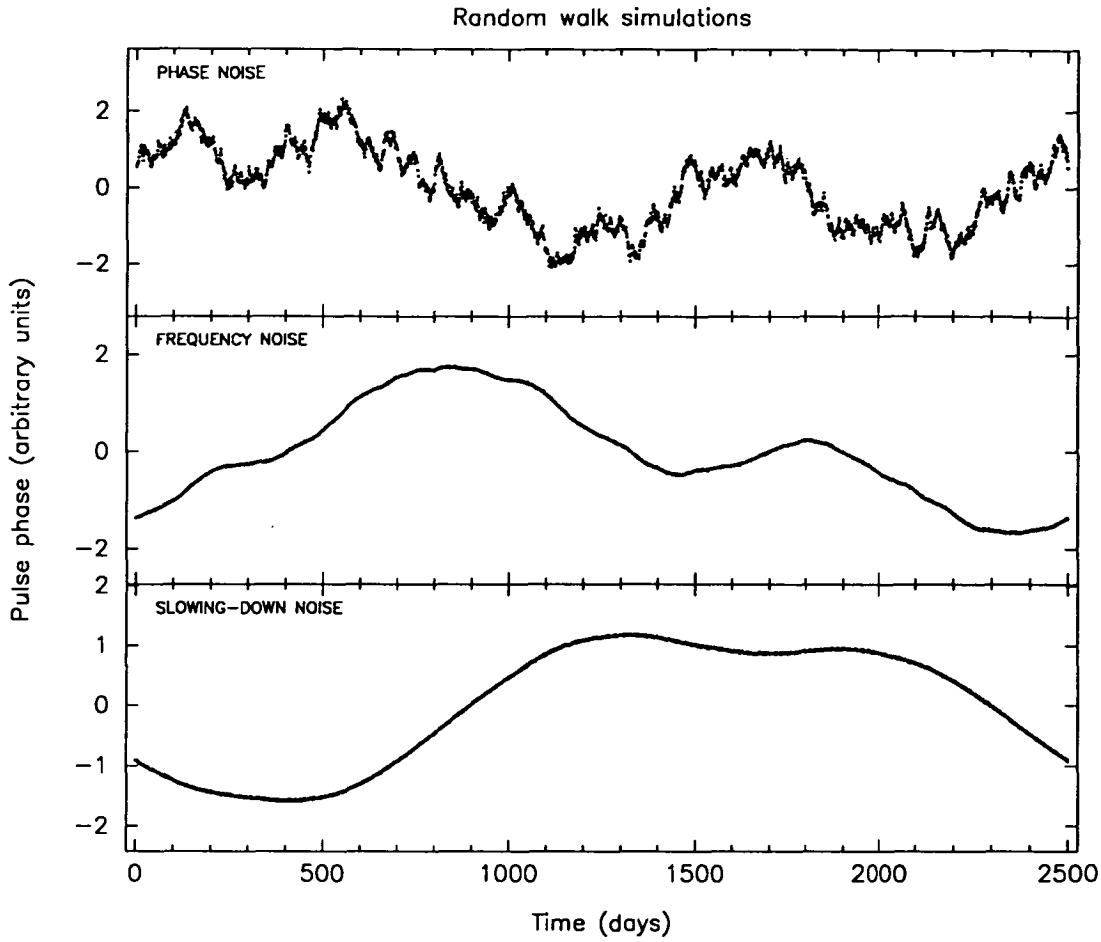

Figure 6.1: Phase plots for one realisation of each kind of random walk process described in the text (PN, FN, SN). These were generated from the same set of Gaussian distributed zero mean steps at an average rate of 1 step per day over a time span of 2500 days. No polynomial subtraction has been performed.

to show that the time series of pulse arrival phases is consistent with a particular noise process. They conclude that it is satisfactory to take an arbitrary time, t_o, as the effective time origin as long as a second-order (or higher) polynomial is fitted to the phases (for $k \leq 2$) before obtaining the residuals. Such polynomial fitting is always done as part of the standard analysis procedure (see Chapter 4).

Strength Parameters

The random walk processes described above can be characterised by their second moments. To see whether such processes are responsible for the observed timing fluctuations, the estimated variance of the pulsar timing residuals is compared with the variance expected for a random walk. The timing noise variance is estimated as

$$\sigma_{TN}^2 = \sigma_R^2 - \sigma_W^2 \tag{6.2}$$

where $\sigma_R^2 = \sigma_R^2(m,T)$ is the mean-square residual from an m-th order polynomial fit over a data span T and

$$\sigma_W^2 = \sigma_M^2 + \sigma_J^2 \tag{6.3}$$

is the mean-square white noise contribution from the measurement uncertainty and pulse jitter, as described in Chapter 4.

The random walks have second moments that are characterised by the *strength parameters*, S_k, where

$$S_0 = R<(\Delta\phi)^2>, \;\; S_1 = R<(\Delta\nu)^2>, \;\; S_2 = R<(\Delta\dot{\nu})^2>, \tag{6.4}$$

(Cordes & Greenstein 1981). The $<>$ denote an ensemble average, and $\Delta\phi$, $\Delta\nu$, $\Delta\dot{\nu}$ are the small steps in the rotation variables which occur with an average rate R. The strength parameters can be estimated from the rms residual, $\sigma_{TN}(m,T)$, after performing a least squares polynomial fit of order m over a data span T. Following Cordes (1980),

$$S_k = C_{k,m}^2 \left[\frac{\sigma_{TN}^2(m,T)}{<\sigma_{RW}^2(T)>_u} \right] S_u \tag{6.5}$$

where $C_{k,m}$ is a correction factor that compensates for the fraction of the timing noise variance absorbed by the polynomial fit, and $<\sigma_{RW}^2(T)>_u$ is the ensemble average second moment for a random walk of unit strength ($S_u = 1$). In practice, ensemble average quantities are not available. Instead, average estimates of the moments such as

$$<\sigma_{RW}^2(T)>_u = \frac{1}{T}\int_0^T dt\,\phi_{RW}^2(t) \tag{6.6}$$

can be made (Cordes & Greenstein 1981), or for unevenly sampled data,

$$<\sigma_{RW}^2(T)>_u = \frac{1}{N}\sum_{j=1}^{N} <\phi_{RW}^2(t_j)>, \quad 0 \le t_1 \le t_N \le T \tag{6.7}$$

where $<\phi_{RW}^2(t_j)>$ is given by

$$S_0 t_j, \;\; \frac{1}{3}S_1 t_j^3, \;\; \frac{1}{20}S_2 t_j^5, \tag{6.8}$$

for PN, FN, SN respectively (Groth 1975a, Cordes 1980) and assuming that the random walks are zero mean processes with unit strengths given by Equation 6.4 with units of s^{-1}, $Hz^2 s^{-1}$, $Hz^2 s^{-3}$ respectively. In the ideal case of uniform sampling, Equation 6.5 becomes

$$S_0 = 2\, C_{0,m}^2\, \sigma_{TN}^2(m,T)\, T^{-1}, \tag{6.9}$$

$$S_1 = 12\, C_{1,m}^2\, \sigma_{TN}^2(m,T)\, T^{-3}, \tag{6.10}$$

$$S_2 = 120\, C_{2,m}^2\, \sigma_{TN}^2(m,T)\, T^{-5} \tag{6.11}$$

for PN, FN and SN respectively. The magnitude of the correction factor increases with the order of the random walk because an m-th order polynomial absorbs a larger fraction of the SN variance than the FN or PN variance. The correction factors also depend on the order of the polynomial used to fit the data. Using random walk simulations, Cordes (1980) found these factors to be: $C_{0,2} \simeq 3.7$, $C_{1,2} \simeq 15.5$, $C_{2,2} \simeq 23.7$, and $C_{0,3} \simeq 4.1$, $C_{1,3} \simeq 27.3$, $C_{2,3} \simeq 71.1$.

Consistency of one of the noise processes with the pulsar data is indicated if S_k is found to be independent of T and if the constraint $RT > 1$ is satisfied (Cordes & Downs 1985). Consistency with one of the noise processes can be measured by using the statistic

$$F = \frac{S(T_{\rm max})}{S(T_{\rm min})} \tag{6.12}$$

where $T_{\rm max}$ and $T_{\rm min}$ are the maximum and minimum time spans from which the strength parameter estimates can be obtained. If the data are consistent with a pure random walk process, $F \approx 1$, otherwise F will be a strong function of $T_{\rm max}/T_{\rm min}$.

Following Cordes & Downs (1985), if $S(T_{\rm max})$ and $S(T_{\rm min})$ are statistically independent (derived from non-overlapping data spans) and have a Gaussian distribution, then $\log F$ will also have a Gaussian distribution with a standard deviation

$$\sigma_{\log F} = \sigma_{\log S}(1 + \frac{1}{N_{\rm min}})^{\frac{1}{2}} \tag{6.13}$$

where $N_{\rm min}$ is the number of independent strength estimates used to estimate $S(T_{\rm min})$. It can be argued that $S(T_{\rm max})$ and $S(T_{\rm min})$ are essentially independent if $T_{\rm min} \ll T_{\rm max}$ since the random walk structure probed by each estimate is very different.

Structure Functions

Structure functions are used to estimate the variance in a time series by means of a "differencing scheme". They provide a useful approach to the analysis of pulsar timing residuals where one is interested in examining the range of time-scales that contribute to the fluctuations. It is also possible to determine whether the fluctuations are significantly different from the activity due to a random walk process.

The m-th order structure function of the phase is defined as

$$D_{\phi}^{(m)}(t,\tau) \equiv < [\Delta_{\phi}^{(m)}(t,\tau)]^2 > \tag{6.14}$$

where

$$\Delta_{\phi}^{(m)}(t,\tau) \equiv \sum_{i=0}^{m} (-1)^i \binom{m}{i} \phi[t + (m-i)\tau] \tag{6.15}$$

is termed the m-th increment of the phase (following Rutman 1978, Lindsay & Chie 1976), τ is the time-scale probed by the differencing scheme and t is the epoch of an individual phase measurement. The relevant features of these functions have been given by Cordes & Downs (1985). An idealised, large rate, random walk process of order k has stationary $(k+1)$-th increments and hence the $(k+1)$th-order structure function is independent of time and has a unique power-law relationship with τ. For PN, $D_\phi^{(1)} \propto \tau$, giving a logarithmic slope (henceforth termed the "structure function slope") of 1. Similarly, for FN, $D_\phi^{(2)} \propto \tau^3$, and for SN, $D_\phi^{(3)} \propto \tau^5$, giving slopes of 3 and 5 respectively.

6.2.2 Analyses and Results

Before any analyses were performed, the dual-frequency phase residual data for each pulsar were combined into a single data set. Combined data points were obtained by taking a weighted mean of the coincident points in the 650 and 800 MHz data sets, i.e.,

$$\delta\phi_c = \left(\frac{\delta\phi_{650}}{\sigma_{650}^2} + \frac{\delta\phi_{800}}{\sigma_{800}^2}\right)\left(\frac{1}{\sigma_{650}^2} + \frac{1}{\sigma_{800}^2}\right)^{-1} \tag{6.16}$$

where $\delta\phi_c$ is the value of the combined residual phase for a particular point, and $\delta\phi_{650}$, σ_{650} and $\delta\phi_{800}$, σ_{800} represent the residual phase and its uncertainty for the 650 and 800 MHz observations respectively. The uncertainty in each of the 650 and 800 MHz data points was taken to be the white noise estimate given in Chapter 4. The uncertainty in the combined data was obtained by using

$$\sigma_c = \left(\frac{1}{\sigma_{650}^2} + \frac{1}{\sigma_{800}^2}\right)^{-\frac{1}{2}} \tag{6.17}$$

For the relatively few epochs where data were recorded at only one of the observing frequencies, the residual phase and its uncertainty (for that frequency) were simply copied across to the new combined data array. Most of the analyses described from this point onwards involve weighted computations, e.g., weighted least squares fits, hence allowing for the uncertainties in the combined data points.

Combination of the two data sets has two main advantages: (i) it improves the sensitivity of the data to be analysed and, hence, the results, (ii) it simplifies the interpretation of the results. It could be argued that one loses the ability to probe the effects of frequency-dependent factors, such as small dispersion measure variations and refractive delays. These propagation effects can produce phase fluctuations that could be misinterpreted as intrinsic timing noise. However, they are generally negligible at medium to high observing frequencies, and their magnitude is very small in comparison to the measurement uncertainties in the data (Foster & Cordes 1989, 1990; also see Chapter 4).

Table 6.1 shows some basic parameters obtained from the combined data for each pulsar in the Mt Pleasant sample. The columns show the pulsar name and rotation period, and then the number of data points (N), data span ($T_{\rm max}$), measurement uncertainty (σ_M), rms white noise (σ_W), rms timing noise (σ_{TN}) and the "signal-to-noise ratio" of the timing noise, arbitrarily defined as the ratio σ_R/σ_W. The timing activity observed in 19 of these pulsars is relatively weak. For these pulsars (noted in Table 6.1), the rms timing noise is typically $\leq$ 2 milliperiods and the signal-to-noise ratio is typically ≤ 2, producing results from strength parameter and structure function analyses in the "noise regime". In the following sections, the discussion will be based around the 26 pulsars displaying higher levels of timing noise.

As discussed in Chapter 4, small and large jumps were identified in the rotation rate of five of these pulsars. The analyses and results presented in this chapter do not include the glitches in PSRs B1727-47 and B1737-30. Allowance was made for these glitches in the arrival-time analysis which produces the phase residuals. Small jumps were also noted in the timing data of PSRs B0740-28, B1240-64, B1641-45 and B1737-30. Analyses have been performed on the phase residuals obtained from timing model fits made both with and without allowance for these small jumps. Plots of the phase residuals for both cases are shown in Appendix C.

Strength Parameter Analysis

Strength parameters and their ratios were estimated from the pulsar phase residuals for each of the three random walk processes, in the manner described in Section 6.2.1. The estimates were made from blocks of data over octave time spans, i.e., $T_n = T_{\rm max}2^{-n}$ $(n = 0, 1, 2, ...)$ with $N_n = 2^n$ such blocks for each octave in T. In most cases, $T_{\rm max} \simeq 2500$ days and $T_{\rm min} = 200 - 300$ days. Because of the restriction imposed by $T_{\rm min}$, the maximum value of n was 3, which corresponds to $N_{\rm min} = 8$ data blocks. Second order polynomial fits were used to obtain the rms timing noise for the strength parameter computations, complemented by third order fits for those pulsars whose phase residuals displayed an intrinsic cubic term and were not consistent with any of the random walk processes.

As a check on the method of analysis for the real data, strength parameter tests were performed on 500 simulated realisations of random walks of order $k = 0, 1, 2$. Figure 6.2 shows histograms of $\log(S_{\rm est}/S)$ for each type of random walk process, where $S_{\rm est}$ and S correspond to the estimated and "true" strength parameters respectively. The histograms follow roughly Gaussian distributions with standard deviations $\sigma_{\log S_{\rm est}} \approx 0.21$, 0.40, and 0.50 for k = 0,1,2 random walks respectively. These results were independent of the signal-to-noise ratio of the random walk, sampling rates and sampling patterns.

Table 6.1: Basic observational parameters and noise estimates for 45 pulsars.

Pulsar PSR B	Period (s)	N	T_{max} (days)	σ_M (mP)	σ_W (mP)	σ_{TN} (mP)	S/N
0403-76[a]	0.5452	210	2461	0.71	1.99	1.86	1
0538-75[a]	1.2458	92	2536	0.50	0.94	0.94	1
0628-28	1.2444	83	2511	0.41	0.82	2.24	3
0736-40	0.3749	92	2549	0.38	0.48	30.96	64
0740-28	0.1667	112	2538	0.21	0.59	6.76	11
0740-28[b]	0.1667	112	2538	0.21	0.59	24.89	42
0808-47[a]	0.5471	76	2512	1.02	2.05	1.35	1
0835-41	0.7516	84	2486	0.12	0.25	1.96	8
0839-53[a]	0.7206	87	2458	0.93	2.62	1.74	1
0905-51[a]	0.2535	88	2511	0.97	2.53	3.31	2
0923-58	0.7395	92	2537	1.27	2.31	23.77	10
0932-52[a]	1.4447	83	2510	0.67	0.92	0.60	1
0940-55	0.6643	85	2537	0.56	1.19	95.04	80
0959-54	1.4365	88	2536	0.21	0.37	56.35	151
1054-62	0.4224	80	2537	0.80	0.97	4.78	5
1056-57[a]	1.1849	77	2489	0.67	1.04	1.11	1
1154-62[a]	0.4005	82	2537	0.96	1.15	2.42	2
1221-63	0.2164	80	2549	0.69	1.29	3.85	3
1240-64	0.3884	98	2513	0.14	0.20	0.37	2
1240-64[b]	0.3884	98	2513	0.14	0.20	4.48	23
1323-58	0.4779	105	2515	0.84	1.74	35.97	21
1323-62	0.5299	77	2537	0.56	1.26	31.59	25
1358-63	0.8427	81	1531	0.40	0.67	31.56	47
1426-66	0.7854	79	2516	0.17	0.40	3.61	9
1449-64	0.1794	83	2537	0.27	0.56	6.81	12
1451-68[a]	0.2633	88	2549	0.22	0.87	1.49	2
1530-53[a]	1.3688	82	2537	0.27	0.53	0.49	1
1556-44	0.2570	76	2536	0.21	0.31	2.25	7
1558-50	0.8642	85	2549	0.50	0.71	133.64	189
1600-49	0.3274	72	2516	0.74	1.43	6.73	5
1641-45	0.4550	91	2549	0.28	0.44	30.45	69
1641-45[b]	0.4550	91	2549	0.28	0.44	29.19	66
1648-42	0.8440	95	2217	1.42	3.75	13.63	4
1700-32[a]	1.2117	100	2524	0.59	0.92	0.69	1
1706-16	0.6530	60	2170	0.23	0.49	22.69	47
1718-32[a]	0.4771	84	2218	0.74	1.10	1.70	2
1727-47	0.8297	146	2515	0.18	0.30	3.38	11
1737-30	0.6066	154	1448	0.99	2.29	136.57	60
1737-30[b]	0.6066	154	1448	0.99	2.29	37.29	16
1737-39	0.5122	76	2548	0.69	0.86	9.54	11
1742-30	0.3674	68	2217	0.37	0.52	6.98	13
1747-46[a]	0.7423	75	2510	0.28	0.65	0.81	2
1749-28	0.5625	83	2548	0.09	0.38	12.78	34
1857-26[a]	0.6122	76	2541	0.63	0.71	0.90	2
1937-26[a]	0.4028	96	2393	0.68	1.67	0.50	1
2045-16[a]	1.9615	78	2541	0.16	0.32	0.63	2
2048-72[a]	0.3413	146	2487	0.56	2.88	2.23	1
2321-61[a]	2.3474	150	2458	0.45	0.82	0.75	1
2327-20[a]	1.6436	82	2522	0.32	0.65	0.92	2

[a] Indicates a pulsar that presently exhibits timing activity which is too weak for a meaningful analysis.

[b] Results obtained when periods jumps are not removed from the arrival-time data.

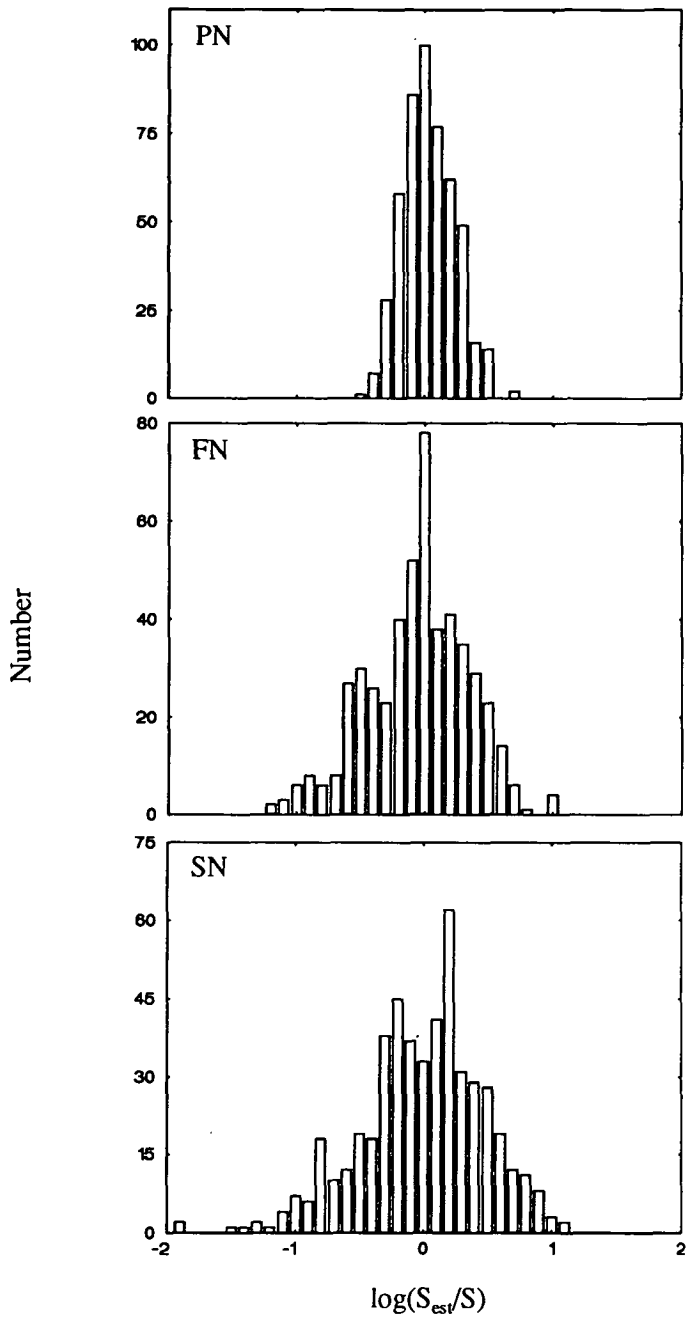

Figure 6.2: Histograms showing the distribution of strength parameter estimates obtained from 500 realisations of type $k = 0,1,2$ random walk processes (corresponding to PN, FN, SN). The simulated data were generated using the same S/N ratio of the timing irregularities and sampling pattern for PSR B0959-54.

Strength Parameter Results and Discussion

The results of the strength parameter analysis for all 45 pulsars are shown in Table 6.2. The first entry for each pulsar corresponds to estimates obtained from the maximum ($T_{\rm max}$) and minimum ($T_{\rm min}$) time spans in the data. The second entry corresponds to estimates obtained from independent time spans, $T_{\rm max}/2$ from one half of the data set, and $T_{\rm min}$ from the other half. Hence, both estimates can be considered statistically independent – the first because $T_{\rm min} \ll T_{\rm max}$, and the second because of the independent time spans used to obtain the estimates.

In Table 6.2, column (4) lists the number of blocks ($N_{\rm min}$, each spanning $T_{\rm min}$ days) used to estimate $S(T_{\rm min})$. The standard deviation in $\log[S(T_{\rm min})]$ given in column (5) was determined from the set of $N_{\rm min}$ strength parameter estimates. Columns (6), (8) and (10) list the strength parameter ratios, F, for phase, frequency and slowing down noise respectively. Columns (7), (9) and (11) give the probabilities of obtaining values of F less than the estimated values. These probabilities can be calculated in two ways: (i) assuming an F-distribution with 1 and $N_{\rm min}$ degrees of freedom, and (ii) using the error function with a standard deviation given by Equation 6.13. The probabilities given in Table 6.2 were obtained using the latter method. A probability close to 0.5 suggests the random walk under investigation is consistent with the data.

The results suggest that idealised random walk processes do not account for all of the observed timing activity. After second order fits, the phase residuals from 8 pulsars, namely PSRs B0628-28, B0835-41, B1054-62, B1221-63, B1426-66, B1556-44, B1600-49 and B1727-47 are consistent with a random walk in ϕ (PN). PSR B1449-64 shows consistency with PN only after third order fits. The results for 5 pulsars, namely PSRs B0736-40, B0940-55, B1323-58, B1323-62 and B1358-63 are consistent with a random walk in ν (FN). PSR B1240-64 shows consistency with FN if previously identified discrete events are not removed from data. After third order fits, PSR B1706-16 also shows consistency with FN. None of the results show consistency with a random walk in $\dot{\nu}$ (SN).

In some cases, the phase residuals after third order fits show little or no timing noise, i.e., they essentially display "white noise" characteristics. However, as noted earlier, the amplitude of the implied frequency second derivative ($\ddot{\nu}$) in each case is much too large to be attributed to pulsar braking.

Excluding the 19 pulsars with a low level of timing noise, the results for the remaining 10 pulsars are inconsistent with all three pure random walk processes. The observed activity for these objects may be due to a mixture of random walk processes (see Cordes & Greenstein 1981) or, alternatively, to microjumps in the rotation frequency or frequency derivative. PSRs B0740-28, B1240-64, B1641-45 and B1737-30 are typical examples of the latter possibility. The jumps in these pulsars account for a significant proportion of the observed timing noise.

Table 6.2: Results of the strength parameter analysis for all 45 pulsars from second order polynomial fits, supplemented by third order fits in some cases.

Pulsar PSR B	T_{max} (days)	T_{min} (days)	N_{min}	σ_{logS}	Strength parameter ratios and probabilities					
					F_{PN}	P_{PN}	F_{FN}	P_{FN}	F_{SN}	P_{SN}
(1)	(2)	(3)	(4)	(5)	(6)	(7)	(8)	(9)	(10)	(11)
0403-76	2461	307	7	0.65	0.12	0.089	0.002	$< 10^{-4}$	$< 10^{-4}$	$< 10^{-4}$
	1230	307	4		0.08	0.067	0.004	0.0004	0.0002	$< 10^{-4}$
0538-75	2536	317	8	0.46	0.03	0.001	$< 10^{-3}$	$< 10^{-4}$	$< 10^{-4}$	$< 10^{-4}$
	1268	317	4		0.44	0.246	0.023	0.0007	0.0013	$< 10^{-4}$
0628-28	2512	314	8	0.80	0.78	0.450	0.011	0.0099	0.0002	$< 10^{-4}$
	1256	314	4		0.25	0.251	0.014	0.0193	0.0008	0.0003
0628-28[a]	2512	314	8	1.03	0.09	0.174	0.001	0.0042	$< 10^{-4}$	$< 10^{-4}$
	1256	314	4		0.10	0.198	0.006	0.0269	0.0003	0.0013
0736-40	2549	318	8	0.65	117.16	0.999	1.549	0.6085	0.0215	0.0078
	1274	318	4		3.44	0.770	0.210	0.1753	0.0132	0.0048
0736-40[a]	2549	318	8	0.65	1.93	0.660	0.026	0.0108	0.0004	$< 10^{-4}$
	1274	318	4		0.30	0.235	0.016	0.0071	0.0010	$< 10^{-4}$
0740-28	2539	317	8	0.11	0.19	$< 10^{-3}$	0.003	$< 10^{-4}$	$< 10^{-4}$	$< 10^{-4}$
	1269	317	4		0.30	$< 10^{-3}$	0.014	$< 10^{-4}$	0.0007	$< 10^{-4}$
0740-28[b]	2539	317	8	0.16	2.27	0.980	0.030	$< 10^{-4}$	0.0004	$< 10^{-4}$
	1269	317	4		4.36	1.000	0.267	0.0008	0.0181	$< 10^{-4}$
0808-47	2513	314	8	0.52	0.09	0.028	0.001	$< 10^{-4}$	$< 10^{-4}$	$< 10^{-4}$
	1256	314	4		0.16	0.087	0.009	0.0002	0.0005	$< 10^{-4}$
0835-41	2486	310	8	0.39	2.70	0.852	0.040	0.0004	0.0006	$< 10^{-4}$
	1243	310	4		1.13	0.550	0.063	0.0028	0.0037	$< 10^{-4}$
0835-41[a]	2486	310	8	0.30	0.88	0.433	0.013	$< 10^{-4}$	0.0002	$< 10^{-4}$
	1243	310	4		0.82	0.395	0.043	$< 10^{-4}$	0.0024	$< 10^{-4}$
0839-53	2458	307	7	0.25	0.07	$< 10^{-3}$	0.001	$< 10^{-4}$	$< 10^{-4}$	$< 10^{-4}$
	1229	307	4		0.41	0.078	0.019	$< 10^{-4}$	0.0011	$< 10^{-4}$
0905-51	2512	314	8	0.88	0.06	0.095	0.001	0.0004	$< 10^{-4}$	$< 10^{-4}$
	1256	314	4		1.12	0.521	0.062	0.1097	0.0038	0.0070
0923-58	2538	317	7	0.55	4.32	0.859	0.069	0.0247	0.0011	$< 10^{-4}$
	1269	317	3		0.10	0.061	0.008	0.0005	0.0005	$< 10^{-4}$
0923-58[a]	2538	317	7	0.84	0.13	0.164	0.002	0.0016	$< 10^{-4}$	$< 10^{-4}$
	1269	317	3		0.06	0.111	0.005	0.0090	0.0003	0.0002
0932-52	2511	313	8	0.67	0.03	0.018	0.001	$< 10^{-4}$	$< 10^{-4}$	$< 10^{-4}$
	1255	313	4		0.19	0.167	0.010	0.0040	0.0006	$< 10^{-4}$
0940-55	2538	317	8	0.68	186.88	0.999	2.553	0.7128	0.0369	0.0241
	1269	317	4		38.12	0.981	2.313	0.6832	0.1470	0.1380
0959-54	2537	317	8	0.45	805.37	1.000	11.643	0.9866	0.1751	0.0581
	1268	317	4		76.57	1.000	4.485	0.9004	0.2766	0.1358
0959-54[a]	2537	317	8	0.57	165.70	1.000	2.406	0.7347	0.0371	0.0093
	1268	317	4		10.01	0.941	0.636	0.3798	0.0422	0.0160
1054-62	2538	317	8	0.98	1.10	0.516	0.016	0.0423	0.0003	0.0003
	1269	317	4		0.11	0.191	0.006	0.0220	0.0004	0.0009
1056-57	2490	311	7	0.28	0.09	$< 10^{-3}$	0.001	$< 10^{-4}$	$< 10^{-4}$	$< 10^{-4}$
	1245	311	4		0.90	0.442	0.046	$< 10^{-4}$	0.0027	$< 10^{-4}$
1154-62	2538	317	8	0.42	0.23	0.078	0.004	$< 10^{-4}$	0.0001	$< 10^{-4}$
	1269	317	4		0.12	0.026	0.008	$< 10^{-4}$	0.0005	$< 10^{-4}$
1221-63	2550	318	8	0.54	1.35	0.591	0.023	0.0021	0.0003	$< 10^{-4}$
	1275	318	4		0.79	0.431	0.051	0.0160	0.0035	$< 10^{-4}$
1221-63[a]	2550	318	6	0.30	0.26	0.035	0.005	$< 10^{-4}$	0.0001	$< 10^{-4}$
	1275	318	4		0.54	0.207	0.034	$< 10^{-4}$	0.0023	$< 10^{-4}$
1240-64	2514	314	7	0.50	0.25	0.132	0.003	$< 10^{-4}$	$< 10^{-4}$	$< 10^{-4}$
	1257	314	4		1.55	0.634	0.084	0.0269	0.0047	$< 10^{-4}$
1240-64[b]	2514	314	7	0.59	26.89	0.989	0.319	0.2142	0.0042	0.0001
	1257	314	4		13.00	0.956	0.735	0.4192	0.0411	0.0171
1323-58	2516	314	7	1.06	12.96	0.838	0.241	0.2921	0.0041	0.0173
	1258	314	4		23.16	0.876	1.264	0.5344	0.0816	0.1783
1323-62	2538	317	8	0.43	24.08	0.999	0.384	0.1795	0.0060	$< 10^{-4}$
	1269	317	4		10.64	0.984	0.676	0.3610	0.0415	0.0019
1358-63	1532	191	8	0.64	310.85	1.000	3.667	0.7953	0.0449	0.0244
	766	191	4		17.55	0.958	1.167	0.5370	0.0659	0.0507
1426-66	2517	314	7	0.67	3.41	0.772	0.048	0.0325	0.0007	$< 10^{-4}$
	1258	314	4		0.74	0.430	0.043	0.0339	0.0026	0.0003
1449-64	2538	317	8	0.35	10.53	0.997	0.132	0.0090	0.0018	$< 10^{-4}$
	1269	317	4		1.33	0.623	0.068	0.0014	0.0038	$< 10^{-4}$

Results of strength parameter analysis, continued ...

Table 6.2: continued.

Pulsar PSR B (1)	T_{max} (days) (2)	T_{min} (days) (3)	N_{min} (4)	σ_{logS} (5)	Strength parameter ratios and probabilities F_{PN} (6)	P_{PN} (7)	F_{FN} (8)	P_{FN} (9)	F_{SN} (10)	P_{SN} (11)
1449-64[a]	2538	317	6	0.73	0.44	0.324	0.005	0.0018	0.0001	$< 10^{-4}$
	1269	317	4		1.19	0.536	0.062	0.0691	0.0035	0.0013
1451-68	2550	318	8	0.68	0.12	0.098	0.002	0.0001	$< 10^{-4}$	$< 10^{-4}$
	1275	318	4		0.04	0.030	0.002	0.0003	0.0001	$< 10^{-4}$
1530-53	2538	317	8	0.60	0.12	0.077	0.002	$< 10^{-4}$	$< 10^{-4}$	$< 10^{-4}$
	1269	317	4		0.35	0.247	0.020	0.0059	0.0013	$< 10^{-4}$
1556-44	2537	317	8	0.81	1.18	0.534	0.018	0.0211	0.0003	$< 10^{-4}$
	1268	317	4		0.14	0.174	0.009	0.0112	0.0006	0.0002
1556-44[a]	2537	317	8	0.64	0.40	0.277	0.006	0.0005	0.0001	$< 10^{-4}$
	1268	317	4		3.45	0.774	0.213	0.1738	0.0137	0.0045
1558-50	2550	318	8	0.43	388.77	1.000	5.189	0.9427	0.0747	0.0065
	1275	318	4		2.24	0.768	0.122	0.0279	0.0072	$< 10^{-4}$
1600-49	2517	314	8	0.28	2.79	0.934	0.040	$< 10^{-4}$	0.0006	$< 10^{-4}$
	1258	314	4		2.23	0.868	0.125	0.0019	0.0074	$< 10^{-4}$
1641-45	2550	318	8	1.17	47.45	0.912	0.646	0.4391	0.0092	0.0498
	1275	318	4		3.60	0.665	0.205	0.2985	0.0122	0.0711
1641-45[b]	2550	318	8	1.18	43.35	0.905	0.588	0.4267	0.0083	0.0481
	1275	318	4		3.45	0.659	0.195	0.2953	0.0116	0.0711
1648-42	2218	277	6	0.36	2.30	0.824	0.042	0.0002	0.0007	$< 10^{-4}$
	1109	277	4		0.09	0.005	0.004	$< 10^{-4}$	0.0003	$< 10^{-4}$
1648-42[a]	2218	277	6	0.30	0.18	0.012	0.003	$< 10^{-4}$	0.0001	$< 10^{-4}$
	1109	277	4		0.07	$< 10^{-3}$	0.003	$< 10^{-4}$	0.0002	$< 10^{-4}$
1700-32	2524	315	8	0.92	0.05	0.093	0.001	0.0008	$< 10^{-4}$	$< 10^{-4}$
	1262	315	4		0.27	0.287	0.014	0.0354	0.0009	0.0014
1706-16	2170	271	6	0.35	289.38	1.000	3.579	0.9294	0.0482	0.0002
	1085	271	2		95.77	1.000	5.060	0.9505	0.2781	0.0964
1706-16[a]	2170	271	6	0.35	61.04	1.000	0.757	0.3744	0.0102	$< 10^{-4}$
	1085	271	2		5.47	0.957	0.294	0.1074	0.0164	$< 10^{-4}$
1718-32	2219	277	6	0.72	0.40	0.303	0.005	0.0018	0.0001	$< 10^{-4}$
	1109	277	4		0.03	0.028	0.001	0.0002	0.0001	$< 10^{-4}$
1727-47	2516	314	8	0.78	2.56	0.688	0.026	0.0286	0.0003	$< 10^{-4}$
	1258	314	4		0.29	0.268	0.013	0.0162	0.0007	0.0002
1727-47[a]	2516	314	8	0.64	0.36	0.252	0.004	0.0001	$< 10^{-4}$	$< 10^{-4}$
	1258	314	4		0.20	0.166	0.009	0.0021	0.0005	$< 10^{-4}$
1737-30	1448	181	8	0.42	481.35	1.000	5.562	0.9545	0.0715	0.0047
	724	181	4		13.68	0.993	0.767	0.4022	0.0410	0.0014
1737-30[a]	1448	181	8	0.47	0.14	0.044	0.002	$< 10^{-4}$	$< 10^{-4}$	$< 10^{-4}$
	724	181	4		0.13	0.044	0.007	$< 10^{-4}$	0.0004	$< 10^{-4}$
1737-30[b]	1448	181	8	0.47	14.15	0.990	0.183	0.0683	0.0026	$< 10^{-4}$
	724	181	4		60.37	1.000	3.386	0.8448	0.1810	0.0775
1737-39	2549	318	8	0.74	6.26	0.846	0.098	0.0989	0.0016	0.0002
	1274	318	4		9.38	0.881	0.552	0.3773	0.0353	0.0391
1742-30	2218	277	6	0.39	15.59	0.998	0.244	0.0734	0.0038	$< 10^{-4}$
	1109	277	4		0.39	0.174	0.018	$< 10^{-4}$	0.0010	$< 10^{-4}$
1742-30[a]	2218	277	6	0.28	0.39	0.087	0.006	$< 10^{-4}$	0.0001	$< 10^{-4}$
	1109	277	4		0.31	0.054	0.014	$< 10^{-4}$	0.0008	$< 10^{-4}$
1747-46	2510	313	8	0.68	0.18	0.150	0.003	0.0002	$< 10^{-4}$	$< 10^{-4}$
	1255	313	4		0.12	0.109	0.007	0.0021	0.0004	$< 10^{-4}$
1749-28	2549	318	8	0.77	15.21	0.926	0.211	0.2042	0.0030	0.0010
	1274	318	4		4.10	0.762	0.241	0.2365	0.0152	0.0172
1857-26	2541	317	8	0.87	0.07	0.104	0.001	0.0006	$< 10^{-4}$	$< 10^{-4}$
	1270	317	4		1.24	0.538	0.074	0.1241	0.0046	0.0084
1937-26	2393	299	7	0.49	0.02	0.001	$< 10^{-3}$	$< 10^{-4}$	$< 10^{-4}$	$< 10^{-4}$
	1196	299	4		0.07	0.017	0.003	$< 10^{-4}$	0.0002	$< 10^{-4}$
2045-16	2541	317	8	1.26	0.05	0.157	0.001	0.0078	$< 10^{-4}$	0.0001
	1270	317	4		0.01	0.062	$< 10^{-3}$	0.0078	$< 10^{-4}$	0.0005
2048-72	2487	310	7	0.41	0.09	0.007	0.001	$< 10^{-4}$	$< 10^{-4}$	$< 10^{-4}$
	1243	310	4		0.30	0.125	0.014	$< 10^{-4}$	0.0007	$< 10^{-4}$
2321-61	2458	307	6	0.39	0.09	0.006	0.001	$< 10^{-4}$	$< 10^{-4}$	$< 10^{-4}$
	1229	307	4		0.13	0.019	0.006	$< 10^{-4}$	0.0003	$< 10^{-4}$
2327-20	2522	315	7	0.90	0.05	0.091	0.001	0.0007	$< 10^{-4}$	$< 10^{-4}$
	1261	315	4		0.64	0.423	0.028	0.0611	0.0014	0.0024

[a]Results obtained after third order polynomial fits.

[b]Results obtained when periods jumps are not removed from the arrival-time data.

Structure Function Analysis

Structure function estimates can be obtained from a span of data by using the definition given in Section 6.2.1, noting that the data represent the residual phase ($\delta\phi$) after a polynomial fit rather than the absolute phase (ϕ). For a random walk with $k = 0$, 1, 2, the first-, second- and third-order structure functions of the residual phase, denoted by $D^{(1)}_{\delta\phi}(\tau)$, $D^{(2)}_{\delta\phi}(\tau)$ and $D^{(3)}_{\delta\phi}(\tau)$ respectively, will have theoretical logarithmic slopes of 1, 3 and 5 respectively.

Equation 6.14 represents an *ensemble average* structure function. In practice, structure function *estimates* are obtained from unevenly sampled data over a time span T by binning pairs of samples whose separations fall within a given range about some lag τ (Cordes & Downs 1985). Given the first-, second- and third-order phase increments as defined by Equation 6.15, the structure function estimates are obtained from

$$D^{(1)}_{\delta\phi}(\tau) = N_\tau^{-1} \sum_{i,j} [\delta\phi(t_j) - \delta\phi(t_i)]^2, \tag{6.18}$$

$$D^{(2)}_{\delta\phi}(\tau) = N_\tau^{-1} \sum_{i,j,k} [\delta\phi(t_k) - 2\delta\phi(t_j) + \delta\phi(t_i)]^2, \tag{6.19}$$

and

$$D^{(3)}_{\delta\phi}(\tau) = N_\tau^{-1} \sum_{i,j,k,l} [\delta\phi(t_l) - 3\delta\phi(t_k) + 3\delta\phi(t_j) - \delta\phi(t_i)]^2 \tag{6.20}$$

where N_τ is the number of terms in the sum of i, j, k successive points with a separation τ.

To obtain reliable structure function estimates, it is important that the tolerance (ϵ) associated with the binning is chosen so that $1 - \epsilon \ll 1$. This is then used to logarithmically bin pairs of samples within a given range, namely,

$$\epsilon\tau \leq t_j - t_i \leq \tau/\epsilon. \tag{6.21}$$

Following Cordes & Downs (1985), the structure functions were calculated using $\epsilon = 0.89$, giving 10 bins per decade in τ. Figure 6.3 is a typical logarithmic plot of the first-, second- and third-order structure functions as a function of the time lag, τ. The structure function slopes were obtained from linear least squares fits to intermediate time lags, bounded by the lags $\tau_{\rm min}$ and $\tau_{\rm max}$. The respective effects of additive noise and polynomial fits are responsible for restricting the slope estimates to these intermediate time lags (Cordes & Downs 1985).

As a check on the method of analysis, tests were performed on simulated random walks, using both uniform sampling and uneven sampling corresponding to the observations of PSR B0959-54. Table 6.3 shows the mean results of these tests for 20 realisations of a random walk in ϕ, ν and $\dot{\nu}$. The columns contain respectively: the type of random walk process, the minimum ($\tau_{\rm min}$) and maximum ($\tau_{\rm max}$) time lags over which the first-, second- and third-order structure function

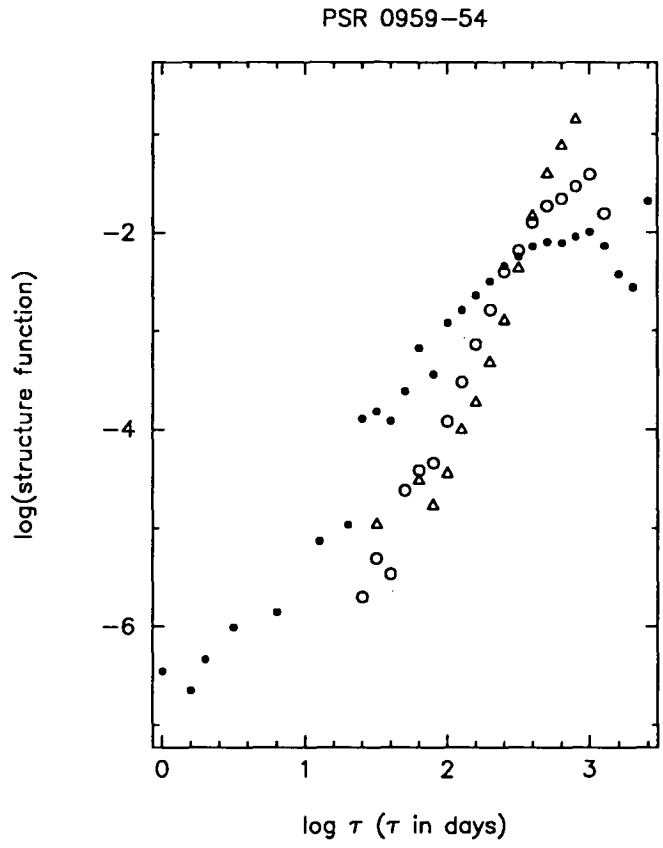

Figure 6.3: First-, second- and third-order structure functions of the timing noise in PSR B0959-54. Key: • = $D^{(1)}_{\delta\phi}$, ○ = $D^{(2)}_{\delta\phi}$, and △ = $D^{(3)}_{\delta\phi}$.

slopes were computed, and the mean slope of each structure function and their 1σ uncertainties. The results show that the structure function slopes are close to the theoretical values and that the estimates are insensitive to the sampling pattern of the data.

Structure Function Results and Discussion

The results for the actual pulsar data are summarised in Table 6.4. The uncertainties in the structure function slopes are the 1σ formal errors and refer to the last digit quoted.

After second order polynomial fits, the results show that: (i) for PSRs B0628-28, B0835-41, B1054-62, B1221-63, B1426-66, B1556-44, B1600-49 and B1727-47, the phase residuals are consistent with PN, (ii) for PSRs B0736-40, B0940-55, B1323-58, B1323-62, B1358-63, B1558-50, B1641-45 and B1706-16, the phase residuals are consistent with FN, (iii) none of the results show consistency with SN, with the possible exception of PSR B1641-45 (using data which includes discrete events), and (iv) for the remaining 10 pulsars with a level of timing noise suitable for analysis, the phase residuals are not consistent with any of the pure random

Table 6.3: Mean structure function slopes obtained from 20 random walk simulations using: (a) uniform 30-day sampling (the approximate interval between observations), and (b) uneven sampling, corresponding to the observations of PSR B0959-54. The slopes obtained from the structure function estimates are close to the theoretical values and show that the estimation method is relatively insensitive to the sampling pattern.

Random walk	$\tau_{\rm min}$ (days)	$\tau_{\rm max}$ (days)	Structure function slopes $D_{\delta\phi}^{(1)}$	Err	$D_{\delta\phi}^{(2)}$	Err	$D_{\delta\phi}^{(3)}$	Err
PN[a]	32,63,100	500	1.0	0.2	1.2	0.3	1.4	0.5
FN[a]	32,63,100	500	1.8	0.1	3.0	0.3	3.4	0.5
SN[a]	32,63,100	500	2.0	0.1	3.7	0.3	4.9	0.5
PN[b]	32,63,100	500	1.0	0.2	1.1	0.4	1.2	0.6
FN[b]	32,63,100	500	1.8	0.2	2.8	0.5	3.3	0.6
SN[b]	32,63,100	500	1.9	0.1	3.6	0.3	4.6	0.5

[a]The random walk time series was uniformly sampled at 30-day intervals.
[b]The random walk time series was sampled at the same epochs as the data from PSR B0959-54.

walk processes. In general, these results are consistent with the conclusions drawn from the strength parameter analysis.

The structure function slopes for some of the remaining pulsars are approximately square-law in $D_{\delta\phi}^{(1)}$, cubic or higher in $D_{\delta\phi}^{(2)}$ and large in $D_{\delta\phi}^{(3)}$ (≥ 4), suggesting that the phase residuals may be dominated by one or more discrete events in $\dot{\nu}$. After removing a third order polynomial, the phase residuals for PSRs B0923-58, B1449-64, B1648-42, B1737-30 and B1742-30 are essentially "white", giving structure function slopes < 1.

The strength parameter and structure function analyses have demonstrated that the timing activity of a number of pulsars is not consistent with an idealised random walk process. Hence, it is necessary to analyse the phase residuals for discrete events, or microjumps, in ν and $\dot{\nu}$. These events may account for much of the observed timing activity in these pulsars.

6.3 Discrete events

Detailed time-domain analyses of the timing behaviour in a sample of 24 pulsars by Cordes & Downs (1985) have shown that most timing activity cannot be modelled in terms of an idealised, large rate random walk process. Instead, the activity

Table 6.4: Results of the structure function analysis for 26 pulsars after second order polynomial fits, supplemented in a few cases with the results after third order fits.

Pulsar	τ_{min}	τ_{max}	Structure function slopes					
PSR B	(days)	(days)	$D_{\delta\phi}^{(1)}$	Err	$D_{\delta\phi}^{(2)}$	Err	$D_{\delta\phi}^{(3)}$	Err
0628-28	10,100,125	400,700,800	0.72	7	1.07	9	1.5	3
0628-28[a]	30	630	0.11	5	0.1	1	0.1	2
0736-40	6,60,60	320,630,630	1.88	9	3.14	6	3.0	2
0736-40[a]	25,60,60	320,500,500	1.5	1	2.0	2	2.3	1
0740-28	6,30,40	100,150,150	1.9	2	1.1	5	0.8	5
0740-28[b]	15,40,60	150,320,320	2.1	3	1.8	2	2.6	3
0835-41	16,30,30	500	1.1	1	1.40	9	1.2	2
0835-41[a]	25,40,60	400	1.23	8	1.23	7	0.9	2
0923-58	25,125,250	630,800,800	1.32	5	2.5	2	5.5	3
0923-58[a]	25,25,60	400,630,500	0.30	5	0.23	5	0.4	1
0940-55	10,30,60	630	1.70	9	3.0	2	3.3	3
0959-54	6,80,100	320	2.1	1	3.3	1	4.0	2
0959-54[a]	15,30,60	500	1.53	7	3.1	1	3.6	1
1054-62	30	320	1.11	8	1.3	2	1.5	5
1221-63	30,60,60	800	0.93	6	1.07	6	1.7	2
1221-63[a]	15,30,50	400	0.4	1	0.8	1	1.5	4
1240-64	15,25,30	1000	0.31	6	0.4	1	0.3	1
1240-64[b]	10,80,100	400,500,500	1.70	6	3.0	1	3.5	2
1323-58	10,100,100	500,500,630	1.80	5	3.3	1	3.5	5
1323-62	10,60,80	250,500,800	1.9	1	2.6	2	3.0	8
1358-63	25,25,30	400	1.47	8	3.22	9	3.7	6
1426-66	20,40,40	320,400,400	1.37	7	1.6	2	1.9	2
1449-64	10,40,60	400,800,800	1.48	7	1.98	3	2.2	3
1449-64[a]	10,30,80	400	0.6	2	0.6	3	0.4	4
1556-44	30,80,100	630	1.03	5	1.83	6	1.73	6
1556-44[a]	10,50,60	400	0.6	2	1.4	2	1.8	3
1558-50	3,30,30	320,320,800	2.3	2	3.6	5	3.3	3
1600-49	20,30,50	500	1.18	8	1.82	8	2.1	1
1641-45	25,40,50	500	1.70	7	2.97	8	3.5	2
1641-45[b]	15,50,100	400,400,500	1.67	7	3.5	2	4.6	3
1648-42	50,100,160	630	1.25	9	1.9	3	3.3	4
1648-42[a]	10,30,30	630	0.13	9	0.4	1	0.6	2
1706-16	25,50,100	150,250,630	1.7	2	3.3	2	3.9	4
1706-16[a]	15,60,100	320,320,500	1.7	1	3.3	1	3.7	2
1727-47	15,25,100	250,250,630	1.12	9	1.1	3	1.9	2
1727-47[a]	15,30,60	320	1.2	1	1.6	3	0.7	4
1737-30	25,25,100	500	1.52	4	3.2	1	5.63	8
1737-30[a]	10,10,30	500	0.17	4	0.28	7	0.6	1
1737-30[b]	10,15,50	160	2.2	2	2.4	2	5.2	6
1737-39	40,80,200	400,630,800	1.6	2	2.76	6	3.9	1
1742-30	25,160,320	630	1.54	4	3.3	2	6.8	5
1742-30[a]	15,40,60	500	0.65	6	0.71	8	0.9	2
1749-28	30,30,80	400,630,800	1.8	1	2.3	1	3.0	2

[a]Results obtained after third order polynomial fits.

[b]Results obtained when periods jumps are not removed from the arrival-time data.

appears to be due to discrete, identifiable jumps in one or more of the timing parameters (ϕ, ν or $\dot{\nu}$), possibly superimposed on an idealised random walk process, or a mixture of such processes.

The significance of discrete events in ν and $\dot{\nu}$ can be tested by comparing the amplitudes of the jumps, $\Delta\nu$ and $\Delta\dot{\nu}$, with the standard deviation of a large rate ($RT \gg 1$) random walk process. For events in ν and $\dot{\nu}$, the standard deviations are given by $\sigma_{\Delta\nu} = \sqrt{S_1 \Delta t}$ and $\sigma_{\Delta\dot{\nu}} = \sqrt{S_2 \Delta t}$ respectively (Cordes & Downs 1985), over a given time Δt. The tests are performed at a given "significance level", N, where a discrete event is considered real if $\Delta\nu/\sigma_{\Delta\nu} \geq N$ or $\Delta\dot{\nu}/\sigma_{\Delta\dot{\nu}} \geq N$. This test for $\Delta\nu$ is essentially the same as the one proposed by Cordes & Helfand (1980), the only difference being that the parameter they tested was the ratio of variances, $r = \Delta\nu^2/(N\sigma_{\Delta\nu})^2$, with $N = 3$. The latter test was used to assess the significance of period discontinuities identified in Chapter 4.

6.3.1 Analysis

For each of the 26 pulsars with a sufficient level of timing noise (see Table 6.1), the phase residuals were averaged over 3–4 days, and these were then used to compute the numerical derivative. Such averaging ensured that the resultant frequency residuals, $\delta\nu(t)$, were relatively free of large noise spikes which can arise from measurement uncertainties in the data when the derivative is computed from closely spaced observations.

Plots of the phase residuals used for the analysis of 24 pulsars can be found in Appendix C. Figure 6.4 shows the two remaining cases, where the $\delta\nu(t)$ are also plotted. Note that the sign of the phase residuals in these plots is defined in the sense of "observed minus predicted *arrival time*". This is consistent with the past use of downward-veering phase residuals to represent a discontinuous increase in the rotation frequency of the Vela pulsar (McCulloch *et al.* 1987, McCulloch *et al.* 1990). The numerical derivatives have been inverted to obtain frequency residuals of the correct sign.

Following Cordes & Downs (1985), the $\delta\nu(t)$ data were used to identify the epochs of discrete events. The data could then be modelled with a small number of piecewise linear segments. Estimates of $\Delta\nu$ and $\Delta\dot{\nu}$ were obtained from least-squares fits to the data either side of the event. In order to allow for measurement uncertainties, events were considered real only if the magnitude of the observed jump was greater than 5σ (i.e., $N = 5$). Experiments on simulated random walk data with similar signal-to-noise ratios as the real data demonstrated the reliability of this test, correctly rejecting fluctuations in the data which appeared to be real. An additional condition was imposed on the significance tests – the jump amplitude had to be significant with respect to the "formal" error of the jump estimate, given approximately by $\delta(\Delta\nu) = \sqrt{2}\sigma_W/\Delta t$ where $\Delta t \simeq 30$ days,

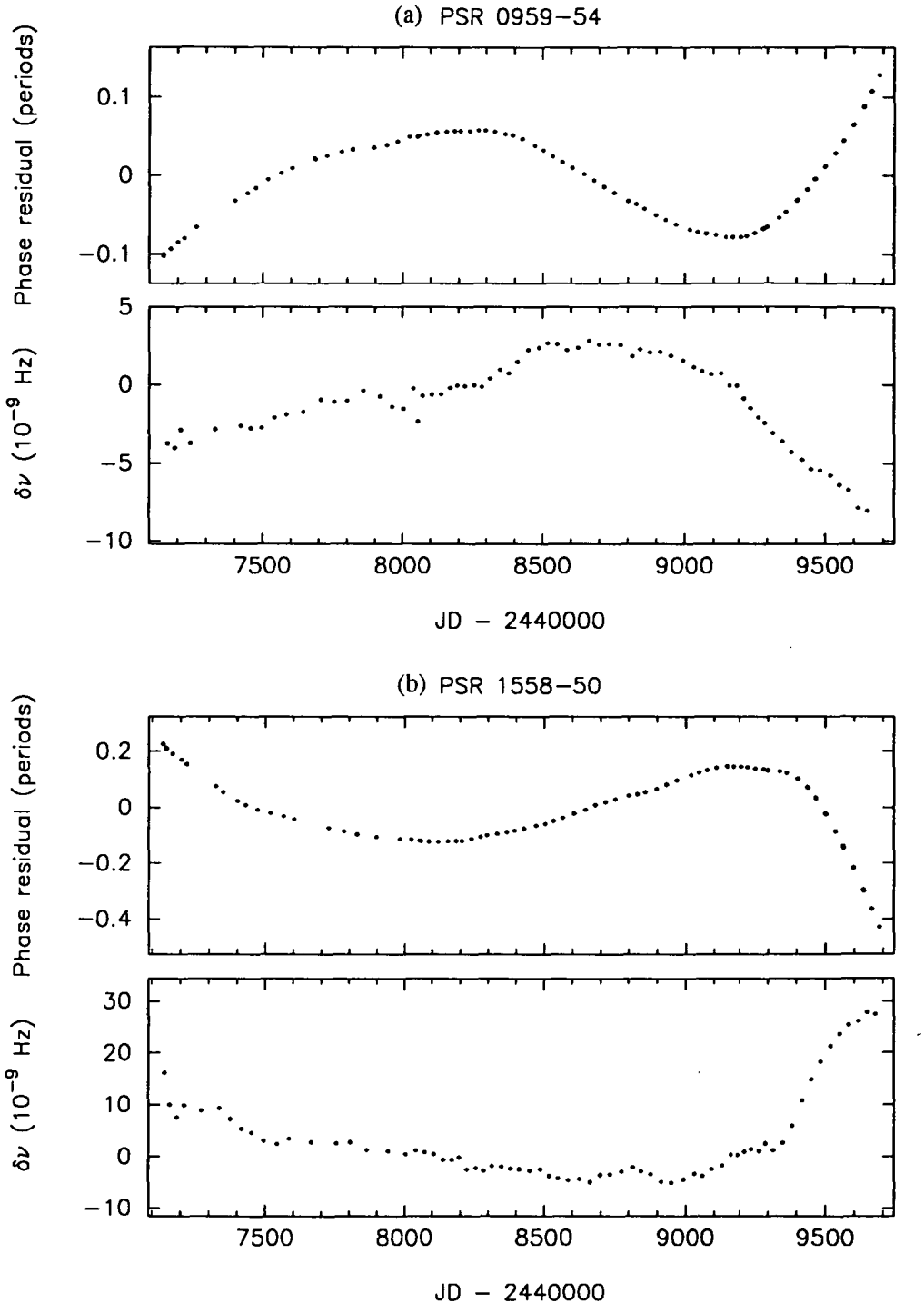

Figure 6.4: Phase residuals resulting from a second order least squares polynomial fit and their first derivative, plotted as a function of epoch for (a) PSR B0959-54, and (b) PSR B1558-50.

and $\delta(\Delta\dot{\nu}) = \sqrt{\delta m_1^2 + \delta m_2^2}$ where δm_1 and δm_2 are the errors in the slopes from the linear fits used to compute $\Delta\dot{\nu}$.

Two methods, A and B, were used to compute S_1 and S_2 and hence the standard deviation for FN and SN processes. Following Cordes & Downs (1985), the data between two events where timing activity was less than usual was used for method A, and the whole data set was used for method B. The rms phase using method A tends to be dominated by events in ν, while for method B, it is dominated by events in $\dot{\nu}$. Hence, greater weight was placed on method A for testing events in ν, and method B for testing events in $\dot{\nu}$.

6.3.2 Results and Discussion

Table 6.5 shows the results of the significance tests on discrete events in ν and $\dot{\nu}$ for 26 pulsars. Columns (3)–(15) contain, respectively: the event epoch and its uncertainty Δt, the amplitude of the jumps in ν and $\dot{\nu}$, the logarithm of the strength parameters used to compute the standard deviation for FN and SN using both methods A and B, the significance level of the magnitude of $\Delta\nu$ and $\Delta\dot{\nu}$ for each event using both methods A and B, and an indication of which events can be considered real.

A total of 76 events in ν and $\dot{\nu}$ were considered using the 5σ threshold test. For the $\Delta\nu$ events, 6 are significant using both methods, 15 are significant using method A only, 4 are significant using method B only, and 51 were not significant. For the $\Delta\dot{\nu}$ events, 2 are significant using method A only, 14 are significant using method B only, and the remaining 60 events were not significant using either method. Column (15) of Table 6.5 indicates which events can be considered real, if account is also taken of the results from the strength parameter and structure function analyses. Of the 76 discrete events tested, 33 of the events in ν, and 34 of the events in $\dot{\nu}$ have a negative amplitude. Of the discrete events which passed the threshold test, 12 out of the 26 events in ν, and 7 out of the 16 events in $\dot{\nu}$ have a negative amplitude.

It is clear from these results that the bulk of the timing activity in a few pulsars can be attributed to microjumps in ν and $\dot{\nu}$. The behaviour evident in the phase residuals of PSR B1240-64 is a clear example of this kind of timing activity. The phase residuals of several others pulsars (e.g., PSR B0923-58) are well-described by a third order polynomial. It has been shown that this cubic term is not due to pulsar braking. However, a single microjump can produce such a cubic term, and so in these cases the timing activity may also be due solely to discrete events. In general, the results obtained so far show that the timing activity in most pulsars is due to a mixture of discrete events and other processes (e.g., random walk processes).

One question that arises from observations of microjumps is whether these

Table 6.5: Results of statistical tests on discrete events in ν and $\dot{\nu}$. See the main text for an explanation of each column.

Pulsar PSR B	Event	Epoch (TJD)	Δt (days)	$\Delta\nu$ (†)	$\Delta\dot{\nu}$ (§)	$\log S_1$ (S_1 in $\mathrm{Hz^2 s^{-1}}$)		$\log S_2$ (S_2 in $\mathrm{Hz^2 s^{-3}}$)		$\lvert\Delta\nu/\sigma_{\Delta\nu}\rvert$		$\lvert\Delta\dot{\nu}/\sigma_{\Delta\dot{\nu}}\rvert$		Real events
						A	B	A	B	A	B	A	B	
[1]	[2]	[3]	[4]	[5]	[6]	[7]	[8]	[9]	[10]	[11]	[12]	[13]	[14]	[15]
0628-28	1	7802	38	+0.3	+0.04	-26.3	-26.9	-39.7	-41.8	2.5	5.0	0.2	1.5	$\Delta\nu$
	2	9193	27	−0.1	−0.05					1.3	2.7	0.3	2.7	
0736-40	1	7645	83	+1.1	+0.3	-25.3	-24.7	-38.7	-39.5	1.9	0.8	0.2	0.5	
	2	8283	25	+0.1	−0.78					0.4	0.2	1.3	3.0	
	3	9319	42	−0.6	−0.48					1.6	0.7	0.6	1.4	
0740-28	1	7645	83	+11	+2.5	-23.5	-24.8	-36.1	-39.6	2.3	10.3	0.1	6.2	$\Delta\nu$,$\Delta\dot{\nu}$
	2	8344	28	+3	+0.1					0.9	4.0	0.0	0.6	
	3	8664	36	+4	+3.3					1.3	6.1	0.2	12.2	$\Delta\nu$,$\Delta\dot{\nu}$
	4	8878	41	−11	−0.7					3.2	14.5	0.0	2.4	$\Delta\nu$
	5	9319	42	−3	−6.7					0.8	3.7	0.4	23.3	$\Delta\dot{\nu}$
0835-41	1	7860	78	+0.2	+0.12	-26.5	-27.0	-40.1	-41.8	1.6	2.9	0.5	3.7	
0923-58	1	8001	116	−0.5	+0.9	-25.6	-24.9	-39.4	-39.8	0.9	0.4	1.6	2.2	
0940-55	1	7460	29	−0.7	−8.1	-24.0	-23.7	-36.8	-38.5	0.4	0.3	1.3	9.0	$\Delta\dot{\nu}$
	2	8171	29	−2	−1.7					1.0	0.7	0.3	1.9	
	3	8452	42	+1	+0.9					0.7	0.5	0.1	0.9	
	4	8699	35	−0.4	+6.5					0.2	0.2	0.9	6.5	$\Delta\dot{\nu}$
	5	8879	42	+0.7	−6					0.4	0.2	0.7	5.1	$\Delta\dot{\nu}$
	6	9032	28	−0.8	+4					0.5	0.4	0.7	5.0	$\Delta\dot{\nu}$
	7	9270	29	−1.5	−4.5					0.9	0.6	0.7	5.0	$\Delta\dot{\nu}$
	8	9483	35	+1.6	+9.3					0.9	0.6	1.4	9.4	$\Delta\dot{\nu}$
0959-54	1	7543	48	+0.2	+0.3	-26.2	-24.1	-39.2	-39.0	1.2	0.1	0.5	0.4	
	2	7920	46	−0.8	−0.3					5.0	0.4	0.5	0.4	$\Delta\nu$
	3	8313	33	+0.5	+0.8					3.6	0.3	1.9	1.4	
	4	8587	36	−0.1	−1.6					0.5	0.1	3.7	2.7	
	5	9130	41	−0.9	−1.84					6.3	0.6	3.9	3.0	$\Delta\nu$
	6	9451	29	+0.2	+0.3					1.5	0.1	0.7	0.5	
1054-62	1	8140	35	−1.9	−0.1	-26.4	-26.2	-40.7	-41.1	17.7	14.7	0.8	1.2	$\Delta\nu$
	2	8285	25	+1.6	−0.1					16.9	13.9	1.4	2.0	$\Delta\nu$
1221-63	1	9130	42	+0.1	+0.1	-26.9	-26.5	-41.5	-41.4	0.8	0.5	2.1	1.8	
1240-64	1	7454	41	+0.4	+0.01	-27.1	-26.3	-40.5	-41.1	7.4	3.0	0.1	0.1	$\Delta\nu$
	2	7963	40	−0.5	−0.03					9.6	3.9	0.3	0.5	$\Delta\nu$
	3	8488	31	+0.5	+0.01					10.0	4.1	0.1	0.2	$\Delta\nu$
	4	9032	28	−0.6	−0.06					12.8	5.2	0.8	1.5	$\Delta\nu$
1323-58	1	7648	160	+0.8	−1.5	-25.6	-24.5	-39.0	-39.3	1.3	0.4	1.2	1.8	
	2	8139	36	−1.3	+0.5					4.8	1.3	1.0	1.4	
	3	8626	42	−0.6	+1.7					2.0	0.6	2.7	4.0	
1323-62	1	8626	42	−2.5	+1.7	-25.2	-24.6	-38.3	-39.5	5.6	2.7	1.3	4.7	$\Delta\nu$
	2	8916	37	−1.6	−2.9					3.8	1.8	2.4	8.7	$\Delta\dot{\nu}$
	3	9352	24	−2.7	+1.2					7.9	3.8	1.2	4.4	$\Delta\nu$
1358-63	1	8551	31	+0.6	−1.8	-25.3	-23.9	-38.8	-38.3	1.6	0.3	2.8	1.5	
	2	9092	36	−1.8	+3.91					4.9	0.9	5.7	3.1	$\Delta\nu$,$\Delta\dot{\nu}$
1426-66	1	8020	74	+0.1	−0.07	-27.0	-26.5	-41.2	-41.3	1.4	0.8	1.2	1.4	
	2	9291	16	+0.8	+0.01					21.8	12.5	0.5	0.6	$\Delta\nu$
1449-64	1	7856	255	−0.4	+0.13	-26.9	-26.0	-41.0	-40.8	2.3	0.8	0.9	0.7	
	2	9131	43	+0.3	+0.20					4.0	1.4	3.4	2.7	
1556-44	1	8257	32	+0.2	+0.03	-26.4	-26.9	-40.0	-41.8	1.7	3.1	0.2	1.4	
	2	8878	42	−0.3	−0.01					2.5	4.5	0.0	0.2	
1558-50	1	7585	38	+0.7	+1.8	-25.1	-23.4	-37.4	-38.2	1.4	0.2	0.5	1.3	
	2	8224	34	−1.9	+0.42					3.7	0.5	0.1	0.3	
	3	8952	36	+0.1	+2.6					0.2	0.0	0.7	1.9	
	4	9319	41	+0.6	+11.1					1.0	0.2	2.8	7.7	$\Delta\dot{\nu}$
	5	9550	28	+2.1	−9.6					4.5	0.7	2.9	8.1	$\Delta\dot{\nu}$

Discrete event tests, continued ...

Table 6.5: Continued.

Pulsar PSR B	Event	Epoch (TJD)	Δt (days)	$\Delta\nu$ (†)	$\Delta\dot{\nu}$ (§)	$\log S_1$ (S_1 in Hz^2s^{-1})		$\log S_2$ (S_2 in Hz^2s^{-3})		$\lvert\Delta\nu/\sigma_{\Delta\nu}\rvert$		$\lvert\Delta\dot{\nu}/\sigma_{\Delta\dot{\nu}}\rvert$		Real events
						A	B	A	B	A	B	A	B	
[1]	[2]	[3]	[4]	[5]	[6]	[7]	[8]	[9]	[10]	[11]	[12]	[13]	[14]	[15]
1600-49	1	8105	34	−0.6	−0.26	-25.5	-26.0	-39.0	-40.8	1.8	3.1	0.5	4.0	
	2	9129	42	+0.5	−0.2					1.6	2.7	0.3	2.6	
1641-45	1	7645	85	+2.7	−1.3	-25.9	-24.7	-39.5	-39.5	9.0	2.1	2.6	2.8	$\Delta\nu$
	2	7860	78	+2.2	−1.1					7.9	1.9	2.5	2.6	$\Delta\nu$
	3	8487	32	+0.1	+0.90					0.6	0.1	3.0	3.2	
	4	8878	42	+0.1	+0.42					0.6	0.1	1.2	1.3	
	5	9291	13	+0.4	+0.79					3.8	0.9	4.1	4.4	
1648-42	1	8587	37	+0.6	−0.5	-25.3	-25.3	-39.4	-40.0	1.4	1.4	1.4	3.0	
1706-16	1	7883	49	−0.7	−0.1	-27.0	-24.8	-39.9	-39.5	3.5	0.3	0.2	0.1	
	2	8552	33	−0.7	+0.01					14.3	1.1	0.1	0.0	$\Delta\nu$
	3	9131	43	−0.4	+1.5					7.3	0.6	6.9	4.4	$\Delta\nu$,$\Delta\dot{\nu}$
	4	9420	34	+0.1	−0.1					2.4	0.2	0.7	0.5	
1727-47	1	7860	77	+0.4	+0.15	-26.3	-26.6	-39.7	-41.4	2.1	2.9	0.4	3.0	
	2	9192	28	+0.2	+0.13					2.2	3.0	0.6	4.4	
1737-30	1	8451	42	+23	+3.7	-25.2	-23.7	-36.1	-38.0	49.7	8.5	0.2	2.1	$\Delta\nu$
	2	9061	28	+14	−2.9					36.4	6.2	0.2	2.0	$\Delta\nu$
	3	9484	35	+12	−2					27.7	4.7	0.1	1.2	$\Delta\nu$
	4	9581	34	+6	+4.0					14.4	2.5	0.4	2.5	$\Delta\nu$
1737-39	1	7964	39	+0.3	−0.48	-26.4	-25.7	-40.1	-40.5	2.6	1.2	2.8	4.8	
	2	8994	50	−0.4	+0.35					2.7	1.2	1.8	3.1	
1742-30	1	8843	28	−0.3	−0.24	-26.7	-25.8	-40.5	-40.5	4.5	1.7	2.9	2.8	
1749-28	1	7646	83	−0.2	+0.34	-26.4	-25.4	-39.1	-40.2	1.3	0.4	0.5	1.6	
	2	8451	42	+0.2	+1.3					1.3	0.4	2.6	9.1	$\Delta\dot{\nu}$
	3	8700	36	−1.6	−1.0					14.6	4.6	2.1	7.5	$\Delta\nu$,$\Delta\dot{\nu}$

† In units of 10^{-9} Hz.
§ In units of 10^{-16} Hz s^{-1}.

events are part of a distribution of jump amplitudes, ranging from unresolved microglitches to microjumps, and possibly glitches. The observational data suggest that microjumps are not simply scaled-down versions of glitches. For example, microjumps are observed as positive and negative changes in ν and $\dot{\nu}$ whereas glitches have a well-defined signature, namely $(\Delta\nu, \Delta\dot{\nu}) = (+, -)$. Also, the microjumps do not appear to be followed by a process of relaxation, although this may be masked if the relaxation time-scale is outside the range of time-scales in the data. These conclusions are supported by analyses based on theoretical models. As discussed in Chapter 2, Alpar *et al.* (1986) have suggested that there is a threshold for glitches produced by vortex unpinning and that physical processes in regions external to the weak and superweak regions explored in postglitch observations may be responsible for the timing noise observed in pulsars.

However, it is possible that the microjumps are part of the same distribution as

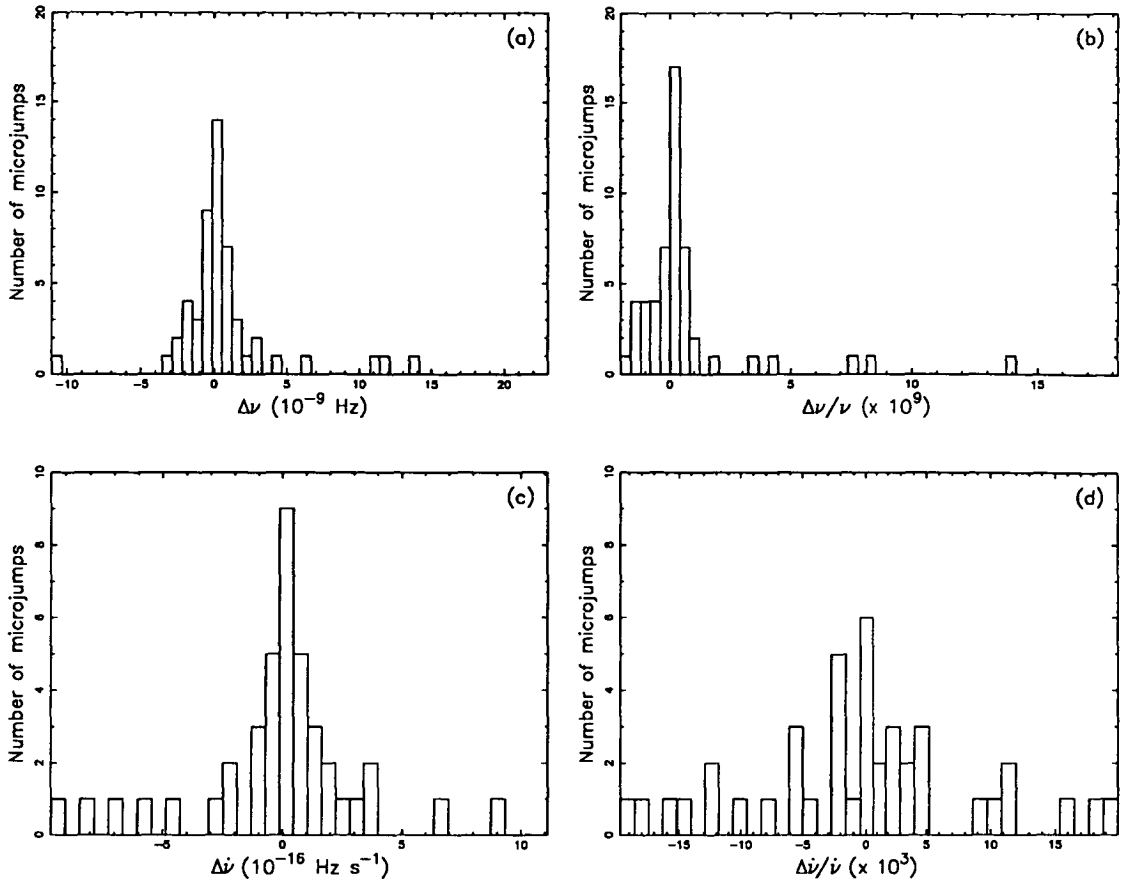

Figure 6.5: Histograms of the actual (i.e., including the sign) and fractional magnitudes of microjumps in ν and $\dot{\nu}$ derived from the Mt Pleasant and JPL pulsar timing data. The mean and median of the data were found to be, respectively: (a) 1.1×10^{-9}, 0.35×10^{-9} Hz; (b) 1.0×10^{-9}, 0.16×10^{-9}; (c) 0.1×10^{-16}, -0.05×10^{-16}, Hz s^{-1}; (d) 0.03×10^{-3}, -0.05×10^{-3}.

the individually indetectable microglitches that are thought to produce the timing noise observed in some pulsars. Figures 6.5 and 6.6 show histograms of jumps in ν and $\dot{\nu}$ plotted in a variety of ways. The data set used to plot the histograms is comprised of jump amplitudes derived from the present work (Table 6.5) and those obtained by Cordes & Downs (1985) from the JPL pulsar timing data. There are 53 jumps in ν and 42 jumps in $\dot{\nu}$ in this combined data set.

Figures 6.5(a),(b) show that there is a slight bias towards positive $\Delta\nu$ events. On the other hand, Figures 6.5(c),(d) show that there is negligible sign preference in $\Delta\dot{\nu}$ events and that there are large individual deviations from this zero mean. The histograms shown in Figure 6.6 (which disregard the sign of the microjumps) suggest that the microjump amplitudes could be part of, for example, an exponential or power-law distribution. If this is the case, then the histograms represent the tail of the distribution of amplitudes greater than the "threshold" values attainable from the data. Microjumps with smaller amplitudes are expected to occur at much higher rates, such that $RT \gg 1$, where R is the step rate and T is the time

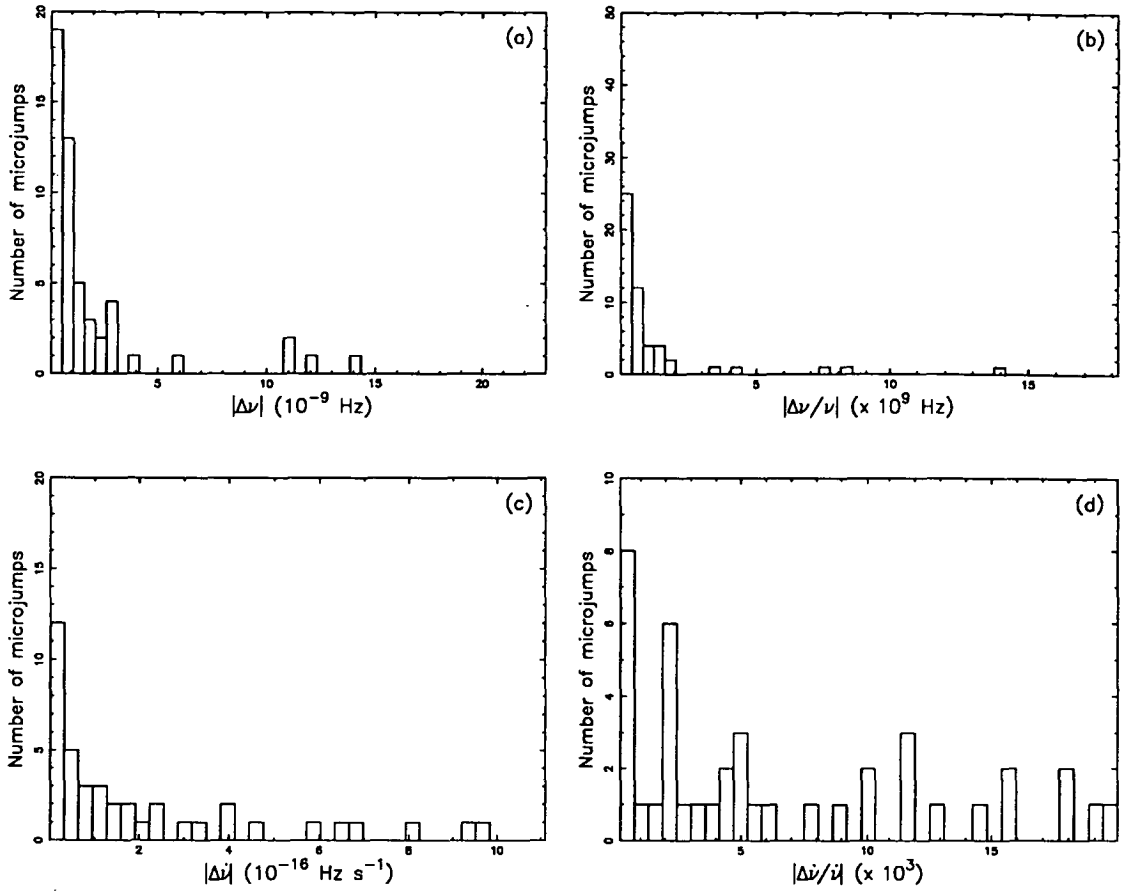

Figure 6.6: Histograms of the absolute value of the actual and fractional magnitudes of microjumps in ν and $\dot{\nu}$ derived from the Mt Pleasant and JPL pulsar timing data.

span of the data. For the combined Mt Pleasant and JPL data, these threshold amplitudes correspond to fractional jumps of $\left(\frac{\Delta\nu}{\nu}\right)_t \simeq 10^{-10}$ and $\left(\frac{\Delta\dot{\nu}}{\dot{\nu}}\right)_t \simeq 5 \times 10^{-4}$. These lower limits are set by the sampling intervals of the timing data, typically $10 - 50$ days, and also the level of white noise.

The results of the analyses performed thus far have been used to determine the degree to which a random process is responsible for the timing noise observed in pulsars. In the next section, the data are probed for other (non-random) causes of timing variations in pulsars which can mimic "timing noise", even though the mechanism may not involve a noise process. These causes have been grouped together as "quasi-periodic oscillations". Some examples include the recovery from a glitch, internal oscillations, free precession, and planetary systems.

6.4 Quasi-periodic Oscillations

6.4.1 Recovery from a Glitch

As discussed in Chapter 2, the vortex creep theory predicts a long-term recovery in $\dot{\nu}$ that is linear in time following a glitch. This behaviour has been observed following each of the Vela glitches. Such a response is expected from older pulsars following similar, although less frequent, glitches (Alpar *et al.* 1989,1993). This linear recovery in $\dot{\nu}$ will produce phase residuals that display a single cycle across the data span and a third order fit will result in a large measured value of the frequency second derivative, $\ddot{\nu}$. This value, and the corresponding "anomalous" braking index is always larger than the $\ddot{\nu}$ and index due to the pulsar braking torque. Furthermore, the magnitude of $\ddot{\nu}$ must be positive.

The timing residuals of a number of pulsars are dominated by a large "positive" cubic term (Table 4.3, negative values of $\ddot{P}$). A good candidate for such a scenario is PSR B1737-30, which is well known for its glitching behaviour. Unfortunately, there is no way of distinguishing between a glitch-induced and, for example, a random-walk-induced cubic term.

6.4.2 Internal Oscillations

As mentioned in Chapter 4, oscillations of the vortex lattice in the neutron superfluid may be excited under certain circumstances, e.g., as a result of a glitch (Ruderman 1970a). These Tkachenko oscillations can produce a periodic wobble in the timing residuals of pulsars. For the fundamental mode,

$$P_{\rm Tk} \simeq 20R\sqrt{P} \quad \text{(month)} \tag{6.22}$$

where R is the stellar radius in units of 10^6 cm and P is the rotation period. Lyne *et al.* (1988) have suggested that the 20-month quasi-sinusoidal deviations observed in the Crab pulsar residuals could be due to some mode of internal oscillation.

The typical period of the fundamental oscillation mode for "long-period" pulsars ($P \simeq 1$ s) is < 2 years. With the exception of PSR B1240-64, which was discussed in Chapter 4, none of the other pulsars in the Mt Pleasant sample have timing residuals with an obvious oscillation period less than 4–5 years. Hence, internal oscillations may not account for the timing noise in any of the Mt Pleasant pulsars. It should be pointed out, however, that the oscillation periods suggested by Equation 6.22 may not be correct because the calculation ignores other effects, such as vortex pinning. Further theoretical work is needed before the observational data can be meaningfully tested.

6.4.3 Free Precession

Soon after the discovery of pulsars, Ruderman (1970b) suggested that free precession of the rotation axis of the neutron star may cause the small amplitude "wobble" observed in the arrival times from the Crab pulsar. The instantaneous spin axis of an isolated pulsar can precess if this axis does not coincide with the symmetry axis due to, for example, a non-spherical shape. Under these conditions, free precession will produce a cyclical change in the angle, α, between the spin axis and the magnetic moment of the pulsar. If the external torque acting on the neutron star depends on α, which is highly likely, e.g., the magnetic dipole radiation model predicts $\dot{\nu} \propto \sin^2 \alpha$, then this will change the torque in a cyclical fashion and may detectable in the timing data of pulsars (Cordes 1993).

The influence of the neutron star superfluid interior on free precession is not well understood. Shaham (1977) has shown that if the superfluid vortex lines are rigidly pinned to the crust, then the precession frequency is of the order of $\omega_p \sim (I_p/I)\Omega$ where (I_p/I) is the fractional moment of inertia of the pinned component and Ω is the angular rotation frequency. For a typical neutron star, $\omega_p \simeq 10^{-2}\Omega$. However, Alpar & Ögelman (1987) have shown that the rigid pinning case does not necessarily apply because a steady state situation can arise in which the superfluid precesses with the crust. Hence, longer precession periods than those predicted by Shaham (1977) cannot be ruled out. Shaham (1977) and Alpar & Ögelman (1987) also predict that pulsar precession is likely to be damped by internal torques on a time-scale $\tau_p \simeq (\Omega/\omega_p)\tau_{cc}$, where τ_{cc} is the crust-core coupling time. This time-scale is typically less than 1000 years, i.e., much shorter than the pulsar spin-down time. In other words, the free precession must be driven continuously by one or more internal or external excitation mechanisms. In isolated pulsars, crustquakes and vortex-crust interactions are feasible excitation mechanisms (Cordes 1993).

Two types of variations may be observed as a result of free precession. Firstly, geometric "wobble" of the beam will produce pulse shape changes as well as timing variations. In practice, these pulse shape changes are difficult to detect, but if observed, the changes will be correlated with the timing variations. Secondly, the timing variations will also receive contributions from "induced-torque variations" and the mechanisms that drive the precession (Cordes 1993). For a wobble angle θ_p between the instantaneous spin vector and the symmetry axis, the timing variations due to beam wobble are

$$\delta\phi_w \sim \frac{\theta_p}{2\pi} \sim 10^{-3.6}\left(\frac{\theta_p}{0.1^\circ}\right) \tag{6.23}$$

rotation cycles with accompanying pulse shape changes

$$\frac{\delta S}{S} \sim \frac{\theta_p}{W} \sim 0.01\left(\frac{\theta_p}{0.1^\circ}\right)\left(\frac{10^\circ}{W}\right) \tag{6.24}$$

where S is a pulse shape parameter and W is the pulse width (Cordes 1993). The induced-torque variation is sinusoidal with frequency ω_p and an amplitude of the order of $\delta\dot{\nu}/\dot{\nu} \sim \theta_p$. The corresponding phase residuals have an amplitude

$$\delta\phi_t \approx \frac{\dot{\nu}\theta_p}{\omega_p^2} \approx 10^{-5.5}\dot{\nu}\left(\frac{\theta_p}{0.1^\circ}\right)\left(\frac{P_p}{100\ \mathrm{d}}\right) \tag{6.25}$$

rotation cycles, where $\dot{\nu}$ is in units of 10^{-15} Hz s^{-1} and P_p is the precession period (Cordes 1993).

There is some observational evidence for neutron star precession. Trümper *et al.* (1986) identified a 35-day modulation in the pulse arrival times from the X-ray pulsar Her X-1 which they attributed to free precession excited by external torques. Jones (1988) has offered a similar explanation to account for the quasi-periodic ($\sim$20 month) oscillations seen in the timing residuals of the Crab pulsar. Assuming the Crab phase residuals are dominated by induced-torque variations, Cordes (1993) obtained a wobble angle $\theta_p \approx 2.3$ arc sec, with corresponding pulse shape changes at a level of $\delta S/S \sim 10^{-4}$. These pulse shape changes are too small to be detectable, by a factor of ~ 100. Cordes (1993) analysed the pulse shape data on a subset of 14 pulsars from the JPL sample. The results showed that pulse shape variations could be attributed to pulse jitter or mode changes in all cases except for the Vela pulsar and PSR B1642-03. These pulsars show long-term secular effects in the pulse shape, with periods of about 100 d and 1000 d respectively. PSR B1642-03 also shows a cyclical variation in the timing residuals. Both effects in this pulsar can be accounted for by a wobble angle $\theta_p \approx 0.5^\circ$ (Cordes 1993). Suleymanova & Shitov (1994) have observed long-term pulse profile changes and period derivative variations in PSR B2217+47 at 102 MHz. They have suggested that these variations are due to free precession of the spin axis with a period greater than 20 years.

If the observed variations in pulse shape and arrival times are the result of free precession, then these data provide yet another avenue for studying the interiors of neutron stars. Larger data sets need to be analysed for these effects. This section presents the results of a pulse shape analysis performed on a subset of the Mt Pleasant pulsar sample. The subset of pulsars was selected on the basis that the residuals showed some sort of cyclical signature, along with the criterion that the profiles had sufficient signal-to-noise for a meaningful analysis.

Analysis

The aim of the analysis was to detect long-term variations in pulse shape that are correlated with the variation evident in the timing residuals. To test this possibility, two measures of pulse shape were considered, namely, the use of the moments of the pulse, and a geometrical shape factor involving the area and perimeter of the pulse profiles. A critical factor in comparing the methods is the

signal-to-noise of the profiles. Methods that use the pulse area and perimeter to measure the pulse shape tend to give poor results for moderate to low signal-to-noise ratios (< 20). These ratios are typical of the profiles obtained from the Mt Pleasant timing observations. On the other hand, Downs & Krause-Polstorff (1986) have found that the moments of the pulse are relatively insensitive to noise. Hence, the latter method was used to measure the pulse shape.

The steps in the analysis for each pulsar were as follows:

- All of the integrated profiles for a given pulsar were examined and those affected by interference were excluded from further analysis.
- A high signal-to-noise standard profile (template) was generated by summing all of the profiles from the first step.
- Each profile was cross-correlated with the template and shifted in phase so that it was aligned with the template. This enabled the moments of each profile to be computed about a common phase reference.
- The nth order moments of the pulse (for n = 1,2,3) and the moments of the difference between the pulse and the template, or the "difference moments" (for n = 0,1,2,3), were computed about a common phase reference as described below. This reference was taken to be the centroid of the template.
- Correlation plots of the nth order moments and difference moments against the timing residuals were generated, along with estimates of the correlation coefficient and its significance.

Furthermore, this analysis was performed separately on the profiles recorded at 670 MHz and 800 MHz because of the well-known frequency dependence of the shape of integrated profiles (e.g., Hankins & Rickett 1986). Also, the results for one observing frequency provide a cross-check on the results for the other.

Following Downs & Krause-Polstorff (1986), the nth order moment μ_n is given by

$$\mu_n = \frac{\sum_i (t_i - P_h)^n d_i}{\sum_i d_i} \tag{6.26}$$

where t_i is the phase within the data record of the profile, d_i is the intensity at time t_i, P_h is the phase reference about which the moment is computed.

To obtain the difference moments, each profile was amplitude-scaled to the template. The nth order difference moments μ_{dn} were then computed using

$$\mu_{dn} = \frac{\sum_i (t_i - P_h)^n (d_i - T_i)}{\sum_i d_i} \tag{6.27}$$

where T_i is the value of the template at t_i. In theory, the difference moments should be more sensitive to pulse shape changes.

Results

The results of the pulse shape analysis are shown in Tables 6.6 and 6.7 for the pulse moments and difference moments respectively. The columns contain, respectively, the pulsar name, observing frequency, number of profiles analysed, median signal-to-noise ratio of the profiles, and the correlation coefficient of the nth order moments (difference moments) with timing residuals for n = 1,2,3 (n = 0,1,2,3), along with the significance level at which the null hypothesis of zero correlation is disproved. Hence, a small probability indicates a significant correlation.

Significant correlation, at the 95% level, between odd moments and the residuals was found for the 670 MHz profiles of PSR B0959-54. No such correlation was found for the 800 MHz profiles. Further investigation revealed nothing unusual about the 670 MHz data or the method of processing. The only obvious difference between the two frequencies is the time span of the data. As a test, a subset of the 670 MHz data, comprising only the profiles recorded at the same epochs as the 800 MHz profiles, was analysed. Similar significant correlations were obtained from this analysis.

Figure 6.7 displays the odd moments alongside the phase residuals for this pulsar, plotted as a function of time. A weak negative correlation between the odd moments and the residuals is evident. Figures 6.8 and 6.9 show the correlation diagrams of moments and difference moments with timing residuals for the 670 MHz profiles of PSR B0959-54. Both the odd moments and difference moments are anticorrelated with the timing residuals.

Discussion

An important requirement in any investigation of subtle pulse shape changes is a stable observing system. Factors such as the integrator time constant, filter bandwidths and instrumental polarization are critical to the experiment. In the present study, variable observing parameters (e.g., time constants, bandwidths) have not been altered for observations of individual pulsars during the 7 years that timing measurements have been made at the Mt Pleasant Observatory. Furthermore, the observing system used to obtain the integrated profiles has not undergone any related modifications with the exception of the installation of the quadrature hybrid into the receiver front end (see Chapter 3). This change took place in September 1991. However, visual inspection of plots of the moment estimates against time does not reveal any anomalies at or beyond this date.

According to Cordes (1993), the induced-torque effect "amplifies" the timing residuals to much larger amplitudes than would be observed from geometrical effects alone. The largest amplification is observed for objects with large period derivatives. Hence, for pulsars with very small values of $\dot{P}$, the timing residuals will be dominated by geometrical wobble of the beam, and for pulsars with larger

Table 6.6: Cross-correlation coefficients of pulse moments with timing residuals for a selection of pulsars.

Pulsar	Freq.	N	S/N	Moments					
PSR B	(MHz)			$n=1$	Prob	$n=2$	Prob	$n=3$	Prob
0736-40	670	82	17.7	-0.073	0.513	0.082	0.467	-0.110	0.325
	800	65	36.0	0.111	0.381	0.078	0.538	0.143	0.254
0923-58	670	63	5.7	-0.091	0.480	-0.129	0.312	-0.085	0.508
	800	70	7.7	-0.046	0.708	0.092	0.447	-0.137	0.257
0940-55	670	76	9.1	0.048	0.680	-0.133	0.251	0.101	0.386
	800	64	10.7	0.034	0.792	-0.014	0.915	0.023	0.855
0959-54	670	71	19.6	-0.327	0.005	-0.087	0.469	-0.369	0.002
	800	61	24.5	0.062	0.634	-0.156	0.228	0.104	0.426
1240-64	670	90	23.0	0.058	0.589	-0.111	0.297	0.058	0.590
	800	73	41.8	-0.211	0.074	-0.045	0.706	-0.216	0.067
1323-58	670	72	5.8	0.010	0.930	0.144	0.228	0.063	0.600
	800	83	11.9	0.072	0.519	-0.212	0.054	0.013	0.907
1323-62	670	63	7.8	-0.040	0.754	-0.179	0.159	-0.201	0.114
	800	57	14.4	0.007	0.960	-0.036	0.792	-0.009	0.949
1358-63	670	62	8.4	0.066	0.612	0.039	0.765	0.057	0.661
	800	78	12.1	0.103	0.371	-0.066	0.566	0.065	0.572
1449-64	670	77	16.9	0.027	0.817	-0.070	0.545	-0.016	0.891
	800	64	27.8	-0.217	0.084	0.202	0.109	-0.209	0.097
1558-50	670	76	7.0	-0.154	0.183	0.000	0.998	0.035	0.767
	800	65	12.6	-0.167	0.183	0.114	0.368	-0.056	0.659
1600-49	670	62	6.5	-0.111	0.391	0.150	0.245	-0.167	0.194
	800	53	9.0	-0.168	0.228	0.027	0.848	-0.130	0.353
1706-16	670	50	11.5	-0.155	0.282	-0.032	0.823	-0.120	0.405
	800	55	22.7	0.166	0.225	-0.214	0.117	0.198	0.148
1737-39	670	65	7.5	-0.030	0.812	0.108	0.393	-0.032	0.797
	800	57	12.4	-0.019	0.889	0.073	0.589	-0.060	0.657
1742-30	670	61	9.5	-0.004	0.975	-0.047	0.722	0.024	0.857
	800	61	17.5	0.014	0.912	-0.034	0.796	0.001	0.991
1749-28	670	78	40.3	0.020	0.864	-0.039	0.738	-0.013	0.913
	800	65	40.1	0.102	0.417	-0.020	0.872	0.099	0.433

Table 6.7: Cross-correlation coefficients of pulse difference moments with timing residuals for a selection of pulsars.

Pulsar	Freq.	N	S/N	Difference Moments							
PSR B	(MHz)			$n=0$	Prob	$n=1$	Prob	$n=2$	Prob	$n=3$	Prob
0736-40	670	82	17.7	0.061	0.584	-0.073	0.513	0.082	0.466	-0.109	0.328
	800	65	36.0	-0.031	0.808	0.111	0.381	0.075	0.551	0.144	0.252
0923-58	670	63	5.7	0.047	0.712	-0.115	0.368	-0.021	0.871	-0.102	0.427
	800	70	7.7	-0.045	0.714	-0.046	0.708	0.041	0.737	-0.140	0.249
0940-55	670	76	9.1	-0.129	0.268	0.048	0.680	-0.132	0.255	0.106	0.364
	800	64	10.7	0.032	0.805	0.032	0.804	-0.013	0.919	0.020	0.873
0959-54	670	71	19.6	0.117	0.332	-0.326	0.006	-0.089	0.459	-0.369	0.002
	800	61	24.5	0.181	0.163	0.066	0.614	-0.159	0.222	0.109	0.405
1240-64	670	90	23.0	-0.076	0.479	0.054	0.611	-0.110	0.301	0.055	0.606
	800	73	41.8	-0.092	0.441	-0.212	0.072	-0.046	0.698	-0.217	0.065
1323-58	670	72	5.8	0.102	0.396	0.045	0.709	0.144	0.227	0.062	0.602
	800	83	11.9	-0.187	0.091	0.042	0.707	-0.212	0.055	0.016	0.883
1323-62	670	63	7.8	-0.050	0.698	-0.049	0.704	-0.180	0.157	-0.204	0.109
	800	57	14.4	-0.001	0.992	0.007	0.961	-0.036	0.793	-0.009	0.949
1358-63	670	62	8.4	-0.093	0.474	0.048	0.712	0.040	0.759	0.044	0.736
	800	78	12.1	0.099	0.389	0.098	0.393	-0.065	0.570	0.064	0.580
1449-64	670	77	16.9	-0.077	0.505	0.025	0.832	-0.069	0.549	-0.016	0.893
	800	64	27.8	0.142	0.262	-0.218	0.084	0.205	0.103	-0.212	0.092
1558-50	670	76	7.0	-0.007	0.950	-0.154	0.183	0.001	0.997	0.036	0.758
	800	65	12.6	0.075	0.550	-0.167	0.185	0.114	0.367	-0.057	0.652
1600-49	670	62	6.5	0.187	0.144	-0.113	0.384	0.143	0.267	-0.163	0.206
	800	53	9.0	0.080	0.567	-0.178	0.201	0.029	0.834	-0.132	0.348
1706-16	670	50	11.5	-0.263	0.065	-0.149	0.303	-0.037	0.800	-0.112	0.440
	800	55	22.7	-0.035	0.800	0.167	0.224	-0.214	0.117	0.198	0.148
1737-39	670	65	7.5	0.120	0.341	-0.048	0.706	0.104	0.410	-0.053	0.676
	800	57	12.4	-0.251	0.059	-0.009	0.950	0.076	0.576	-0.051	0.709
1742-30	670	61	9.5	-0.068	0.603	-0.003	0.979	-0.047	0.720	0.021	0.871
	800	61	17.5	-0.065	0.617	0.016	0.905	-0.034	0.795	0.001	0.994
1749-28	670	78	40.3	0.015	0.897	0.020	0.864	-0.038	0.743	-0.013	0.913
	800	65	40.1	0.187	0.135	0.102	0.417	-0.017	0.891	0.100	0.430

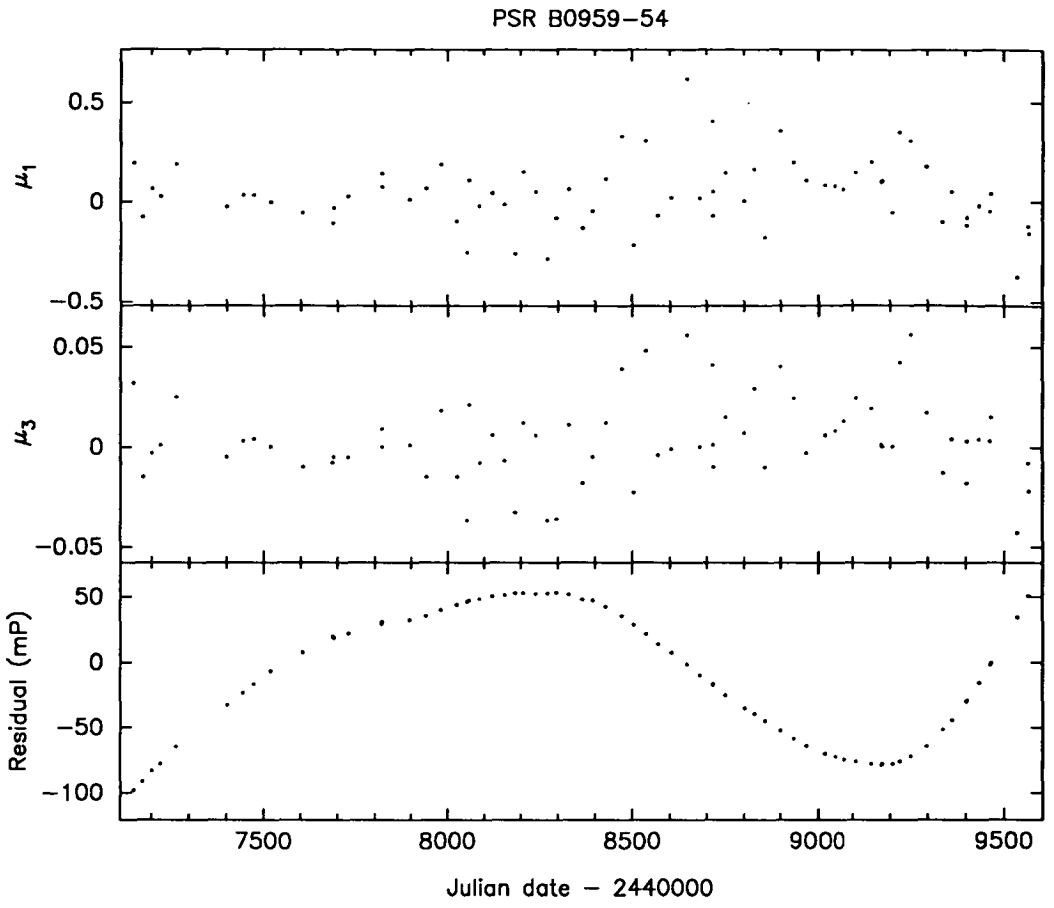

Figure 6.7: Odd moments and phase residuals for PSR B0959-54, plotted as a function of time.

$\dot{P}$, induced-torque variations will dominate. The latter is the dominant regime for PSR B1642-03 (Figure VII, Cordes 1993). As mentioned earlier, Cordes has found cyclical changes in the pulse shape and timing residuals of this pulsar, which can be accounted for by free precession with a wobble angle $\theta_p \sim 0.5°$.

PSR B0959-54 also falls into the torque-dominated regime. If the pulse shape and timing residual variations observed for this pulsar are due to free precession, then the wobble angle can be estimated by using Equation 6.25. From Figure 6.7, a lower limit for the precession period, P_p, is ~ 2500 days, and the amplitude of the timing residuals is ~ 0.075 cycles, giving a wobble angle $\theta_p \leq 0.15°$.

The discrepancy in the findings at the two observing frequencies is more likely to be due to an observational or instrumental effect than a physical, frequency-dependent effect intrinsic to the pulsar (e.g., different geometry arising from precession because the radio frequency of the emission is dependent on altitude above the poles of the neutron star). It is possible that the subtle pulse shape changes measured in the 670 MHz profiles have been smeared out of the 800 MHz profiles to some extent. The post-detection time constant can be ruled out as a cause because it is smaller for the 800 MHz observations (0.2 ms) than the 670 MHz

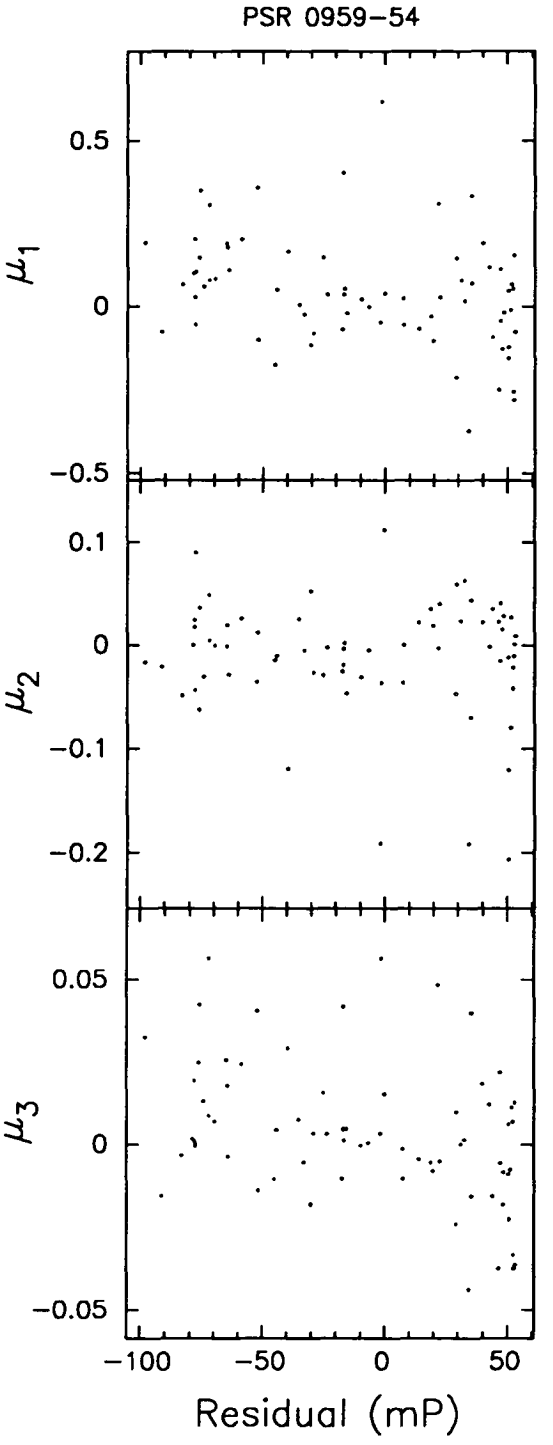

Figure 6.8: Correlation plots of nth order moments against timing residuals, for n = 1,2,3.

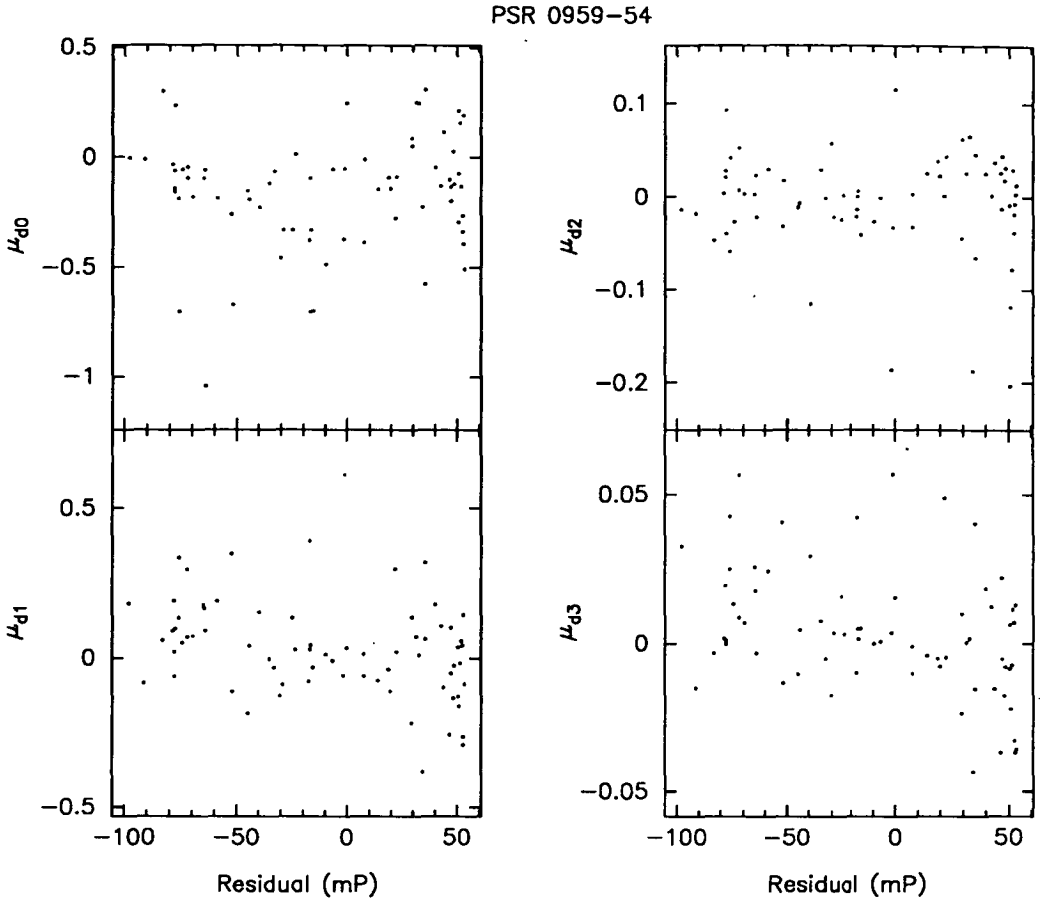

Figure 6.9: Correlation plots of nth order difference moments against timing residuals, for n = 0,1,2,3.

observations (0.6 ms). One possibility is the dispersion smearing in the profiles. As described in Chapter 3, the smearing in the profiles at both observing frequencies was less than 2% of the pulsar period. However, there is a difference of ~ 2 milliperiods in the amount of smearing between the two observing frequencies because, for historical reasons, the ratio of the filter bandwidths used (i.e., 2) is not exactly equal to $(800/670)^3$.

Free precession in pulsars may also result in secular pulse intensity variations (Glendenning 1990). In fact, such intensity variations were observed by Suleymanova & Shitov (1994) in a component of the integrated profiles of PSR B2217+47. Therefore, a logical extension of this work would be to investigate the long-term variations in pulsar flux in order to determine if there is any correlation with the pulse shape changes. However, a requirement of this analysis is the reprocessing of 7 years of timing data in order to obtain the relevant flux calibration information. This large task is intended for a future date.

6.4.4 Planets

The potential of pulsar timing to detect planets around neutron stars[1] has been considered in the past (Richards *et al.* 1970, Demiański & Prószyński 1979, Bailes *et al.* 1991), but none of these apparent discoveries withstood the test of time. However, the discovery of two (and possibly three) planets orbiting the millisecond pulsar PSR B1257+12 (Wolszczan & Frail 1992, Wolszczan 1993,1994) has seen a resurgence in the examination of pulsar timing data for the sinusoidal signature of orbiting bodies. At the time of writing, no other definite candidates for planetary systems had been uncovered.

Although independent observations of PSR B1257+12 have confirmed the two-planet postulate (Backer 1993), for evolutionary reasons (van den Heuvel 1993) a number of alternative explanations have been proposed. Several authors have shown that, under certain conditions, a model involving free precession can produce timing effects that mimic orbiting planets (Nelson *et al.* 1990, Dolginov & Stepinski 1993, Gil *et al.* 1993, Glendenning 1995). Even though it is possible to arrange the relative orientation of the pulsar spin and magnetic axes, the line of sight to the observer, and the geometry of the emission region so that a double sinusoidal signal is produced when precession, nutation or crust-core relative rotation are invoked, there remain several fundamental difficulties. For example, the precession must be driven (see Section 6.4.3), secular pulse shape changes are not seen (Kaspi & Wolszczan 1993), and at times the oscillation amplitude is large enough to imply that the pulsar is actually speeding up (Rees 1993). At present the planetary hypothesis appears to be the most sound. Confirmation (or otherwise) will be possible over the next few years, as predictable periodic perturbations of the two orbits (e.g., see Malhotra 1993, Rasio *et al.* 1993) should be measurable in the pulse arrival times.

A number of computationally intensive methods have been used to place limits on pulsar planetary systems (e.g., Thorsett & Phillips 1992). Using the JPL database, Thorsett *et al.* (1993) found that an Earth-mass planet would be only marginally detectable in the data of most of the pulsars but a Jupiter-mass planet would be detectable at a level $\geq 100\sigma$. Bailes *et al.* (1993) used the Jodrell Bank database to search for planets and have also not found any definite candidates, with the possible exception of PSR B0329+54. Demiański & Prószyński (1979) had earlier found an 1100-day periodicity in the timing residuals of this pulsar over an 8-year span. Bailes *et al.* (1993) have found a similar periodicity, along with a second one with a period of 2370 days.

This section presents the results of an analysis that checks for the presence of sinusoidal features in the timing residuals. The aim of the analysis is to determine

[1]Either from the Doppler shifts in the rotation frequency or by using a phase method which involves counting individual pulses and measuring the delays in the arrival of the nth pulse due to the light travel time across the pulsar "orbit".

if a planetary system can account for some or all of the observed timing noise in a pulsar. In practice, this aim is very difficult to achieve because the coherent oscillations due to the planet(s) will be intermixed with white and red noise (intrinsic timing noise) arising from other mechanisms. Another difficulty is the limited time span of the data, which restricts the range of orbital periods that can be tested. In general, long-period pulsars are unlikely to have planetary systems for evolutionary reasons (van den Heuvel 1993) whereas planets are more likely to be found orbiting millisecond pulsars. The latter follows naturally from the widely accepted view that millisecond pulsars once possessed an accretion disk. Also, timing noise in these pulsars is extremely small, allowing easier detection of planets.

For these reasons, the detection of a planet around any of the long-period pulsars in the Mt Pleasant sample is highly unlikely. Consequently, more attention has been given to other possible explanations of timing noise. The analysis presented here is only of a preliminary nature.

Analysis

A quick way to look for sinusoidal features in the timing residuals is to Fourier transform the data. Unfortunately, FFTs cannot be used directly because of the uneven sampling in archival pulsar timing data. Press & Rybicki (1989) have developed a fast algorithm for spectral analysis of unevenly sampled data that is based on the Lomb-Scargle method. This method is known to be a powerful way to find and test the significance of weak periodic signals. This algorithm was used to obtain Lomb-Scargle periodograms from the timing residuals of a selection of pulsars.

The phase residuals used in the Lomb-Scargle analysis were obtained in the manner described in Chapter 4, i.e., by fitting the timing data with a second order polynomial, together with a fit for position and dispersion measure. A further step taken for the purposes of the Lomb-Scargle analysis was to remove from the data the microjumps identified in Chapter 4. In a few cases, the residuals after a third order polynomial fit were used.

One feature to be expected from this analysis is a large spike at very low frequencies because the residual plots of many pulsars show a long-term trend with a period close to the time span of the data (up to $T = 2500$ days in the present study). This is a common feature in pulsar timing residuals and it is unlikely to be due to a planet. Hence, any sinusoidal features with a period longer than $\sim T/2$ days indicated by the periodogram was ignored.

Table 6.8: Results of a Lomb-Scargle analysis.

Pulsar PSR B	N	Order	Period (days)	Significance level
0736-40	92	3	–	86%
0740-28	112	2	264	97%
0835-41	84	3	537	99%
0923-58	92	3	–	79%
0940-55	85	2	–	43%
0959-54	88	3	–	78%
1054-62	80	2	–	30%
1323-58	105	2	–	$< 1\%$
1323-62	77	2	960	97%
1358-63	81	2	–	82%
1426-66	79	2	–	73%
1556-44	76	3	–	$< 1\%$
1558-50	85	2	–	43%
1600-49	72	2	–	20%
1641-45	91	2	730	98%
1706-16	60	2	–	91%
1727-47	64	3	485,690	98%, 99%
1737-39	76	2	–	$< 1\%$
1742-30	68	3	–	72%
1749-28	83	2	–	87%

Results

Figure 6.10 shows three examples of the Lomb-Scargle periodograms obtained from the analysis. The maximum frequency in the plots corresponds to the "average" Nyquist frequency in the data. A spectral oversampling factor of 10 was used in each case.

Table 6.8 lists the pulsars used in the analysis and the most significant periodic features which were evident in the Lomb-Scargle periodogram. The columns list the pulsar name, the order of the polynomial fit used to obtain the residuals that were analysed, the period (in days) of any cyclical features that are significant at a level $\geq 95\%$ (against the hypothesis of random noise), and the level of significance of the feature. The significance of the largest spike is also quoted here if it is $< 95\%$. Typically, a significance level of 95% corresponds to a spike in the periodogram with peak power greater than ~ 8.0 for the Mt Pleasant data. The large spike at the lowest frequency in the periodogram is ignored, for reasons outlined above.

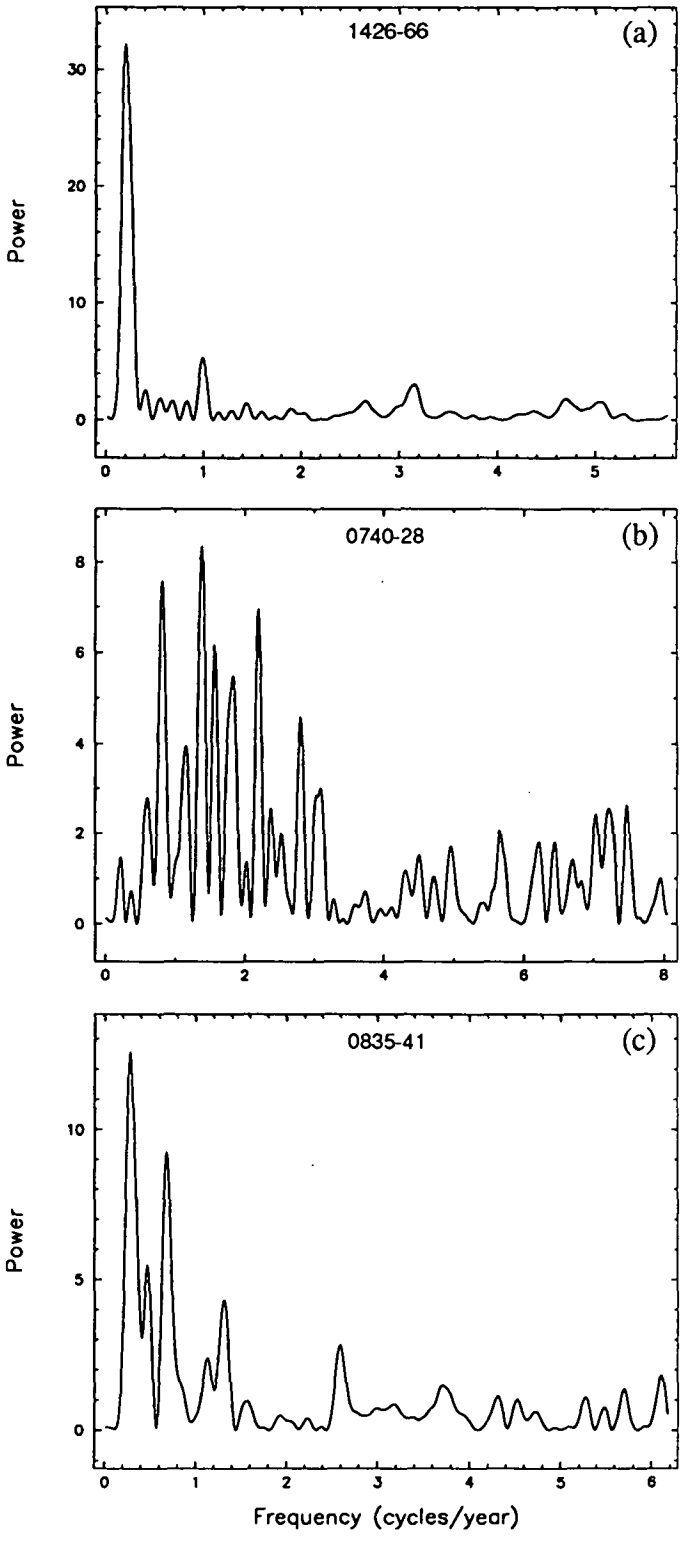

Figure 6.10: Lomb-Scargle periodograms obtained for: (a) PSR B1426-66, (b) PSR B0740-28, and (c) PSR B0835-41. The large spike at the lowest frequency has been ignored because such long-period features are common in pulsar timing residuals and, hence, are unlikely to be due to a planet.

Discussion

The results show that the timing data for some pulsars are worthy of more detailed analyses, especially on PSRs B0740-28, B0835-41, B1323-62, B1641-45 and B1727-47. The present results are difficult to interpret because the contribution from intrinsic timing noise is unknown. Timing noise can easily mimic the effect of one or more orbiting planets and, equally, an ensemble of planets can mimic timing noise.

Cordes (1993) has performed a series of simulations to assess the detectability of planets around pulsars in the presence of red and white noise. The results show that Earth-mass planets with orbital periods of $1 - 5$ yr are only marginally detectable around some long-period pulsars with an intrinsic noise level as low as 1 ms. Interpretation of the data is complicated by the removal of (at least) a second order polynomial and a position fit, along with the finite and unevenly sampled data sets used in the analysis (Cordes 1993). Red noise also makes it harder to detect multiple planets.

All of these findings suggest that planets are difficult to detect around long-period pulsars. Hence, alternative mechanisms that can produce timing noise should be thoroughly explored in the first instance and if the data are not consistent with any of them, the planetary hypothesis should be investigated further. The timing noise of 5 out of the 6 pulsars mentioned above can be accounted for by a pure random walk process or discrete events (or a combination of both). The remaining pulsar, PSR B0740-28, shows low-level timing noise (after allowance for microjumps) that is not attributable to a random walk process. As mentioned earlier in the thesis, this low-level activity could be due to small jumps in ν and $\dot{\nu}$ occurring every $100 - 200$ days. This point was also made by Manchester *et al.* (1983). More regular timing observations of this pulsar are needed to distinguish between the possible causes of the observed timing noise.

6.5 Summary of Results

In this section, the timing activity of individual pulsars is summarised, based on all the results from the previous sections.

The data for PSRs B0403-76, B0538-75, B0808-47, B0839-53, B0905-51, B0932-52, B1056-57, B1154-62, B1451-68, B1530-53, B1700-32, B1718-32, B1747-46, B1857-26, B1937-26, B2045-16, B2048-72, B2321-61 and B2327-20 show little or no timing activity. The results of the analyses for PSRs B0628-28, B0835-41, B1054-62, B1221-63, B1426-66, B1556-44, B1600-49 and B1727-47 are roughly consistent with a random walk in ϕ. Tests on discrete events indicate that jumps in ν are significant for three of these pulsars (see Table 6.5). Furthermore, significant sinusoidal features were detected in the residuals of PSRs B0835-41 and B1727-47.

Although the timing activity in these pulsars can be attributed to PN, further analysis to examine the possibility of planetary systems may be worthwhile.

PSR B0736-40: The analyses suggest the behaviour of this pulsar is consistent with a random walk in ν. No discrete events were found to be significant with respect to a 5σ threshold test.

PSR B0740-28: The results of the strength parameter and structure function analyses are not consistent with a pure random walk process. The 5σ threshold tests on the discrete events indicate that three $\Delta\nu$ and $\Delta\dot{\nu}$ events are significant. Low-level timing noise remains after the effects of these jumps are removed from the data. This activity appears to be comprised of smaller events, occurring every 100–200 days. However, these could not be tested due to the paucity of data between each event. A sinusoidal feature in the phase residuals, with a period of about 260 days, was also found to be significant. Hence, more regular observations are needed to investigate the nature of this periodicity in the data.

PSR B0923-58: The results for this pulsar are not consistent with a pure random walk process and there are no discrete events. Timing noise is dominated by a large cubic term. Little timing activity is evident after a third order polynomial fit. However, the amplitude of the implied frequency second derivative is much too large to be attributed to pulsar braking. A single, unresolved jump in ν or $\dot{\nu}$ could easily give rise to such a cubic term. This interpretation is supported by the structure function analysis which gave a large slope of $\sim$5.5 for $D^{(3)}_{\delta\phi}$.

PSR B0940-55: The results of the strength parameter and structure function analyses show reasonable consistency with a random walk in ν. Also, six events in $\dot{\nu}$ are significant. Three of these events have negative amplitudes.

PSR B0959-54: The results are not consistent with a pure random walk process. It appears that some of the activity is due to discrete events. Two events in ν were found to be significant. A weak correlation between pulse shape changes and timing residuals was found for this pulsar. Hence, the timing activity in this pulsar may be due to a combination of discrete events and free precession. In this scenario, it is quite possible that these microjumps drive the precession.

PSR B1240-64: The phase residuals for this pulsar appear piecewise linear, indicating events in ν which occur roughly once every 500 days. All four such events appear to be significant. An interesting feature of these jumps is their alternating nature. Continued monitoring of this pulsar will enable a more detailed analysis of the observed trend. The strength parameter and structure function analyses indicate consistency with FN if the jumps in ν are not modelled in the arrival-time analysis. Low-level activity is also evident between these events but analysis of the residuals excluding the jumps produces inconclusive results due to low S/N.

PSR B1323-58: The structure function results for this pulsar are consistent with frequency noise and there are no significant events in ν or $\dot{\nu}$.

PSR B1323-62: The strength parameter and structure function results suggest consistency with FN. Two events in ν and one in $\dot{\nu}$ passed the threshold test. Hence, most of the timing activity of this pulsar may be due to discrete events, superimposed on a random walk process. However, a significant sinusoidal feature with a period of 960 days was detected in the phase residuals, suggesting the planetary system hypothesis may warrant further investigation.

PSR B1358-63: The results of the analyses show moderate consistency with FN. One jump is resolved in both ν and $\dot{\nu}$.

PSR B1449-64: The results for this pulsar are inconclusive. There are no significant events in ν or $\dot{\nu}$. The data are well described by a third order polynomial. However, the derived amplitude of $\ddot{\nu}$ is too large to be due to pulsar spin-down, indicating that the observed activity may be due to an unresolved event in ν or $\dot{\nu}$.

PSR B1558-50: The timing noise of this pulsar is the largest in the whole sample. The results of the strength parameter analysis are inconsistent with a pure random walk process, whereas the structure function slopes seem to suggest consistency with FN. Two events in $\dot{\nu}$ were found to be significant.

PSR B1641-45: This pulsar has undergone three period discontinuities (two large and one small) in the time interval 1977–1989 (Manchester *et al.* 1978, 1983, Flanagan 1993). The span of the Mt Pleasant observations includes the most recent event, which occurred in 1989. Hence, the data were analysed in two ways, namely, by using the phase residual data that: (i) did not include the jump (the jump was modelled in the arrival-time analysis), and (ii) included the jump. For method (i), the strength parameter results are not consistent with a pure random walk process, whereas the structure function slopes are roughly consistent with FN. The strength parameter results for method (ii) are similar to those obtained by using method (i), whereas the third order structure function slope is much larger. In fact, the structure function results are roughly consistent with SN. This could be due to the jump in $\dot{\nu}$ identified by Flanagan. The fractional change in ν and $\dot{\nu}$ derived from the Mt Pleasant data agree with the estimates quoted by Flanagan (1993) within the 2σ level. However, a threshold test on the jump indicates that only $\Delta\nu$ is significant. Another jump in ν is also significant. A significant sinusoidal feature with a period of 730 days was detected in the phase residuals of this pulsar, suggesting the planetary system hypothesis warrants further investigation.

PSR B1648-42: Large measurement uncertainties make it difficult to meaningfully probe the data on this pulsar. The present results are inconsistent with a pure random walk process and the analysis produced only one candidate event but it was not significant at the 5σ level.

PSR B1706-16: The results of the strength parameter analysis show reasonable consistency with FN, especially after third order polynomial fits. This interpretation is supported by the structure function analysis, although the slope of $D^{(3)}_{\delta\phi}$ is

larger than expected (close to 4). An event in $\dot{\nu}$ can give rise to such an increase in the structure function slope. In fact, three events were found to be significant, two in ν and one in $\dot{\nu}$.

PSR B1737-30: This pulsar undergoes period discontinuities at a greater rate than any other known pulsar (McKenna & Lyne 1990). Analyses were carried out on phase residual data which both included and excluded four discrete jumps within the observational data span. The phase residual data excluding the jumps show a large cubic term, whose amplitude is much too large to be due to pulsar braking. It is possible that this third order term is due to the long-term relaxation from a previous glitch which is linear in time. The phase residual data which include the jumps are shown in Appendix C. The strength parameter and structure function analyses using both sets of data gave results which are inconsistent with a pure random walk process. Instead, most activity seems to be due to discrete events, although least squares fits between events show that additional activity is present. All four events in ν are significant, but they do not appear to be accompanied by a significant jump in $\dot{\nu}$. A large jump (glitch) occurred at approximately TJD 9240 which was not included in these analyses. This glitch was modelled in the arrival-time analysis which produces the post-fit phase residuals.

PSR B1737-39: Timing activity is not attributable to a pure random walk process or distinct events. The large third order structure function slope ($\sim$4.0) indicates that some of the observed activity may be due to one or more unresolved events in $\dot{\nu}$. One such event is almost significant (see Table 6.5).

PSR B1742-30: Strength parameter and structure function analyses give results which are not attributable to a pure random walk process or distinct events. The phase residuals after a third order fit show little evidence of timing activity. However, the implied value of $\ddot{\nu}$ is too large to be due to pulsar spin-down. The structure function analysis gave a large slope for $D^{(3)}_{\delta\phi}$ (> 6), indicating that most of the observed activity may be due to an unresolved event in $\dot{\nu}$.

PSR B1749-28: The results are not consistent with a pure random walk process. The significance tests demonstrate that discrete events produce much of the timing activity of this object. Three events are significant, one in ν and two in $\dot{\nu}$.

Five of the pulsars in the Mt Pleasant timing survey overlap with the JPL sample of objects studied by Cordes & Downs (1985). They are PSRs B0628-28, B0736-40, B1706-16, B1749-28 and B2045-16. The data from the Mt Pleasant observations of PSR B2045-16 show little timing activity (see phase residual plot in Appendix C), whereas the JPL data show a significant cubic term which Cordes & Downs have attributed to jumps in $\dot{\nu}$. It appears that there have not been any significant jumps in this pulsar during the 7 years of Mt Pleasant observations. For PSR B0628-28, the results are consistent with PN and the level of timing activity over this time interval is less than that found by Cordes & Downs. These authors

found that a pure random walk process was not responsible for the timing activity. Instead, they found a jump in $\dot{\nu}$ was significant. This jump can easily account for the difference in the level of timing noise between the two data sets. Another interpretation of the observed differences in the consistency (or lack thereof) with a random walk process is discussed below. The results for the remaining three pulsars are similar to those obtained from the JPL data, with the exception of PSR B1707-16. The present data have revealed three microjumps whereas none of the events tested in the JPL data set were found to be significant.

As a final point, it is worthwhile considering the effect of the time span of the data on the results obtained from the analyses. It is possible that the slope of the power spectrum of the phase fluctuations in some pulsars steepens towards lower fluctuation frequencies (longer time-scales), i.e., the fluctuations have a composite spectrum. Alpar *et al.* (1986), Cheng (1987a,b) and Jones (1990d) have discussed this possibility in relation to their theories of timing noise. In relation to the time domain analyses presented in this chapter, a composite spectrum of phase fluctuations could show apparent consistency with PN if the time span of the data probed is relatively short, FN over longer time spans, and SN over very long time spans.

Alternatively, a composite spectrum could be one explanation for results which do not show consistency with a pure random walk process. This inconsistency is especially true if the power at a given fluctuation frequency is underestimated because the observing time-scales are smaller, or not much longer, than the time-scales of the variations due to timing noise. A similar problem has been discussed by Deshpande & Nityananda (1990) in connection with intensity variations due to refractive scintillations. They have shown that the modulation amplitude of long-term (refractive) intensity variations of pulsars can be substantially underestimated if the observing time spans are not much longer than the variation time-scales themselves.

6.6 Conclusions

A variety of analyses have been performed on the phase residuals obtained from timing measurements on 45 pulsars. From the results, it can be concluded that the: (i) present level of timing noise of 19 pulsars is too small to obtain meaningful results; (ii) timing noise of 7 pulsars is consistent with a pure random walk process (five with PN, two with FN); (iii) timing noise of 7 pulsars can be attributed to microjumps superimposed on a random walk process; (iv) timing noise of 7 pulsars can be attributed to microjumps plus other activity (in the case of PSR B0959-54, this activity may be due to the effects of free precession of the pulsar); and (v) timing noise of 5 pulsars is unidentified or unresolved. The phase residuals of three pulsars in this last category are well described by a large cubic term plus

low-level noise. The cubic term could easily arise from a microjump in ν or $\dot{\nu}$, in which case these pulsars would be placed in category (iv). The microjumps in ν and $\dot{\nu}$ observed from pulsars in categories (iii) and (iv) have amplitudes of both signs, with $|\Delta\nu| \simeq 5 \times 10^{-10} - 2 \times 10^{-8}$ Hz and $|\Delta\dot{\nu}| \simeq 1 - 10 \times 10^{-16}$ Hz s^{-1}.

The timing data for relatively few pulsars show consistency with a pure random walk process, suggesting that a mixture of noise processes or some other mechanism is responsible for the timing noise of most pulsars. Non-random causes such as internal superfluid oscillations, free precession and orbiting planets cannot be entirely ruled out as possible explanations, but they are extremely unlikely. In the present work, the timing activity of PSR B0959-54 may be due to a combination of the effects of free precession and microjumps.

Recent theories of physical mechanisms responsible for the observed timing noise have considered torque variations both internal to the neutron star, and those originating from the pulsar magnetosphere (Cordes & Greenstein 1981, Alpar *et al.* 1986, Cheng 1987a,b,1989, Cheng *et al.* 1988, Jones 1990d). These theories have been reviewed in Chapter 2.

As described in Chapter 2, Alpar *et al.* (1986) have proposed three models for timing noise, involving pure unpinning, mixed and external events. Alpar *et al.* (1986) conclude that timing noise is probably due to physical processes in regions external to the weak and superweak pinning regions of the crustal superfluid. The range of event signatures resulting from the present work, along with those found by Cordes & Downs (1985) and Cordes *et al.* (1988), show that none of these models, by themselves, predict the varied nature of the observed microjumps. Furthermore, none of the models are able to explain the occurrence of positive jumps in $\dot{\nu}$.

In this respect, the magnetospheric model proposed by Cheng (1987a,b) provides a suitable explanation. As discussed in Chapter 2, the proposed mechanisms can produce pure frequency noise as well as mixed processes involving a combination of SN and PN, or SN and FN, at low and high fluctuation frequencies respectively. There is a degree of support for this model since some of the observed timing activity cannot be attributed to a *pure* random walk process. Further investigation of this model necessitates the estimation of timing noise power spectra, which is considered in Chapter 8. Like other models, however, this model is based on the premise of a noise process, i.e., it does not appear to address the fact that the bulk of the timing activity in a number of pulsars is due to a small number of discrete events in ν and $\dot{\nu}$, whose magnitude can be of either sign. Furthermore, none of the results showed consistency with a SN process.

According to Jones (1990d), the occurrence of microjumps in ν and $\dot{\nu}$ of either sign, as well as the observed "two-component" power spectra of some pulsars, can arise as a result of transitions between regions of pinned and corotating superfluid vortices within the neutron star. Although a full quantitative solution is yet to

be published, it appears that this theoretical model can account for most of the results obtained from the timing noise analyses.

Two further questions must be answered in order to test the theoretical models more thoroughly, namely: (i) are the (resolved) *microjumps* part of a continuous distribution of microglitches that comprise a noise process which is observed as timing noise ?; and (ii) why is there no observed relaxation following the microjumps ?

Firstly, the results presented in this chapter indicate that the microjump amplitudes are part of a broad distribution which may have a power-law or an exponential form. Hence, a description of timing noise in terms of a noise process appears to be justified. The only exception to this generalisation occurs in the few cases where almost all of the timing activity is due to a small number of (larger) discrete events. The microquake model proposed by Pines & Shaham (1972) may be applicable in these cases, because it predicts that the time to the next microquake is proportional to the size of the quake which preceded it. The only difficulty with this explanation is that the microquakes cannot cause a positive jump in $\dot{\nu}$. This means that the microquakes must invoke some other mechanism which produces such a response.

The second unresolved issue is considerably more complicated because the absence of observed relaxation may be due to observational restrictions or the limitations of the data analysis rather than being genuine. For example, a short relaxation time-scale will not be evident in sparsely sampled arrival-time data or, alternatively, the effect of a long recovery is simply absorbed into the estimate of $\Delta\dot{\nu}$. Also, if the Q of the exponential recovery is small, the relaxation may be masked by the white noise in the data. According to the vortex creep theory, relaxation times become longer as a pulsar ages and hence the explanation given above, in the context of the long-recovery, is the most likely. On the other hand, a physical interpretation of the lack of observed relaxation is that the superfluid response to a microjump (whatever its cause) may be negligible, as in the "external event" model of Alpar *et al.* (1986).

Further comparisons of the observations and theories are necessary. By testing theoretical models such as these, observations of the timing activity of pulsars ultimately provide a further avenue to probe the structure and dynamics of neutron stars.

Chapter 7

The Timing Noise of the Vela Pulsar

7.1 Introduction

The Vela pulsar, PSR B0833-45, is the most well-studied of all pulsars in the southern sky. It emits pulses at approximately 89 ms intervals and has a characteristic age of about 11,000 years. Its emission extends across a wide range of the electromagnetic spectrum, with pulses having been observed at radio, optical and gamma-ray wavelengths.

The wealth of data obtained from radio timing observations of the Vela pulsar since its discovery has provided valuable input to theoretical models of the structure and dynamics of neutron stars (see Chapter 2). These observations have revealed the occurrence of ten[1] large glitches which have taken place at an average rate of one glitch every 2–3 years. A typical large glitch is characterised by an abrupt increase in ν with an amplitude of $\Delta\nu/\nu \simeq 2 \times 10^{-6}$, accompanied by a jump in $\dot{\nu}$ with an amplitude of $\Delta\dot{\nu}/\dot{\nu} \simeq 1\%$. In addition, two smaller (though characteristically similar) glitches have also occurred, taking place shortly after glitches 2 (Cordes *et al.* 1988) and 9 (described in Section 7.3.4). Table 7.1 lists the epochs and observed parameters of the Vela glitches that have occurred to date. For the early glitches, the epochs are only approximate. The observed parameters for the large glitches have been taken from Alpar *et al.* (1993), Chau *et al.* (1993) and references therein for glitches 1 to 9, and McCulloch (private communication, 1995) for glitch 10.

In addition to these obvious period discontinuities, the postglitch recovery in the Vela pulsar is also characterised by a high level of timing noise. This aspect has been investigated by Cordes *et al.* (1988) who used the data collected by the

[1]There was also an intermediate-size glitch about one month after the tenth Vela glitch (McCulloch, private communication, 1994).

Table 7.1: Observing parameters and epochs of glitches in the Vela pulsar.

Glitch	Epoch (JD−2440000)	Date	$\Delta\nu/\nu$ (10^{-6})	$\Delta\dot{\nu}/\dot{\nu}$ (10^{-2})
1	∼280	1969 Feb	2.35	1.3
2	∼1190	1971 Aug	2.05	1.8
2′	∼1310	1971 Dec	0.012	0.2
3	∼2680	1975 Sep	1.99	1.1
4	∼3690	1978 Jul	3.06	1.8
5	4888.6	1981 Oct 10	1.14	0.9
6	5192.1	1982 Aug 10	2.05	2.0
7	6258.4	1985 Jul 12	1.30	1.5
8	7520.3	1988 Dec 24	1.81	16.0
9	8457.9	1991 Jul 20	2.71	39.0
9′	8550.8	1991 Oct 20	0.006	0.6
10a	9559.5	1994 Jul 26	0.86	—
10b	9591.7	1994 Aug 27	0.20	—

facilities at JPL at approximately weekly intervals over a period of 14.5 years[2]. As described in Chapter 2, Cordes *et al.* have found that microjumps in ν and $\dot{\nu}$ are the basic events that underlie the timing noise of the Vela pulsar, as opposed to much smaller events comprising a random walk process. One of the problems encountered by Cordes *et al.* was the relatively coarse (weekly) sampling of the data. This made it difficult to distinguish between the rise time and decay time of events that are apparently resolved.

The Mt Pleasant observations of the Vela pulsar described below have been recorded at intervals of approximately two minutes. The aim of this chapter is to extend the work of Cordes *et al.* (1988) by making use of these phase measurements with much better time resolution.

7.2 Observations and Data Reduction

Long-term observations of the Vela pulsar have been undertaken by the Physics Department at the University of Tasmania since 1981. Daily timing and polarization data have been collected during this time. From October 1981 until May 1986,

[2]These timing observations ended in March, 1983.

Table 7.2: Observing parameters of the 14-metre system.

	Centre frequency (MHz)		
Observing parameter	635	954	1391
3dB predetection B/W (MHz)	0.25	0.80	2.0
Dispersion smearing (mP)	6	6	5
Post-detection time constant (μs)	470	470	470
Typical pulse S/N ratio[a]	> 20	> 30	$\simeq 15$
Measurement uncertainty[a] (μs)	80	50	120

[a] These values refer to profiles obtained from $\sim$2 minute integrations.

the observations were made with an equatorially mounted 14-metre parabolic antenna located at the Llanherne Radiophysics Observatory [see Klekociuk (1989) for further details]. These observations were restricted to a maximum of 5.4 hours duration each day due to the limitations of the telescope mount. The telescope system was originally equipped with a 635 MHz receiver, but this was extended in March 1986 with the inclusion of a 954 MHz receiver. At about this time, the Mt Pleasant Observatory was established with the ex-NASA 26-metre telescope, and in August 1988, the 14-metre antenna was also moved to Mt Pleasant. No data were collected between August 1986 and August 1988. The mount was extensively rebuilt during the course of the relocation. As a result of this improvement, it has been possible to observe the Vela pulsar from rising to setting, which amounts to 18 hours each day at this latitude. A third receiver, optimised for a frequency of 1391 MHz, was added to the system in April 1990.

Hence, the Vela timing data from Llanherne span postglitch regions 5 ($R_{5\text{-}6}$), 6 ($R_{6\text{-}7}$), and part of 7 ($R_{7\text{-}8}$), and the Mt Pleasant data span part of postglitch region 7 and regions 8 ($R_{8\text{-}9}$), 9 ($R_{9\text{-}10}$), and 10 ($R_{10\text{-}}$). For simplicity, the 635, 954 and 1391 MHz observations will henceforth be referred to as the L (low), H (high) and T (third) band observations respectively. In April 1994, the centre frequency of the H band was shifted to 990 MHz to avoid interference from new digital telephone channels. The parameters for each observing band used to make measurements with the 14-m system are summarised in Table 7.2. A disc/crossed-dipole feed is used for L and H band observations, and a helical feed is used at the third frequency. Apart from the daily duration of the observations, there are two minor differences between the Llanherne and Mt Pleasant observations, namely the sampling rate (256 vs 200 samples per period respectively), and the length of each integration (1008 vs 1344 pulse periods, corresponding to $\sim$1.5 min. and $\sim$2 min. respectively). The temperature corresponding to the system noise at each frequency is approximately 60 K.

The daily Vela data are stored and reduced on a regular basis by observatory staff and Prof. P. McCulloch. The standard arrival-time analysis is performed on the data with some minor additional processing. Local arrival times are referred to the solar system barycentre in the usual way and the barycentric arrival times are modelled using the TEMPO2 software. The post-fit phase residuals are then used to: (i) identify bad data points, and (ii) obtain an empirical model to correct the systematic error in the local arrival times that is introduced by a diurnal effect.

The bad points are removed from the local arrival time files and the data are once again taken through the various stages of the analysis. One or two such iterations are usually sufficient to remove most of the outlying points. The diurnal effect is manifested as a systematic error of about ± 2 milliperiods in the phase residuals. This error is prominent because the Vela pulses have a high degree of linear polarization. As the telescope tracks this source, the position angle of the linear polarization vector rotates with respect to the antenna. Imperfections in the receiving system, such as non-orthogonal dipoles, unequal orthogonal channel gains and a helical antenna with non-unity axial ratio, result in a (sidereal) diurnal variation in the pulse shape, arrival times and the observed flux. The postfit phase residuals from the TEMPO2 analysis are binned into hour angle ranges and averaged. The resultant residuals are then used as a model for the diurnal corrections.

As a by-product of the standard analysis, the Vela barycentric arrival-time data obtained from the 2-minute integrations are "compressed" by a factor of 25. That is, each compressed data point is the equivalent of a 50 minute integration, and so the measurement noise will be a factor of 5 smaller than the 2-minute data. The compressed barycentric arrival-time data were used in the timing noise analysis described in this chapter because of the superior signal-to-noise. The loss of time resolution of the phase estimates by a factor of 25 is not significant because the measurement noise is the limiting factor when attempting to resolve an event in the data over shorter time-scales.

7.3 Timing Noise Analysis and Results

The vast quantity of Vela data collected at the Mt Pleasant Observatory can be put through a range of methods of statistical analysis. Three of these methods were used in Chapter 6, namely, the estimation of strength parameters and structure functions, and significance tests on apparent jumps in ν and $\dot{\nu}$. These methods will also be used in this chapter to analyse the Vela data.

However, before any analyses can be performed, it is necessary to remove the effects of the postglitch relaxation from the data for each region. This is the first step in the timing noise analysis, which is described below.

7.3.1 Postglitch Models

There are two approaches that can be used to model the postglitch relaxation. One approach is to perform TEMPO-style modelling of the arrival phases, as described elsewhere in the thesis. The other approach is to model the relaxation using the second derivative of the phase data, $\dot{\nu}(t)$, using a least squares method such as that employed by Alpar *et al.* (1993) and Chau *et al.* (1993). It is extremely difficult to model the long-term relaxation using the first approach because of the high level of timing activity in the Vela pulsar. This is evidenced by the fact that most postglitch phase fits have only extended to $\sim$100 days after a glitch. Hence, the second approach was used for the purposes of long-term modelling. On the other hand, the time resolution and accuracy of the phase estimates make the first approach more suitable for analysing timing noise, as described in Sections 7.3.3 and 7.3.4.

Figures 7.1–7.4 display the relaxation in $\dot{\nu}$ following glitches 6–9. The data for postglitch region 5 have not been included in the analysis because they contain large gaps and are poorer in quality than the other regions. The $\dot{\nu}(t)$ data were obtained by successively fitting a second order polynomial phase model to 10-day blocks of data, sliding each fit by an interval of 1 day. The epoch for each value of $\dot{\nu}$ was taken to be near the middle of the time span fitted. The timing activity immediately following a glitch is most likely to be absorbed into the glitch fit and so the timing noise analysis will focus on the data commencing $\sim$50 days after a glitch and extending to the next glitch. Hence, an elaborate empirical model, such as the one employed by Alpar *et al.* (1993) and Chau (1993) (Equation 2.17), is not needed to model the postglitch relaxation for the purposes of the timing noise analysis. The remnant offset due to the 10 hour and 3.2 day exponential decay terms is negligible after a time interval of 50 days.

The recovery in $\dot{\nu}(t)$ was modelled with a single exponential term and a long-term recovery that is linear in time (corresponding to a new value of $\ddot{\nu}$), using the equation

$$\Delta\dot{\nu}(t) = A_{\Delta\dot{\nu}} e^{-t/\tau} + \ddot{\nu}t + C \qquad (7.1)$$

where $\Delta\dot{\nu}(t) = \dot{\nu}(t) - \dot{\nu}_{cr}$ and taking $\dot{\nu}_{cr} = 15.58 \times 10^{-12}$ Hz s^{-1}. For the last five glitches, this latter value of the frequency derivative has not been surpassed in the postglitch recovery before the occurrence of the next glitch. It is arbitrary in the sense that it only has a bearing on the constant term in Equation 7.1, which is not used. Table 7.3 shows the parameters obtained from the fits for the four postglitch regions to be analysed. The columns contain, respectively, the postglitch region, observing frequency band of the data used, observatory where the data were collected, data span fitted, amplitude and time constant of the exponential term (where $A_{\Delta\nu} = A_{\Delta\dot{\nu}}\tau$), the frequency second derivative describing the long-term linear recovery and the constant term in Equation 7.1. The estimates of the frequency second derivative are roughly in agreement with

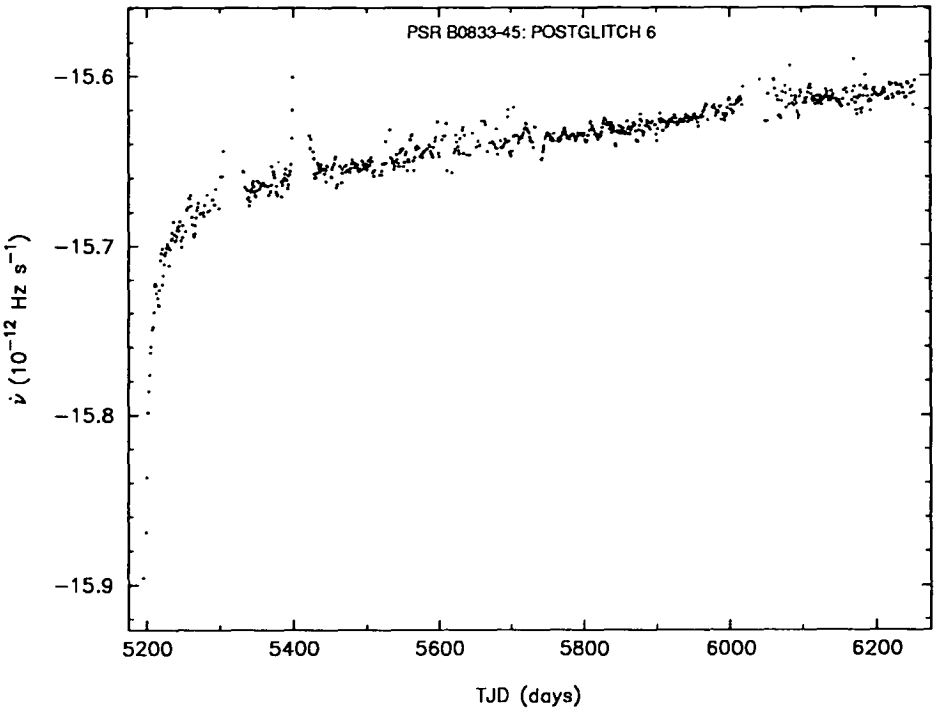

Figure 7.1: The change in the frequency derivative following glitch 6 and preceding glitch 7.

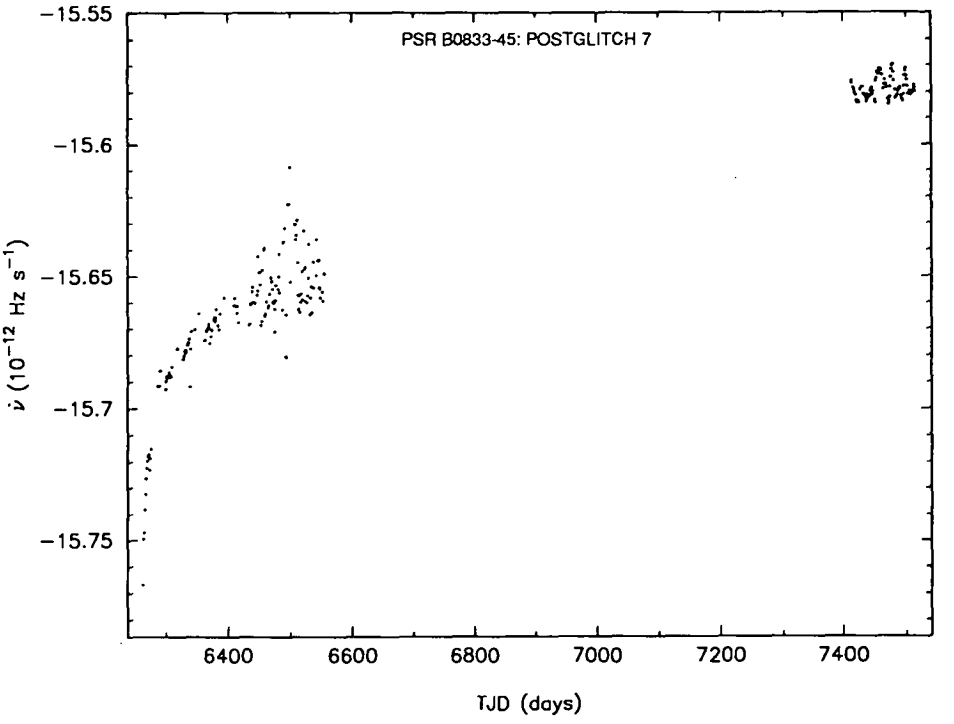

Figure 7.2: The change in the frequency derivative following glitch 7 and preceding glitch 8.

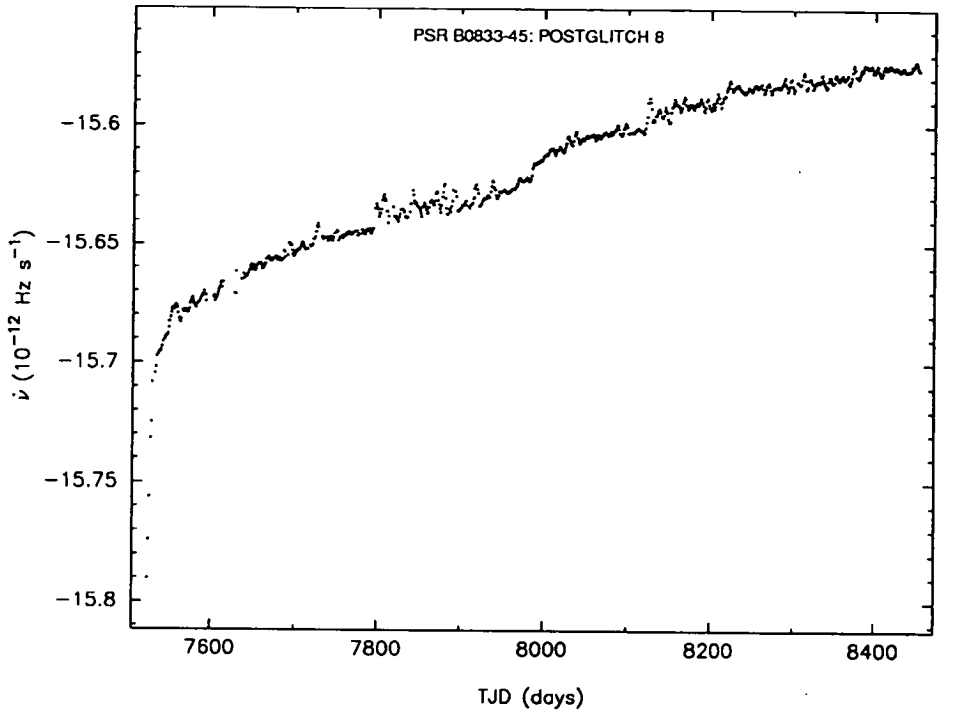

Figure 7.3: The change in the frequency derivative following glitch 8 and preceding glitch 9.

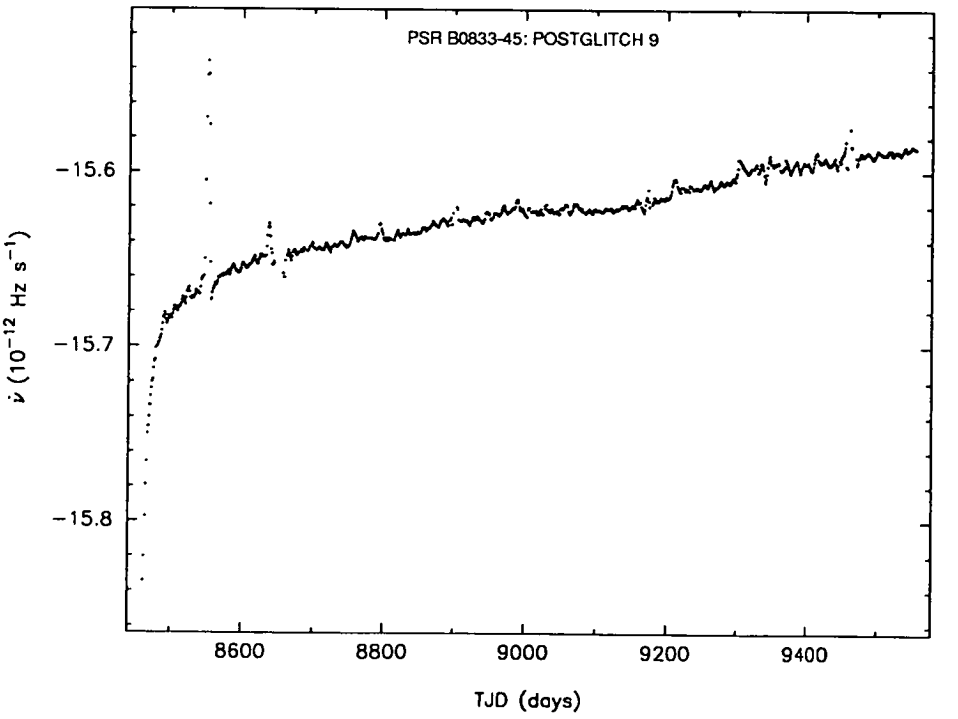

Figure 7.4: The change in the frequency derivative following glitch 9 and preceding glitch 10.

Table 7.3: Details of the postglitch regions 6 – 9 and the parameters obtained using a simple model of the recovery in $\dot{\nu}$, starting ~50 days after each glitch.

Postglitch region	Band	Observatory	Data span (TJD)	$A_{\Delta\nu}$ (μHz)	τ (days)	$\ddot{\nu}$ (10^{-22} Hz s^{-2})	C (10^{-14} Hz s^{-1})
R_{6-7}	L	Llanherne	5240–6258	0.324	81.4	6.6	-8.6
R_{7-8}	L	Llanherne	6310–6563				
	H	Mt Pleasant	7400–7520	0.222	35.4	9.1	-9.2
R_{8-9}	H	Mt Pleasant	7570–8457	0.542	138.5	6.0	-8.0
R_{9-10}	H	Mt Pleasant	8500–9559	0.261	56.4	7.7	-7.9

those obtained by Alpar *et al.* (1993) and Chau *et al.* (1993) as part of their phenomenological model of the postglitch relaxation.

The method was checked by generating the $\dot{\nu}(t)$ data once again, but with allowance for the single exponential and long-term linear recovery. The adequacy of this method in removing the effect of the intermediate to long-term postglitch relaxation can be seen by comparing Figures 7.1–7.4 with the "residual" $\delta\dot{\nu}(t)$ plots in Figures 7.5–7.9. Region R_{7-8} has been split in two in the latter group of figures because of the large gap in the data.

The plots in Figures 7.5–7.9 were generated as follows. The amplitude and time constant for each postglitch region were incorporated into the TEMPO2 glitch model (Equation 4.10) and the frequency second derivative was added to the spin-down model (Equation 4.9). These parameters were then used in conjunction with a second order spin-down model to fit the arrival phases for each region to obtain the phase residuals, $\delta\phi(t)$. The numerical derivatives of the phase residuals, namely the frequency $\delta\nu(t)$ and frequency derivative $\delta\dot{\nu}(t)$ residuals, were obtained by performing short (10-day) second order polynomial fits to the arrival phases and allowing for the long-term relaxation and spin-down terms. Short-term fluctuations are clearly evident in the $\delta\dot{\nu}(t)$ plots, but are generally not obvious in the integrals $\delta\nu(t)$ and $\delta\phi(t)$. Hence, the $\delta\nu(t)$ curves shown in Figures 7.5–7.9 were detrended to highlight the short-term fluctuations. Detrending was achieved by removing a running linear trend from the data, as described by Cordes *et al.* (1988). A time span of 200 days was used for detrending these data, except for R_{6-7}, which did not need detrending owing to the two short spans of data. A consequence of the detrending is that the derivative of the plotted $\delta\nu(t)$ is not the same as the plotted $\delta\dot{\nu}(t)$.

The phase residuals for each postglitch region obtained from the analysis described above were then used for the strength parameter and structure function analyses. These are described in Section 7.3.3. In the next section, consideration

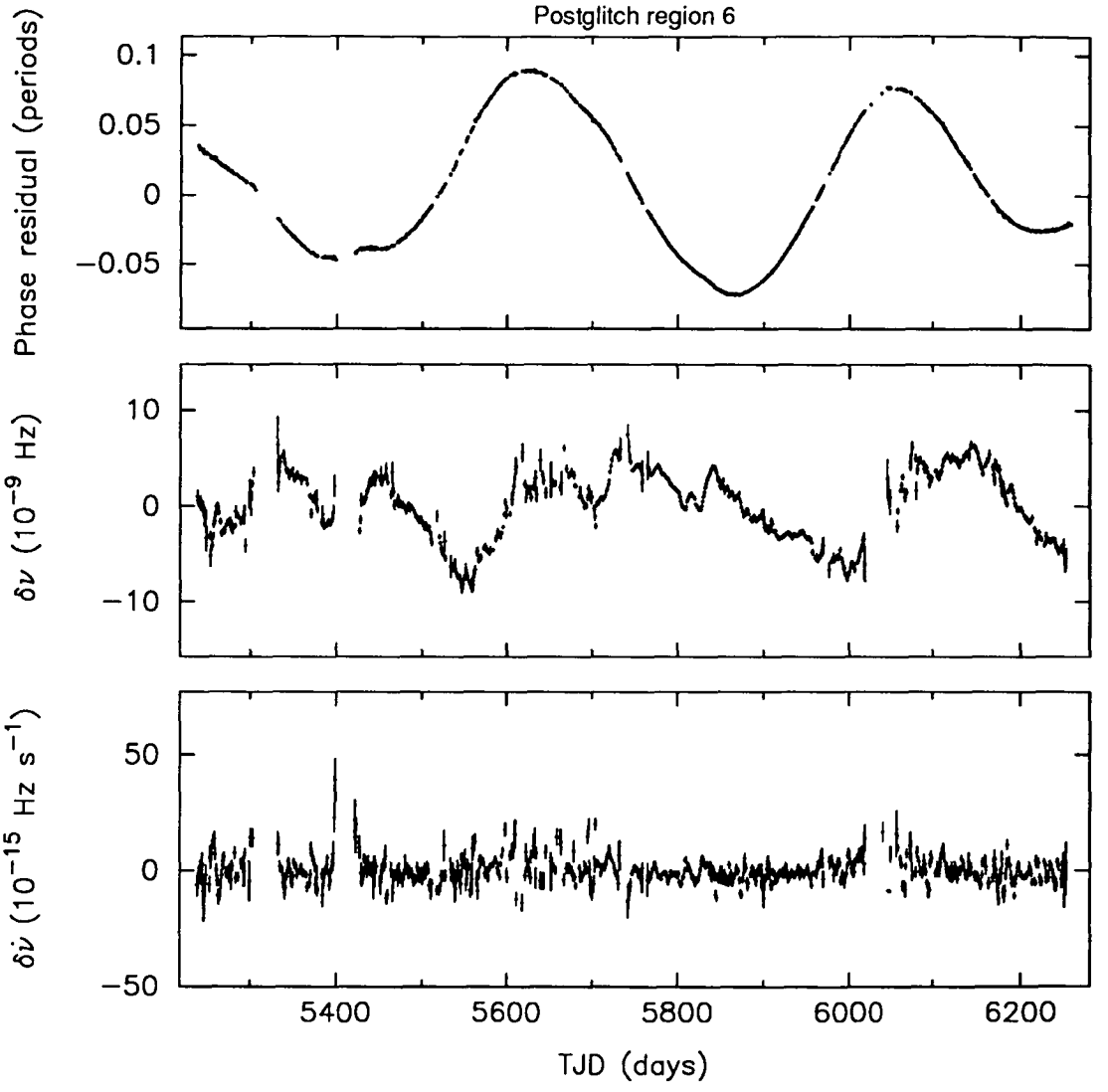

Figure 7.5: The phase, frequency and frequency derivative residuals for the interval between Vela glitches 6 and 7. The error bars represent the 1σ formal errors from the short polynomial fits described in the text.

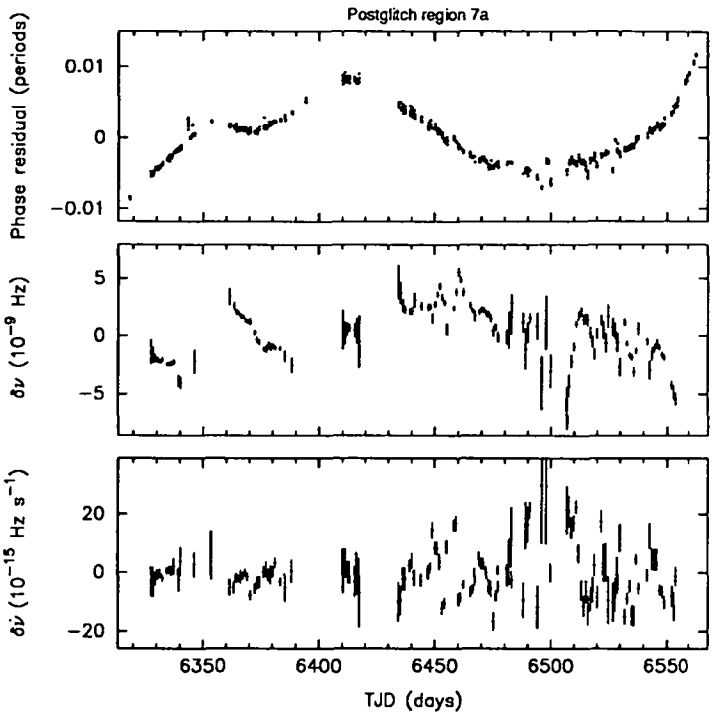

Figure 7.6: The phase, frequency and frequency derivative residuals for the first 250 days after glitch 7 (for which data were available). The error bars represent the 1σ formal errors from the short polynomial fits described in the text.

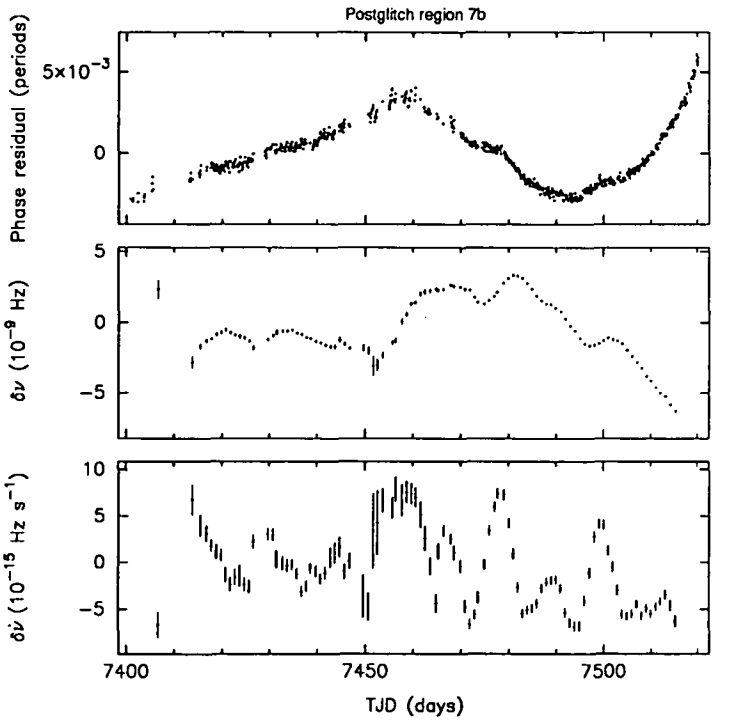

Figure 7.7: The phase, frequency and frequency derivative residuals for the last 120 days after glitch 7 and before glitch 8 (for which data were available). The error bars represent the 1σ formal errors from the short polynomial fits described in the text.

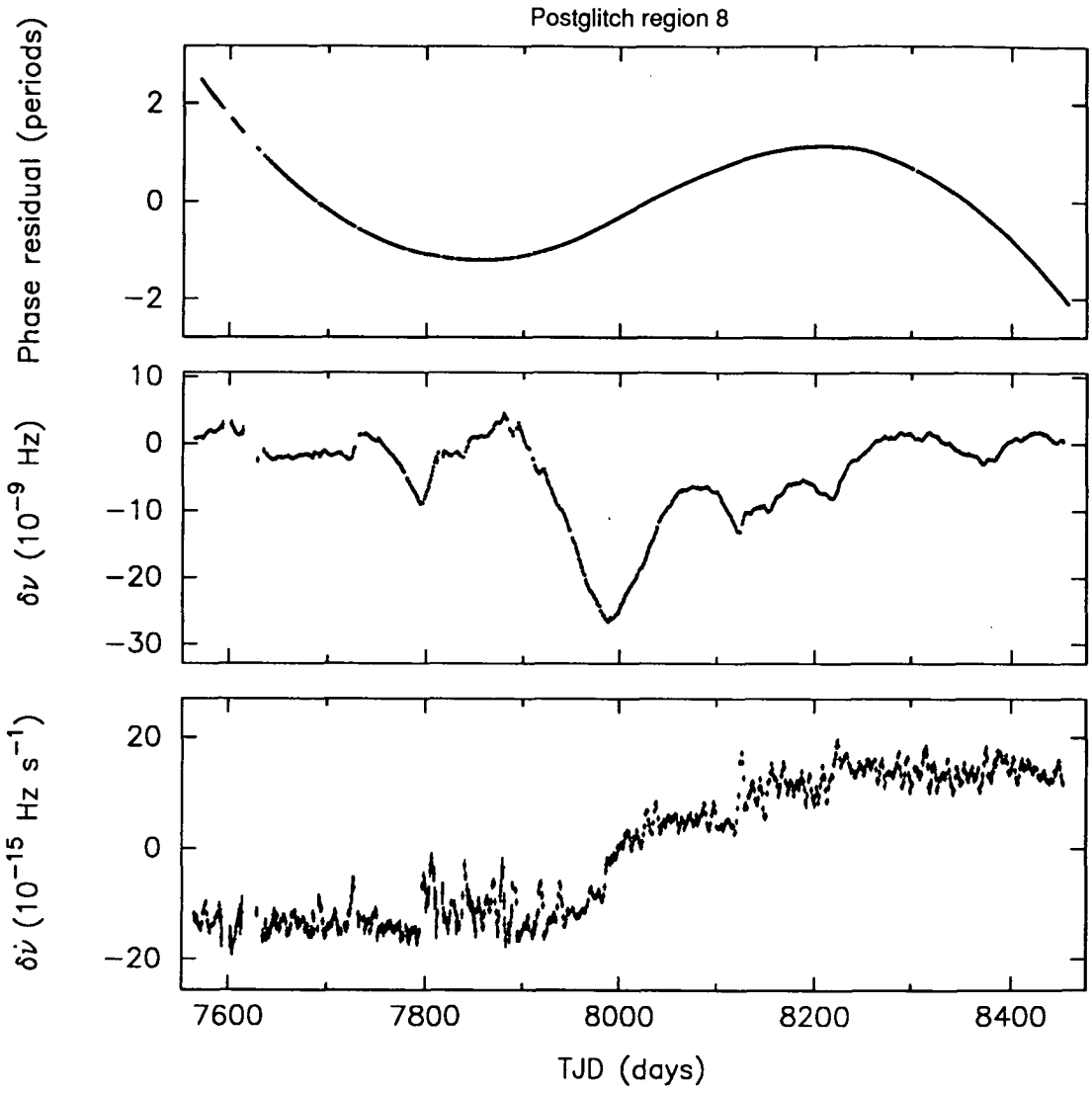

Figure 7.8: The phase, frequency and frequency derivative residuals for the interval between Vela glitches 8 and 9. The error bars represent the 1σ formal errors from the short polynomial fits described in the text.

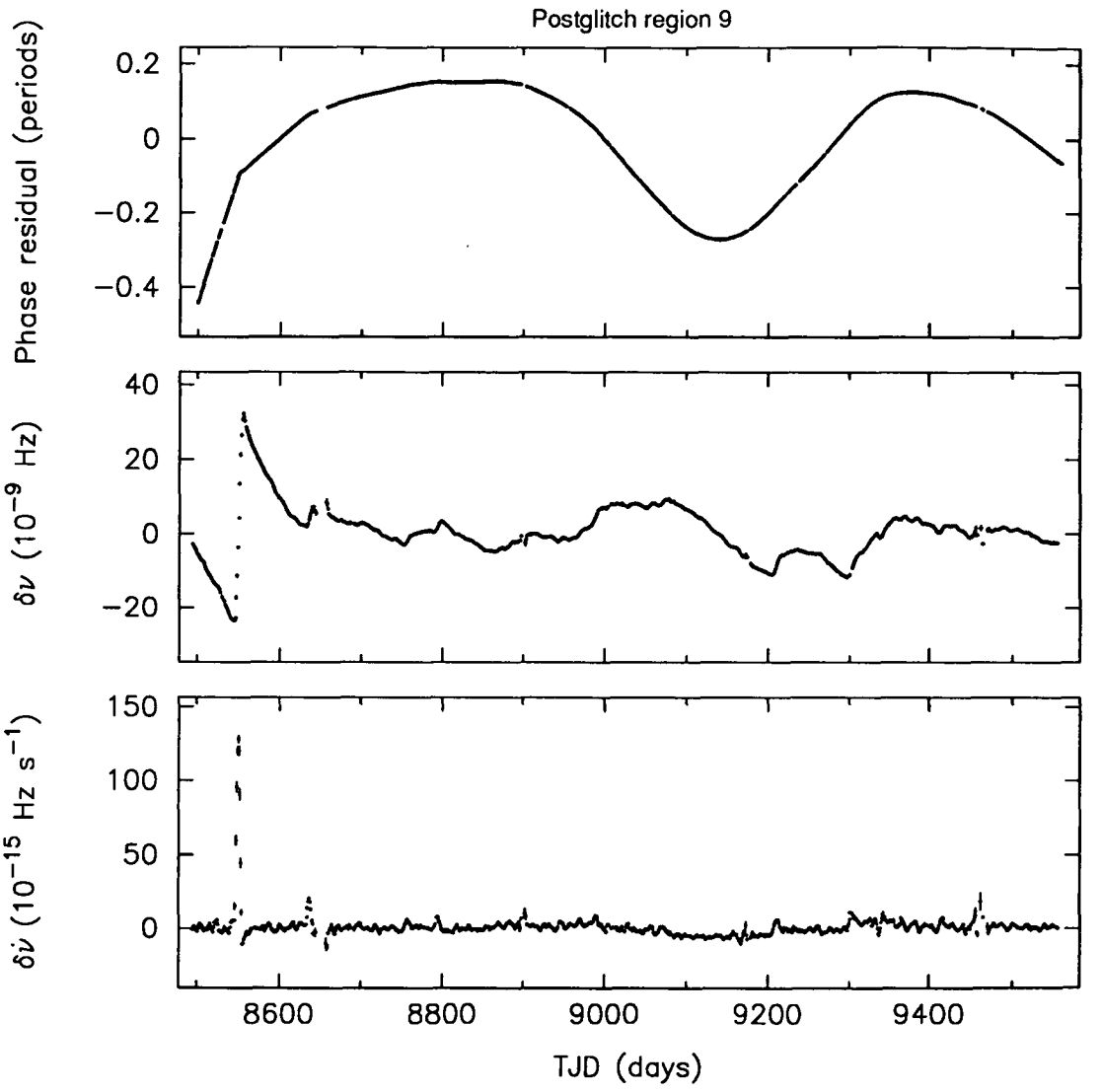

Figure 7.9: The phase, frequency and frequency derivative residuals for the interval between Vela glitches 9 and 10. The error bars represent the 1σ formal errors from the short polynomial fits described in the text.

is given to the various factors that may affect the arrival times and, hence, the results of the analyses.

7.3.2 Other Considerations

As described in earlier chapters, a white noise estimate is used to quantify the level of phase fluctuations (that are uncorrelated from sample to sample), i.e., over short time-scales. A number of sources contribute to the white noise, including measurement uncertainties, pulse jitter, pulse shape changes and interstellar scintillations. Cordes & Downs (1985) have considered that the white noise is dominated by measurement noise and pulse jitter. However, in Chapter 4 it was shown that most white noise estimates significantly exceed the measurement noise. Downs & Krause-Polstorff (1986) have also found that some of the excess noise does not have a straightforward explanation. There is some evidence that some of the excess noise in the Vela data collected at Mt Pleasant may be due to the phase estimation procedure. The cross-correlation procedure using 5-point parabolic interpolation to locate the maximum correlation can introduce errors of up to 15 μs in the arrival phases derived from the 2-minute integrations (Deshpande & McCulloch 1992).

In any case, the white noise estimate used in the timing noise analysis measures the combined effects of all such factors. A study of timing noise over short time-scales ($\leq$ hours) is beyond the scope of this chapter, in which the aim is to investigate the fluctuations over longer time-scales. In this regard, factors that can affect the arrival times over longer time-scales must be considered, such as position/ephemeris errors, interstellar refraction, and dispersion measure fluctuations. Ephemeris errors are believed to contribute no more than 4 μs, and interstellar refraction effects are believed to be negligible, for reasons outlined earlier in the thesis. It is possible that small DM variations contribute a slow fluctuation to the timing residuals, as opposed to the sudden changes associated with microjumps. However, using dual-frequency data (L and H bands) to investigate the DM changes toward the Vela pulsar during a 200-day interval, Klekociuk (1989) found that fluctuations on a time-scale of days were not significant with respect to the measurement uncertainties. The only long-term variation in the DM toward Vela reported so far is the well-established slow decrease of 0.040 $\mathrm{cm^{-3}pc\,yr^{-1}}$ (Hamilton *et al.* 1977,1985).

In order to assess whether frequency-dependent effects have a bearing on the results of the analyses, some trial strength parameter and structure function analyses (described in Section 7.3.3) were undertaken using the phase residuals derived from the 635 MHz and 954 MHz data. One would expect frequency-dependent effects such as refractive delays and dispersion fluctuations to be more noticeable in the 635 MHz observations, since these effects scale as a positive power of the

observing wavelength. In fact, the trials showed that there was no significant difference between the results obtained at each frequency. This is partly due to the higher level of white noise in the 635 MHz data. In general, the time-variable, frequency-dependent effects appear to be "buried" in the white noise or, alternatively, the random noise in the parameter used to quantify the timing noise.

On the other hand, time-variable effects that do not have a frequency dependence are difficult to separate from the intrinsic timing noise in the residuals. One example of such an effect is the "wobble" due to free precession. As discussed in Chapter 6, free precession may also result in detectable changes in the pulse shape and intensity. Cordes (1993) has detected pulse shape changes in the integrated profiles of the Vela pulsar, with a characteristic time-scale of ~ 100 days. As yet, no long-term study of intensity variations in the Vela pulsar has been reported. Clearly, a thorough investigation of the Vela pulsar timing data for the effects of free precession is required.

7.3.3 Strength Parameters and Structure Functions

As described in Chapter 6, a least squares polynomial fit to the phase residuals over an octave time span, $T_n = T_{\max} 2^{-n}$, can be used to characterise the timing noise present in the data. The net rms timing noise, $\sigma_{TN}(m, T_n)$, from an m-th order fit is obtained by quadratic subtraction of the white noise estimate from the rms timing noise (Equation 6.2).

The white noise in the data for each postglitch region was estimated from phase differences of samples separated by less than $\Delta t_{\max} = 0.1$ days, using Equation 4.31. Third order polynomials were then fitted to octave time spans for postglitch regions $R_{6\text{-}7}$, $R_{7\text{-}8}$, $R_{8\text{-}9}$ and $R_{9'\text{-}10}$. Region $R_{7\text{-}8}$ was dealt with in two parts because of a large gap in the data. For postglitch region 9, only the data after the small glitch (9′) were analysed. The results of the analysis are shown Table 7.4. The columns contain, respectively, the postglitch region, the white noise estimate, the number of blocks (N_n) used to calculate the average timing noise over a time span T_n, the rms average timing noise (σ_{TN}) after quadratic subtraction of the white noise, and the standard deviation of individual values of σ_{TN} about the mean. As noted by Cordes *et al.* (1988), the timing noise is obviously nonstationary, i.e., it increases as a positive power of T. Furthermore the dependence on T steepens for time-scales $T \geq 300$ days.

In order to get a more complete picture of the timing noise in the Vela pulsar, the data in Table 7.4 were combined with those given by Cordes *et al.* (1988, Table 4). The data analysed by Cordes *et al.* span the first six Vela glitches. The combined data are displayed as a log-log plot in Figure 7.10. This plot clearly shows the steepening that occurs beyond $T = 300$ days. The slope from a linear fit to the points in the two different regimes is simply the exponent of the scaling

Table 7.4: Timing noise of the Vela pulsar computed over octave time spans for different postglitch regions. Uncertainties are 1σ and refer to the last digit quoted.

Postglitch region	σ_W (μs)	N_n	T_n (days)	σ_{TN} (ms)	Err
$R_{6\text{-}7}$	21.1	1	1017	4.2	
		2	508	1.6	2
		4	254	0.28	5
		8	127	0.09	2
		15	63	0.036	3
		31	31	0.026	2
$R_{7\text{-}7a}$	22.2	1	245	0.16	
		2	122	0.11	2
		4	61	0.055	4
$R_{7b\text{-}8}$	12.2	1	119	0.111	
		2	59	0.022	2
		4	29	0.018	1
$R_{8\text{-}9}$	12.9	1	886	10.0	
		2	443	1.3	5
		4	221	0.25	6
		8	110	0.06	1
		16	55	0.017	2
		26	27	0.010	1
$R_{9'\text{-}10}$	13.7	1	989	9.9	
		2	494	1.9	6
		4	247	0.26	3
		8	123	0.09	2
		16	61	0.022	3
		30	30	0.011	1

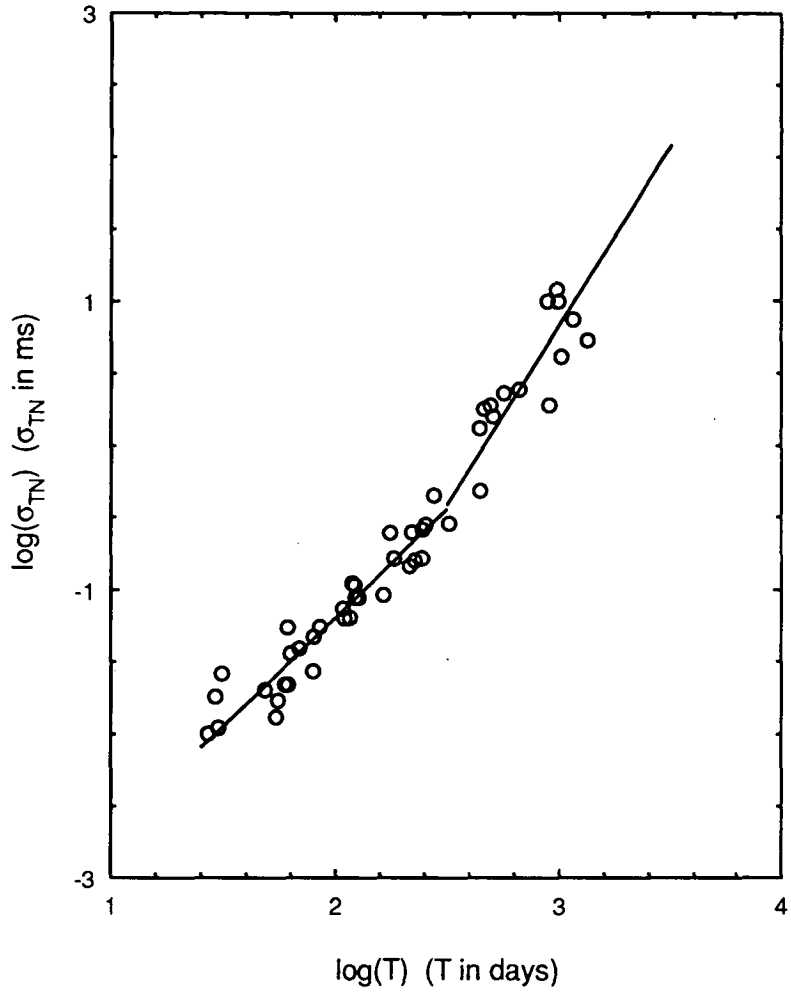

Figure 7.10: Plot showing how the level of timing noise in the Vela pulsar scales with data block length using the data from the intervals between all 10 Vela glitches.

with T of the timing noise. The fits shown in Figure 7.10 have been made with fixed slopes of 1.5 and 2.5, for reasons discussed below. However, a least squares fit to the data for $T \leq 300$ days yields an exponent of 1.42, and for $T > 300$ days, the fit yields an exponent of 2.15.

Cordes *et al.* (1988) have shown that the scaling of timing noise with block length can be modelled in terms of a random walk process comprised of many small steps in ν and $\dot{\nu}$. From Equations 6.10 and 6.11, the measured timing noise variance can be modelled as

$$\sigma^2_{TN}(3,T) = \tfrac{1}{12}C^{-2}_{1,3}S_1T^3 + \tfrac{1}{120}C^{-2}_{2,3}S_2T^5 \qquad (7.2)$$

using third order polynomial fits. In terms of the plot in Figure 7.10, these processes will result in exponents of 1.5 and 2.5 for FN and SN respectively. This model assumes that the two processes are statistically independent, so that an admixture of FN and SN yields a phase variance that is the sum of the individual

variances. Independence is guaranteed if the $\Delta\nu$ and $\Delta\dot{\nu}$ events occur at independent times, or if the amplitudes are uncorrelated, or both conditions. This "uncorrelated admixture" model is supported by both the JPL data analysed by Cordes *et al.* and the Mt Pleasant data (see Section 7.3.4).

Hence, the data indicate that the phase residuals are dominated by $\Delta\nu$ events for $T \leq 300$ days and $\Delta\dot{\nu}$ events over longer time spans. Cordes *et al.* (1988) have used the "cross-over" point to estimate the typical magnitudes of these events. They have found that $\Delta\nu \simeq 5 \times 10^{-9}$ Hz and $\Delta\dot{\nu} \simeq 2 \times 10^{-15}$ Hz s^{-1}. Discrete events are considered in the next section.

The admixture of FN and SN described above is also expected to be evident from a strength parameter analysis, since $S_k \propto \sigma_{TN}^2$. Strength parameters were computed as described in Chapter 6 and plotted as a function of octave time spans for the three types of random walks. Figure 7.11 illustrates the time dependence of the strength parameters obtained for postglitch regions $R_{6\text{-}7}$ to $R_{9'\text{-}10}$. The plots show that S_0 varies strongly with T, S_1 is almost independent of T only for time spans up to ~ 300 days, and S_2 is roughly independent of T only for time spans greater than ~ 300 days. Hence, a model in which events in ν dominate over shorter time-scales and events in $\dot{\nu}$ dominate over longer time-scales seems justified.

The structure function analysis described in Chapter 6 was also applied to the Vela data for postglitch regions 6, 8 and 9. This analysis is useful because, for a random walk of order k, a structure function of order $k+1$ or higher is independent of time and has a logarithmic slope that is uniquely determined by k (Cordes & Downs 1985). Hence, second and third order structure functions are relevant to the $k = 1, 2$ random walks indicated by the results obtained thus far.

Before computing the structure functions, the phase residuals for each postglitch region were averaged so that approximately one point per day was available for analysis. Apart from reducing the noise in the structure functions for small time lags, this procedure greatly reduces the computing time needed to obtain the estimates. The triplet of structure functions, $\Delta_\phi^{(m)}(t, \tau)$ for $m = 1, 2, 3$, was computed for postglitch regions 6, 8 and 9, subject to the following constraints: (i) a tolerance, $\epsilon = 0.944$, was used to bin the samples, corresponding to 20 bins per decade in τ; (ii) the intervals between pairs and triplets of samples were not allowed to vary by more than 2% of their separation. This restriction prevents a significant bias from appearing in the third order structure function as a square-law term (Cordes & Downs 1985). The structure functions are shown in Figure 7.12. The structure functions slopes derived from intermediate lags are given in Table 7.5.

The structure function results indicate that events in $\dot{\nu}$ dominate the timing noise of the Vela pulsar. As expected, the first order structure functions are "saturated", with slopes of ~ 1.9. This is also the case for the second order

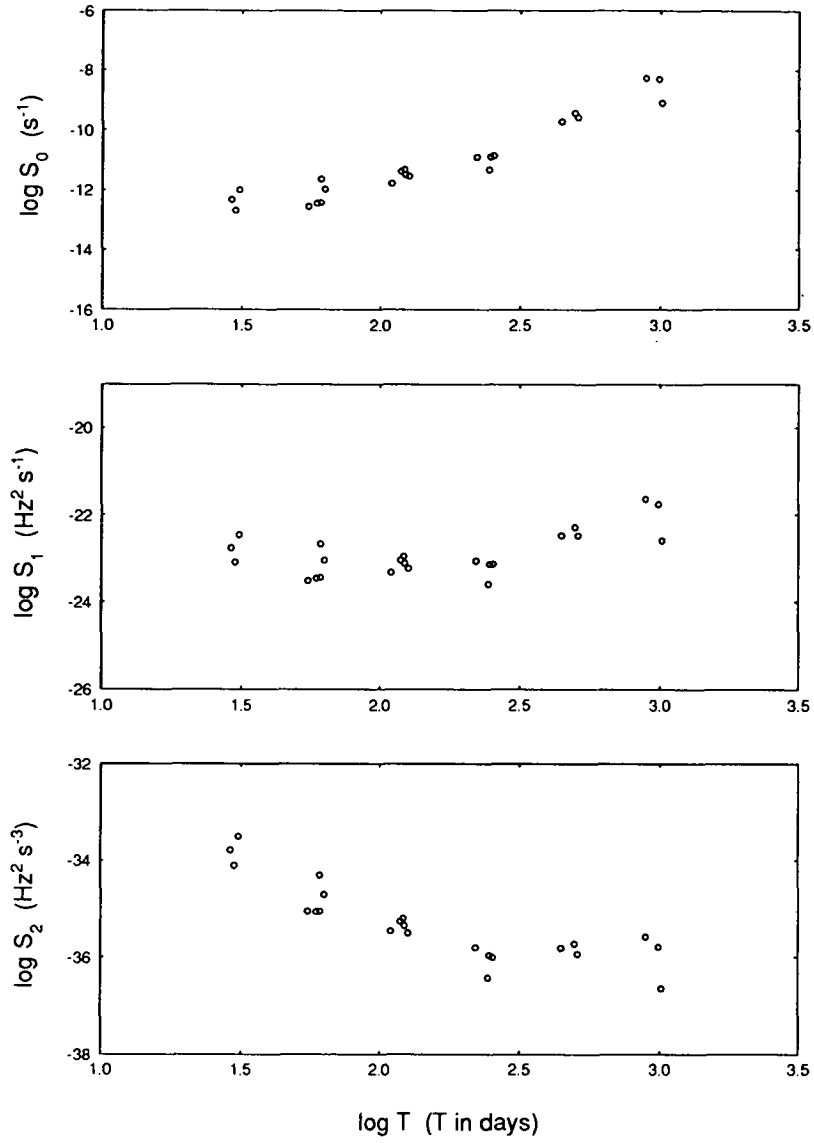

Figure 7.11: Log-log plot showing how the strength parameter for each kind of random walk process varies with the time span. The data from postglitch regions $R_{6\text{-}7}$–$R_{9'\text{-}10}$ are all shown in the figure.

Table 7.5: Results of the structure function analysis of timing noise in the Vela pulsar for three postglitch regions. The quoted uncertainties are the 1σ formal errors and refer to the last digit quoted.

Postglitch region	τ_{min} (days)	τ_{max} (days)	Structure function slopes $D^{(1)}_{\delta\phi}$	Err	$D^{(2)}_{\delta\phi}$	Err	$D^{(3)}_{\delta\phi}$	Err
$R_{6\text{-}7}$	3,13,20	63,79,126	2.01	1	3.68	1	4.49	3
$R_{8\text{-}9}$	6,10,25	100,158,251	1.87	1	3.87	1	5.72	5
$R_{9'\text{-}10}$	4,8,35	100,100,158	1.95	1	3.79	2	4.91	3

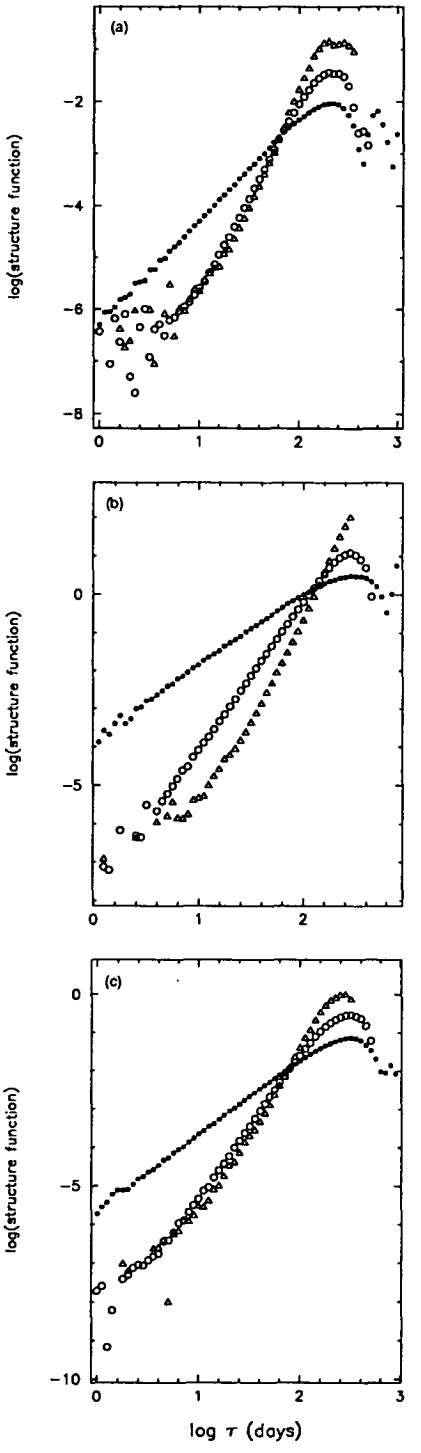

Figure 7.12: First, second and third order structure functions of the timing noise in the Vela pulsar for postglitch regions: (a) $R_{6\text{-}7}$, (b) $R_{8\text{-}9}$, and (c) $R_{9'\text{-}10}$. Key: $\bullet = D^{(1)}_{\delta\phi}$, $\circ = D^{(2)}_{\delta\phi}$, and $\triangle = D^{(3)}_{\delta\phi}$.

structure functions, with slopes of ~ 3.8. The third order structure functions have typical slopes of ~ 5, which suggests the data are consistent with SN. The structure function slope for region $R_{8\text{-}9}$ is somewhat larger than the other two regions. This can be attributed to one or two relatively large jumps in $\dot{\nu}$ near the middle of this region (see Section 7.3.4). These jumps produce a large cubic term in the phase residuals.

7.3.4 Microjumps

Cordes *et al.* (1988) identified microjumps in the JPL Vela data using the $\delta\dot{\nu}(t)$ time sequences. They identified individual events and applied a 3σ significance test on the amplitudes to see if the events were "real" with respect to fluctuations in a random walk process. This was done in much the same way as the 5σ tests applied in Chapter 6 and by Cordes & Downs (1985). In the $\delta\dot{\nu}(t)$ plots, a microjump in ν will appear as a pulse, while a microjump in $\dot{\nu}$ will simply appear as a step. Such jumps, as well as combinations of both types of jumps, are evident in Figures 7.5–7.9. One of the problems arising from the limited time resolution in the $\delta\dot{\nu}(t)$ data analysed by Cordes *et al.* (1988) is the inability to obtain a meaningful limit on the rise time or decay time associated with a jump. The high time-resolution Mt Pleasant data should be more useful in this regard.

Analysis

The analysis of microjumps in the rotation rate of the Vela pulsar was performed using the averaged arrival phases – one data point every 50 minutes (as described earlier). Provided the contribution of white noise is small, the use of the phase data rather than the $\delta\dot{\nu}(t)$ data has two major advantages: (i) higher time resolution, and (ii) avoidance of the smoothing or "smearing" effects introduced by the short polynomial fits used to generate the $\delta\dot{\nu}(t)$ data. The latter advantage is particularly important if some microjumps are separated in time by less than the span of the short polynomial fits. Using a significance test with $N = 3$, microjumps will be resolved if their rate $R \leq (N^2\delta t)^{-1}$, where δt is the typical sample interval in the data. For the JPL data, microjumps are resolved if they occur less often than once every ~ 63 days (Cordes *et al.* 1988). The present work suggests that microjumps occur at a higher rate than this value.

Hence, the $\delta\dot{\nu}(t)$ data were only used as a guide for identifying the epochs of candidate events, while the nature, magnitudes and precise epochs of the events were determined using the phase data. In the first instance, the candidate events (sharp slope changes) were identified by fitting the phase data with a polynomial over spans of ~ 10 days. After this initial identification, a TEMPO2-style analysis was performed, using a scaled-down version of the "glitch function" (Equation 4.10). This function allows for discrete jumps in ν, $\dot{\nu}$ and $\ddot{\nu}$. Initial guesses for

the magnitude of the microjumps, $\Delta\nu$ and $\Delta\dot{\nu}$, were obtained by fitting several days of phase data on either side of the candidate event, using a third order polynomial with fixed $\ddot{\nu}$ (as described earlier). The TEMPO2 analysis then proceeded as follows: (i) the pre-jump data were fitted with a third order polynomial with constant $\ddot{\nu}$; (ii) the rotation parameters so derived were held constant and the reduced glitch function, using the initial guesses, was fitted to the data spanning the candidate jump to obtain the jump parameters relative to the spin-down model; (iii) the new estimates of the epoch, $\Delta\nu$, $\Delta\dot{\nu}$ and $\Delta\ddot{\nu}$ (where applicable) were then used as input parameters to the glitch function to improve the fit; and (iv) procedure (iii) was repeated until the fit converged to a solution.

The magnitudes and epochs of all the candidate microjumps in postglitch regions $R_{6\text{-}7}$ to $R_{9'\text{-}10}$ were obtained using this iterative technique. Convergence to a solution was achieved with, typically, less than five iterations, indicating that rise and decay times may not be observable in the microjumps. This aspect is considered further in Section 7.4. In a few instances, convergence could not be achieved because the event amplitude was very small. In these instances, the best-fit parameters were used, together with estimates of the errors that reflect such uncertainty.

Next, the candidate events were tested against the hypothesis that they are merely due to fluctuations arising from a random walk process comprised of many events which are too small to resolve individually. As described in Chapter 6, FN and SN processes have standard deviations of $\sigma_{\Delta\nu} = \sqrt{S_1\Delta t}$ and $\sigma_{\Delta\dot{\nu}} = \sqrt{S_2\Delta t}$ respectively. A 3σ test was applied to the microjump amplitudes, i.e., the $\Delta\nu$ were tested against $3\sigma_{\Delta\nu}$ and the $\Delta\dot{\nu}$ were tested against $3\sigma_{\Delta\dot{\nu}}$.

The strength parameters S_1 and S_2 can be estimated in a number of ways, e.g., from Figure 7.10 or Figure 7.11 for $T < 300$ d and $T > 300$ d, from the slope of a plot of σ_{TN}^2 against T^3 or T^5, or individually from each postglitch region in a manner similar to that described in Chapter 6. The most reliable estimate of the mean strength parameter was obtained using the first of these methods. Using the uncorrelated admixture model, the two slopes in Figure 7.10 are described by

$$2\log\sigma_{TN} = 14.8 + \log S_1 + 3\log T \tag{7.3}$$

for $T < 300$ d, and

$$2\log\sigma_{TN} = 22.8 + \log S_2 + 5\log T. \tag{7.4}$$

for $T > 300$ d. Furthermore, at the cross-over point ($T = 300$ d),

$$S_1 \simeq 9.45 \times 10^{12} S_2. \tag{7.5}$$

Using the data plotted in Figure 7.10, which was taken from all nine postglitch regions, the estimated strength parameters for the Vela pulsar are

$$S_1 \simeq 6.8 \times 10^{-24} \quad \mathrm{Hz^2\ s^{-1}}, \tag{7.6}$$

$$S_2 \simeq 7.2 \times 10^{-37} \quad \mathrm{Hz^2\ s^{-3}}. \tag{7.7}$$

Tests

A number of tests were performed to assess the sensitivity and validity of the method of analysis described above. Microjumps were simulated by inserting discontinuous changes in ν and $\dot{\nu}$ of various magnitudes into a "quiet" region of the Vela timing data. The data span from TJD 7746 to TJD 7776 was used for this purpose. This also enabled an assessment of the effect of white noise in the estimation of the microjumps parameters, as well as a determination of the limit of detectability of the microjumps.

The jump magnitudes used in the tests were in the ranges $\Delta\nu = \pm(0.001-0.01)$ μHz and $\Delta\dot{\nu} = \pm(0.001 - 0.01)$ pHz s^{-1}, as well as zero for one parameter or the other. When applied to the simulated data, the iterative technique described above produced the correct microjump amplitudes and epoch, within the uncertainties. Furthermore, the technique was able to identify microjumps as small as 10^{-9} Hz and 10^{-15} Hz s^{-1}. As a further check, a $\dot{\nu}(t)$ sequence was generated using the simulated microjumps. The plot showed the pulses and steps resulting from microjumps in ν and $\dot{\nu}$ for larger magnitudes, but microjumps as small as 10^{-9} Hz and 10^{-15} Hz s^{-1} could not be distinguished from the "noise" in $\dot{\nu}(t)$.

The ability to detect and measure a simple exponential relaxation after a microjump was also tested (microjump relaxation is discussed in Section 7.4). An example of the parameters that were used, using the notation of Equation 4.10, is as follows: $\Delta\nu_c = 5 \times 10^{-9}$ Hz, $\Delta\dot{\nu}_c = 0$, $\Delta\nu_1 = 2 \times 10^{-8}$ Hz, and $\tau_1 = 5$ d. As expected, a simple fit for $\Delta\nu$ and $\Delta\dot{\nu}$ using the iterative technique gave false estimates. However, the post-jump residuals clearly showed the cubic-like variation expected from fitting an exponential function with a second order polynomial. The model was extended to allow for an exponential decay, resulting in accurate estimates of the simulated microjump parameters. In another test, the time constant of the simulated microjump was increased to 50 days. In this case, it was not possible to detect the exponential term using the simple $\Delta\nu$, $\Delta\dot{\nu}$ fit over short time spans ($\sim$ 20 days) because a large proportion of the exponential decay is absorbed into the $\Delta\dot{\nu}$ term. The "remnant" cubic was not evident because it is masked by the white noise in the data. In general, the tests demonstrated that the technique used in the microjump analysis gives valid results.

Results

The results of the significance tests are shown in Table 7.6. The columns contain, respectively, the postglitch region analysed, the epoch of the microjump, an upper limit to the rise time of the jump (Δt), the magnitude of the microjump in ν ($\Delta\nu$), the 1σ uncertainty in $\Delta\nu$ (refers to the last digit quoted), the significance level of the microjump in ν ($|\Delta\nu/\sigma_{\Delta\nu}|$), the magnitude of the microjump in $\dot{\nu}$ ($\Delta\dot{\nu}$), the 1σ uncertainty in $\Delta\dot{\nu}$ (refers to the last digit quoted), and the significance level of

the microjump in $\dot{\nu}$ ($|\Delta\dot{\nu}/\sigma_{\Delta\dot{\nu}}|$).

Out of the 140 events in ν and $\dot{\nu}$ that were tested, a total of 84 events in ν (65 of which have a *positive* magnitude) and 120 events in $\dot{\nu}$ (62 of which have a *positive* magnitude) were found to be significant with respect to the 3σ test. In fact, most of these jumps are significant at a level $> 5\sigma$. The linear correlation coefficient obtained from the amplitudes of the 74 events comprised of jumps in both ν and $\dot{\nu}$ was 0.09, justifying the use of the "uncorrelated admixture model".

Like the microjumps observed in other pulsars (Chapter 6), the microjumps listed in Table 7.6 also display a complete range of event signatures, i.e., ($\Delta\nu$,$\Delta\dot{\nu}$) with signs $(\pm,\pm)$, $(\pm,0)$ and $(0,\pm)$. The examples in Figure 7.13 illustrate the varied nature of these microjumps. Microjumps account for most, but not all, of the timing activity in the Vela pulsar. This can be seen in Figure 7.14, which shows the residual phase after allowance is made for the microjumps that occurred between TJD 7920 and TJD 8095. The residuals show a quasi-sinusoidal oscillation with a period of $\sim$100 days.

A plot of the distribution of microjump amplitudes is also useful as it can provide a clue to the relationship between microjumps and other sources of timing activity (e.g., microglitches). Histograms of both the actual magnitudes and absolute magnitudes of the $\Delta\nu$ and $\Delta\dot{\nu}$ events were generated, since the former distributions have a gap in a small range around zero amplitude. The histograms are shown in Figure 7.15. The microjumps in ν have a range $|\Delta\nu| \simeq 10^{-9} - 10^{-8}$ Hz, with mean values $\mu_{\Delta\nu} = 1.9 \times 10^{-9}$ Hz and $\mu_{|\Delta\nu|} = 3.1 \times 10^{-9}$ Hz. The microjumps in $\dot{\nu}$ have a range $|\Delta\dot{\nu}| \simeq 0.5 - 10 \times 10^{-15}$ Hz s^{-1}, with mean values $\mu_{\Delta\dot{\nu}} = 0.4 \times 10^{-15}$ Hz s^{-1} and $\mu_{|\Delta\dot{\nu}|} = 2.9 \times 10^{-15}$ Hz s^{-1}.

The small glitch 9′

Almost 100 days after the ninth Vela glitch, there was another glitch whose size was 2–3 orders of magnitude smaller than the large glitches (see Table 7.1). Figure 7.16(a) shows the phase residuals around the time of glitch 9′. If this glitch is fitted with the simple microjump model (fit for $\Delta\nu$, $\Delta\dot{\nu}$ and epoch), the postglitch residuals display a cubic-like term, as shown in Figure 7.16(b). Such a feature is characteristic of a second order polynomial fit to an exponential function, the latter resulting from the postglitch relaxation. Furthermore, the cubic term was found to persist regardless of the postglitch data span used in the fit. Hence, the glitch function (Equation 4.10), with a single exponential term, was used to model the glitch. This model provided an excellent fit to the data. The resulting parameters for the glitch and postglitch decay are listed in Table 7.7. The quoted errors are 1σ and refer to the last digit quoted. The parameters are very similar to those obtained by Cordes *et al.* (1988) for the small glitch 2′. Glitch 9′ is also clearly seen in Figure 7.4. The decay parameters ($\Delta\nu_1, \tau_1$) obtained from the phase data

Table 7.6: Results of statistical tests on apparent microjumps in ν and $\dot{\nu}$. See the main text for an explanation of each column.

Region	Epoch (TJD)	Δt (days)	$\Delta\nu$ (†)	Err	Sig.	$\Delta\dot{\nu}$ (§)	Err	Sig.
R_{6-7}	5257.6	0.6	2.4	3	4.0	3.15	8	16.3
	5301.9	0.2	6.84	8	20.0			
	5369.1	0.4	-2.8	1	5.8	-0.66	4	4.2
	5427.9	0.8				2.5	9	11.2
	5438.3	0.4	3.36	7	6.9	-3.52	6	22.3
	5480	1.0				0.8	1	3.2
	5561.5	0.4	2.9	2	6.0	2.79	8	17.7
	5598.5	0.4	2.27	6	4.7			
	5682.1	0.4	-3.6	2	7.4	-0.85	9	5.4
	5720.7	0.1	4.98	3	20.5	-1.54	1	19.5
	5780	2.0				-1.76	8	5.0
	5812.6	0.3	2.4	2	5.7	-1.0	3	7.3
	5831.2	0.1	5.88	5	24.3	0.56	2	7.1
	5890	1.0				2.0	8	8.0
	5901.9	0.3	-1.77	6	4.2	-0.58	2	4.2
	5962	2.0				2.1	1	6.0
	5994.1	0.7				1.6	3	7.7
	6015.0	0.3	3.6	2	8.6	-2.0	2	14.6
	6047.2	0.2	5.3	3	15.5	0.9	2	8.1
	6073.3	0.3	4.1	1	9.8	-1.07	7	7.8
	6110.7	0.2	4.2	2	12.3	-0.5	1	4.5
	6141	1.3				-1.5	9	5.3
	6230	1.0				1.0	2	4.0
R_{7-8}	6319.4	0.7	2.5	1	3.9	-1.5	1	7.2
	6355.3	0.7	5.6	6	8.7	-2.0	7	9.6
	6372.0	0.6				7	2	36.2
	6406.8	0.2	5.8	1	16.9	1.33	3	11.9
	6469.5	0.3	-3.3	2	7.9			
	6550.3	0.7	-3.0	9	4.7	-2	1	9.6
	7418.0	0.7				-1.9	8	9.1
	7429.6	0.2	2.0	1	5.8	1.46	6	13.1
	7457.1	0.2	4.2	4	12.3	1.8	6	16.1
	7468.5	0.8				-6	1	26.9
	7478.07	0.6	5.49	9	29.2	1.26	9	20.6
	7500.1	0.1	3.05	9	12.6	-1.18	9	15.0
R_{8-9}	7576.5	0.2	2.4	2	7.0	2.6	2	23.3
	7588.6	0.3				0.65	8	4.8
	7610.7	0.3	-1.26	6	3.0	-5.7	3	41.7
	7644	1.0				1.10	1	4.4
	7696	2.0				-1.3	5	3.7
	7726.3	0.1	4.29	8	17.7	1.62	7	20.5
	7746	2.0				-1.33	5	3.8
	7776	1.0				-1.17	8	4.7
	7798.8	0.2	4.3	4	12.5	2.6	9	23.3
	7805.9	0.3	3.1	8	7.4	3	2	22.0

Discrete event tests, continued ...

Table 7.6: Continued.

Region	Epoch (TJD)	Δt (days)	$\Delta\nu$ (†)	Err	Sig.	$\Delta\dot{\nu}$ (§)	Err	Sig.
R_{8-9}	7815	3.0				-3.4	1	7.9
	7842.0	0.2	2.6	2	7.6	1.0	2	9.0
	7860.5	0.4	-2.0	4	4.1	7	2	44.4
	7866.5	0.2	-3.0	1	8.8	-0.8	8	7.2
	7874.9	0.2	-4.8	4	14.0	4	2	35.9
	7881.5	0.4	-2.8	9	5.8	-14	2	88.8
	7892.0	0.2	3.9	2	11.4			
	7918.4	0.5	3.0	9	5.5	8	4	45.4
	7922.8	0.2	-2.5	2	7.3	-5.5	2	49.3
	7939.7	0.2	3.8	7	11.1	-7	5	62.8
	7941.6	0.2	-1.3	1	3.8	7.63	3	68.4
	7969.6	0.3				3.0	1	22.0
	7987.4	0.3				6.0	3	43.9
	7998.1	0.2				2.9	2	26.0
	8008.3	0.4				1.17	9	7.4
	8028.2	0.2	2.0	2	5.8	1.0	6	9.0
	8035.8	0.2				2.43	1	21.8
	8086.1	0.3	1.5	2	3.6	-0.9	4	6.6
	8096.9	0.2	1.29	4	3.8			
	8125.32	0.08	4.1	2	18.9	4.6	2	65.2
	8139.0	0.2	1.9	2	5.5	-3	1	26.9
	8145.8	0.2	3.2	2	9.3	-1.4	7	12.6
	8154.4	0.1	3.2	2	13.2	7.5	2	95.1
	8195	2.0				-1.9	4	5.4
	8209	2.0				1.6	6	4.5
	8221.2	0.1	2.2	2	9.1	5.1	1	64.7
	8238.0	0.3				-1.34	2	9.8
	8272.0	0.6				-1.3	1	6.7
	8286.8	0.2	1.04	4	3.0			
	8314.3	0.2	2.11	5	6.2	-0.40	5	3.6
	8338.8	0.2	2.5	5	7.3			
	8340.44	0.08	-2.73	3	12.6	0.60	3	8.5
	8370.5	0.2	-2.3	2	6.7	5.2	6	46.6
	8379.0	0.2	-2.3	3	6.7	-2.9	5	26.0
	8389.3	0.3				-0.8	1	5.9
	8420	1.0				-1.35	9	5.4
	8438	1.0				-1.3	4	5.2
	8448.0	0.2	2.6	2	7.6	-2.6	5	23.3
R_{9-10}	8504.3	0.2	3.8	2	11.1	7.3	3	65.4
	8517.2	0.2	3.8	5	11.1	-9	3	80.7
	8522.8	0.1	4.7	2	19.4	8.7	1	110.3
	8544.1	0.4	3.0	9	6.2	4	2	25.4
	8588.8	0.3	1.3	1	3.1	-2.7	3	19.8
	8600.3	0.3	1.4	1	3.3	1.5	1	11.0
	8616.8	0.2	2.8	4	8.2	-2	2	17.9

Discrete event tests, continued ...

Table 7.6: Continued.

Region	Epoch (TJD)	Δt (days)	$\Delta\nu$ (†)	Err	Sig.	$\Delta\dot{\nu}$ (§)	Err	Sig.
$R_{9\text{-}10}$	8625.0	0.2	1.7	2	5.0	4.5	3	40.3
	8637.37	0.05	9.5	3	55.4	-7	1	125.5
	8663.7	0.1	5.6	4	23.1	5.7	9	72.3
	8670.0	0.3				7.81	5	57.2
	8698.7	0.3				-0.75	6	5.5
	8748.6	0.2	-2.2	2	6.4	2.3	5	20.6
	8758.3	0.2	1.8	2	5.2	-1.6	2	14.7
	8795.9	0.1	3.25	5	13.4	-2.69	7	34.1
	8817.7	0.4				1.47	2	9.3
	8850.0	0.6				1.13	8	5.8
	8869.8	0.3	1.4	2	3.3			
	8882.0	0.2	1.7	1	5.0	1.2	2	10.8
	8896.6	0.3	1.86	6	4.4			
	8921.8	0.3				0.5	1	3.7
	8937.9	0.5				-2.1	8	11.9
	8944.8	0.3				1.72	5	12.6
	8968.5	0.2	1.55	8	4.5	0.99	8	8.9
	8988.5	0.1	3.3	1	13.6	-0.9	2	11.4
	9002	2.0				-1.41	5	4.0
	9044.0	0.3	-1.6	2	3.8	-1.1	2	8.1
	9057.1	0.3	1.7	1	4.0	-2.7	3	19.8
	9071.65[a]	0.04	4.16	1	27.1	-3.74	3	75.0
	9156.1	0.3	2.0	1	4.8			
	9173.3[b]	0.2				2.0	1	17.9
	9209.21	0.06	5.11	6	27.2	4.13	3	67.6
	9261.5	0.3	1.6	2	3.8	-3.1	9	22.7
	9270	1.0				3.25	2	13.0
	9300.5	0.2	2.9	4	8.5	8.8	5	78.9
	9311.9	0.2	-1.86	7	5.4	-2.60	4	23.3
	9339.0	0.1	-2.87	6	11.8	1.40	7	17.8
	9361	1.0				-2	2	8.0
	9368.1	0.3	2.0	2	4.8	-4.4	6	32.2
	9378.0	0.7				4	1	19.2
	9385	2.0				-1.14	5	3.2
	9408	1.0				-5	1	20.0
	9414.2	0.1	4.0	2	16.5	6.7	2	84.9
	9428	2.0				-2.2	1	6.2
	9454	1.0				2.78	2	11.1
	9500.9	0.2	2.19	6	6.4	2.01	2	18.0
	9540	2.0				1.2	1	3.4

† In units of 10^{-9} Hz.

§ In units of 10^{-15} Hz s^{-1}.

[a] This jump was accompanied by a sudden decrease in $\ddot{\nu}$ with a magnitude $\Delta\ddot{\nu} = -(3.1 \pm 0.5) \times 10^{-22}$ Hz s^{-2}.

[b] This jump was accompanied by a sudden increase in $\ddot{\nu}$ with a magnitude $\Delta\ddot{\nu} = +(2 \pm 1) \times 10^{-22}$ Hz s^{-2}.

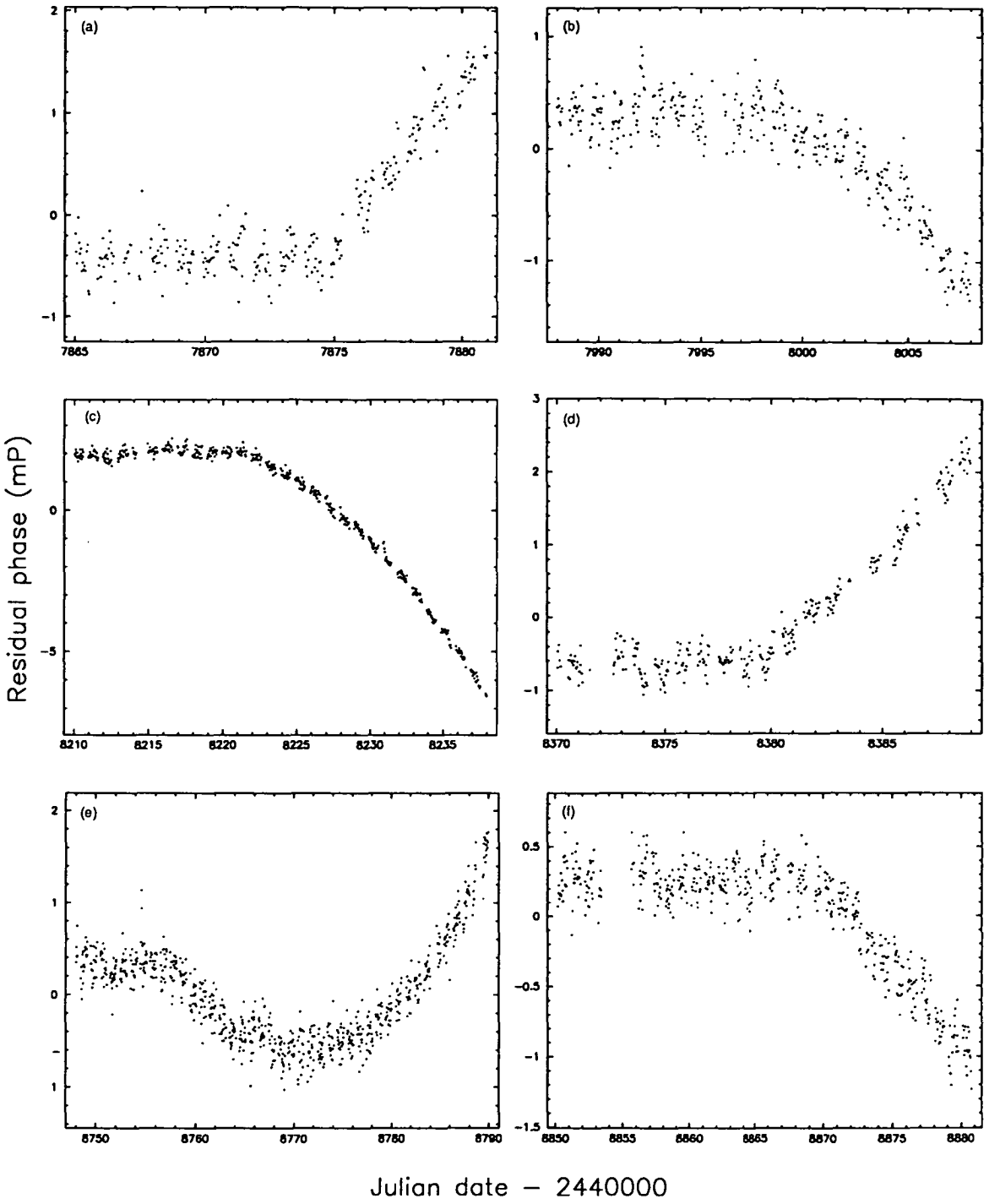

Figure 7.13: Some examples of the varied nature of the microjumps observed in the rotation rate of the Vela pulsar. The microjump epochs and signatures are: (a) TJD 7874.9, (−, +); (b) TJD 7998.1, (0,+); (c) TJD 8221.2, (+,+); (d) TJD 8379.0, (−, −); (e) TJD 8758.3, (+, −); (f) TJD 8869.8, (+,0).

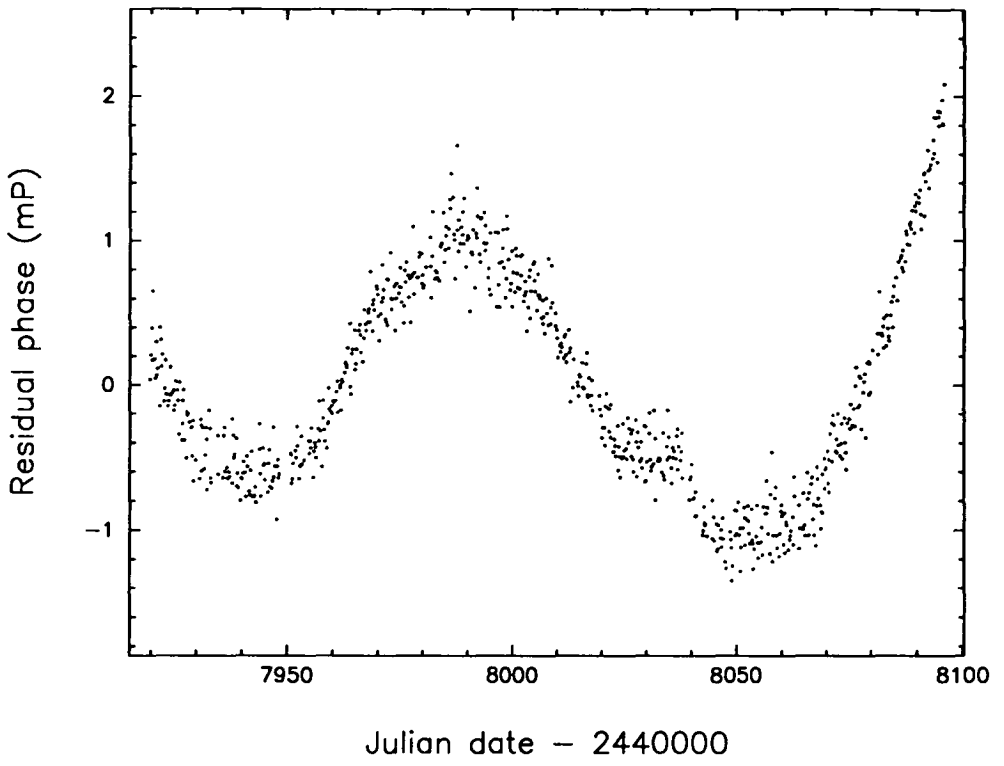

Figure 7.14: Residual timing activity after allowance is made for microjumps that occurred between TJD 7920 and TJD 8095.

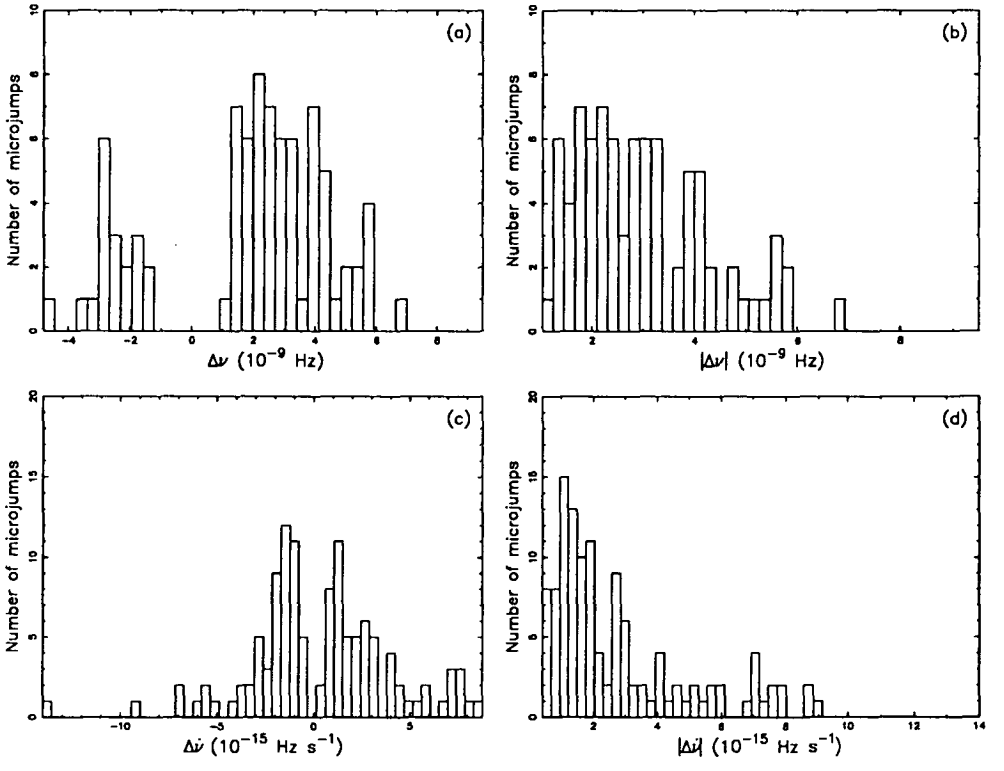

Figure 7.15: Histograms of the actual magnitudes, (a) & (c), and absolute magnitudes, (b) & (d), of the microjumps in ν and $\dot{\nu}$.

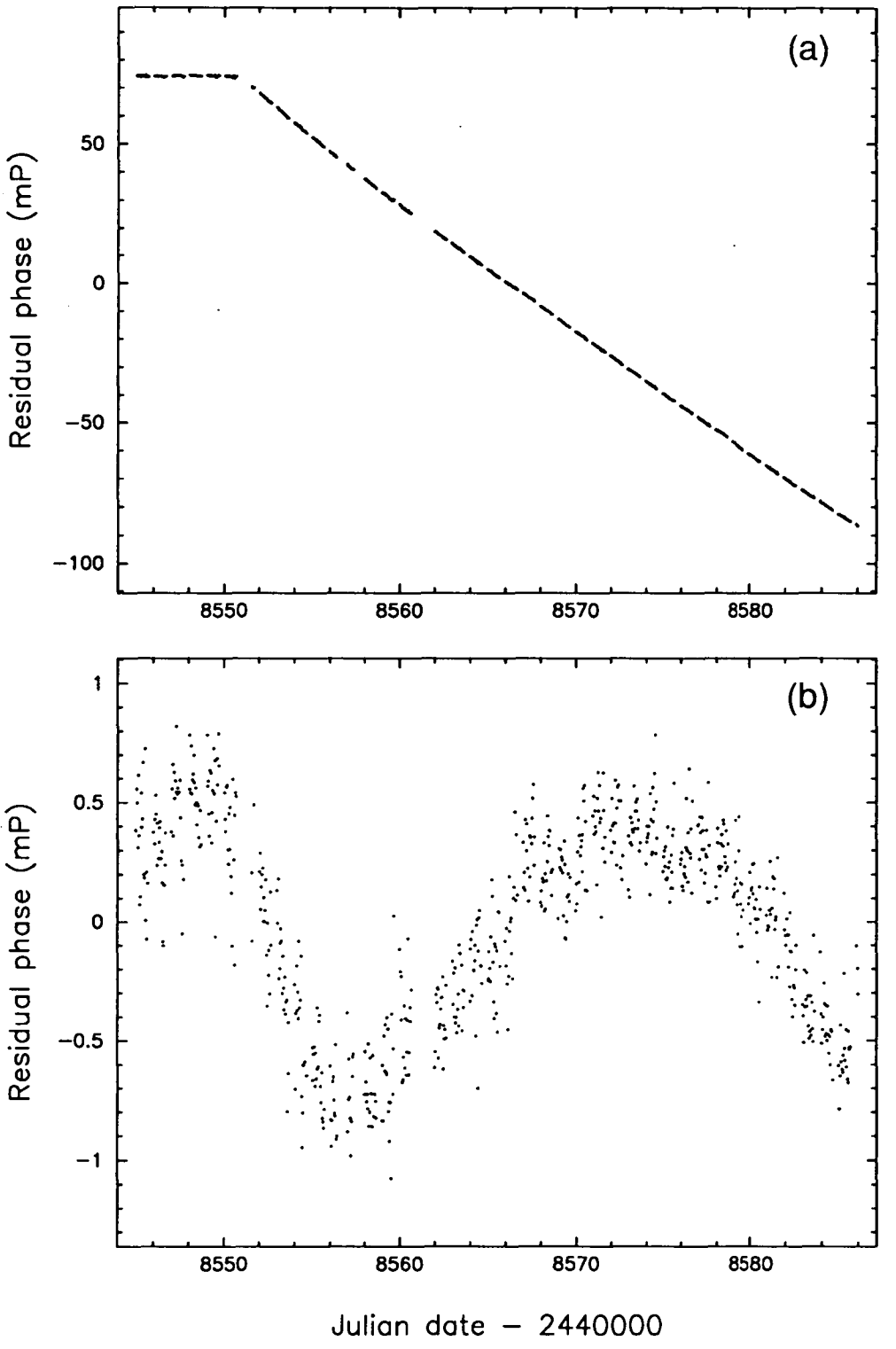

Figure 7.16: The small glitch 9′. (a) The deviation in the phase residuals as a result of the glitch. (b) The phase residuals after fitting for a jump in the rotation frequency and frequency derivative but not an exponential relaxation. The rms phase residual in this case is $\sim 29\mu$s.

Table 7.7: Derived parameters for glitch 9′. Uncertainties are 1σ and refer to the last digit quoted.

Range fitted (TJD)	8545 – 8586
Glitch epoch (TJD)	8550.85 ± 4
RMS residual of fit (μs)	16.4
$\Delta\nu_c$ (10^{-8} Hz)	5.33 ± 4
$\Delta\dot{\nu}_c$ (10^{-15} Hz s^{-1})	-1.3 ± 1
$\Delta\nu_1$ (10^{-8} Hz)	1.01 ± 4
τ_1 (days)	6.2 ± 4

were checked by fitting to Equation 7.1 the $\dot{\nu}(t)$ data following this glitch. This method yielded $\Delta\dot{\nu}_1 = -15.8 \times 10^{-15}$ Hz s^{-1} and $\tau_1 \simeq 7.3$ days. The value of $\Delta\dot{\nu}_1$ corresponds to a magnitude $\Delta\nu_1 \simeq 0.01\mu$Hz. Hence, both methods give similar results.

7.4 Discussion

The results show that the timing noise in the Vela pulsar is dominated by microjumps in ν and $\dot{\nu}$, although other low-level activity is also evident. The latter may be due to free precession, with a typical period of ~ 100 days. Although more detailed analyses are required before any firm conclusions can be drawn, a possible scenario is one in which the microjumps are the exciting mechanism for the free precession.

The microjumps in the Vela pulsar exhibit the complete range of event signatures ($\pm\Delta\nu$, $\pm\Delta\dot{\nu}$, $\Delta\nu = 0$, $\Delta\dot{\nu} = 0$). Of the 140 events tested, approximately 60% of the events in ν and 85% of the events in $\dot{\nu}$ were found to be significant with respect to a random walk process. Almost 80% of the microjumps in ν and $\sim 50\%$ of the microjumps in $\dot{\nu}$ have positive magnitudes. Approximately 3360 days of timing data were analysed, implying that microjumps occur roughly once every 30–40 days. The analysis of the JPL data by Cordes *et al.* (1988) revealed an event rate of once every ~ 100 days. The difference in results can be attributed to the sampling interval, Δt, which is an important factor in the statistical tests performed on individual events. The Mt Pleasant data are obtained from daily timing observations, whereas the JPL data were only obtained on a weekly basis.

The high quality data obtained for postglitch regions $R_{8\text{-}9}$ and $R_{9\text{-}10}$ have revealed two interesting features in the postglitch recovery of the Vela pulsar. In $R_{8\text{-}9}$, a number of relatively large positive jumps in $\dot{\nu}$ occurred, producing visible

steps in the long-term postglitch recovery of $\dot{\nu}$. Each of these steps is also visible as a large 'V' in the $\delta\nu(t)$ plot in Figure 7.8. The most obvious step occurred around TJD 7987. Such steps are not as prominent in other postglitch regions. For $R_{8\text{-}9}$, at least, the recovery of $\dot{\nu}$ toward a steady state proceeds via a continuous process, such as thermally activated vortex creep, and a series of random microjumps, punctuated by a number of distinct positive-going steps. In the case of $R_{9\text{-}10}$, in addition to the small glitch 9', the microjump analysis revealed two seemingly discrete jumps in $\ddot{\nu}$ which cannot be attributed to a succession of jumps in $\dot{\nu}$ of the same sign. The jumps in $\ddot{\nu}$ appear as changes in the slope of $\delta\dot{\nu}(t)$ in the time interval TJD 9070 - TJD 9180. Cordes *et al.* (1988) also identified this type of behaviour in earlier postglitch regions, classifying it as a "ramp" event.

The general results of the timing noise analyses, as well as those specific to postglitch regions 8 and 9, require scrutiny in terms of the theoretical models of timing noise that were discussed in Chapter 2, namely: (i) a triggering event followed by a vortex creep response (Alpar *et al.* 1986); (ii) magnetospheric fluctuations (Cheng 1987a,b, 1989); and (iii) corotation of vortices with the superfluid (Jones 1990d). The results, particularly the specific features, must also be interpreted in the context of the postglitch recovery of the Vela pulsar. A brief review of the nature of this recovery follows, using the vortex creep model described in Chapter 2.

In the vortex creep theory, a glitch in the Vela pulsar involves a sudden transfer of unpinned vortices from a region A_1, through a region B, and repinning further from the rotation axis in a region A_2 (a vortex "discharge"). At the time of the glitch, vortex creep is stopped temporarily, decoupling regions A from the crust. Since the external torque now acts on less moment of inertia, the spin-down rate suddenly increases. After a glitch, the regions A are gradually filled by the continuous vortex creep process, and the spin-down rate gradually heals back toward a steady state. This recovery has a linear dependence on time. Alpar & Pines (1992) have called these regions "vortex traps" because they withhold vortices from the regions B (termed "vortex capacitors") until a critical number of stored vortices is reached. Region B apparently plays no role in the postglitch recovery of the Vela pulsar (Alpar *et al.* 1993). The recovery in $\dot{\nu}$ is a consequence of the nonlinear regime of vortex creep in regions A, with a Fermi-function dependence on time. The linear dependence on time corresponds to the special case where the glitch-induced offset in the steady state lag, $\delta\omega$, varies linearly with position r in the nonlinear response region. On the other hand, if vortex creep was present in regions B, there would be no recovery in $\dot{\nu}$ until a time t_0 after the glitch. At this time, the Fermi-function response would involve an increase in the slope of $\dot{\nu}(t)$ or even a step-like positive change (Alpar *et al.* 1989,1993).

The observational data show that the linear recovery proceeds in an irregular fashion. The irregularities are comprised of positive and negative jumps in ν and

$\dot{\nu}$, which can be explained by one or more of the theoretical models of timing noise, and the unusual steps in $\dot{\nu}$ and $\ddot{\nu}$. The latter behaviour is suggestive of a Fermi-function response involving a very small part of the B regions, although the gross features of the postglitch recovery suggest that these regions are already well established vortex capacitors in the Vela pulsar (Alpar & Pines 1992). The exceptions to this picture are the two small Crab-like glitches 2′ and 9′. In the Crab pulsar glitches, the change in the spin-down rate does not completely decay away. This "persistent shift" in $\dot{\nu}$ is not possible unless the coupling parameters change at the time of the glitch. Alpar & Pines (1992) suggest that such a change is the signature of a newly formed vortex trap/capacitor. The small glitches in the Vela pulsar probably signal the last bits of vortex trap being formed. A persistent shift in $\dot{\nu}$ is resolved in the data following glitch 9′. As shown in Section 7.3.4, this permanent offset has a magnitude of $\Delta\dot{\nu}_c = -1.3 \times 10^{-15}$ Hz s^{-1}.

An alternative approach is to consider all of the observed microactivity in terms of timing noise models. Using such an approach, the jumps in $\ddot{\nu}$ would have to be considered, for example, from the point of view of the superposition of a series of unresolved microjumps in $\dot{\nu}$ of the same sign. Also, timing noise models must be able to explain the complete range of event signatures. Cordes *et al.* (1988) have found that none of the vortex creep models of timing noise considered by Alpar *et al.* (1986), in isolation, can account for the range of timing activity observed in the Vela pulsar. These models do not account for positive jumps in $\dot{\nu}$, which must involve a sudden coherent repinning of uncoupled vortices or inward movement of vortices. Similar arguments apply to the present set of observations. Cordes *et al.* (1988) do point out, however, that the observed activity could be produced by a crustquake followed by a superfluid response, provided that the crustquakes can produce moment of inertia changes of both signs. Crustquake models can be rejected as the sole cause of microactivity because the condition

$$\frac{\Delta\Omega_c}{\Omega_c} = -\frac{\Delta\dot{\Omega}_c}{|\dot{\Omega}_c|} = -\frac{\Delta I_c}{I_c} \tag{7.8}$$

is not satisfied by the observed microjumps (Cordes *et al.* 1988).

As discussed in Chapters 2 and 6, the theoretical models proposed by Cheng (1987a,b) and Jones (1990d) are both capable of producing the range of event signatures. However, these theories are not without their difficulties – the former model does not easily explain the low event rates observed in some pulsars and the latter model does not explain a blue component in the power spectrum of $\dot{\nu}$ fluctuations. Two general features distinguish the Vela timing noise results from those obtained for the "slow rotators" considered in Chapter 6. Firstly, the microjumps in the rotation frequency of the Vela pulsar are dominated by positive events ($\sim 80\%$ are $+\Delta\nu$ events). This result provides some support for the pure unpinning hypothesis of $\Delta\dot{\nu}$ events, but crustquakes are also not ruled out. The superfluid rotation model of Jones (1990d) also predicts a dominance

of $+\Delta\nu$ events, both in number and in magnitude. Secondly, the distribution of microjumps in ν and $\dot{\nu}$ do not follow a power-law or exponential distribution, as both distributions appear to fall off toward the small amplitude end. Although most of the *candidate* events were resolved in the analysis, this result could be a "selection effect" in the sense that small amplitudes are difficult to detect.

All of the proposed timing noise models predict a relaxation time-scale τ following the jump. In the case of the Alpar and Cheng models, this is the thermal relaxation time due to vortex creep. In the Jones model, the relaxation time has a radius dependence. However, no relaxation was evident from the analysis of microjumps in the Vela pulsar or the slow rotators considered in Chapter 6. Some reasons for the lack of observed relaxation were given in Chapter 6, e.g., τ may be outside the range of time-scales that can be probed with the data. The model proposed by Cheng (1987b) assumes that $R^{-1} \simeq \tau$. This implies that the relaxation time of microjumps in the Vela pulsar is 30–40 days and, hence, its effect may have been absorbed into the fit for $\Delta\dot{\nu}$. In terms of the latest glitch model of the Vela pulsar (Alpar *et al.* 1993), it also implies that the superweak pinning region is involved. This is supported by the spontaneous unpinning scenario outlined by Cheng *et al.* (1988), who have suggested that unpinning events originate in the superweak regions. Another reason for the lack of observed relaxation is the possibility that the Q of the jump is so small that the recovery is masked by the white noise in the data. However, this rules out pure vortex unpinning as a mechanism, which requires $Q = 1$. In the model proposed by Jones (1990d), the relaxation time can be approximated by $\tau = 282P$ days, where P is the period in seconds. Hence, $\tau \simeq 25$ days for the Vela pulsar, and so similar arguments apply to this model.

As a final point, it is worthwhile considering the issue of the rise time of the microjumps, because this "coupling time" can further constrain the mechanisms responsible for the timing noise. The reduced glitch model used to estimate the microjump parameters makes the assumption that the jump is instantaneous. Clearly, this is physically impossible. The simplest feasible model of a spin-up or spin-down event involves an exponentially decreasing discontinuity. For example, a spin-up in ν can be modelled using

$$\Delta\nu(t) = \Delta\nu_j(1 - e^{-t/\tau_c}), \tag{7.9}$$

where $\Delta\nu_j$ is the size of the jump and τ_c is the coupling time. Such a rise time has not been observed in the analysis of microjumps in the Vela pulsar. Some of the most important factors that determine the minimum observable coupling time are the amplitude of the microjump, the level of white noise in the data, and time interval between each phase estimate. Phillips (1993) performed a series of simple statistical tests on simulations of the large Vela glitches fitted by the "instantaneous" glitch model. For the 2-minute data, the tests showed that the coupling time could be as long as 4 minutes and still not be detected. In

the case of the microjump analysis, the situation is far worse because the jump amplitude is approximately four orders of magnitude smaller, while the other two factors effectively negate each other. Phillips found that $\tau_c(\mathrm{max}) \propto \Delta\nu^{-2/3}$, which implies that the minimum observable (or maximum actual) coupling time for the microjumps is ~ 1.2 days.

7.5 Summary

A preliminary analysis of the daily Vela timing data recorded over the period 1987–1994 has shown that the timing activity in this object is dominated by discrete microjumps in its rotation frequency and frequency derivative. However, after allowance is made for these discrete events, other low-level activity is apparent. More detailed analyses are required to quantify the nature of these low-level fluctuations.

During a postglitch recovery period, the Vela pulsar undergoes both positive and negative jumps in ν and $\dot{\nu}$ with fractional magnitudes $|\Delta\nu/\nu| \simeq 10^{-9} - 10^{-10}$ and $|\Delta\dot{\nu}/\dot{\nu}| \simeq 3 - 60 \times 10^{-5}$. These microjumps occur roughly once every 30–40 days. The microactivity following the eighth Vela glitch was also characterised by a series of distinct steps in the linear recovery of $\dot{\nu}$. Shortly after the ninth Vela glitch, a small Crab-like glitch occurred which relaxed back toward the steady state with a time-scale of ~ 6 days. This small glitch left a tiny remnant offset in the spin-down rate. Also following the ninth glitch, there is evidence of discrete changes in $\ddot{\nu}$.

The results have been discussed in terms of current theories of pulsar timing noise. While some mechanisms, in isolation, can be ruled out as a possible cause of the timing noise (e.g., pure vortex unpinning), the results indicate that a combination of mechanisms is responsible. At present, both the magnetospheric (Cheng 1987a,b) and corotating vortex (Jones 1990d) models are able to explain most of the observations.

In the next chapter, the Vela data are probed in the frequency domain by using the power spectral density of the phase fluctuations.

Chapter 8

Power Spectrum Analysis of Timing Noise

8.1 Introduction

As mentioned in previous chapters, power spectra of pulsar rotation fluctuations can provide additional information about the mechanisms responsible for timing noise. In fact, most of the theoretical models of timing noise described in Chapter 2 make predictions in terms of a power spectrum of the fluctuations. Furthermore, these models are based on a statistical description of fluctuations in one or more of the three observables - ϕ (PN), ν (FN) or $\dot{\nu}$ (SN), each resulting in a simple power-law spectrum. On the other hand, the quasi-periodic oscillations considered in Chapter 6 will produce a narrow-band signature in the power spectrum. The aim of this chapter is to assess the viability of the various theoretical models by comparing the observed power spectra with those predicted by the theories.

The nomenclature that has been used for the three simple random walk processes, namely PN, FN and SN, is unambiguous in the context of pulsar work, but can be confusing when applied more generally. The general nomenclature emphasises the variable in which the process is stationary, i.e., white noise (Lamb 1981). Hence, PN, FN and SN correspond to processes that produce white noise in ν, $\dot{\nu}$ and $\ddot{\nu}$ respectively. These random walk processes have a "red" power spectrum (i.e., excess power at low frequencies) in the variable ϕ, and can be considered as a repeated integral of white noise in ϕ. Since ϕ, ν and $\dot{\nu}$ are simply related by differentiation, the power spectra are related by factors of f^2: $P_\nu(f) \sim f^{-2} P_\phi(f)$ and $P_{\dot{\nu}}(f) \sim f^{-2} P_\nu(f)$. Deeter & Boynton (1982) use the terminology "r-th order red noise", denoting a variable $x(t)$ which is the r-fold integral of white noise. That is, the r-th time derivative, $x^r(t)$, reduces to white noise. Hence, the power spectrum of $x(t)$ obeys the law $P_x(f) \sim f^{-2r}$. The orders $r = 1$, 2 and 3 correspond to phase, frequency and slowing-down noise respectively.

To investigate successfully all of the proposed noise processes over a frequency range of a decade, a dynamic range of at least six orders of magnitude must be attainable. Conventional Fourier transform (FT) techniques fail when they are used to estimate the spectral power density that is characteristic of red noise processes, particularly from an unevenly sampled time sequence. A basic reason is that there is substantial power "leakage" through the sidelobes of the equivalent power density estimators that can very easily mask any steep variations in the spectrum. While dealing with steep red spectra, simple FT techniques produce meaningless power spectra with a steepest power-law slope of ~ -2. The situation is further complicated by the unevenly sampled time series that inevitably arise from practical astronomical observations. Interpolation of the data does not help much as the spectral contamination resulting from the interpolation seriously affects the spectral power estimation at high frequencies. Hence, the above issues must be considered if one is to correctly recover red noise spectra from the timing data.

Detailed analyses of pulsar timing noise have been undertaken by a number of workers. The techniques employed by these workers are briefly reviewed in the context of an alternative method presented in this chapter.

8.1.1 Analysis of Timing Noise: A Review of Techniques

As mentioned in Chapter 2, Boynton *et al.* (1972) were the first to publish work on timing noise. Using standard Fourier techniques, they found that the timing residuals of the Crab pulsar had a power spectrum most closely resembling a frequency noise model. The difficulties involved in the estimation of power spectra using conventional techniques prompted workers to develop alternative (time-domain) techniques to analyse the noise process, the methodology of which has been described by Groth (1975a), Cordes (1980) and Cordes & Downs (1985). Some of these techniques were used in Chapter 6.

Groth (1975a) developed a new technique which accounted for the effects of uneven sampling and non-uniform data quality. The method consists of the expansion of the data into a set of orthonormal polynomials, from which one can extract the slow-down parameters and the degree to which they are contaminated by the noise, as well as a strength parameter for the model noise process which best fits the data. Hence, the method requires the input of an *assumed* model for the noise process, the result being a consistency check of the validity of the model.

Cordes (1980) developed a method similar to that of Groth (1975a), except that it uses the integrated variance rather than a decomposition of the variance into polynomial components. In the same way as Groth (1975a), he assumes a model and tests for consistency with that model. However, Cordes points out that showing consistency of a random walk is a necessary but not a sufficient condition

for demonstrating that a random process is occurring in the rotation of the pulsar.

As described in Chapter 6, Cordes & Downs (1985) analysed the pulse phase residuals and their derivatives in the time domain by examining the polynomial coefficients and residuals from polynomial fits made over a variety of data spans and time origins. The method was partly described in Cordes (1980) and used by Cordes & Helfand (1980), but it is augmented with a more sophisticated error analysis and through the study of structure functions of the phase.

Other workers have approached the problem by obtaining estimates of the power spectra of the time series. Deeter & Boynton (1982) and Deeter (1984) have developed a general mathematical framework, specifically designed for unevenly sampled data, leading to a power density estimation technique which is valid for red power-law spectra. Their method is essentially an extension of the work of Groth (1975a). The method uses orthonormal polynomials as power density estimators whose frequency response is such that leakage through the sidelobes of the transfer function is minimised (hence correct estimation of power density for processes which are "red"), while sacrificing frequency resolution to a certain extent. Their modest one-octave frequency resolution is enough to identify features like the step in $P_{\dot{\nu}}(f)$ characteristic of a viscously-coupled crust-core model driven by white torque noise. A true power spectrum calculated in this manner allows the power-law behaviour over the available frequency range to be tested directly rather than assuming this result as Groth (1975a) and Cordes (1980) have done. This power spectrum technique has been applied to pulsar timing data by Boynton & Deeter (1986) and Deeter *et al.* (1989).

During the course of 1992, a completely different technique for the spectral analysis of unevenly sampled data was developed by the author and his colleagues at the University of Tasmania (Deshpande, D'Alessandro & McCulloch, 1995 – see Appendix E). The technique is based on the CLEAN algorithm and is described in detail in the next section. The main motivation for this work stemmed from the fact that none of the other methods are specifically tailored to producing reliable spectral estimates with a *high dynamic range.* This is an extremely important requirement when obtaining power spectra of pulsar *phase* residuals. As mentioned elsewhere, these spectra are extremely steep. Although the power density spectrum of the $\dot{\nu}$ fluctuations, $P_{\dot{\nu}}(f)$, is more closely related to the response of the neutron star to torque fluctuations, the derivation of such a spectrum has a number of disadvantages compared to the estimation of the spectrum of the phase fluctuations, $P_{\phi}(f)$. This is because the pulse phase is the quantity directly measured in timing observations of pulsars. For example, the $\dot{\nu}(t)$ estimates invariably result from some sort of "smoothing" process, e.g., from short polynomial fits, as described in Chapter 7. This restricts the useful span of the spectrum to low frequencies because fewer independent data points over the time span are available for deriving the spectrum. Also, the contribution of white noise in the pulse phase

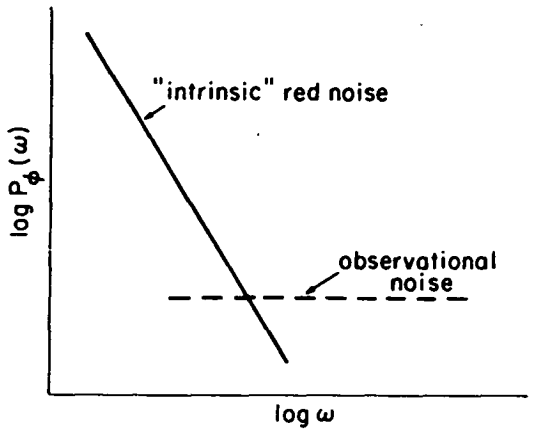

Figure 8.1: Limitation on the observability of intrinsic red phase noise posed by the measurement process (white noise in the pulse phase); (after Boynton 1981).

translates into "blue" noise in the spectrum of the $\dot{\nu}(t)$ fluctuations. However, in principle, the technique to be described can be applied to any type of pulsar timing residual data set, e.g., phase, frequency or frequency derivative residuals.

Two features will be evident in a simple power-law spectrum of the phase fluctuations – a steep red noise component at lower frequencies, and a white noise component which may begin dominating at higher frequencies. In practice, the observability of the intrinsic noise process is restricted at high frequencies by this "observational noise" rather than the Nyquist sampling limit, as shown in Figure 8.1. The white noise estimates obtained in previous chapters represent the level of this observational noise. The lower the "signal-to-noise" of the timing activity, the further toward low frequencies one must look in order to detect the red noise in the spectrum.

After the development of the technique based on CLEAN, it was discovered that a similar idea had already been implemented by Roberts *et al.* (1987) for the time-series spectral analysis of unequally spaced data. A variant of their technique has been used by Green *et al.* (1993) to study rapid X-ray variability in active galactic nuclei. It should be stressed, however, that like other methods, the technique developed by Roberts *et al.* does not address the "high dynamic range" requirement that is important in the analysis of pulsar timing noise. The present technique will now be described in more detail.

8.2 A technique for power spectral estimation using CLEAN

Uneven (or incomplete) sampling of a function limits the dynamic range in the estimation of its Fourier components. This problem is routinely encountered when

dealing with aperture synthesis data. In that case, the sampling in the spatial frequency domain is incomplete and often uneven and one is interested in high dynamic range imaging. A deconvolution technique called CLEAN (Hogbom 1974, Schwarz 1978) is commonly used to obtain high dynamic range images from the often patchy sampling of visibilities. An almost direct analogy of this situation is the estimation of power spectra from unevenly sampled pulsar timing residuals. Considering this, the possibility of using the basic CLEAN algorithm has been investigated as a method for enhancing the dynamic range in the estimation of spectra from the timing residuals.

Assuming $R(t)$ and $S(f)$ to be a Fourier transform pair, where $R(t)$ is the true continuous time sequence of pulsar timing residuals and $S(f)$ is the spectrum of $R(t)$, the true power spectrum is obtained simply as $|S(f)|^2$. Let $x(t)$ be the sampling function which is unity at the sampled epochs and zero elsewhere. The spectrum $S_D(f)$ of the sampled sequence $R'(t)$, where $R'(t) = R(t).x(t)$, can be written as

$$S_D(f) = S(f) * X(f) \tag{8.1}$$

where $X(f)$ is the Fourier transform of $x(t)$ and $*$ denotes convolution. The aim is to obtain an estimate of $S(f)$ given the estimates of $S_D(f)$ and $X(f)$.

The "dirty spectrum", $S_D(f)$, and the "dirty response function", $X(f)$, are not available directly from observations. If the span of $x(t)$ is T, then the dirty response function can be estimated with a frequency resolution of $\Delta f = (1/T)$. However, it is desirable to oversample this response function and the dirty spectrum by a factor of two or more to improve the performance of the deconvolution by the CLEAN algorithm. The extent in frequency ($f_{\max}$) over which the spectral estimation may be performed is not unique in the case of an unevenly sampled time sequence. However, it can be argued that a more appropriate span corresponds to that implied by an average sampling rate for the time sequence, i.e., 0 to $N/(2T)$ where N is the number of time samples. The extent of the dirty response function is then twice that of the spectrum to be CLEANed. With this understanding, the functions $S_D(f)$ and $X(f)$ can be computed at discrete frequencies by Fourier transforming the measured time sequence of the pulsar timing residuals and the sampling function respectively. This operation is performed by summing the spectral contributions from each of the sampled points of the time sequence. In this way, gridding of the time samples is not required, avoiding the possible phase jitter due to quantised sampling intervals.

It should be noted that the complex spectra thus obtained are Hermitian symmetric in nature, unlike in the case of aperture synthesis data. The CLEAN algorithm to be used therefore needs the following minor modifications: (i) while searching for the maximum in the spectrum to be CLEANed, phases in the spectrum are ignored, i.e., the location of the maximum spectral amplitude is found. But the actual contribution at that location is considered including the phase; and

(ii) the search for the maximum is made only over one half of the spectrum but subtraction of a scaled (by a complex quantity) version of the response function is performed over both halves of the spectrum after accounting for the Hermitian symmetric contribution. This makes the algorithm somewhat faster and, more importantly, ensures the Hermitian symmetry in the CLEANed spectrum.

The resulting CLEANed spectrum corresponds to a time sequence which is an interpolated and/or extrapolated version of the original unevenly sampled time sequence, while being consistent with the original time sequence at the epochs of measurement. As super-resolution in the spectrum is not a top priority, the CLEANed spectrum is to be restored to a resolution which is approximately the original resolution (i.e., $1/T$). In applications such as aperture synthesis imaging, the CLEANed versions are restored to a desired resolution by convolving the CLEANed components in the image with a Gaussian CLEAN beam (i.e., without any sidelobes). Spectral smoothing with a Gaussian would also be satisfactory in the present case if the spectrum were to be linear and is to be viewed on a linear frequency scale. As mentioned earlier, the spectra of pulsar timing residuals are more likely to be power-law in form, making restoring functions with long tails undesirable. Hence, a half-a-cycle cosine bell was used as the restoring function, with a half-power width close to the original resolution. After the CLEANed complex spectra are restored to a desired resolution, the power spectra are computed in the usual way.

8.3 Tests on Simulated Data

The performance of the technique described above was tested by application to simulated time sequences of pulse phase corresponding to steep red spectra. The simulated time sequences were generated for 5 cases, namely, white noise, phase noise, frequency noise, slowing-down noise and a test sine wave. This was done first with uniform 30-day sampling ($\sim$ sampling interval of Mt Pleasant data). A white noise contribution of 0.1% was added to the simulations of PN, FN and SN to demonstrate the effect of even a small amount of measurement error on the high frequency end of the power spectrum. The CLEAN technique was used on this set of simulated data. The procedure gives the expected output power spectra in the case of uniformly sampled time sequences. This can be seen in Figure 8.2 for the first four cases, where the power-law spectra in phase have logarithmic (or spectral) slopes of 0.4 ± 0.2, -1.8 ± 0.1, -3.8 ± 0.1 and -6.0 ± 0.1 (1σ uncertainties). Spectral slopes of 0, -2, -4 and -6, respectively, are expected for these simulated data.

The unevenly sampled versions were obtained from the simulated time sequences described above by using sampling functions encountered in practice. The sampling pattern for PSR B1641-45 was chosen for this purpose. Although this

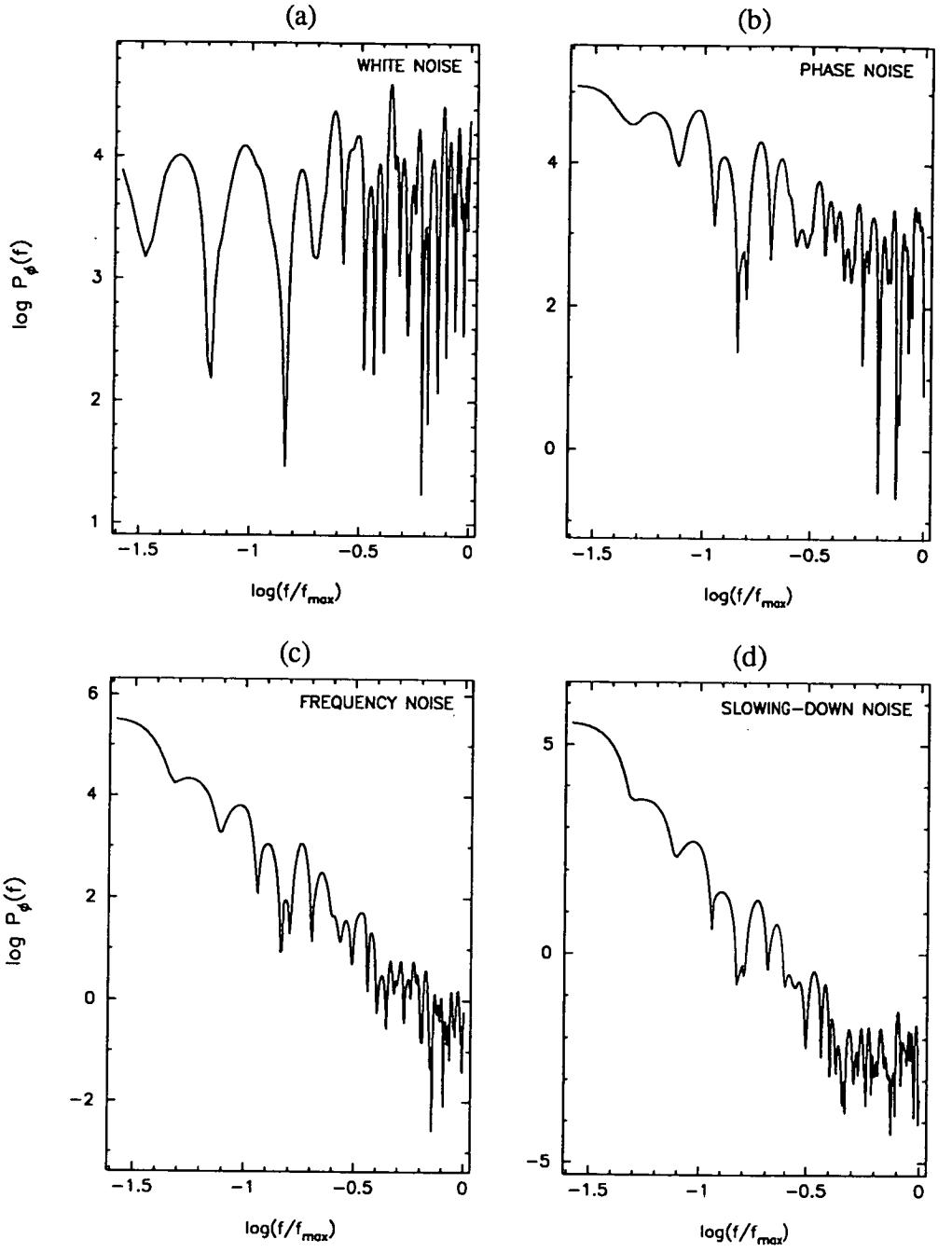

Figure 8.2: Power density spectra of white noise, phase noise, frequency noise and slowing-down noise simulations, respectively, using 30-day uniform sampling.

sampling function is free of any large gaps, it has substantial non-uniformity and should be treated as a situation close to the worst case of uneven sampling. If large gaps comparable to the total time span itself exist in the sampled data, it is more appropriate to use the portions of the time sequences that avoid such gaps.

These data were subjected to a number of different procedures, including the CLEAN technique, in order to evaluate their performance. The other procedures include: (i) interpolation of the time sequence at evenly spaced epochs using a low-order polynomial, followed by the use of a standard FFT on the interpolated data, (ii) use of the Lomb-Scargle periodogram method for unevenly sampled data (Press & Rybicki 1989), (iii) use of suitable-order harmonic fits to the time sequence giving the best fit estimates of the power spectrum (similar to the method used by Boynton *et al.* 1972), and (iv) some variants of these methods. Of these other procedures, the third method was found to perform much better than the others. However, even in this case, the slopes of the reconstructed red spectra were consistently lower than those expected.

Figures 8.3 and 8.4 show the power spectra before and after the application of the CLEAN procedure respectively. The improvement in the dynamic range and the quality of reconstruction due to the CLEANing is clearly visible. The spectral slopes obtained from the standard discrete FT correspond to -0.2 ± 0.2, -1.6 ± 0.1, -2.1 ± 0.2 and -4.3 ± 0.2, and for the CLEANed spectra the slopes are 0.1 ± 0.1, -2.0 ± 0.2, -4.1 ± 0.2 and -5.9 ± 0.2 (1σ uncertainties). However, the reconstruction of the spectra at the higher frequency end is comparatively poor, particularly for the SN data which result in the steepest spectra. Real data include measurement uncertainties that contribute a white noise component to the spectrum, masking the steep drops in the spectral power towards the high frequency end of the red spectra. The simulations show that even a moderate amount of random measurement noise will dominate the contributions at the high frequency end of the spectrum.

In summary, the performance of the CLEAN procedure is satisfactory since it reconstructs the steep spectra very well over the medium to low frequency range with a dynamic range exceeding 6 orders of magnitude.

8.4 Power Spectral Analyses and Results

A total of 18 pulsars from the Mt Pleasant sample were suitable for power spectral analysis. These pulsars were selected on the basis that the signal-to-noise of the timing activity was sufficient (typically ≥ 10) to obtain a meaningful spectrum. As a matter of convention before any sort of Fourier transformation, the mean of the phase residual data for these pulsars was removed. This mean should be very small in practice, according to the definition of "residuals", but small differences can arise as a result of combining the dual frequency data into a single data

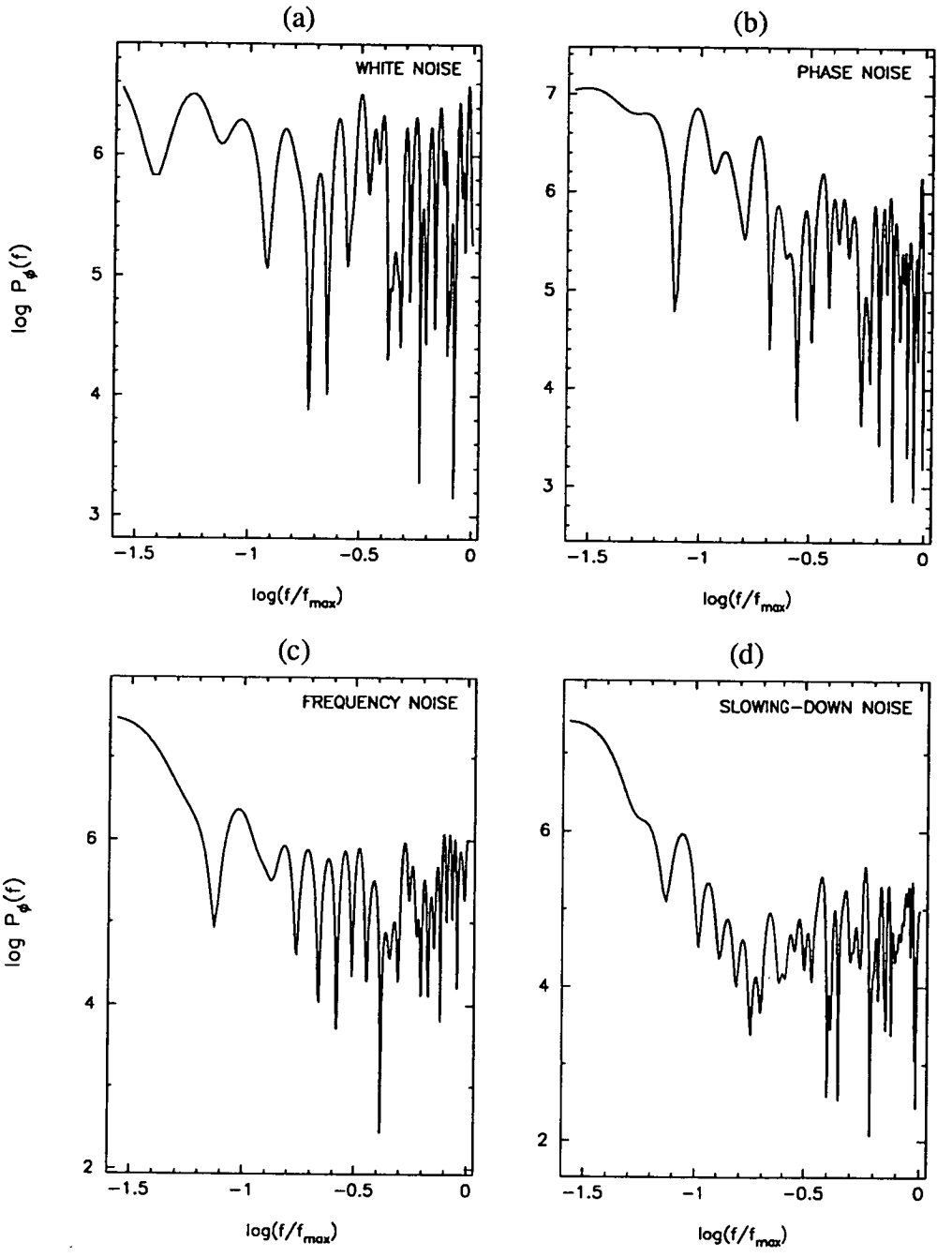

Figure 8.3: Power density spectra of unevenly sampled WN, PN, FN and SN time sequences. The sampling was generated according to the observations of PSR B1641-45. The spectra were obtained using conventional discrete Fourier-transform techniques.

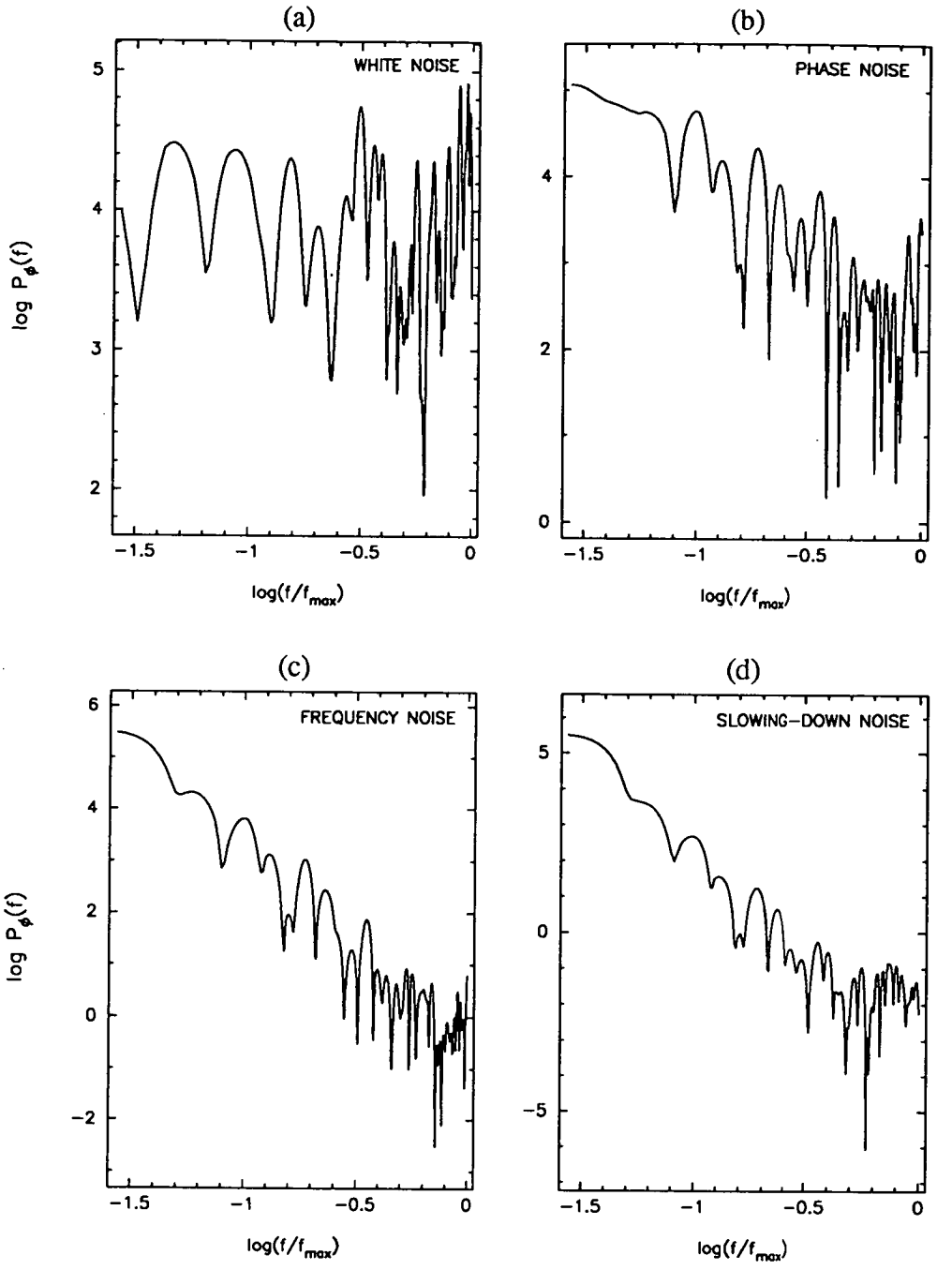

Figure 8.4: Power density spectra of the unevenly sampled WN, PN, FN and SN time sequences. The sampling was generated according to the observations of PSR B1641-45. The spectra were obtained using the technique based on CLEAN .

sequence (see Chapter 6). If standard Fourier techniques are applied to a time series with a non-zero mean, the resulting spectrum contains a DC component (and its sidelobes). However, CLEAN also removes this DC component and its sidelobes, and so this is not a problem.

The CLEAN technique was then applied to the zero-mean phase residual data of the 18 chosen pulsars. The power density spectra in ϕ for these pulsars are shown in Figures 8.5–8.7. The power spectra are displayed in the conventional manner, i.e., as a log-log plot of power spectral density against frequency. The reasons for such a representation have been discussed by Deeter (1984) and Boynton & Deeter (1986). In the context of the pulsar timing noise investigated in this chapter, the most important reason is the fact that the log-log representation reveals very readily any power-law behaviour in the power spectrum.

Logarithmic slopes were obtained from the CLEANed spectra by performing linear least squares fits to the spectral estimates over the available frequency range, i.e., where the power exceeded the white noise. In most of the spectra, the cross-over point (i.e., the point where the white noise begins to swamp the red noise) occurs at $\log(f/f_{\max}) \leq -0.5$. This implies the shortest autocorrelation time that can be probed in the Mt Pleasant pulsar observations is ~ 190 days. In some cases, a single linear fit did not adequately model the spectrum. A "two-component" linear model was used for these spectra. The results of the linear fits to the spectra are presented in Table 8.1. The columns contain, respectively, the pulsar name, the signal-to-noise of the timing activity, the frequency range over which the slope was estimated, the spectral slope and its 1σ formal uncertainty.

In order to check the validity of the derived slopes, time sequences corresponding to PN, FN and SN were generated using the same sampling pattern, signal-to-noise, time span, etc. as the data for each pulsar. The CLEAN technique was then applied to these time sequences to obtain their power spectra. The spectral slopes obtained for the PN, FN and SN simulations were in the range -1.7 to -2.3, -3.8 to -4.3 and -5.7 to -6.3 respectively, with typical 1σ uncertainties of ~ 0.2 in individual estimates.

The CLEAN technique was also applied to the timing residuals of the Vela pulsar. These residuals were averaged so that the sampling interval was approximately 1 day. Power spectra in ϕ and $\dot{\nu}$ were computed using the data from postglitch regions 6, 8 and 9. These spectra are shown in Figure 8.8. The slopes derived from linear fits to the spectra are given in Table 8.2. The columns contain, respectively, the postglitch region of the data analysed, whether the phase or frequency derivative residuals were used to compute the spectrum, the frequency range over which the slope was estimated, the spectral slope and its 1σ formal uncertainty.

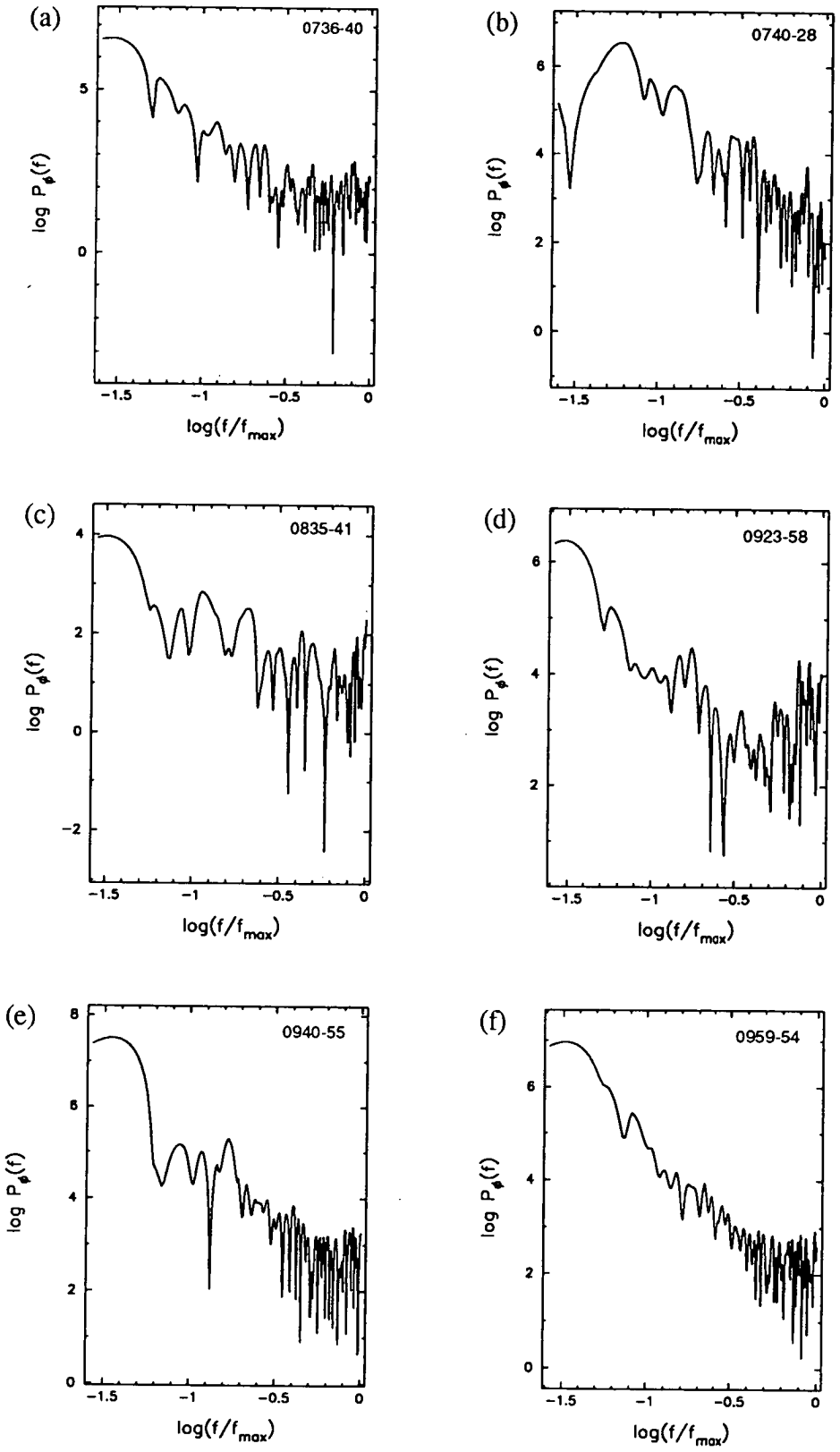

Figure 8.5: Power density spectra of the phase residuals for six southern pulsars. The units of power density are arbitrary. The frequency scale has been normalised using $f_{\max}$, as defined by the Nyquist limit.

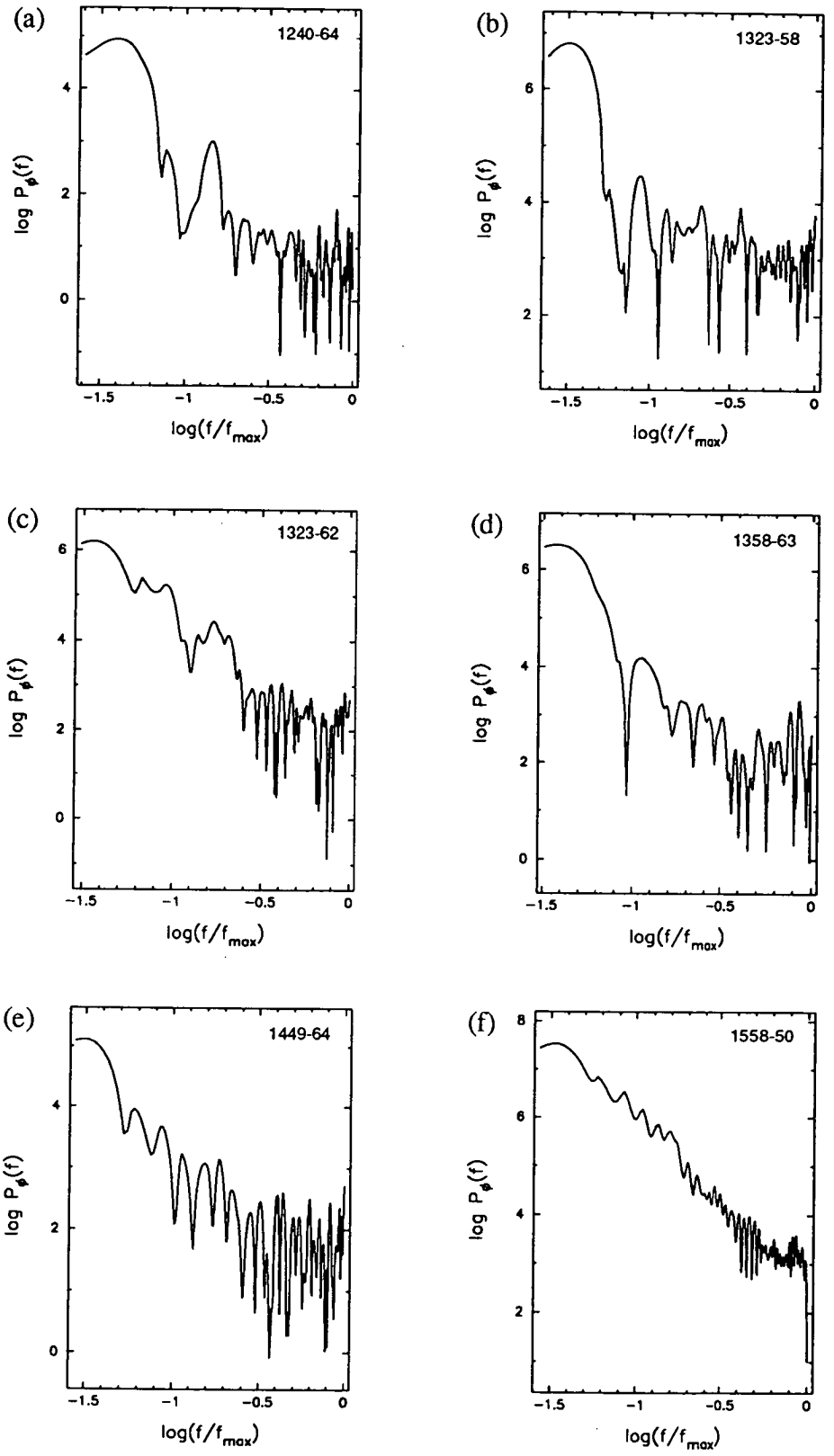

Figure 8.6: Power density spectra of the phase residuals for six southern pulsars. The units of power density are arbitrary. The frequency scale has been normalised using $f_{\max}$, as defined by the Nyquist limit.

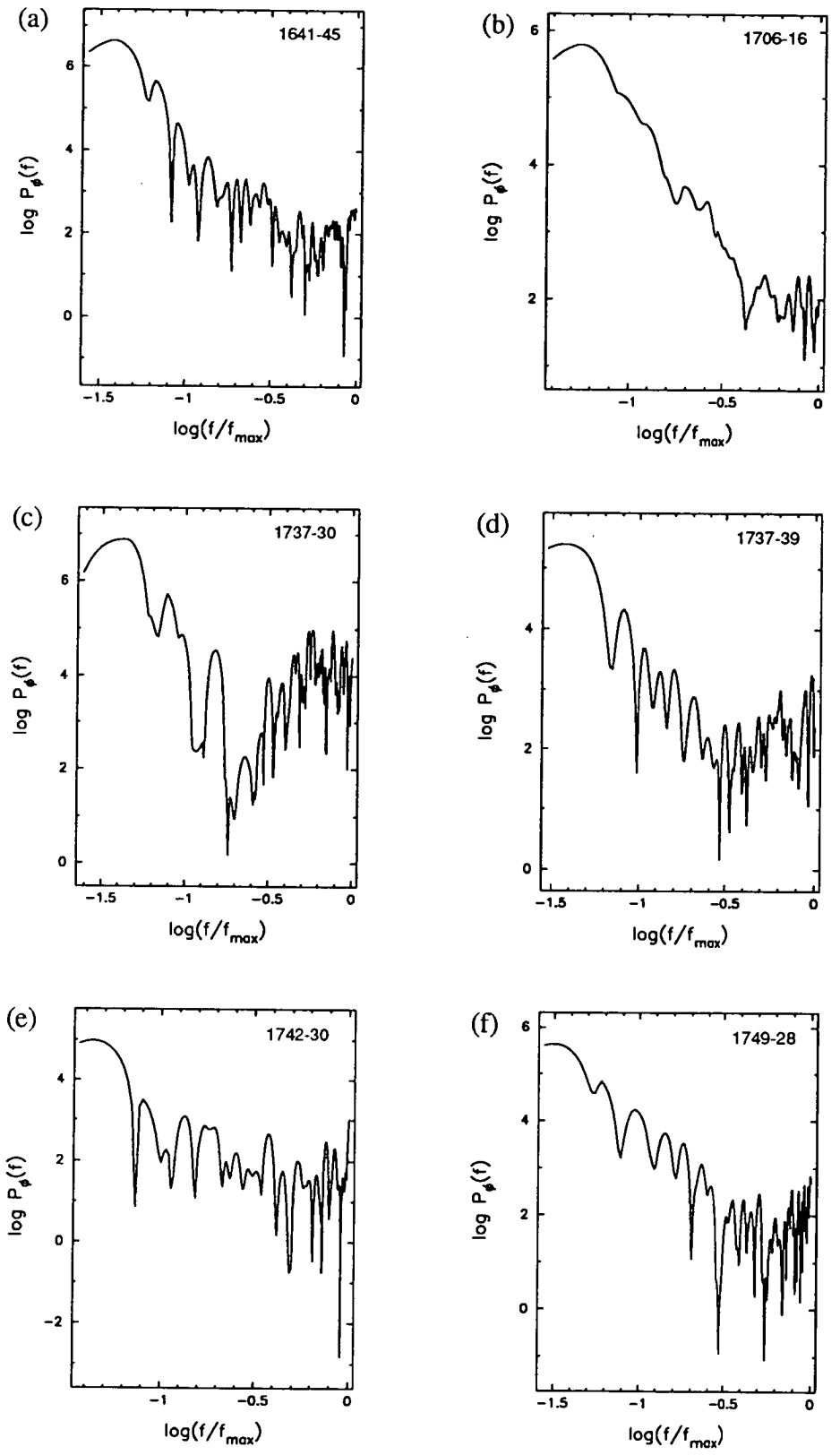

Figure 8.7: Power density spectra of the phase residuals for six southern pulsars. The units of power density are arbitrary. The frequency scale has been normalised using $f_{\max}$, as defined by the Nyquist limit.

Table 8.1: Logarithmic slopes obtained from linear least squares fits to the CLEANed power spectra of the timing noise in 18 pulsars.

PSR B	S/N	Freq. range	Slope	Err
0736−40	64	−1.6,−0.5	−5.2	0.4
0740−28	42	−1.3,−0.3	−3.4	0.2
0835−41	8	−1.6,−0.5	−2.1	0.2
0923−58	10	−1.6,−1.2	−4.6	0.6
		−1.3,−0.6	−2.3	0.3
0940−55	80	−1.6,−1.2	−5.0	0.9
		−1.3,−0.5	−2.4	0.2
0959−54	151	−1.6,−0.9	−4.8	0.2
		−0.9,−0.4	−2.7	0.2
1240−64	23	−1.6,−0.7	−4.3	0.4
1323−58	21	−1.6,−0.8	−4.7	0.5
1323−62	25	−1.6,−0.5	−3.9	0.2
1358−63	47	−1.6,−0.9	−6.1	0.7
		−1.0,−0.5	−3.1	0.3
1449−64	12	−1.6,−1.0	−4.0	0.3
		−1.2,−0.5	−2.6	0.3
1558−50	189	−1.6,−0.4	−3.6	0.1
1641−45	69	−1.6,−1.0	−5.9	0.5
		−1.0,−0.4	−2.3	0.3
1706−16	47	−1.3,−0.4	−4.1	0.6
1737−30	16	−1.6,−0.8	−5.4	0.5
1737−39	11	−1.6,−0.5	−3.9	0.2
1742−30	13	−1.6,−0.5	−3.3	0.3
1749−28	34	−1.6,−0.4	−4.0	0.2

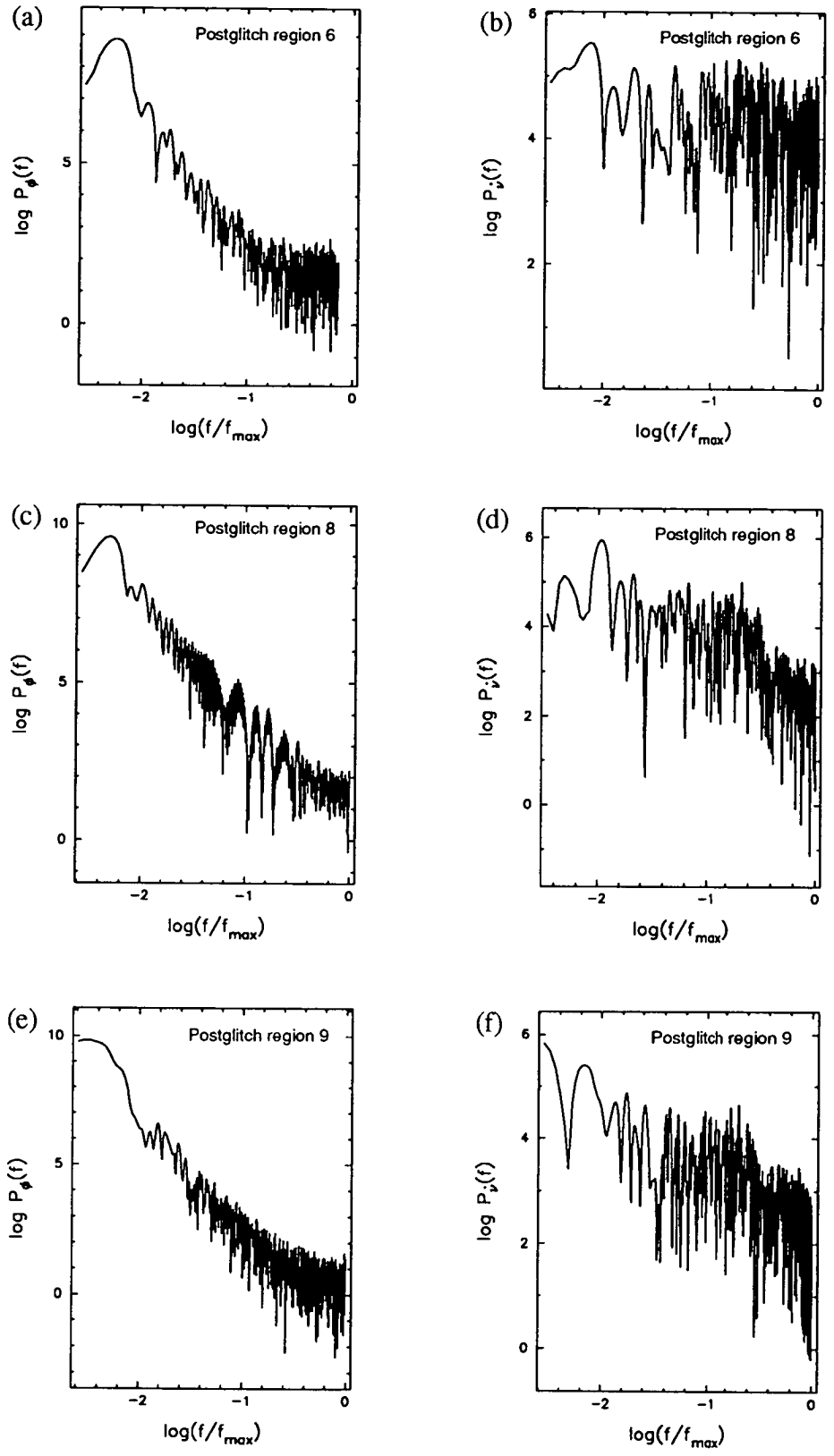

Figure 8.8: Power density spectra of the fluctuations in ϕ and $\dot{\nu}$ for postglitch regions 6, 8 and 9 of the Vela pulsar data.

Table 8.2: Logarithmic slopes obtained from linear least squares fits to the CLEANed power spectra of the timing noise in the Vela pulsar.

Region	Data type	Freq. range	Slope	Err
$R_{6\text{-}7}$	$\phi(t)$	$-2.4,-1.7$	-6.0	0.5
		$-1.7,-0.9$	-3.6	0.2
	$\dot{\nu}(t)$	$-2.4,-0.9$	-0.4	0.1
$R_{8\text{-}9}$	$\phi(t)$	$-2.4,-1.3$	-4.2	0.2
		$-1.3,-0.5$	-3.1	0.1
	$\dot{\nu}(t)$	$-2.5,-0.4$	-0.9	0.1
$R_{9'\text{-}10}$	$\phi(t)$	$-2.6,-1.5$	-5.8	0.3
		$-1.5,-0.8$	-3.6	0.2
	$\dot{\nu}(t)$	$-2.6,-1.5$	-1.8	0.2

8.5 Discussion

The spectral slopes obtained in the previous section provide a useful comparison with the results obtained in Chapter 6 using time-domain methods. The spectrum for PSR B0835-41 has a slope of ~ -2, consistent with a pure PN process. Likewise, the spectra for PSRs B1240-64, B1323-58, B1323-62 and B1706-16 have slopes of ~ -4, consistent with a pure FN process. The timing noise spectra for PSRs B0736-40, B0740-28, B1558-50, B1737-30, B1737-39, B1742-30 and B1749-28 also have power-law slopes, in the range -3.3 to -5.4. Regardless of whether or not these slopes are consistent with those expected for a pure random walk process (i.e., $-2, -4, -6$), they cannot be interpreted in a straightforward manner because the time-domain analyses did not show consistency with such noise processes. The remaining six pulsars have composite power spectra that are most easily described using a two-component slope model. The time-domain analyses performed on four of these pulsars were inconclusive, while for the other two, they showed rough consistency with FN.

Although a single power-law slope of -3.6 adequately modelled the power spectrum for PSR B1558-50, there is some evidence of structure in the spectrum not dissimilar to one of the models proposed by Alpar *et al.* (1986). Power-law fits over the logarithmic frequency ranges -2.0 to -0.8 and -0.7 to -0.45 yield slopes of ~ -3, while the slope over the range -0.8 to -0.7 is ~ -9. Translated into a power spectrum of fluctuations in $\dot{\nu}$, this spectrum is similar to the Alpar *et al.* "mixed event" model shown in Figure 2.4(b), although the slopes are not exactly the same. The "step" or "knee" in the spectrum is marginally significant ($\sim 2\sigma$) and occurs at $\log(f/f_{\max}) \simeq -0.75$. At this point in the spectrum, $f \approx 1/\tau$, where

τ is the relaxation time-scale of the response to the triggering events (Alpar *et al.* 1986). For PSR B1558-50, this time-scale is approximately 340 days.

Three pulsars in the present sample overlap with the JPL pulsar sample analysed by Boynton & Deeter (1986) for power spectrum investigations, namely PSRs B0736-40, B1706-16 and B1749-28. The spectral slopes obtained for these pulsars are in good agreement with the estimates obtained by Boynton & Deeter. Cheng (1987b) has interpreted the Boynton & Deeter spectra for the latter two pulsars in terms of his SN/PN magnetospheric model, but there is no evidence of two such components in the spectra derived from the Mt Pleasant data for these pulsars. However, the extent of the spectra is not very large in the present case and the white noise may have masked the high frequency component which, in the Boynton & Deeter spectra, becomes significant at relatively high frequencies.

The applicability of the various theoretical models to observations of pulsar timing noise has been discussed elsewhere in the thesis, based on the results of time-domain analyses. The power spectra presented in this chapter also enable some conclusions to be drawn in this regard. It is clear that the timing noise of some pulsars is well described by a single power-law spectrum while for others, a composite spectrum is a more appropriate description. The models proposed by Alpar *et al.* (1986), Cheng (1987a,b) and Jones (1990d) predict a range of slopes in $P_{\dot{\nu}}(f)$, ranging from +2 to −2. The main limitation of these models is the fact that they only predict *even* spectral slopes (with the possible exception of the model proposed by Jones). This is because they assume that *purely white noise* exists in the r-th derivative of the phase. However, the power spectral estimates obtained in the present work, as well as those obtained by Boynton & Deeter (1986), show that the timing noise of some pulsars has spectral power varying as odd powers of the fluctuation frequency. Both the Alpar *et al.* and Cheng models can account for any single, "even" power-law slopes in the observed $P_{\phi}(f)$, if the range of time-scales or fluctuation frequencies spanned by the data is restricted to that part of a composite spectrum. For example, in Chapter 6, the timing noise of eight pulsars was found to be consistent with a PN process (one of these, PSR B0835-41, was confirmed by the power spectrum analysis) which can be explained using the microglitch model proposed by Alpar *et al.* (1986) and Cheng (1987b), in the limit of $f\tau \ll 1$. On the other hand, the Jones model only predicts slopes ≥ 4 in $P_{\phi}(f)$. The data for three out of the seven pulsars with composite power spectra, namely PSRs B0940-55, B1358-63 and B1641-45, can be accommodated by the magnetospheric SN/PN model proposed by Cheng (1987b), i.e., a red/blue composite spectrum in $\dot{\nu}$.

The power spectra obtained from the Vela phase residuals for postglitch regions 6 and 9 clearly show a change in slope which is indicative of a composite spectrum. The slope at the low frequency end of the spectrum is ~ -6 and at

the higher frequency end it is ~ -4, a result which is consistent with the findings presented in Chapter 6. The $P_{\dot{\nu}}(f)$ spectrum obtained by Boynton & Deeter (1986) for the Vela pulsar does not show the higher frequency component (probably because of the sparse data used in their computation). The composite power spectrum obtained for the Vela pulsar is easily accommodated by the magnetospheric SN/FN model proposed by Cheng (1987b) and the corotating vortex model proposed by Jones (1990d). In the former model, the unpinning region of the microglitches is predicted to lie between the superweak and weak pinning regions, which are characterised by two distinct thermal relaxation times, τ^{SW} and τ^{W} (Cheng 1987b). An estimate of τ can be obtained from the point in the spectrum where the slope changes. At this point, $f\tau \approx 1$. From Table 8.2, this point corresponds to $\log(f/f_{\max}) \simeq -1.5$, which gives a value of $\tau \simeq 60$ days. Hence, the region in question does appear to lie between the superweak ($\tau^{SW} \leq 32$ d) and weak ($\tau^{W} \gg \tau^{SW}$) regions in the Vela pulsar. The results obtained from the phase residuals for postglitch region 8 and the $\dot{\nu}(t)$ residuals for all three regions are inconclusive. The spectrum obtained for postglitch region 8 is not distinctly composite like the other two regions and the spectra in $\dot{\nu}$ are relatively noisy, owing to the lower S/N of the $\dot{\nu}(t)$ residuals. Based on the $P_{\phi}(f)$ spectra, one would expect to get $P_{\dot{\nu}}(f)$ spectra with slopes close to -2 at the low frequency end of the spectrum. Only the result for postglitch region 9 comes close to this expectation.

8.6 Summary

Spectral analysis of the residual pulse arrival times of pulsars is a useful tool for testing the theoretical models that have been developed to explain the timing noise observed in these objects. Power spectra of pulsar timing residuals may be described by one or a combination of power laws. As these spectra are expected to be very steep, it is important to ensure high dynamic range in the estimation of the spectrum. This is difficult in practice since one is, in general, dealing with timing measurements made at unevenly spaced epochs.

This chapter has presented a technique based on CLEAN to obtain high dynamic range spectra from unevenly sampled data. The performance of this technique was shown to be very good, overcoming the previously noted problems associated with obtaining reliable power spectral estimates from unevenly sampled time sequences. Estimates of the power spectrum of the phase residuals for 18 southern pulsars were obtained using this technique, as well as spectra in ϕ and $\dot{\nu}$ for the Vela pulsar. For the former, most of the spectra could be modelled using a single power-law or a composite (two-component) fit. For the Vela pulsar, the analysis revealed a previously unseen second component toward the high frequency end of the power spectrum of the phase residuals. In general, the results show that the timing noise of some pulsars can be accommodated by one or more of the

theoretical models. In other cases, none of the models provide an appropriate explanation for the observations (e.g., odd power-law slopes in the spectra).

The power spectrum for PSR B1558-50 contains a step which, if interpreted in terms of the "mixed event" model proposed by Alpar *et al.* (1986), suggests a relaxation time-scale of $\tau \geq 300$ days in response to the triggering events. The higher frequency end of the composite spectra obtained for the Vela pulsar may result from microglitches, which originate somewhere between the superweak and weak pinning regions and are characterised by a relaxation time-scale of ~ 60 days.

Chapter 9

Conclusions

This thesis has presented an analysis of new timing data at frequencies of 670 MHz and 800 MHz for a sample of 45 southern pulsars. The timing observations were made with the 26-metre telescope located at the Mt Pleasant Observatory in southern Tasmania over a period of seven years. This long-term pulsar study has produced a number of findings which are summarised in this final chapter.

9.1 Concluding remarks

At the most basic level, the timing measurements have yielded more accurate periods, period derivatives, positions and dispersion measures for most of the pulsars studied. Detectable changes in the dispersion measure of several pulsars have provided a means of estimating the scale-sizes and electron densities of irregularities within the turbulent interstellar medium. These values were found to be $\sim$0.5 pc and up to 10^4 cm^{-3} respectively. Further monitoring of dispersion measures will undoubtedly provide more information about the interstellar medium in specific directions.

The timing measurements have revealed abrupt jumps in the rotation rate of five pulsars. Two of these jumps are large enough to be classified as glitches. One of these glitches occurred in PSR B1727-47 and is the first reported glitch in this pulsar since its discovery. The other glitch occurred in PSR B1737-30 which, along with a number of smaller jumps, maintained the high jump rate of 1–2 per year that was noted previously. The contrasting glitch behaviour displayed by these pulsars reinforces the theory that, as a pulsar ages, it glitches less frequently. No postglitch relaxation was observed for either of these pulsars, a result which is difficult to explain within the context of current glitch models. PSR B1240-64 has undergone a succession of five jumps of alternating sign over a 7-year period. This constitutes the first reported case of such behaviour, which appears highly unlikely to be caused by chance or an artefact of the analysis. Tkachenko oscillations,

precession of the neutron star and the effects of a binary system were investigated in the light of these observations, but all were ruled out as possible causes.

Polarimetric data at 670 MHz and 800 MHz have been presented for eighteen of the more bright pulsars in the sample. Since there is no published polarimetry near 800 MHz for these pulsars, these measurements provide a valuable interpolation point between the 600 MHz and 1600 MHz measurements made in the past. The integrated profiles display properties that are in general agreement with trends extrapolated from the other frequencies. Rotation measures have also been derived for these pulsars. Nine of these estimates are more accurate than previous determinations. The RMs (and the DMs) for two pulsars, PSRs B1556-44 and B1727-47, are found to have changed significantly over the last decade or two. These changes suggest a dense, magnetised electron cloud has moved across the line of sight. The electron density of such a region was estimated to be ~ 200 cm^{-3} and the longitudinal component of the magnetic field was found to be as large as 16 μG. Both of these estimates are consistent with typical conditions thought to exist in the inhomogeneous regions of the interstellar medium. Finally, the success of the polarimetric observations demonstrates that, despite the limitations of the observing system (namely, the modest time resolution and the moderate sensitivity achievable with a 26-metre telescope), useful results can still be obtained.

The main thrust of the thesis was an investigation of pulsar timing noise. Such a study was motivated by the fact that our understanding of this phenomenon is still poor. In fact, only a few theoretical and observational papers have been published on this topic in more than a decade. The preliminary analysis of timing noise presented here has provided independent confirmation of a significant positive correlation with period derivative and a negative correlation with pulsar age. The former tends to support a vortex-line coupling theory of timing noise, since the strength of a noisy contribution from the coupling between components is likely to depend on the angular velocity difference and, hence, on the spin-down rate. The latter correlation indicates that younger pulsars are the best candidates for probing the interior of neutron stars. No significant correlation with pulsar period or other parameters was found.

Detailed study of the timing behaviour of the Mt Pleasant pulsars has more than doubled the number of objects that can be used to gain a better understanding of timing noise. The results presented in this thesis have shown that the level of timing noise in almost half of the pulsars is relatively low, even when viewed over a 7-year span. The timing noise in most of the remaining pulsars can be attributed to distinct microjumps, plus a varying degree of other timing activity (e.g., a random walk process, free precession). A description of timing noise in terms of a pure random walk process is inadequate in most cases, indicating that a mixture of known noise processes, or some other mechanism, is required to explain the timing noise of most pulsars.

Microjumps are the predominant form of activity in a number of pulsars. These microjumps were found to occur in both the rotation frequency and frequency derivative of the pulsar and they display a range of event signatures. The microjump amplitudes form the tail-end of a continuous distribution of amplitudes extending down to microglitch level. A further characteristic of the microjumps is the absence of observed relaxation. If this feature is genuine, the implication is that the superfluid response to a microjump is negligible. Hence, an "external event" model, such as the one proposed by Alpar *et al.* (1986), together with the magnetospheric model proposed by Cheng (1987a,b), could account for the observed nature of the microjumps in ν and $\dot{\nu}$.

In one case, PSR B0959-54, pulse shape variations were found to be weakly correlated with the timing variations, suggesting that free precession may be responsible for the observed timing noise. The implied wobble angle was found to be $\leq 0.15°$. Microjumps were also detected in this pulsar and, hence, a scenario in which the microjumps drive the precession, with both of these effects contributing to the observed timing noise, is a distinct possibility.

An investigation of timing noise in the Vela pulsar has shown that the long-term recovery from a glitch proceeds in an irregular fashion and it appears that some components of this star never achieve rotational equilibrium before the arrival of the next glitch. The microactivity during the postglitch recovery phase of this pulsar is dominated by microjumps in ν and $\dot{\nu}$ which occur every 30–40 days. These microjumps are characterised by a range of event signatures, but with a predominance of positive jumps in ν. The latter result supports an unpinning, or possibly a crustquake, mechanism as the cause of the microjumps. The microactivity following the eighth Vela glitch is also punctuated by a small number of relatively large positive-going steps in the frequency derivative and, following the ninth Vela glitch, discrete changes in the frequency second derivative. It is unclear whether these less frequent events are associated with the recovery from a glitch or whether they are simply particular examples of the varied nature of the microjumps. The analysis of post-microjump data did not reveal evidence of a relaxation process. However, theoretical models predict relaxation time-scales of the order of the inter-jump time, which would not be easily detected in the data. In the Vela pulsar, such a relaxation time implies that the superweak pinning region is involved.

A small Crab-like glitch was found to occur shortly after the ninth Vela glitch. This event was characterised by an exponential recovery with a 6-day time-scale and a small but significant long-term, unrecovered component of the initial change in the frequency derivative. In the context of the Alpar *et al.* (1993) glitch model of the Vela pulsar, this small glitch probably signals the last bits of vortex trap being formed in the otherwise well-established B regions of the star.

Power spectra of the pulsar timing residuals were derived using a novel technique based on the CLEAN algorithm. This technique was designed to overcome the problems inherent in the spectral analysis of unevenly sampled data, particularly when a high dynamic range is required. In general, the derived spectra are well-described by a single- or double-component power-law model. The power spectrum for PSR B1558-50 contains a marginally significant step which, if interpreted in terms of the "mixed event" model proposed by Alpar *et al.* (1986), implies a relaxation time-scale of $\tau \geq 300$ days in response to the triggering events. The power spectrum of the phase residuals for the Vela pulsar was found to be composite in nature, with a previously unseen second component toward the high-frequency end of the spectrum. The latter component may result from microglitches which originate somewhere between the superweak and weak pinning regions, as suggested by the Cheng (1987b) magnetospheric model. This is supported by the data, which imply a characteristic relaxation time-scale of ~ 60 days.

Finally, a number of conclusions can be drawn regarding the applicability of the three main theoretical models of pulsar timing noise, namely, those proposed by Alpar *et al.* (1986), Cheng (1987a,b;1989) and Jones (1990d). None of the models proposed by Alpar *et al.* (1986) are, by themselves, able to account for the range of microactivity evident in the pulsars studied. In particular, none of the Alpar *et al.* models are able to explain the occurrence of positive-going jumps in $\dot{\nu}$. However, these models do support observations in a few cases, for example, where the timing activity is consistent with phase noise, and the step in the power spectrum for PSR B1558-50.

There is considerably more support for the Cheng magnetospheric model, which incorporates the ideas of Alpar *et al.*, and the Jones corotating vortex model. Both of these models are able to account for the wide range of microjump event signatures, as well as single and composite power-law spectra of the timing noise. However, neither model can explain *all* of the observations. The magnetospheric model does not easily explain the fact that the bulk of the timing activity in a number of pulsars is due to a *small* number of microjumps in ν and $\dot{\nu}$. The corotating vortex model does not explain a spectrum, or a spectral component, of the $\dot{\nu}$ fluctuations which is "blue". Both the magnetospheric and corotating vortex models provide promising bases for a better understanding of pulsar timing noise. However, they may need to be modified in the light of these observational results in order that predictions can be sharpened. This is particularly relevant in the case of the latter model, for which a full quantitative solution is yet to be published.

All of the above results and conclusions serve to demonstrate the usefulness of a long-term pulsar timing program. Indeed, our understanding of pulsar timing noise will only continue to improve as long as the observational data continue to

accumulate and be subjected to a wide variety of analytical techniques. In this way, further comparisons of the observations and theories can be made. By thoroughly testing the theoretical models against observations of the timing activity of pulsars, it should be possible to further probe the structure and dynamics of neutron stars.

9.2 Scope for future work

The work leading to the findings presented in this thesis has suggested a number of areas of possible future research. These are briefly summarised below.

Apart from the obvious benefits of continuing this long-term pulsar timing program, four pulsars require further monitoring. These objects are: (i) PSR B0959-54, to provide confirmation of the precession effects suggested by the present work; (ii) PSR B1240-64, to establish if the alternating microjump behaviour continues, providing further clues to the mechanism responsible; (iii) PSR B1727-47, to monitor the postglitch relaxation, if any; and (iv) PSR B1737-30, as this pulsar is one of the best candidates for gathering vital glitch data.

The existing timing data for the 45 pulsars in the Mt Pleasant survey can also be used to study long-term ($\geq$ days) intensity variations. The main aim of such a study would be to quantify the possible effects of refractive interstellar scintillation. However, it would also appear valuable to investigate the possible correlation of the intensity variations with the timing variations, with the object of establishing in which cases free precession might apply (e.g., PSR B0959-54). Past observations of intensity variations have been conducted over relatively short data spans, typically no more than one year (e.g., Stinebring & Condon 1990, Kaspi & Stinebring 1992), making it difficult to measure or confirm longer refractive time-scales. This situation has been improved by the recent work of LaBrecque *et al.* (1994), whose data span covered a 4-year observing period. However, the Mt Pleasant observations will almost double this latter time span. Furthermore, the dual-frequency data will enable the frequency scaling of the variations to be investigated. This information is useful for testing the predictions of refractive interstellar scintillation theories.

The study of timing noise in the Vela pulsar has also highlighted a number of areas requiring further investigation. The findings have suggested that free precession may be the origin of the low-level timing activity in this pulsar. A study of long-term pulse-shape changes and intensity variations would be useful in this regard. The possible contribution of dispersion measure fluctuations to the timing noise is another area requiring detailed investigation. Because the Vela timing data are recorded at three frequencies, analysis should provide a means of distinguishing between dispersive and non-dispersive effects. Consideration must also be given to the new theory of temporal variation of pulsar dispersion measure proposed by Wu & Chian (1995). The high quality and quantity of the Vela data

obtained at the Mt Pleasant Observatory should provide a better understanding of the short-term (sub-day) excess phase noise reported by Downs & Krause-Polstorff (1986). These data should also be useful for performing an in-depth analysis of the Vela timing noise in terms of a chaotic dynamical process, along similar lines to the work of Harding *et al.* (1990).

Appendix A

A Description of Polarization

From a basic study of electromagnetism, it is well known that an electromagnetic wave in free space undergoes transverse oscillations and the electric (E) and magnetic (B) field vectors lie in a plane perpendicular to the direction of propagation. The precise direction of the electric (or magnetic) field vector in this plane is said to determine the state of *polarization* of the wave.

Consider a plane, monochromatic, electromagnetic wave propagating in the $+z$ direction, with x and y components of the electric field (similarly for the magnetic field),

$$E_x = E_{o_x} \cos(\omega t - kz + \phi_x) \tag{A.1}$$

$$E_y = E_{o_y} \cos(\omega t - kz + \phi_y) \tag{A.2}$$

where $\delta = \phi_x - \phi_y$ is the phase difference of the two components and $E_{o_{x,y}}$ are the amplitudes.

In order to observe the path traced out by the tip of the electric vector in the x-y plane as time progresses, that is, determine the state of polarization, let $z = 0$. The resultant electric vector becomes

$$E = E_{o_x} \cos(\omega t + \phi_x)\,\mathbf{i} + E_{o_y} \cos(\omega t + \phi_y)\,\mathbf{j} \tag{A.3}$$

where $\mathbf{i}$, $\mathbf{j}$ are the unit vectors in the x and y directions respectively. Expanding, eliminating time, t, to allow construction of the *vibration curve* of E_y vs E_x, and combining these equations gives

$$\left(\frac{E_x}{E_{o_x}}\right)^2 + \left(\frac{E_y}{E_{o_y}}\right)^2 - 2\left(\frac{E_x}{E_{o_x}}\right)\left(\frac{E_y}{E_{o_y}}\right)\cos\delta = \sin^2\delta \tag{A.4}$$

This is the general equation for an ellipse, and the wave is said to be *elliptically* polarized. Having obtained a general function in terms of E_x and E_y, it is useful to consider particular values of the phase difference, δ.

In the case where $\delta = \pm n\pi$ ($n = 0, 1, 2, 3, \ldots$), Equation A.4 reduces to

$$E_y = \pm\left(\frac{E_{o_y}}{E_{o_x}}\right) E_x \tag{A.5}$$

This is the equation of a straight line, and so the wave is *linearly* polarized. The slope of the linear polarization vector is determined by the ratio of the amplitudes of E_y and E_x.

In the case where $\delta = \pm\frac{n\pi}{2}$ $(n = 1, 2, 3, ...)$, Equation A.4 reduces to

$$\left(\frac{E_x}{E_{o_x}}\right)^2 + \left(\frac{E_y}{E_{o_y}}\right)^2 = 1 \tag{A.6}$$

This is the equation of an ellipse, and so the wave is *elliptically* polarized. If $E_{o_x} = E_{o_y}$, the resulting wave is *circularly* polarized. It can be shown (e.g., see Kraus 1950, Kraus 1986) that if $\delta = +\frac{\pi}{2}$ (i.e., E_x leads E_y by 90° in phase) the electric-field vector rotates *counter-clockwise* if the wave is approaching. Similarly, rotation is *clockwise* if $\delta = -\frac{\pi}{2}$. In modern usage, the wave is said to be *right-hand polarized* if, as it propagates towards the observer, the tip of the electric vector rotates counter-clockwise, and vice-versa for a *left-hand polarized* wave. Note that in some of the literature (e.g., Born & Wolf 1975), the classical or "optics" convention is used, which is opposite to the system just described. The modern convention uses the "natural" definition – the concept of the right-hand and left-hand screw.

In all other situations, where the phase difference is any arbitrary constant (as is the ratio of amplitudes, E_{o_y}/E_{o_x}), the vibration curve is once again an ellipse (described by Equation A.4), but with its major axis inclined at an angle ψ to the x and y axes. Introducing a new set of axes, X and Y, along the major and minor axes of the ellipse respectively, the electric field components E_x and E_y can be written in terms of E_X and E_Y, where

$$E_x = E_X \cos\psi - E_Y \sin\psi \tag{A.7}$$

and

$$E_y = E_X \sin\psi + E_Y \cos\psi. \tag{A.8}$$

Substituting these equations into the general equation (A.4) yields

$$\psi = \frac{1}{2}\arctan\left(\frac{2E_{o_x}E_{o_y}\cos\delta}{E_{o_x}^2 - E_{o_y}^2}\right) \tag{A.9}$$

Hence, given the amplitudes E_{o_x} and E_{o_y}, and the phase difference, δ, the angle of tilt of the polarization ellipse can be calculated.

It is worthwhile considering the polarization states produced by combining two of the states. It has already been shown that two orthogonal "linearly polarized" waves (E_x and E_y) will produce a wave which is linearly, circularly, or elliptically polarized, depending on the phase difference, δ. Hecht & Zajac (1987) show that a linearly polarized wave is obtained from two circularly polarized waves of opposite rotation and equal amplitude. The fact that such a wave can be considered as

the sum of two opposite circularly polarized waves is important in a discussion of the Faraday effect. Following from the above, it can be shown that two opposite circularly polarized waves of differing amplitudes result in an elliptically polarized wave. Kraus (1950) proves this for the general case, and shows that the rotation of the ellipse is in the direction of rotation of the circular wave with the larger amplitude.

In the previous discussion it was assumed that the waves are monochromatic, i.e., that the orthogonal components of the waves have identical frequencies and a constant amplitude and phase. This means the wave is coherent and completely polarized. However, observations in radio astronomy are conducted within a finite bandwidth, Δf, consisting of the superposition of many waves with independent amplitudes and phases that vary with time, resulting in a randomly polarized, or unpolarized, signal. However, if Δf is small compared to the mean frequency of observation, $\bar{f}$, the polarization state varies slowly (since the *coherence time* is inversely proportional to Δf), and is essentially constant over a long period of time. The wave is said to be *quasimonochromatic* and is partially polarized.

For the general case of partial polarization, a method is required for describing the *state* and *degree* of polarization of a wave, in terms of variables that are readily observed. The Poincaré Sphere (see Rohlfs 1986, Kraus 1986) is a representation that permits easy visualisation of the different states of polarization, and this follows naturally to the Stokes parameters (introduced by Sir George Stokes in 1852) which describe both the state and degree of polarization. These four quantities are functions only of the measurable properties of electromagnetic waves, namely the amplitude and phase difference. For a plane, monochromatic (completely polarized) wave, they are given by (Kraus 1986):

$$I = \frac{1}{Z}(E_{o_x}^2 + E_{o_y}^2) \tag{A.10}$$

$$Q = \frac{1}{Z}(E_{o_x}^2 - E_{o_y}^2) \tag{A.11}$$

$$U = \frac{2E_{o_x}E_{o_y}}{Z}\cos\delta \tag{A.12}$$

$$V = \frac{2E_{o_x}E_{o_y}}{Z}\sin\delta \tag{A.13}$$

where E_{o_x} and E_{o_y} are the amplitudes of the two orthogonal components of the wave, δ is the phase difference and Z is the intrinsic impedance of the medium. The parameter I is simply the total intensity received ($I = I_x + I_y$), Q and U are the linearly polarized intensities with respect to the x and y axes and at 45° to these axes respectively, and V is the circularly polarized intensity. Using the modern convention, the parameter V is defined in the sense of left-hand minus right-hand circularly polarized intensity, so if $V > 0$, the radiation has a tendency towards left-handedness and vice versa.

For the general case of a quasimonochromatic wave, the Stokes parameters can be rewritten as

$$I = \frac{1}{Z}(<E_{o_x}^2> + <E_{o_y}^2>) \tag{A.14}$$

$$Q = \frac{1}{Z}(<E_{o_x}^2> - <E_{o_y}^2>) \tag{A.15}$$

$$U = \frac{2}{Z} < E_{o_x} E_{o_y} \cos\delta > \tag{A.16}$$

$$V = \frac{2}{Z} < E_{o_x} E_{o_y} \sin\delta > \tag{A.17}$$

The <> brackets denote that the values are rms time averages, since E_{o_x}, E_{o_y} and δ are slowly varying functions of time.

From these equations and Equation A.9, it follows that

$$I^2 \geq Q^2 + U^2 + V^2, \tag{A.18}$$

$$d = \frac{\sqrt{Q^2 + U^2 + V^2}}{I} \tag{A.19}$$

and

$$\psi = \frac{1}{2} \arctan\left(\frac{U}{Q}\right) \tag{A.20}$$

where d is the degree of polarization ($0 \leq d \leq 1$) and ψ is the position angle of the linear polarization vector.

Hence, the Stokes parameters are extremely useful for systematically analysing and describing the state and degree of polarization of a quasimonochromatic wave in terms of directly measurable quantities, namely, amplitudes and phase differences. This method of description is used extensively in the study of the radio emission from pulsars, which often has a high degree of linear polarization and some circular polarization.

Appendix B

Calibration of the Stokes Parameters U & V

Correct calibration of the U and V Stokes parameters necessitates the removal of any phase difference between the X and Y signals that is introduced by the receiver, e.g., because of a difference in the path lengths through the receiver system or a phase difference between the X and Y filters. This "instrumental phase", ϕ_i, can be removed by "derotating" the data. The derotation information is derived from a linearly polarized calibration (CAL) signal and a known phase delay introduced into the system.

If a linearly polarized CAL signal is radiated equally into the X and Y dipoles, then one can measure intensities corresponding to the polarization parameters I_X, I_Y, U and V *for the* CAL *signal*, hereafter called I'_X, I'_Y, U' and V'. Let the signals from the X and Y dipoles be given by

$$E_x = E_o \sin(\omega t + \phi_x) \tag{B.1}$$

and

$$E_y = E_o \sin(\omega t + \phi_y) \tag{B.2}$$

where the phase difference $\delta = \phi_x - \phi_y$. The component system gains can be defined as follows (see also Chapter 3):

G_X = gain in the X channel,
G_Y = gain in the Y channel,
G_{M_X} = gain of the X multiplier,
G_{M_Y} = gain of the Y multiplier,
G_{M_U} = gain of the U multiplier, and
G_{M_V} = gain of the V multiplier.

Provided there is no instrumental phase in the receiving system, one expects to measure I'_X, I'_Y and U' which are non-zero, and V' which is zero for a linearly polarized CAL signal. However, V' is usually non-zero, even for the most carefully constructed receiver. Hence, the aim of the calibration procedure is to remove this instrumental circular polarization.

From the definition of the Stokes parameters (see Appendix A),

$$I'_X = \tfrac{1}{2} G_{M_X} G_X^2 E_o^2, \tag{B.3}$$

$$I'_Y = \tfrac{1}{2} G_{M_Y} G_Y^2 E_o^2, \tag{B.4}$$

$$U' = G_{M_U} G_X G_Y E_o^2 \cos\phi_i, \tag{B.5}$$

$$V' = \pm G_{M_V} G_X G_Y E_o^2 \sin\phi_i, \tag{B.6}$$

where U' is the "in-phase product" of the X and Y signals and V' is the "quadrature" product of the X and Y signals. The latter product is achieved by placing a 90° phase shift between the X and Y signals using an LC circuit, as described in Chapter 3 (not to be confused with the phase shift inserted by the hybrid circuit). The parameter V' can have either sign, in order that the derotation process is kept as general as possible. That is, both a 90° phase *delay* and *advance* must be considered, or alternatively, the possibility that the phase shift from the LC circuit is in either the X or Y channel. Later, it is shown that this sign ambiguity is automatically removed in the derotation process.

The only difference between the overall gains of U' and V' is the multiplier gain, which is defined by the ratio $K_{UV} = \frac{G_{M_U}}{G_{M_V}}$. Hence, there are two unknown quantities, K_{UV} and ϕ_i, requiring two independent measurements, namely, one with no inserted phase (hereafter called "measurement 1") and another with a phase delay inserted in the X or Y RF channel (hereafter called "measurement 2"; also see Chapter 3). A phase delay of 90° is convenient but any non-zero (or equivalent) phase delay is acceptable. In the following treatment, the former value will be assumed, and then the general result will be quoted.

Since U' and V' are orthogonal, the situation is best described graphically. Figure B.1(a) is a representation of measurement 1, and shows that if there is an instrumental phase, ϕ_i, between the X and Y channels, the measured intensities U'_1 and V'_1 are components of the true intensity U expected from a linearly polarized CAL signal. The V'-U' axis system must be rotated in order to obtain the true values U and V. Hence,

$$U = U'_1 \cos\phi_i + V'_1 \sin\phi_i, \tag{B.7}$$

$$V = -U'_1 \sin\phi_i + V'_1 \cos\phi_i, \tag{B.8}$$

and allowing for differing gains so that both U and V have the same gain, namely $G_U = G_{M_U} G_X G_Y$,

$$G_U U = U'_1 \cos\phi_i + K_{UV} V'_1 \sin\phi_i, \tag{B.9}$$

$$G_U V = -U'_1 \sin\phi_i + K_{UV} V'_1 \cos\phi_i. \tag{B.10}$$

A similar situation applies for measurement 2 [Figure B.1(b)], so for a 90° phase delay,

$$G_U U = -U'_2 \sin\phi_i + K_{UV} V'_2 \cos\phi_i, \tag{B.11}$$

$$G_U V = -U_2' \cos\phi_i - K_{UV} V_2' \sin\phi_i. \tag{B.12}$$

Equating B.9 & B.11 and B.10 & B.12, multiplying by $\sin\phi_i$ and $\cos\phi_i$ respectively, and adding, one finds that

$$K_{UV} = -\frac{U_2'}{V_1'}. \tag{B.13}$$

Substituting Equation B.13 into one of the intermediate equations gives

$$U_1' V_1' = -U_2' V_2' \tag{B.14}$$

and from the definitions B.5 and B.6,

$$\tan\phi_i = -\frac{U_2'}{U_1'} = \frac{V_1'}{V_2'} \tag{B.15}$$

or simply

$$\phi_i = \arctan\left[K_{UV}\left(\frac{V_1'}{U_1'}\right)\right]. \tag{B.16}$$

The product $K_{UV}V_1'$ takes care of the sign ambiguity described earlier since it will always be positive, i.e., if V_1' is negative, then K_{UV} is negative. This product also appears in the derotation equations, so any ambiguity in the hardware relating to the sign convention of the V parameter is automatically removed.

For the more general case of a $(90+\gamma)°$ phase delay, Equations B.11 and B.12 become

$$G_U U = -U_2' \sin(\phi_i + \gamma) + K_{UV} V_2' \cos(\phi_i + \gamma), \tag{B.17}$$

$$G_U V = -U_2' \cos(\phi_i + \gamma) - K_{UV} V_2' \sin(\phi_i + \gamma). \tag{B.18}$$

Manipulating the equations in a similar manner as before, one finds that

$$K_{UV} = -\left(\frac{U_2' \cos\gamma}{V_1' + V_2' \sin\gamma}\right), \tag{B.19}$$

and

$$\phi_i = \arctan\left(\frac{-U_2' V_1' \cos\gamma}{U_1' V_1' + U_1' V_2' \sin\gamma}\right). \tag{B.20}$$

Using these equations, the polarization data are calibrated by calculating K_{UV} and ϕ_i, derotating the CAL information and then the actual data.

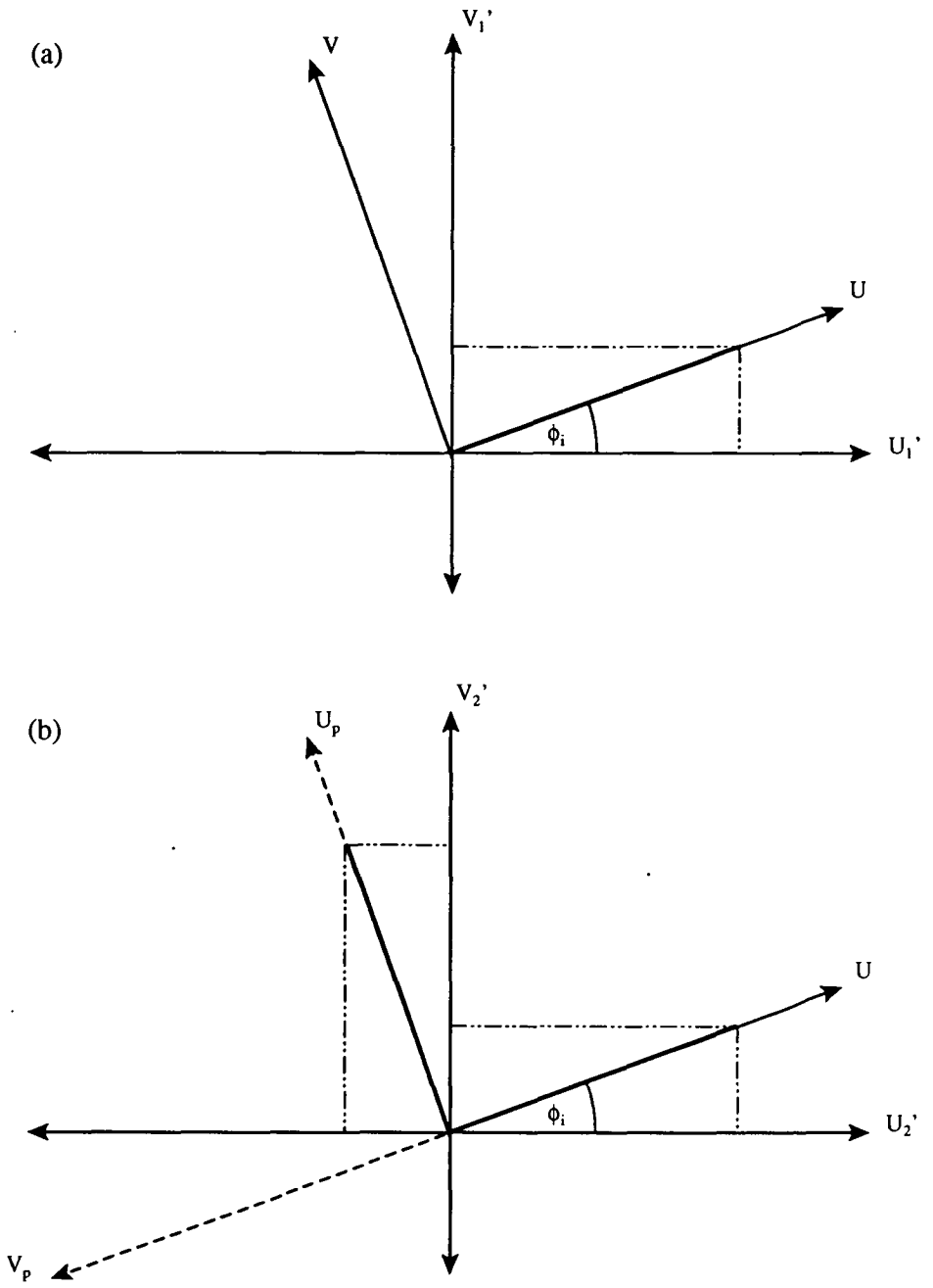

Figure B.1: Graphical representation of the Stokes parameters U and V, which are orthogonal. (a) For measurement 1 (no phase delay inserted), the measured parameters U_1' and V_1' are components of the true intensity U of the linearly polarized CAL signal. (b) For measurement 2 (90° phase delay inserted), the V-U co-ordinate system has been rotated 90° to the V_P-U_P system. If the U and V gains are the same, then $V_2' = U_1'$ and $U_2' = -V_1'$. However, equal gains are difficult to achieve in practice and so the difference must be allowed for in the calibration procedure.

Appendix C

Plots of Phase Residuals

This appendix displays the phase residuals obtained for each pulsar: (a) from a fit for period, period derivative (i.e., using a second order polynomial), position, dispersion measure and, for PSRs B0740-28, B1240-64, B1641-45, B1727-47 and B1737-30, jumps in the rotation rate (**Figure C.1**), (b) as for Figure C.1, with no allowance for small jumps in the rotation rate of PSRs B0740-28, B1240-64, B1641-45 and B1737-30 (**Figure C.2**), (c) as for Figure C.1, but with the addition of the period second derivative, i.e., using a third order polynomial (**Figure C.3**).

The residuals are displayed in the sense of *measured minus predicted arrival times*, and are expressed in thousandths of the pulse period or milliperiods.

Key: • = 650 MHz data, o = 800 MHz data.

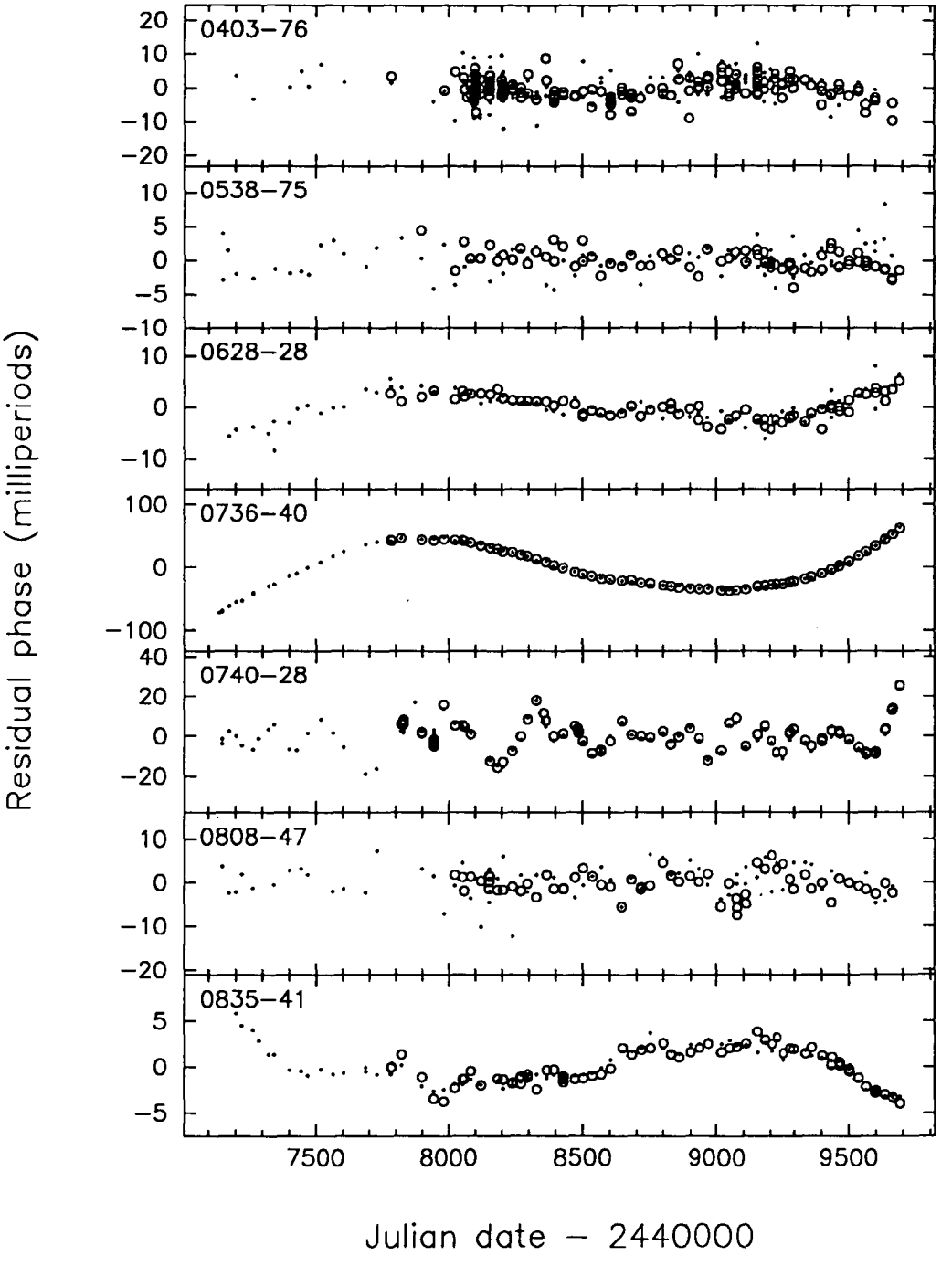

Figure C.1: (a) Phase residuals obtained for PSRs B0403-76, B0538-75, B0628-28, B0736-40, B0740-28, B0808-47 and B0835-41 after second order polynomial fits.

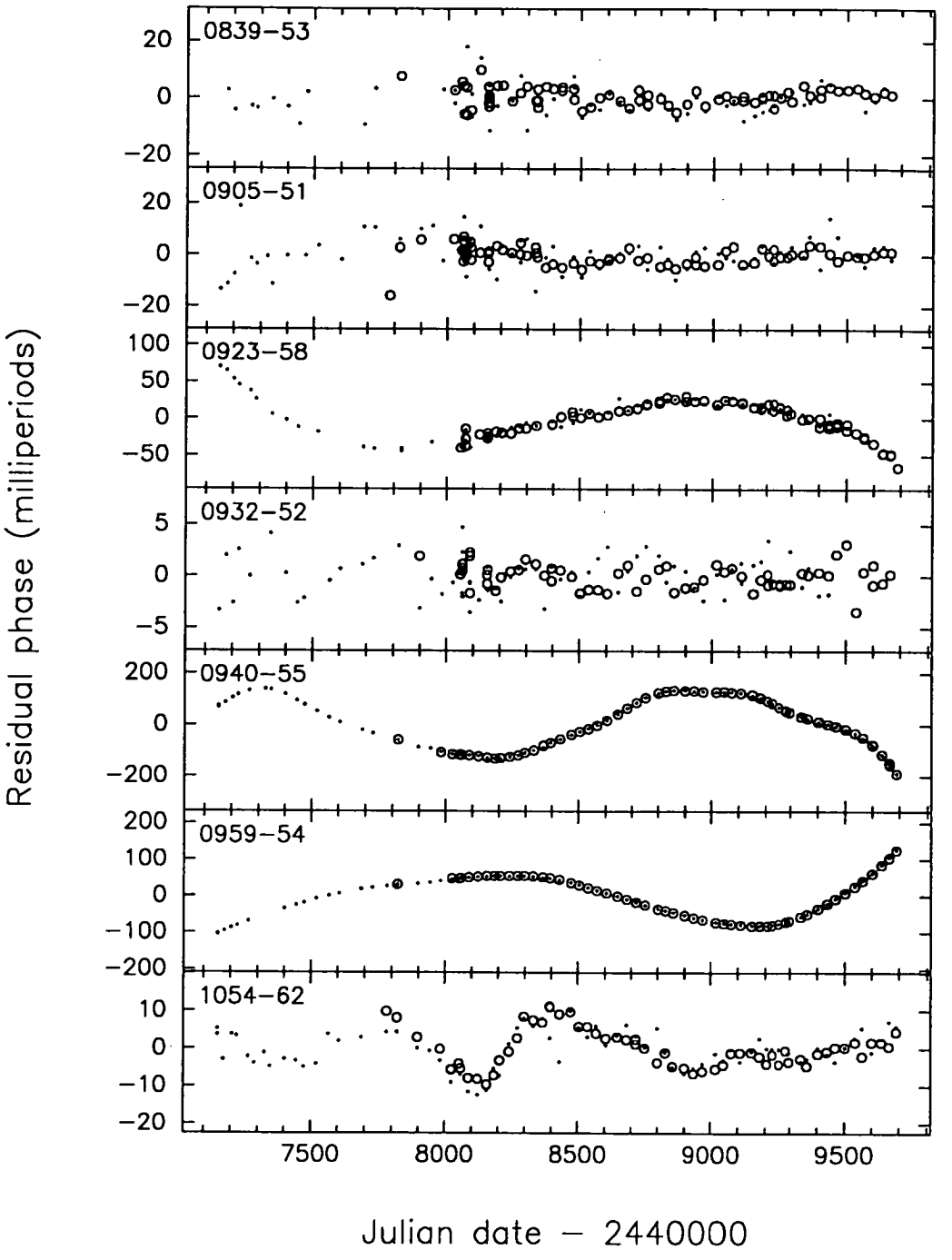

Figure C.1: (b) Phase residuals obtained for PSRs B0839-53, B0905-51, B0923-58, B0932-52, B0940-55, B0959-54 and B1054-62 after second order polynomial fits.

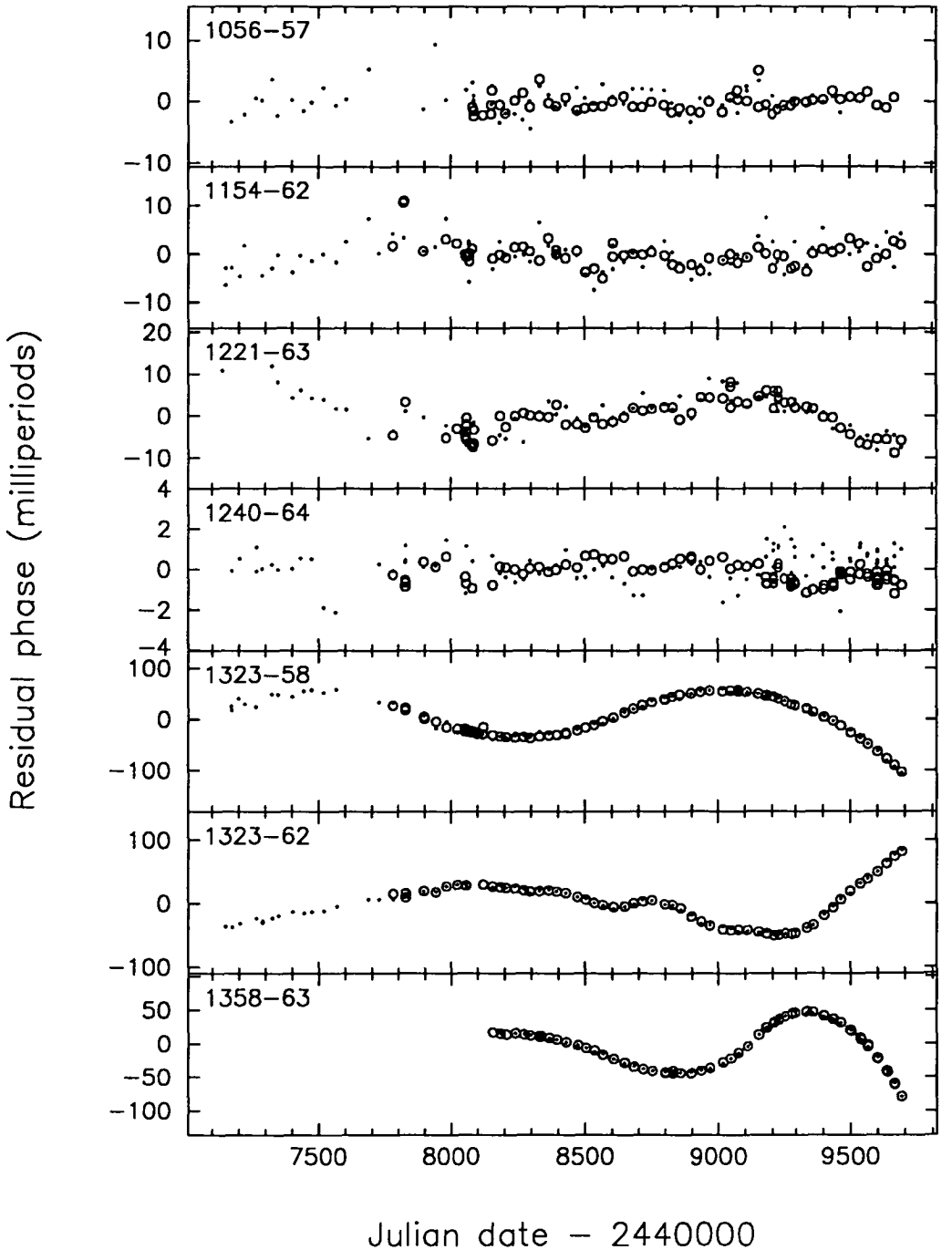

Figure C.1: (c) Phase residuals obtained for PSRs B1056-57, B1154-62, B1221-63, B1240-64, B1323-58, B1323-62 and B1358-63 after second order polynomial fits.

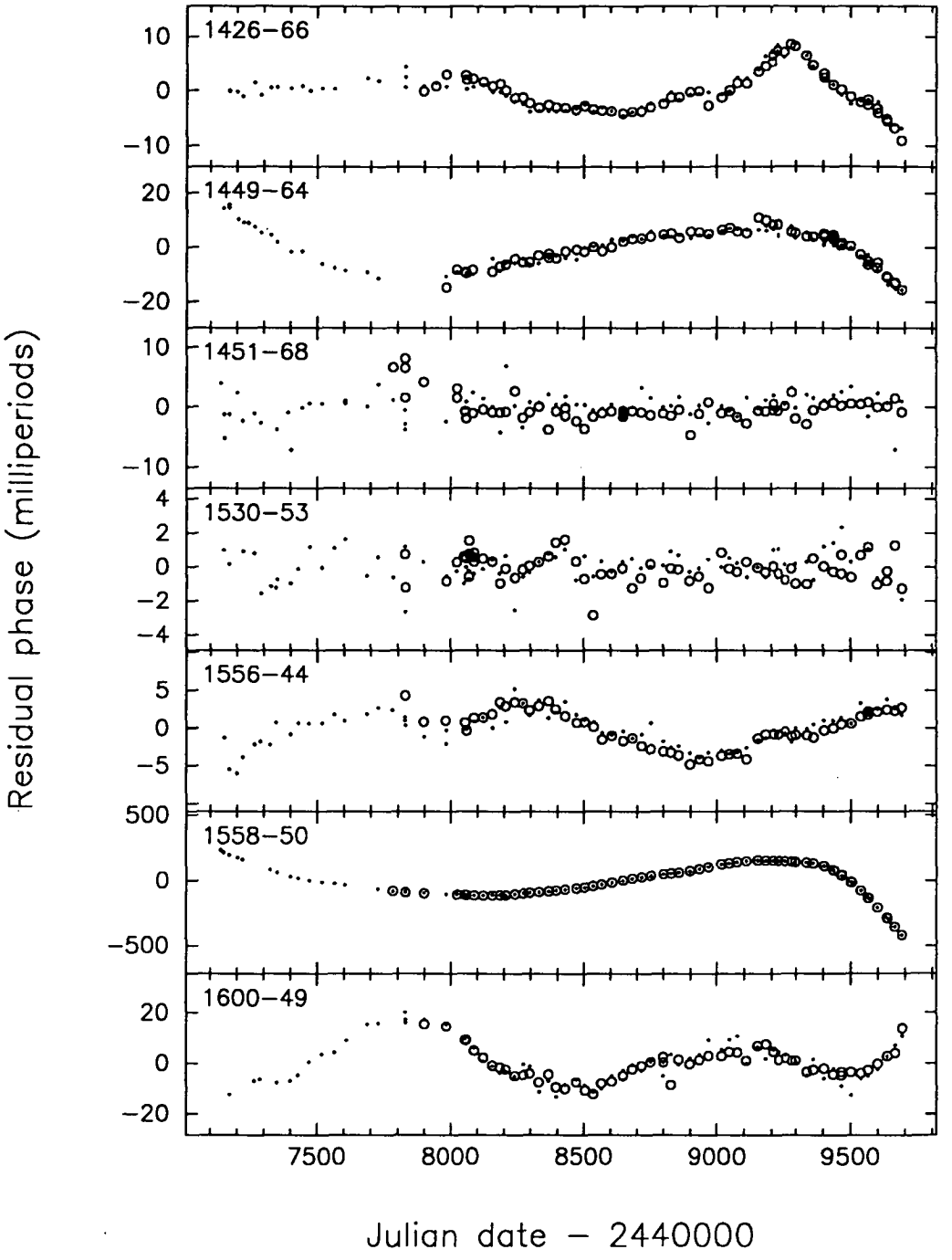

Figure C.1: (d) Phase residuals obtained for PSRs B1426-66, B1449-64, B1451-68, B1530-53, B1556-44, B1558-50 and B1600-49 after second order polynomial fits.

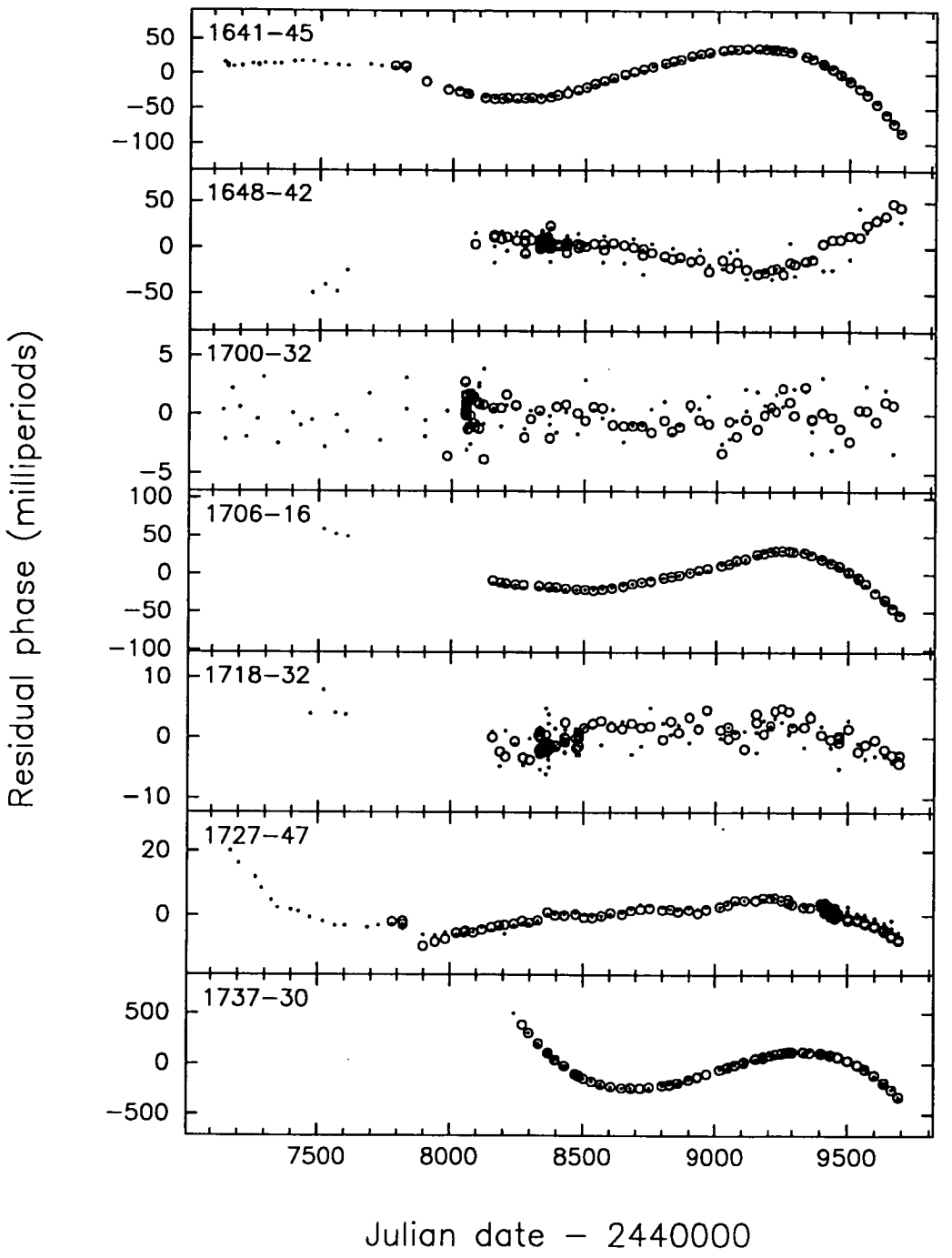

Figure C.1: (e) Phase residuals obtained for PSRs B1641-45, B1648-42, B1700-32, B1706-16, B1718-32, B1727-47 and B1737-30 after second order polynomial fits.

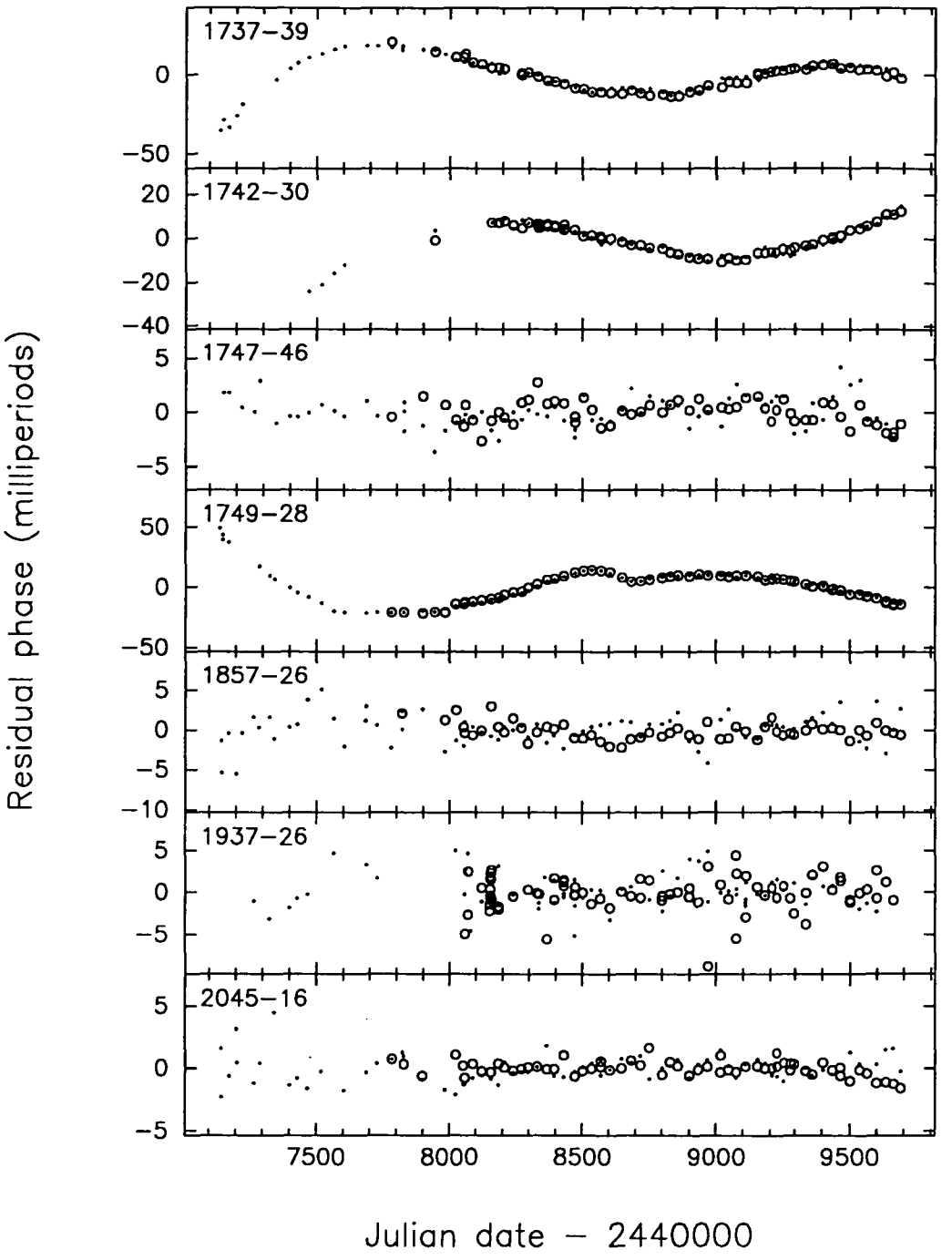

Figure C.1: (f) Phase residuals obtained for PSRs B1737-39, B1742-30, B1747-46, B1749-28, B1857-26, B1937-26 and B2045-16 after second order polynomial fits.

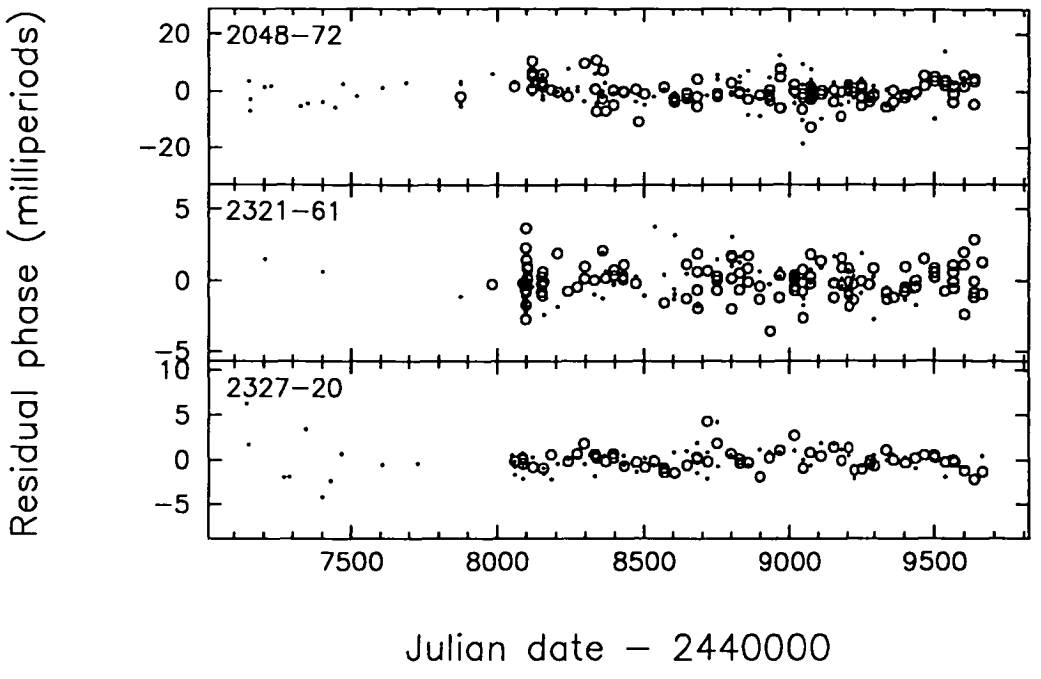

Figure C.1: (g) Phase residuals obtained for PSRs B2048-72, B2321-61 and B2327-20 after second order polynomial fits.

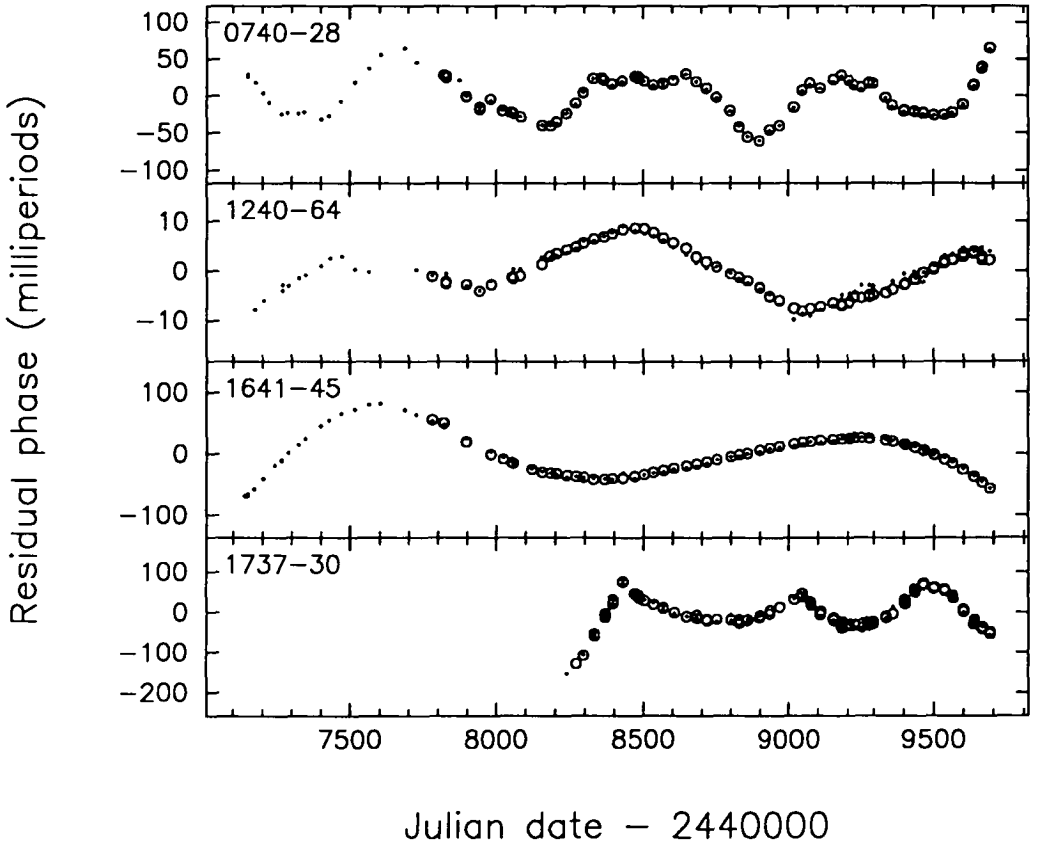

Figure C.2: Phase residuals obtained for PSRs B0740-28, B1240-64, B1641-45, and B1737-30 when no allowance is made for small jumps in the rotation rate.

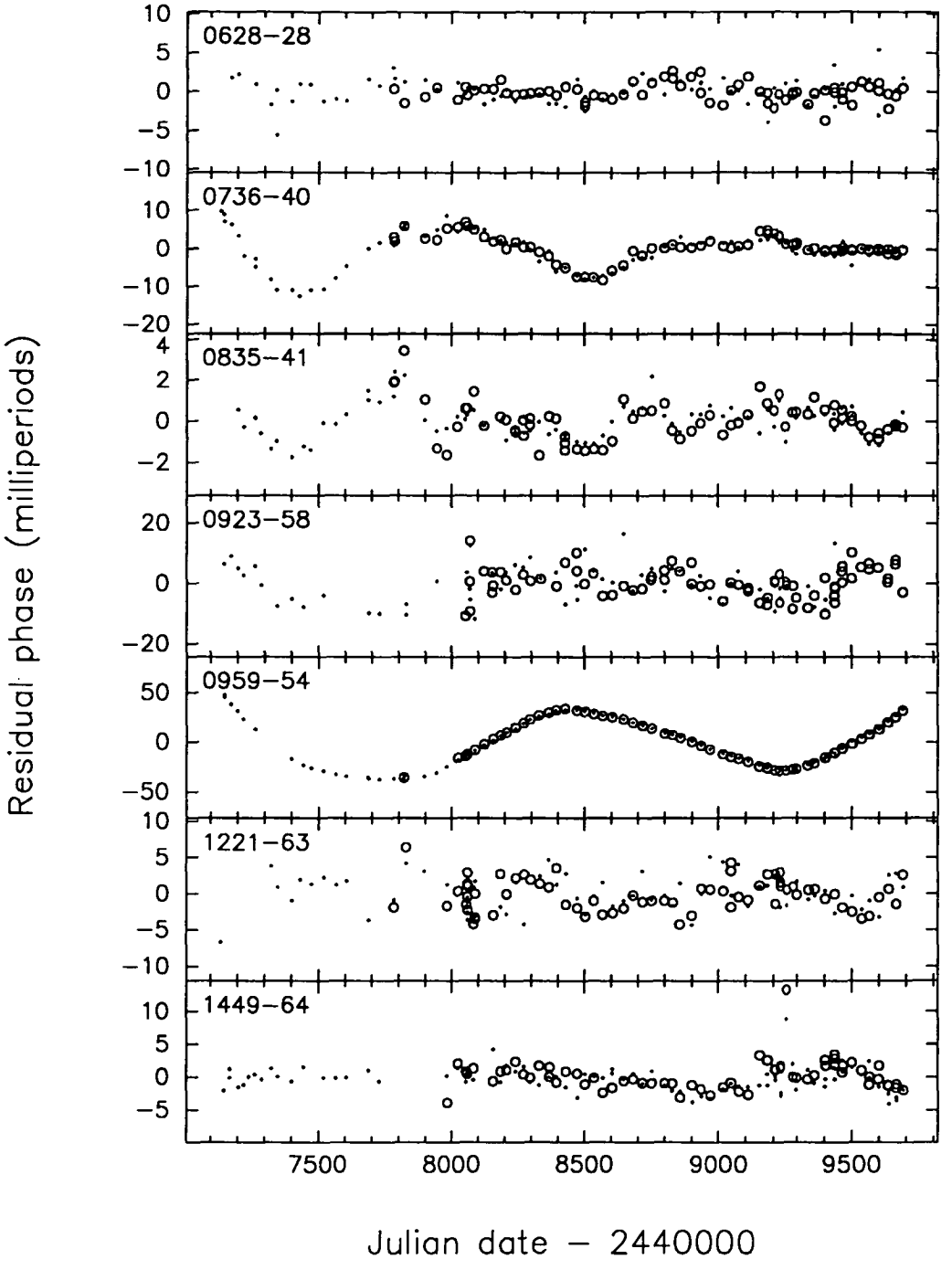

Figure C.3: (a) Phase residuals obtained for PSRs B0628-28, B0736-40, B0835-41, B0923-58, B0959-54, B1221-63 and B1449-64 after third order polynomial fits.

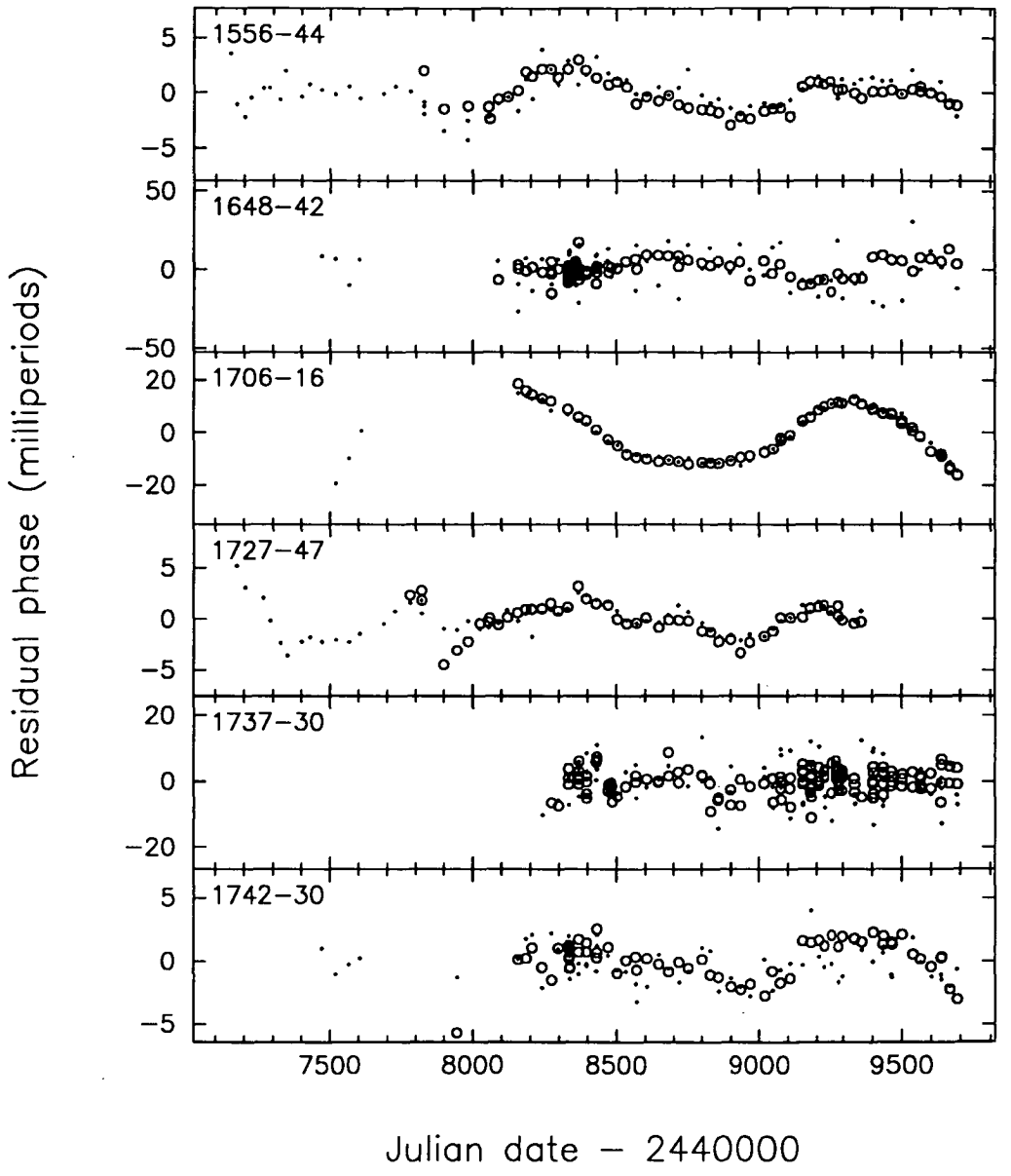

Figure C.3: (b) Phase residuals obtained for PSRs B1556-44, B1648-42, B1706-16, B1727-47, B1737-30 and B1742-30 after third order polynomial fits.

Appendix D

Pulse Profiles

This appendix presents plots of stable pulse profiles (or *templates*) for each pulsar at 670 and 800 MHz. These templates are used in the cross-correlation procedure to obtain local arrival times.

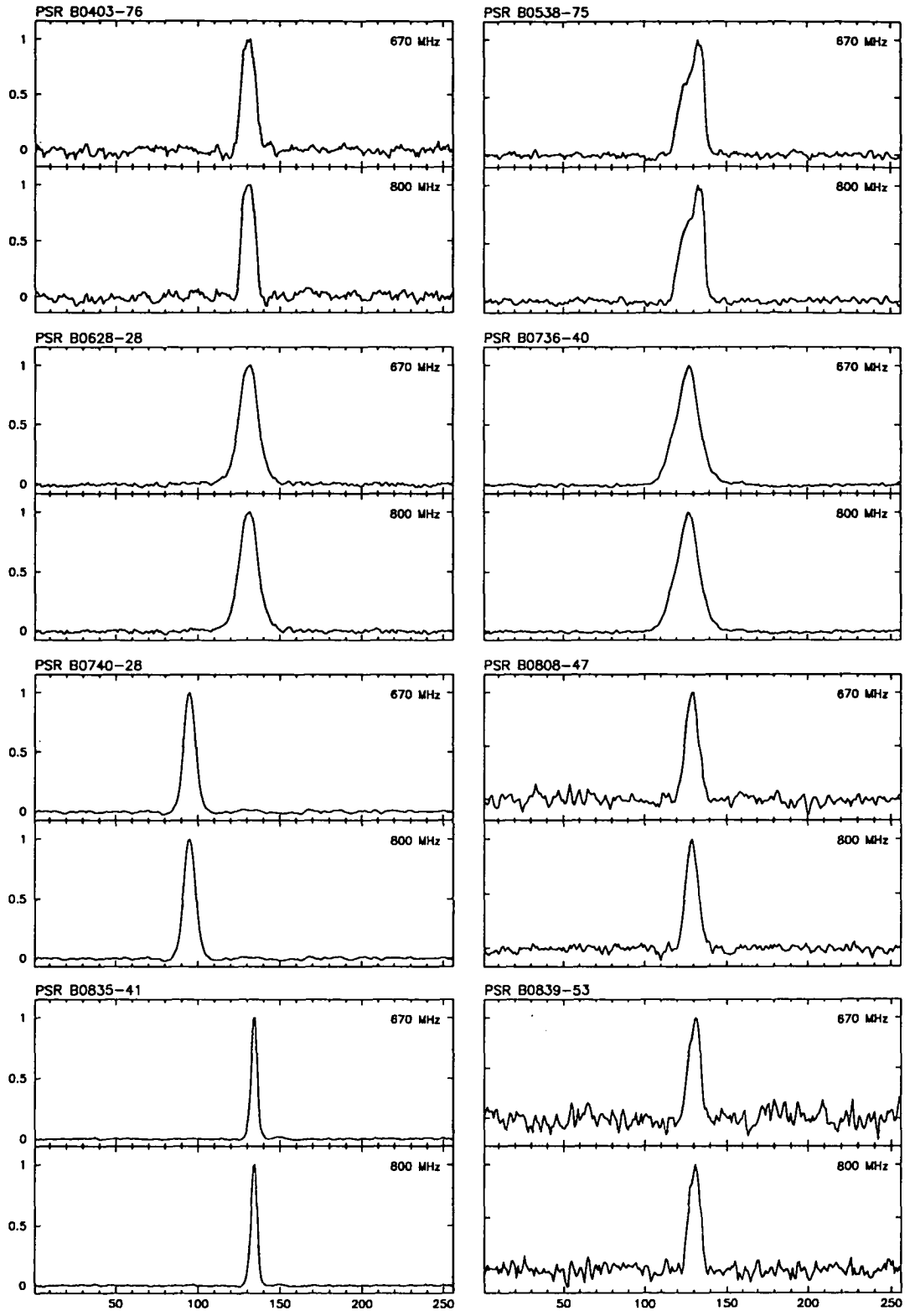

Figure D.1: Pulse profiles.

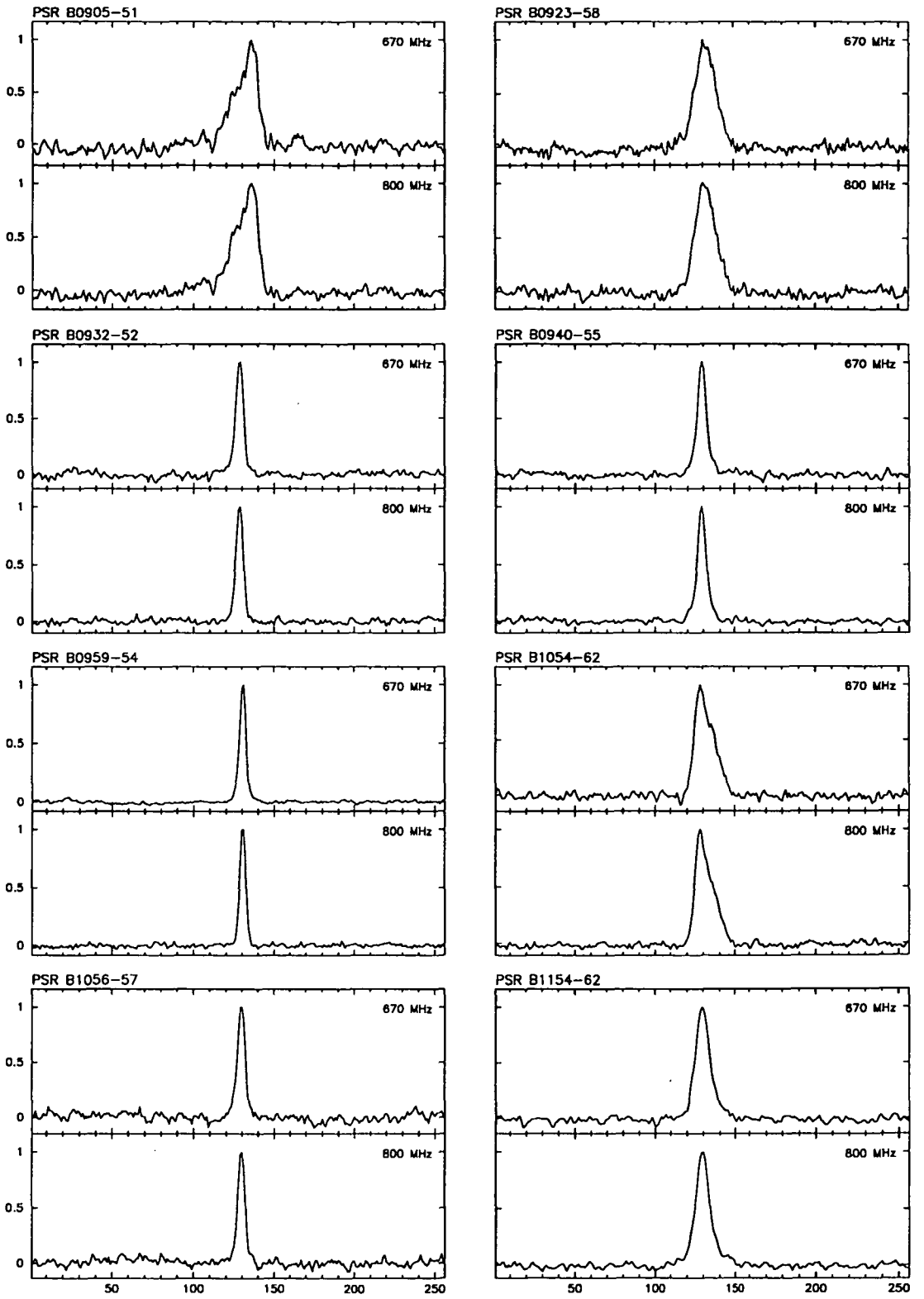

Figure D.1: Pulse profiles, continued.

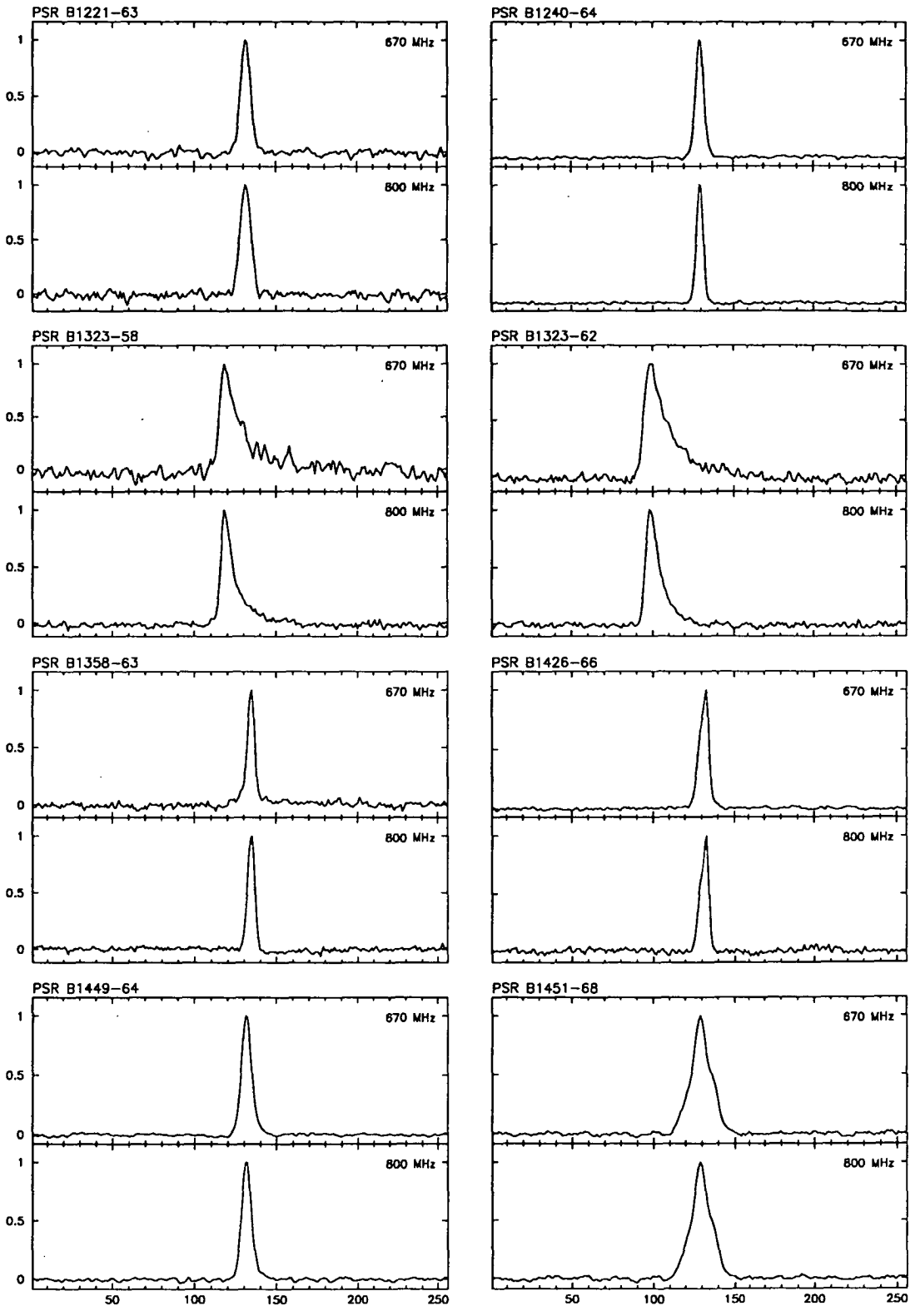

Figure D.1: Pulse profiles, continued.

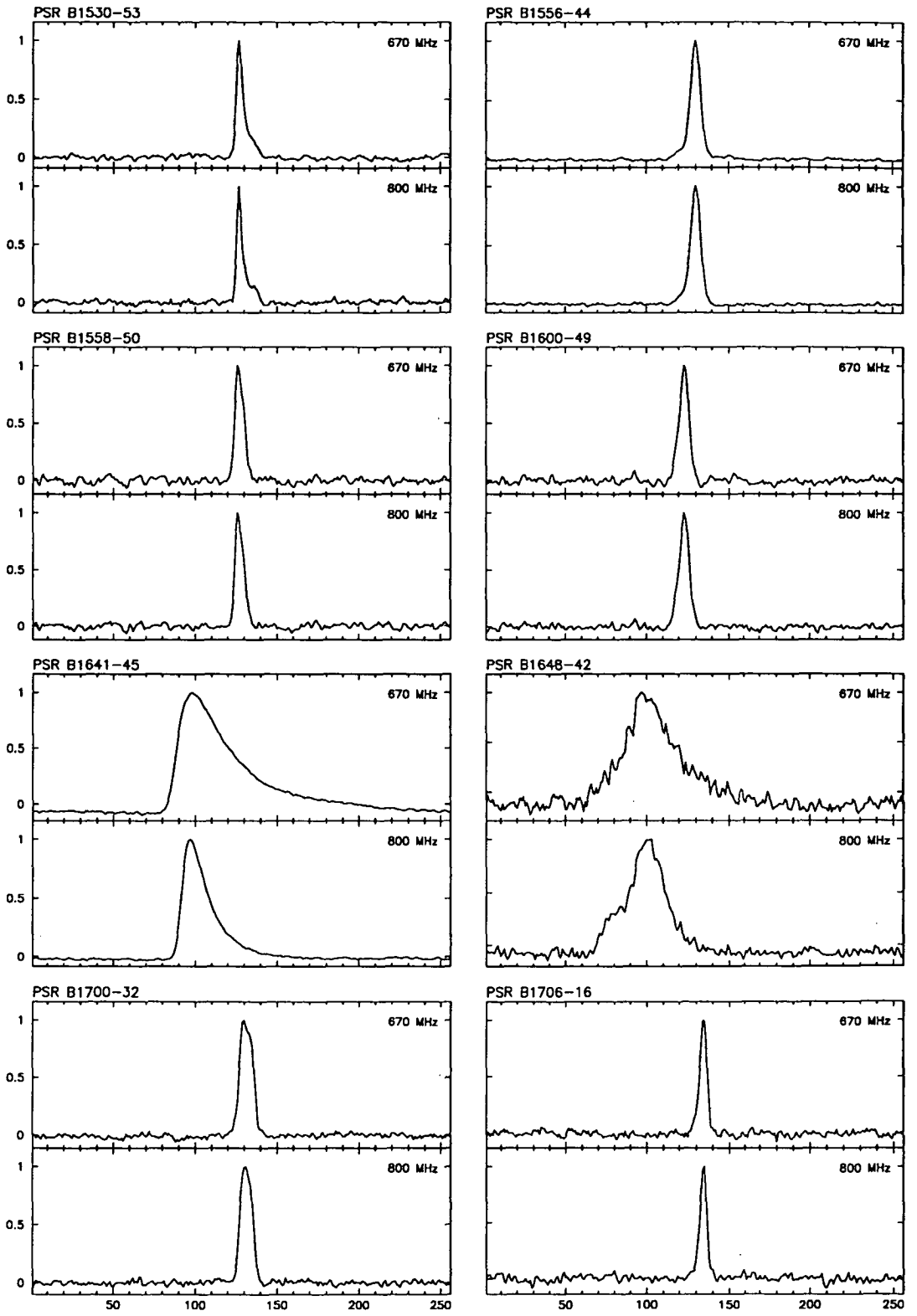

Figure D.1: Pulse profiles, continued.

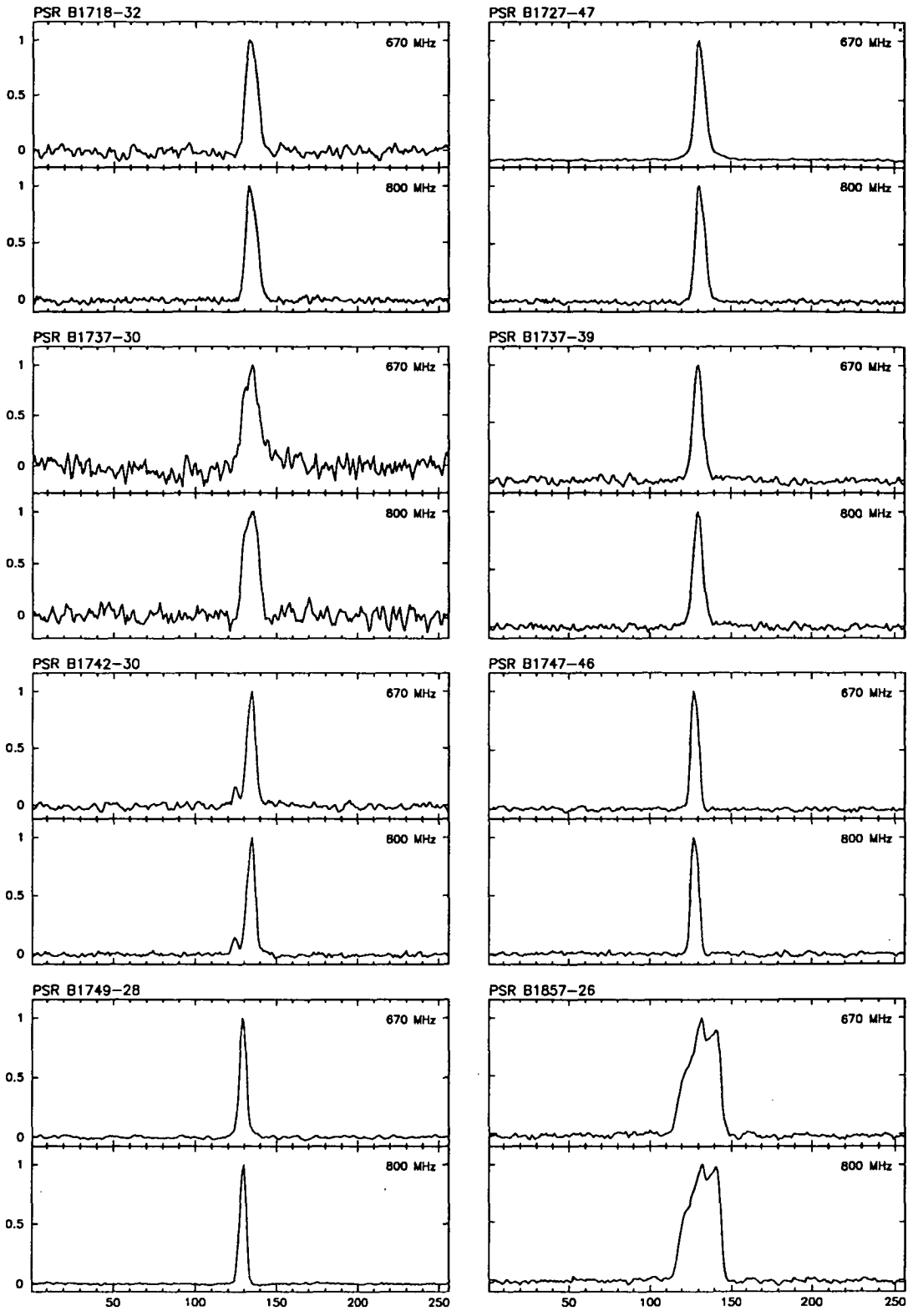

Figure D.1: Pulse profiles, continued.

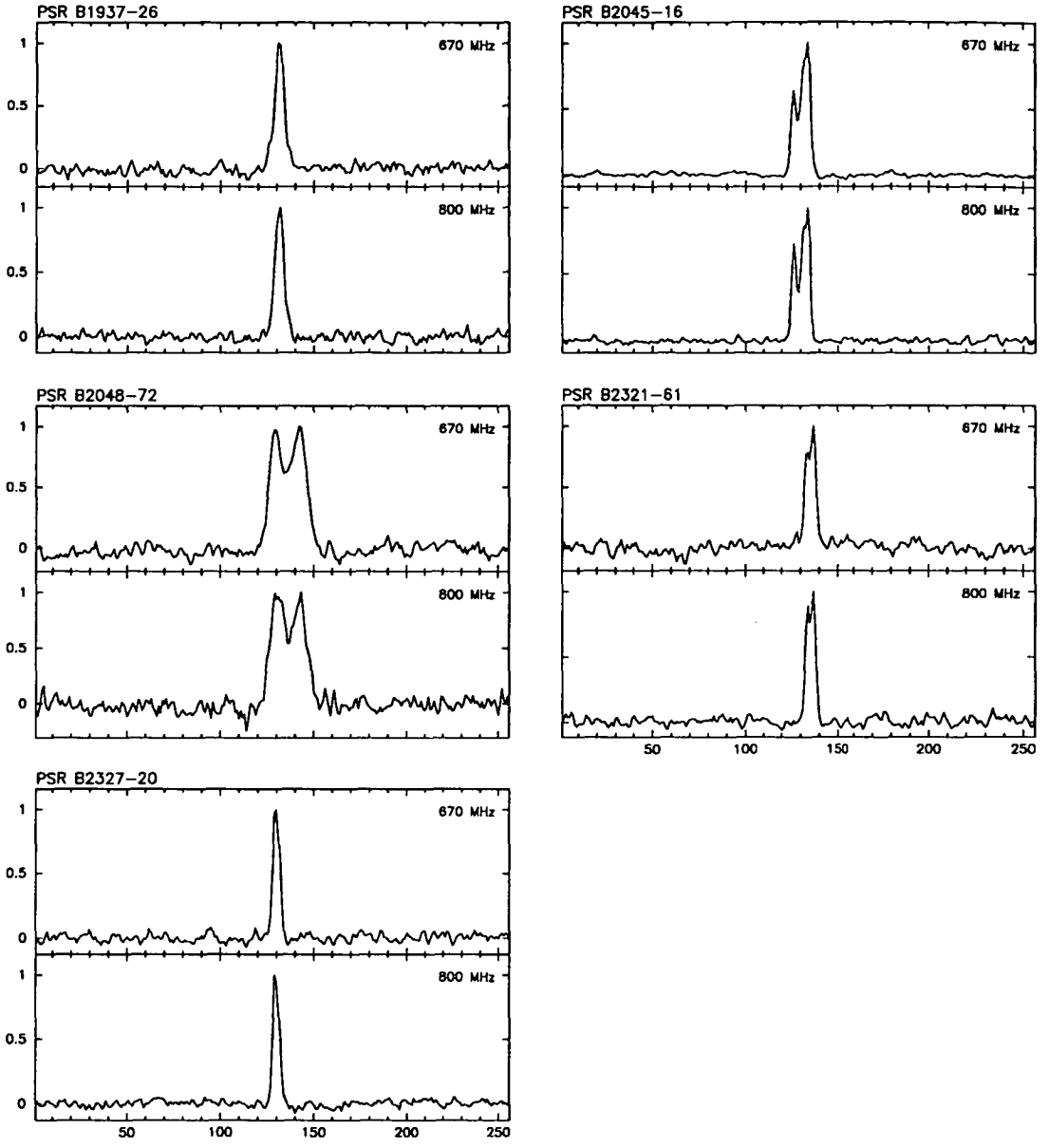

Figure D.1: Pulse profiles, continued.

Appendix E

Publications

Listed below are the author's publications in scientific journals resulting from particular aspects of the research conducted during the course of this project.

[1] D'Alessandro, F., McCulloch, P.M., King, E.A., Hamilton, P.A. & McConnell, D., 1993, "Timing observations of southern pulsars - 1987 to 1991", *Mon. Not. R. Astron. Soc.*, **261**, 883-894.

[2] D'Alessandro, F., McCulloch, P.M., Hamilton, P.A. & Deshpande, A.A., 1995, "The timing noise of 45 southern pulsars", accepted by *Mon. Not. R. Astron. Soc.*, in press.

[3] Deshpande, A.A., D'Alessandro, F. & McCulloch, P.M., 1995, "Application of CLEAN in the power spectral analysis of non-uniformly sampled pulsar timing data", submitted to *Mon. Not. R. Astron. Soc.*

References

Alpar, M.A., Anderson, P.W., Pines, D. & Shaham, J., 1981, "Giant glitches and pinned vorticity in the Vela and other pulsars", *Astrophys. J.*, **249**, L29-L33.

Alpar, M.A., Anderson, P.W., Pines, D. & Shaham, J., 1984a, "Vortex creep and the internal temperature of neutron stars. I. General theory", *Astrophys. J.*, **276**, 325-334.

Alpar, M.A., Anderson, P.W., Pines, D. & Shaham, J., 1984b, "Vortex creep and the internal temperature of neutron stars. II. Vela pulsar", *Astrophys. J.*, **278**, 791-805.

Alpar, M.A. & Baykal, A., 1994, "Expectancy of large pulsar glitches: a comparison of models with the observed glitch sample", *Mon. Not. R. Astron. Soc.*, **269**, 849-856.

Alpar, M A., Chau, H.F., Cheng, K.S. & Pines, D., 1993, "Postglitch relaxation of the Vela pulsar after its first eight large glitches: A re-evaluation with the vortex creep model", *Astrophys. J.*, **409**, 345-359.

Alpar, M A., Chau, H.F., Cheng, K.S. & Pines, D., 1994, "Postglitch relaxation of the Crab pulsar: evidence for crust cracking", *Astrophys. J.*, **427**, L29-L31.

Alpar, M.A., Cheng, K.S. & Pines, D., 1989, "Vortex creep and the internal temperature of neutron stars: Linear and nonlinear response to a glitch", *Astrophys. J.*, **346**, 823-832.

Alpar, M.A., Cheng, K.S., Pines, D. & Shaham, J., 1988, "The large glitch from PSR 0355+54 and its post-glitch relaxation", *Mon. Not. R. Astron. Soc.*, **233**, 25-31.

Alpar, M.A. & Ho, C., 1983, "Expectancy of large pulsar glitches", *Mon. Not. R. Astron. Soc.*, **204**, 655-667.

Alpar, M.A., Langer, S. & Sauls, J.A., 1984, "Rapid postglitch spin-up of the superfluid core in pulsars", *Astrophys. J.*, **282**, 533-541.

Alpar, M.A., Nandkumar, R. & Pines, D., 1985, "Vortex creep and the internal temperature of neutron stars: The Crab pulsar and PSR 0525+21", *Astrophys. J.*, **288**, 191-195.

Alpar, M.A., Nandkumar, R. & Pines, D., 1986, "Vortex creep and the internal temperature of neutron stars: Timing noise in pulsars", *Astrophys. J.*, **311**, 197-213.

Alpar, M.A. & Ögelman, H., 1987, "Neutron star precession and the dynamics of the superfluid interior", *Astron. Astrophys.*, **185**, 196-202.

Alpar, M.A. & Pines, D., 1992, " Pulsar glitches and neutron star superfluidity – A 1992 perspective", preprint.

Anderson, P.W. & Itoh, N., 1975, "Pulsar glitches and restlessness as a hard superfluidity phenomenon", *Nature*, **256**, 25-27.

Arzoumanian, Z., Nice, D.J., Taylor, J.H. & Thorsett, S.E., 1994, "Timing behaviour of 96 radio pulsars", *Astrophys. J.*, **422**, 671-680.

Backer, D.C., 1976, "Pulsar average wave forms and hollow-cone beam models", *Astrophys. J.*, **209**, 895-907.

Backer, D.C., 1989, "Pulsars", in *Galactic and Extragalactic Radio Astronomy* (eds. Verschuur, G.L. & Kellermann, K.I.), pp. 480-521, Springer-Verlag Inc., New York.

Backer, D.C., 1993, "A pulsar timing tutorial and NRAO Green Bank observations of PSR 1257+12", in *Planets Around Pulsars* (eds. Phillips, J.A., Thorsett, J.E. & Kulkarni, S.R.), pp. 11-18, Astronomical Society of the Pacific, San Francisco.

Backer, D.C. & Hellings, R.W., 1986, "Pulsar timing and general relativity", *Ann. Rev. Astron. Astrophys.*, **24**, 537-575.

Bailes, M., Lyne, A.G. & Shemar, S.L., 1991, "A planet orbiting the neutron star PSR 1829-10", *Nature*, **352**, 311-313.

Bailes, M., Lyne, A.G. & Shemar, S.L., 1993, "Limits on pulsar planetary systems from the Jodrell Bank timing database", in *Planets Around Pulsars* (eds. Phillips, J.A., Thorsett, J.E. & Kulkarni, S.R.), pp. 19-30, Astronomical Society of the Pacific, San Francisco.

Bailes, M., Manchester, R.N., Kesteven, M.J., Norris, R.P. & Reynolds, J.E., 1990, "The proper motions of six southern radio pulsars", *Mon. Not. R. Astron. Soc.*, **247**, 322-326.

Baym, G., Pethick, C., Pines, D. & Ruderman, M., 1969, "Spin up in neutron stars: The future of the Vela pulsar", *Nature*, **224**, 872-874.

Blandford, R.D. & Narayan, R., 1985, "Low-frequency variability of pulsars", *Mon. Not. R. Astron. Soc.*, **213**, 591-611.

Blandford, R.D., Narayan, R. & Romani, R.W., 1984, "Arrival-time analysis for a millisecond pulsar", *J. Astrophys. Astr.*, **5**, 369-388.

Blandford, R.D. & Teukolsky, S.A., 1976, "Arrival-time analysis for a pulsar in a binary system", *Astrophys. J.*, **205**, 580-591.

Born, M. & Wolf, 1975, "Principles of Optics", Pergamon Press, Oxford.

Boynton, P.E., 1981, "Pulse timing and neutron star structure", in *Pulsars* (IAU symposium no. 95, eds. Sieber, W. & Wielebinski, R.), pp. 279-290, Riedel, Dordrecht.

Boynton, P.E. & Deeter, J.E., 1986, "Power spectra of the noise in rotation for 24 pulsars", preprint.

Boynton, P.E., Groth, E.J., Hutchinson, D.P., Nanos, G.P., Partridge, R.B., & Wilkinson, D.T., 1972, "Optical timing of the Crab pulsar, NP0532", *Astrophys. J.*, **175**, 217-241.

Brand, J., Blitz, L. & Wouterloot, J.G.A., 1986, "The velocity field of the outer Galaxy in the Southern Hemisphere", *Astron. Astrophys. Suppl. Ser.*, **65**, 537-550.

Chau, H.F., McCulloch, P.M., Nandkumar, R. & Pines, D., 1993, "Post-glitch relaxation following the ninth glitch of the Vela pulsar", *Astrophys. J.*, **413**, L113-L116.

Cheng, K.S., 1987a, "Outer magnetospheric fluctuations and pulsar timing noise", *Astrophys. J.*, **321**, 799-804.

Cheng, K.S., 1987b, "Could glitches inducing magnetospheric fluctuations produce low-frequency timing noise ?", *Astrophys. J.*, **321**, 805-812.

Cheng, K.S., 1989, "A model of pulsar timing noise", in *Timing Neutron Stars* (eds. Ögelman, H. & van den Heuvel, E.P.J.), pp. 503-509, Kluwer Academic Publishers, Dordrecht.

Cheng, K.S., Alpar, M.A., Pines, D. & Shaham, J., 1988, "Spontaneous superfluid unpinning and the inhomogeneous distribution of vortex lines in neutron stars", *Astrophys. J.*, **330**, 835-846.

Cheng, K.S., Ho, C. & Ruderman, M., 1986a, "Energetic radiation from rapidly spinning pulsars. I. Outer magnetospheric gaps", *Astrophys. J.*, **300**, 500-521.

Cheng, K.S., Ho, C. & Ruderman, M., 1986b, "Energetic radiation from rapidly spinning pulsars. II. Vela and Crab", *Astrophys. J.*, **300**, 522-539.

Coles, W.A., Frehlich, R.G., Rickett, B.J. & Codona, J.L., 1987, "Refractive scintillation in the interstellar medium", *Astrophys. J.*, **315**, 666-674.

Cordes, J.M., 1978, "Observational limits on the location of pulsar emission regions", *Astrophys. J.*, **222**, 1006-1011.

Cordes, J.M., 1980, "Pulsar Timing. II. Analysis of random walk timing noise: Application to the Crab pulsar", *Astrophys. J.*, **237**, 216-226.

Cordes, J.M., 1986, "Space velocities of radio pulsars from interstellar scintillation", *Astrophys. J.*, **311**, 183-196.

Cordes, J.M., 1993, "The detectability of planetary companions to radio pulsars", in *Planets Around Pulsars* (eds. Phillips, J.A., Thorsett, J.E. & Kulkarni, S.R.), pp. 43-60, Astronomical Society of the Pacific, San Francisco.

Cordes, J.M. & Downs, G.S., 1985, "JPL pulsar timing observations. III. Pulsar rotation fluctuations", *Astrophys. J. Suppl. Ser.*, **59**, 343-382.

Cordes, J.M., Downs, G.S. & Krause-Polstorff, J., 1988, "JPL pulsar timing observations. V. Macro and microjumps in the Vela pulsar 0833-45", *Astrophys. J.*, **330**, 847-869.

Cordes, J.M. & Greenstein, G., 1981, "Pulsar timing. IV. Physical models for timing noise processes", *Astrophys. J.*, **245**, 1060-1079.

Cordes, J.M. & Helfand, D.J., 1980, "Pulsar timing. III. Timing noise of 50 pulsars", *Astrophys. J.*, **239**, 640-650.

Cordes, J.M., Pidwerbetsky, A. & Lovelace, R.V.E., 1986, "Refractive and diffractive scattering in the interstellar medium", *Astrophys. J.*, **310**, 737-767.

Cordes, J.M., Weisberg, J.M. & Boriakoff, V., 1985, "Small-scale electron density turbulence in the interstellar medium", *Astrophys. J.*, **288**, 221-247.

Cordes, J.M., Weisberg, J.M., Frail, D.A., Spangler, S.R., & Ryan, M., 1991, "The galactic distribution of free electrons", *Nature*, **354**, 121-124.

Cordes, J.M., Wolszczan, A., Dewey, R.J., Blaskiewicz, M. & Stinebring, D.R., 1990, "Timing and scintillations of the millisecond pulsar 1937+214", *Astrophys. J.*, **349**, 245-261.

Costa, M.E., 1989, *Ph.D. Thesis*, University of Tasmania.

Costa, M.E., McCulloch, P.M. & Hamilton, P.A., 1991, "Polarization observations of 17 southern pulsars at 600 MHz", *Mon. Not. R. Astron. Soc.*, **252**, 13-18.

D'Alessandro, F., McCulloch, P.M., King, E.A., Hamilton, P.A. & McConnell, D., 1993, "Timing observations of southern pulsars - 1987 to 1991", *Mon. Not. R. Astron. Soc.*, **261**, 883-894.

D'Alessandro, F., McCulloch, P.M., Hamilton, P.A. & Deshpande, A.A., 1995, "The timing noise of 45 southern pulsars", *Mon. Not. R. Astron. Soc.*, in press.

Davis, M.M., Taylor, J.H., Weisberg, J.M. & Backer, D.C., 1985, "High-precision timing observations of the millisecond pulsar PSR 1937+21", *Nature*, **315**, 547-550.

de Deuge, M., 1985, *Honours Thesis*, University of Tasmania.

Deeter, J.E., 1984, "Techniques for the estimation of red power spectra. II. Evaluation of alternative methods", *Astrophys. J.*, **281**, 482-491.

Deeter, J.E. & Boynton, P.E., 1982, "Techniques for the estimation of red power spectra. I. Context and methodology", *Astrophys. J.*, **261**, 337-350.

Deeter, J.E., Boynton, P.E., Lamb, F.K. & Zylstra, G., 1989, "Vela X-1 pulse timing. II. Variations in pulse frequency", *Astrophys. J.*, **336**, 376-393.

Demiański, M. & Prószyński, M., 1979, "Does PSR0329+54 have companions?", *Nature*, **282**, 383-385.

Deshpande, A.A. & McCulloch, P.M., 1992, "An internal report on the performance of some pulse phase estimation procedures", Physics Department, University of Tasmania.

Deshpande, A.A. & Nityananda, R., 1990, "Statistics of refractive pulsar scintillation: effect of limited data length", *Astron. Astrophys.*, **231**, 199-201.

Dewey, R.J. & Cordes, J.M., 1989, "The scaling of radio pulsar timing noise with spin parameters", in *Timing Neutron Stars* (eds. Ögelman, H. & van den Heuvel, E.P.J.), pp. 119-124, Kluwer Academic Publishers, Dordrecht.

Dolginov, A.Z. & Stepinski, T.F., 1993, "On quasiperiodic variations of pulsars' periods: An alternative to the planetary interpretation of PSR 1257+12", in *Planets Around Pulsars* (eds. Phillips, J.A., Thorsett, J.E. & Kulkarni, S.R.), pp. 61-70, Astronomical Society of the Pacific, San Francisco.

Downs, G.S., 1982, "JPL pulsar timing observations: Spinups in PSR 0525+21", *Astrophys. J.*, **257**, L67-L70.

Downs, G.S. & Krause-Polstorff, J., 1986, "JPL pulsar timing observations. IV. Excess phase noise", *Astrophys. J. Suppl. Ser.*, **62**, 81-107.

Downs, G.S. & Reichley, P.E., 1983, "JPL pulsar timing observations. II. Geocentric arrival times", *Astrophys. J. Suppl. Ser.*, **53**, 169-240.

Flanagan, C.S., 1993, "A second giant glitch in PSR 1641-45", *Mon. Not. R. Astron. Soc.*, **260**, 643-646.

Fomalont, E.B., Goss, W.M., Lyne, A.G., Manchester, R.N. & Justtanont, K., 1992, "Positions and proper motions of pulsars", *Mon. Not. R. Astron. Soc.*, **258**, 497-510.

Foster, R.S. & Cordes, J.M., 1989, "Simulation of interstellar scattering effects on pulsar timing", in *Timing Neutron Stars* (eds. Ögelman, H. & van den Heuvel, E.P.J.), pp. 125-129, Kluwer Academic Publishers, Dordrecht.

Foster, R.S. & Cordes, J.M., 1990, "Interstellar propagation effects and the precision of pulsar timing", *Astrophys. J.*, **364**, 123-135.

Gardner, F.F., Morris, D. & Whiteoak, J.B., 1969, "The linear polarization of sources between 11 and 20 cm wavelengths", *Aust. J. Phys.*, **22**, 813-819.

Gardner, F.F. & Whiteoak, J.B., 1966, "The polarization of cosmic radio waves", *Ann. Rev. Astron. Astrophys.*, **4**, 245-292.

Gil, J.A., Jessner, A. & Kramer, M., 1993, "Are there really planets around PSR 1257+12 ?", *Astron. Astrophys.*, **271**, L17-L20.

Glendenning, N.K., 1990, "Modulation of pulsar signals by deformation of the star", *Astrophys. J.*, **359**, 186-191.

Glendenning, N.K., 1995, "Test of when free precession of a pulsar cannot mimic an orbiting planet", *Astrophys. J.*, **440**, 881-883.

Gold, T., 1968, "Rotating neutron stars as the origin of the pulsating radio sources", *Nature*, **218**, 731-732.

Goldreich, P. & Julian, W.H., 1969, "Pulsar electrodynamics", *Astrophys. J.*, **157**, 869-880.

Gordon, M.A., 1988, "HII regions and radio recombination lines", in *Galactic and Extragalactic Radio Astronomy* (eds. Verschuur, G.L. & Kellermann, K.I.), pp. 37-92, Springer-Verlag, New York.

Georgelin, Y.M. & Georgelin, Y.P., 1976, "The spiral structure of our galaxy determined from HII regions", *Astron. Astrophys.*, **49**, 57-79.

Green, A.R., McHardy, I.M. & Lehto, H.J., 1993, "On the nature of rapid X-ray variability in active galactic nuclei", *Mon. Not. R. Astron. Soc.*, **265**, 664-680.

Greenstein, G., 1979a, "Thermal-timing instability in neutron stars", *Nature*, **277**, 521-523.

Greenstein, G., 1979b, "Pulsar timing observations, X-ray transients, and the thermal-timing instability in neutron stars", *Astrophys. J.*, **231**, 880-895.

Greenstein, G., 1981, "Glitches, timing noise, and pulsar thermometry", in *Pulsars* (IAU symposium no. 95, eds. Sieber, W. & Wielebinski, R.), pp. 291-298, Riedel, Dordrecht.

Groth, E.J., 1975a, "Timing of the Crab pulsar. II. Method of analysis", *Astrophys. J. Suppl. Ser.*, **29**, 443-451.

Groth, E.J., 1975b, "Timing of the Crab pulsar. III. The slowing down and the nature of the random process", *Astrophys. J. Suppl. Ser.*, **29**, 453-465.

Gullahorn, G.E. & Rankin, J.M., 1982, "Pulsar timing irregularities", *Astrophys. J.*, **260**, 520-537.

Gupta, Y., Rickett, B.J. & Coles, W.A., 1993, "Refractive interstellar scintillation of pulsar intensities at 74 MHz", *Astrophys. J.*, **403**, 183-201.

Hamilton, P.A., Hall, P.J. & Costa, M.E., 1985, "Changing parameters along the path to the Vela pulsar", *Mon. Not. R. Astron. Soc.*, **214**, 5p-8p.

Hamilton, P.A. & Lyne, A.G., 1987, "Faraday rotation measurements on 163 pulsars", *Mon. Not. R. Astron. Soc.*, **224**, 1073-1081.

Hamilton, P.A., McCulloch, P.M., Ables, J.G. & Komesaroff, M.M., 1977, "Polarization characteristics of southern pulsars – I. 400 MHz observations", *Mon. Not. R. Astron. Soc.*, **180**, 1-18.

Hamilton, P.A., McCulloch, P.M., Manchester, R.N., Ables, J.G. & Komesaroff, M.M., 1977, "Detection of change in rotation measure of the Vela pulsar", *Nature*, **265**, 224-225.

Hankins, T.H. & Rickett, B.J., 1975, "Pulsar signal processing", in *Methods in Computational Physics* (eds. Alder, B., Fernbach, S. & Rotenberg, M.), vol. 14, pp. 56-129, Academic Press, New York.

Hankins, T.H. & Rickett, B.J., 1986, "Frequency dependence of pulsar profiles", *Astrophys. J.*, **311**, 684-693.

Harding, A.K., Shinbrot, T. & Cordes, J.M., 1990, "A chaotic attractor in timing noise from the Vela pulsar ?", *Astrophys. J.*, **353**, 588-596.

Hecht, E. & Zajac, A., 1987, "Optics", Addison-Wesley Publ. Co., USA.

Hewish, A., Bell, S.J., Pilkington, J.D.H., Scott, P.F. & Collins, R.A., 1968, "Observation of a rapidly pulsating radio source", *Nature*, **217**, 709-713.

Högbom, J.A., 1974, "Aperture synthesis with a non-regular distribution of interferometer baselines", *Astron. Astrophys. Suppl. Ser.*, **15**, 417-426.

Jones, P.B., 1988, "Excitation of small-amplitude free precession in the Crab pulsar", *Mon. Not. R. Astron. Soc.*, **235**, 545-550.

Jones, P.B., 1990a, "Rotation of the neutron-drip superfluid in pulsars: The resistive force", *Mon. Not. R. Astron. Soc.*, **243**, 257-262.

Jones, P.B., 1990b, "Rotation of the neutron-drip superfluid in pulsars: Temperature-dependence of the resistive force", *Mon. Not. R. Astron. Soc.*, **244**, 675-679.

Jones, P.B., 1990c, "Rotation of the neutron-drip superfluid in pulsars: Period discontinuities and internal temperatures", *Mon. Not. R. Astron. Soc.*, **246**, 315-323.

Jones, P.B., 1990d, "The generation of timing noise by superfluid rotation in pulsars", *Mon. Not. R. Astron. Soc.*, **246**, 364-367.

Jones, P.B., 1991, "Rotation of the neutron-drip superfluid in pulsars: The interaction and pinning of vortices", *Astrophys. J.*, **373**, 208-212.

Jones, P.B., 1992, "Rotation of the neutron-drip superfluid in pulsars: The Kelvin phonon contribution to dissipation", *Mon. Not. R. Astron. Soc.*, **257**, 501-506.

Jones, P.B., 1993, "Rotation of the neutron-drip superfluid in pulsars: Evidence for corotating vortices", *Mon. Not. R. Astron. Soc.*, **263**, 619-627.

Kaspi, V.M. & Stinebring, D.R., 1992, "Long term pulsar flux monitoring and refractive interstellar scintillation", *Astrophys. J.*, **392**, 530-542.

Kaspi, V.M., Taylor, J.H. & Ryba, M.F., 1994, "High precision timing of millisecond pulsars. III. Long-term monitoring of PSRs B1885+09 and B1937+21", *Astrophys. J.*, **428**, 713-728.

Kaspi, V.M. & Wolszczan, A., 1993, "A preliminary analysis of pulse profile stability in PSR 1257+12", in *Planets Around Pulsars* (eds. Phillips, J.A., Thorsett, J.E. & Kulkarni, S.R.), pp. 81-86, Astronomical Society of the Pacific, San Francisco.

Klekociuk, A.R., 1989, *PhD thesis*, University of Tasmania.

Koribalski, B., Johnston, S., Weisberg, J.M. & Wilson, W., 1995, "HI line measurements of eight southern pulsars", *Astrophys. J.*, **441**, 756-764.

Kraus, J.D., 1950, "Antennas", McGraw-Hill Book Co. Inc., N.Y.

Kraus, J.D., 1986, "Radio Astronomy", 2nd ed., Cygnus-Quasar Books, Ohio.

LaBrecque, D.R., Rankin, J.M. & Cordes, J.M., 1994, "Long-term intensity variations of 20 pulsars", *Astron. J.*, **108**, 1854-1859.

Lamb, F.K., 1981, "Neutron star properties from observations of pulsars and pulsing X-ray sources", in *Pulsars* (IAU symposium no. 95, eds. Sieber, W. & Wielebinski, R.), pp. 303-319, Riedel, Dordrecht.

Lamb, F.K., Pines, D. & Shaham, J., 1978a, "Period variations in pulsating X-ray sources. I. Accretion flow parameters and neutron star structure from timing observations", *Astrophys. J.*, **224**, 969-987.

Lamb, F.K., Pines, D. & Shaham, J., 1978b, "Period variations in pulsating X-ray sources. II. Torque variations and stellar response", *Astrophys. J.*, **225**, 582-590.

Lindsey, W.C. & Chie, C.M., 1976, "Theory of oscillator instability based upon structure functions", *Proc. IEEE*, **64**, 1652-1666.

Lorimer, D.R., Yates, J.A., Lyne, A.G. & Gould D.M., 1995, "Multifrequency flux density measurements of 280 pulsars", *Mon. Not. R. Astron. Soc.*, **273**, 411-421.

Lyne, A.G., 1987, "A massive glitch in an old pulsar", *Nature*, **326**, 569-571.

Lyne, A.G., 1992, "Glitches as probes of neutron star interiors", in *Pulsars as Physics Laboratories* (eds. Blandford, R.D., Hewish, A., Lyne, A.G. & Mestel, L.), pp. 29-37, Oxford University Press, Cambridge, 1993.

Lyne, A.G. & Manchester, R.N., 1988, "The shape of pulsar radio beams", *Mon. Not. R. Astron. Soc.*, **234**, 477-508.

Lyne, A.G. & Pritchard, R.S., 1987, "A glitch in the Crab pulsar", *Mon. Not. R. Astron. Soc.*, **229**, 223-226.

Lyne, A.G., Pritchard, R.S. & Smith, F.G., 1988, "Crab pulsar timing 1982-87", *Mon. Not. R. Astron. Soc.*, **233**, 667-676.

Lyne, A.G., Pritchard, R.S. & Smith, F.G., 1993, "23 years of Crab pulsar rotational history", *Mon. Not. R. Astron. Soc.*, **265**, 1003-1012.

Lyne, A.G. & Smith, F.G., 1989, "Pulsar rotation measures and the Galactic magnetic field", *Mon. Not. R. Astron. Soc.*, **237**, 533-541.

Lyne, A.G. & Smith, F.G., 1990, *Pulsar Astronomy*, Cambridge University Press, Cambridge.

McCulloch, P.M., Hamilton, P.A., Manchester, R.N. & Ables, J.G., 1978, "Polarization characteristics of southern pulsars – II. 640 MHz observations", *Mon. Not. R. Astron. Soc.*, **183**, 645-676.

McCulloch, P.M., Hamilton, P.A., McConnell, D. & King, E.A., 1990, "The Vela glitch of Christmas 1988", *Nature*, **346**, 822-824.

McCulloch, P.M., Hamilton, P.A. & Royle, G.W.R. & Manchester, R.N., 1983, "Daily observations of a large period jump of the Vela pulsar", *Nature*, **302**, 319-321.

McCulloch, P.M., Klekociuk, A.R., Hamilton, P.A. & Royle, G.W.R., 1987, "Daily observations of three period jumps of the Vela pulsar", *Astrophys. J.*, **40**, 725-730.

McCulloch, P.M., Komesaroff, M.M., Ables, J.G., Hamilton, P.A. & Rankin, J.M., 1973, "Improved parameters for 15 southern pulsars", *Astrophys. Lett.*, **14**, 169-170.

McKenna, J. & Lyne, A.G., 1990, "PSR1737-30 and period discontinuities in young pulsars", *Nature*, **343**, 439-450.

Malhotra, R., 1993, "Orbital dynamics of PSR 1257+12 and its two planetary companions", in *Planets Around Pulsars* (eds. Phillips, J.A., Thorsett, J.E. & Kulkarni, S.R.), pp. 89-106, Astronomical Society of the Pacific, San Francisco.

Manchester, R.N., 1972, "Pulsar rotation and dispersion measures and the Galactic magnetic field", *Astrophys. J.*, **172**, 43-52.

Manchester, R.N., 1974, "Structure of the local Galactic magnetic field", *Astrophys. J.*, **188**, 637-644.

Manchester, R.N., 1992, "Radio pulsar timing", in *The Structure and Evolution of Neutron Stars* (eds. Pines, D., Tamagaki, R. & Tsuruta, S.), pp. 32-49, Addison-Wesley Publishing Co., California.

Manchester, R.N., Durdin, J.M. & Newton, L.M., 1985, "A second measurement of a pulsar braking index", *Nature*, **313**, 374-376.

Manchester, R.N., Hamilton, P.A. & McCulloch, P.M., 1980, "Polarization characteristics of southern pulsars – III. 1612 MHz observations", *Mon. Not. R. Astron. Soc.*, **192**, 153-177.

Manchester, R.N., Newton, L.M., Goss, W.M. & Hamilton, P.A., 1978, "Detection of a large period discontinuity in the longer period pulsar PSR 1641-45", *Mon. Not. R. Astron. Soc.*, **184**, 35p-37p.

Manchester, R.N., Newton, L.M., Hamilton, P.A., & Goss, W.M., 1983, "Pulsar timing observations at Tidbinbilla – 1975 to 1981", *Mon. Not. R. Astron. Soc.*, **202**, 269-285.

Manchester, R.N. & Peterson, B.A., 1989, "A braking index for PSR 0540-69", *Astrophys. J.*, **342**, L23-L25.

Manchester, R.N. & Taylor, J.H., 1972, "Parameters of 61 pulsars", *Astrophys. Lett.*, **10**, 67-69.

Manchester, R.N. & Taylor, J.H., 1977, *Pulsars*, W.H. Freeman & Co., San Francisco.

Manchester, R.N. & Taylor, J.H., 1981, "Observed and derived parameters for 330 pulsars", *Astron. J.*, **86**, 1953-1973.

Manchester, R.N., Taylor, J.H. & Huguenin, G.R., 1973, "Frequency dependence of pulsar polarization", *Astrophys. J.*, **179**, L7-L10.

Megeath, S.T., Herter, T., Gull, G.E. & Houck, J.R., 1990, "Infrared and radio measurements of the density structure of compact HII regions", *Astrophys. J.*, **356**, 534-543.

Michel, F.C., 1982, "Theory of pulsar magnetospheres", *Rev. Mod. Phys.*, **54**, 1-66.

Michel, F.C., 1987, "A pulsar emission model: Observational tests", *Astrophys. J.*, **322**, 822-830.

Michel, F.C., Hawthorn, J.B. & Lyne, A.G., 1990, "Quasi-linear response in a glitching pulsar", *Mon. Not. R. Astron. Soc.*, **246**, 624-627.

Nelson, R.W., Finn, L.S. & Wasserman, I., 1990, "Trompe l'oeil binary pulsars", *Astrophys. J.*, **348**, 226-231.

Newton, L.M., Manchester, R.N. & Cooke, D.J., 1981, "Pulsar parameters from timing observations", *Mon. Not. R. Astron. Soc.*, **194**, 841-850.

Ostriker, J.P. & Gunn, J.E., 1969, "On the nature of pulsars. I. Theory", *Astrophys. J.*, **157**, 1395-1417.

Pacini, F., 1968, "Rotating neutron stars, pulsars and supernova remnants", *Nature*, **219**, 145-146.

Pandharipande, V.R., Pines, D. & Smith, R.A., 1976, "Neutron star structure – Theory, observation and speculation", *Astrophys. J.*, **208**, 550-566.

Phillips, C.J., 1993, *Honours Thesis*, University of Tasmania.

Phillips, J.A. & Wolszczan, A., 1991, "Time variability of pulsar dispersion measures", *Astrophys. J.*, **382**, L27-L30.

Phillips, J.A. & Wolszczan, A., 1992, "Precision measurements of pulsar dispersion", *Astrophys. J.*, **385**, 273-81.

Pines, D. & Alpar, M.A., 1985, "Superfluidity in neutron stars", *Nature*, **316**, 27-32.

Pines, D. & Alpar, M.A., 1992, "Inside neutron stars: A 1990 perspective", in *The Structure and Evolution of Neutron Stars* (eds. Pines, D., Tamagaki, R. & Tsuruta, S.), pp. 7-31, Addison-Wesley Publishing Co., California.

Pines, D. & Shaham, J., 1972, "Microquakes and macroquakes in neutron stars", *Nature*, **235**, 43-49.

Pines, D., Shaham, J. & Ruderman, M., 1972, "Corequakes and the Vela pulsar", *Nature Phys. Sci.*, **237**, 83-84,96.

Prentice, A.J.R. & ter Haar, D., 1969, "On HII regions and pulsar distances", *Mon. Not. R. Astron. Soc.*, **146**, 423-444.

Press, W.H. & Rybicki, G.B., 1989, "Fast algorithm for spectral analysis of unevenly sampled data", *Astrophys. J.*, **338**, 277-280.

Qiao, G., Manchester, R.N., Lyne, A.G. & Gould, D.M., 1995, "Polarization and Faraday rotation measurements of southern pulsars", *Mon. Not. R. Astron. Soc.*, **274**, 572-588.

Radhakrishnan, V., 1991, "The polarization of pulsar radiation", in *The Magnetospheric Structure and Emission Mechanisms of Radio Pulsars* (IAU colloquium no. 128, eds. Hankins, T., Rankin, J. & Gil, J.), Uni. Zielona Gora Press, Poland.

Radhakrishnan, V. & Cooke, D.J., 1969, "Magnetic poles and the polarization structure of pulsar radiation", *Astrophys. Lett.*, **3**, 225-229.

Radhakrishnan, V. & Rankin, D.J., 1990, "Toward an empirical theory of pulsar emission. V. On the circular polarization in pulsar radiation", *Astrophys. J.*, **352**, 258-266.

Rand, R.J. & Lyne, A.G., 1994, "New rotation measures of distant pulsars in the inner Galaxy and magnetic field reversals", *Mon. Not. R. Astron. Soc.*, **268**, 497-505.

Rankin, J.M., 1983, "Toward an empirical theory of pulsar emission: I. Morphological taxonomy", *Astrophys. J.*, **274**, 333-358.

Rankin, J.M., 1986, "Toward an empirical theory of pulsar emission. III. Mode changing, drifting subpulses, and pulse nulling", *Astrophys. J.*, **301**, 901-922.

Rankin, J.M., 1990, "Toward an empirical theory of pulsar emission. IV. Geometry of the core emission region", *Astrophys. J.*, **352**, 247-257.

Rankin, J.M., Campbell, D.B., Isaacman, R.B., & Payne, R.R., 1988, "The Crab Nebula: Secular variations in the Faraday rotation of the pulsar and the great 1974-5 scattering event", *Astron. Astrophys.*, **202**, 166-172.

Rasio, F.A., Nicholson, P.D., Shapiro, S.L. & Teukolsky, S.A., 1993, "Orbital evolution of the PSR 1257+12 planetary system", in *Planets Around Pulsars* (eds. Phillips, J.A., Thorsett, J.E. & Kulkarni, S.R.), pp. 107-119, Astronomical Society of the Pacific, San Francisco.

Rawley, L.A., Taylor, J.H. & Davis, M.M., 1988, "Fundamental astrometry and millisecond pulsars", *Astrophys. J.*, **326**, 947-953.

Rees, M.J., 1993, "Concluding remarks", in *Planets Around Pulsars* (eds. Phillips, J.A., Thorsett, J.E. & Kulkarni, S.R.), pp. 367-370, Astronomical Society of the Pacific, San Francisco.

Richards, D.W., Pettengill, G.H., Counselman, C.C. & Rankin, J.M., 1970, "Sinusoidal oscillation in arrival times of pulses from NP 0532", *Astrophys. J.*, **160**, L1-L6.

Rickett, B.J., 1969, "Frequency structure of pulsar intensity variations", *Nature*, **221**, 158-159.

Rickett, B.J., 1977, "Interstellar scattering and scintillation of radio waves", *Ann. Rev. Astron. Astrophys.*, **15**, 479-504.

Rickett, B.J., 1986, "Refractive interstellar scintillation of radio sources", *Astrophys. J.*, **307**, 564-574.

Rickett, B.J., 1990, "Radio propagation through the turbulent interstellar plasma", *Ann. Rev. Astron. Astrophys.*, **28**, 561-605.

Rickett, B.J., Coles, W.A. & Bourgois, G., 1984, "Slow scintillation in the interstellar medium", *Astron. Astrophys.*, **134**, 390-395.

Rickett, B.J. & Lyne, A.G., 1990, "Intensity variations of the Crab pulsar and refractive interstellar scintillation", *Mon. Not. R. Astron. Soc.*, **244**, 68-75.

Ritchings, R.T., 1976, "Pulsar single pulse intensity measurements and pulse nulling", *Mon. Not. R. Astron. Soc.*, **176**, 249-263.

Roberts, D.H., Lehar, J. & Dreher, J.W., 1987, "Time series analysis with CLEAN. I. Derivation of a spectrum", *Astron. J.*, **93**, 968-989.

Rohlfs, K., 1986, "Tools of Radio Astronomy", Springer-Verlag, Berlin.

Romani, R.W., Narayan, R., & Blandford, R., 1986, "Refractive effects in pulsar scintillation", *Mon. Not. R. Astron. Soc.*, **220**, 19-49.

Ruderman, M.A., 1968, "Crystallization and torsional oscillations of superdense stars", *Nature*, **218**, 1128-1129.

Ruderman, M.A., 1969, "Neutron starquakes and pulsar periods", *Nature*, **223**, 597-598.

Ruderman, M.A., 1970a, "Long-period oscillations in rotating neutron stars", *Nature*, **225**, 619-620.

Ruderman, M.A., 1970b, "Pulsar wobble and neutron starquakes", *Nature*, **225**, 838-839.

Ruderman, M.A., 1972, "Pulsars: Structure and Dynamics", *Ann. Rev. Astron. Astrophys.*, **10**, 427-476.

Ruderman, M.A., 1976, "Crust-breaking by neutron superfluids and the Vela pulsar glitches", *Astrophys. J.*, **203**, 213-222.

Ruderman, M., 1991, "Neutron star crustal plate tectonics. III. Cracking, glitches, and gamma-ray bursts", *Astrophys. J.*, **382**, 587-593.

Ruderman, M., 1992, "Neutron star crust breaking and magnetic field evolution", in *The Structure and Evolution of Neutron Stars* (eds. Pines, D., Tamagaki, R. & Tsuruta, S.), pp. 353-370, Addison-Wesley Publishing Co., California.

Ruderman, M.A. & Sutherland, P.G., 1975, "Theory of pulsars: polar gaps, sparks, and coherent microwave radiation", *Astrophys. J.*, **196**, 51-72.

Rutman, J., 1978, "Characterisation of phase and frequency instabilities in precision frequency sources: fifteen years of progress", *Proc. IEEE*, **66**, 1048-1075.

Ryba, M.F. & Taylor, J.H., 1991, "High-precision timing of millisecond pulsars. I. Astrometry and masses of the PSR 1855+09 system", *Astrophys. J.*, **371**, 739-748.

Scheuer, P.A.G., 1968, "Amplitude variations in pulsed radio sources", *Nature*, **218**, 920-922.

Schwarz, U.J., 1978, "Mathematical-statistical description of an iterative beam-removing technique (method CLEAN)", *Astron. Astrophys.*, **65**, 345-356.

Shaham, J., 1977, "Free precession of neutron stars: Role of possible vortex pinning", *Astrophys. J.*, **214**, 251-260.

Sieber, W., 1982, "Causal relationship between pulsar long-term intensity variations and the interstellar medium", *Astron. Astrophys.*, **113**, 311-313.

Siegman, B.C., Manchester, R.N. & Durdin, J.M., 1993, "Timing parameters for 59 pulsars", *Mon. Not. R. Astron. Soc.*, **262**, 449-455.

Smith, F.G., 1977, *Pulsars*, Cambridge University Press, Cambridge.

Standish, M. (Jr.), 1982, "Orientation of the JPL Ephemerides, DE200/LE200, to the Dynamical Equinox of J2000", *Astron. Astrophys.*, **114**, 297-302.

Stinebring, D.R. & Condon, J.J., 1990, "Pulsar flux stability and refractive interstellar scintillation", *Astrophys. J.*, **352**, 207-221.

Stinebring, D.R., Ryba, M.F., Taylor, J.H. & Romani, R.W., 1990, "Cosmic gravitational-wave background: limits from millisecond pulsar timing", *Phys. Rev. Lett.*, **65**, 285-288.

Suleymanova, S.A. & Shitov, Y.P., 1994, "Secular variations of the integrated pulse profile of, and torque on, PSR 2217+47: Precession of the neutron star ?", *Astrophys. J.*, **322**, L17-L20.

Taylor, J.H., 1989, "Timing binary and millisecond pulsars", in *Timing Neutron Stars* (eds. Ögelman, H. & van den Heuvel, E.P.J.), pp. 17-26, Kluwer Academic Publishers, Dordrecht.

Taylor, J.H., 1992, "Pulsar timing and relativistic gravity", in *Pulsars as Physics Laboratories* (eds. Blandford, R.D., Hewish, A., Lyne, A.G. & Mestel, L.), pp. 117-134, Oxford University Press, Cambridge, 1993.

Taylor, J.H. & Cordes, J.M., 1993, "Pulsar distances and the galactic distribution of free electrons", *Astrophys. J.*, **411**, 674-684.

Taylor, J.H., Hulse, R.A., Fowler, L.A., Gullahorn, G.E. & Rankin, J.M., 1976, "Further observations of the binary pulsar PSR 1913+16", *Astrophys. J.*, **206**, L53-L58.

Taylor, J.H., Manchester, R.N. & Lyne, A.G., 1993, "Catalog of 558 pulsars", *Astrophys. J. Suppl. Ser.*, **88**, 529-568.

Taylor, J.H. & Stinebring, D.R., 1986, "Recent progress in the understanding of pulsars", *Ann. Rev. Astron. Astrophys.*, **24**, 285-327.

Taylor, J.H. & Weisberg, J.M., 1989, "Further experimental tests of relativistic gravity using the binary pulsar PSR 1913+16", *Astrophys. J.*, **345**, 434-450.

Taylor, J.H., Wolszczan, A., Damour, T. & Weisberg, J.M., 1992, "Experimental constraints on strong-field relativistic gravity", *Nature*, **355**, 132-136.

Thomson, R.C. & Nelson, A.H., 1980, "The interpretation of pulsar rotation measures and the magnetic field of the Galaxy", *Mon. Not. R. Astron. Soc.*, **191**, 863-870.

Trümper, J., Kahabka, P., Ögelman, H., Pietsch, W. & Voges, W., 1986, "EXOSAT observations of the 35 day cycle of Hercules X-1: Evidence for neutron star precession", *Astrophys. J.*, **300**, L63-L67.

Thorsett, S.E. & Phillips, J.A., 1992, "Rocks around the clock: Limits on pulsar planetary systems", *Astrophys. J.*, **387**, L69-L71.

Thorsett, S.E., Phillips, J.A. & Cordes, J.M., 1993, "A search for planets in archival timing data: The JPL data set", in *Planets Around Pulsars* (eds. Phillips, J.A., Thorsett, J.E. & Kulkarni, S.R.), pp. 31-33, Astronomical Society of the Pacific, San Francisco.

van den Heuvel, E.P.J., 1993, "Formation and evolution of pulsars", in *Planets Around Pulsars* (eds. Phillips, J.A., Thorsett, J.E. & Kulkarni, S.R.), pp. 123-148, Astronomical Society of the Pacific, San Francisco.

van Ommen, T.D., 1992, *Ph.D. Thesis*, University of Tasmania.

Weisberg, J.M., Siegel, M.H., Frail, D.A. & Johnston, S., 1995, "Neutral hydrogen absorption measurements of four distant pulsars and the electron density in the inner Galaxy", *Astrophys. J.*, **447**, 204-210.

Weisberg, J.M. & Taylor, J.H., 1984, "Observations of post-Newtonian timing effects in the binary pulsar PSR 1913+16", *Phys. Rev. Lett.*, **52**, 1348-1350.

Wolszczan, A. & Frail, D.A., 1992, "A planetary system around the millisecond pulsar PSR1257+12", *Nature*, **355**, 145-147.

Wolszczan, A., 1993, "PSR 1257+12 and its planetary companions", in *Planets Around Pulsars* (eds. Phillips, J.A., Thorsett, J.E. & Kulkarni, S.R.), pp. 3-10, Astronomical Society of the Pacific, San Francisco.

Wolszczan, A., 1994, "Toward planets around neutron stars", *Astrophys. Sp. Sci.*, **212**, 67-75.

Wu, X. & Chian, A.C.-L., 1995, "Temporal variation of pulsar dispersion measure", *Astrophys. J.*, **443**, 261-264.

Wu, X., Manchester, R.N., Lyne, A.G. & Qiao, G., 1993, "Mean pulse polarization of southern pulsars at 1560 MHz", *Mon. Not. R. Astron. Soc.*, **261**, 630-646.

Xilouris, K.M., Rankin, J.M., Seiradakis, J.H. & Sieber, W., 1991, "Polarimetric observations of 20 weak pulsars at 1700 MHz", *Astron. Astrophys.*, **241**, 87-97.

Xilouris, K.M., Seiradakis, J.H., Gil, J., Seiber, W. & Wielebinski, R., 1995, "Pulsar polarimetric observations at 10.55 GHz", *Astron. Astrophys.*, **293**, 153-165.